_____   _____
Datum   Unterschrift

Ciò che appare non è
e ciò che è non appare

Aknowledgements

Abstract

The role of simulations for characterising material properties is becoming increasingly relevant in many research fields, due to the large amount of information calculations can provide and due to their accuracy and reliability. On one side, simulations can be successfully exploited for purely theoretical investigations, where they can be of enormous advantage for the design of new materials with innovative or tailored properties. On the other side, they can support and complement experiments, thanks to their capability of investigating structures and properties not or not easily accessible in experiments.

Within the present work, density functional theory (DFT) simulations are applied to the study of technologically relevant hybrid inorganic organic systems, that play a fundamental role for numerous organic (opto-)electronic applications.

A consistent part of the thesis deals with the investigation of structural and electronic properties of interfaces between coinage metals and self-assembled monolayers (SAMs) of organic molecules. Prototypical systems are thiol based SAMs on the Au(111) surface, due to their stability and ease of preparation. As alternative to thiols, selenoles have been recently proposed. They have the same valence electron configuration and could show superior properties in terms of film quality. In this context, the stability of thiol and selenol based aromatic SAMs is investigated. Both experiments and simulations show that the strength of the Au–Se bond leads to the weakening of the bond between the Se docking group and the molecular backbone. Thanks to the simulations, the crucial impact of surface reconstructions could be identified.

SAM covered metals are often present in organic electronic devices for multiple purposes An important one is the modification of the electrode work function and the consequent adjustment of the energy level alignment at metal/semiconductor interfaces. This advantageous modification is due to so called collective electrostatics effects. They are based on the feature of periodically arranged dipolar units of inducing shifts in the electrostatic potential energy. In this work several metal/SAM interfaces are characterised, in particular SAMs of mono-, bi- and tridentate thiols on the Au(111) surface, combining the calculated results with experimental ones. The joint investigations allow fully understanding structural and electronic properties and how the latter are affected by the aforementioned collective electrostatic effects. Collective electrostatic effects are not only responsible for modifying the work function of the metal substrate, but also relevantly affect the core level binding energies within the SAM. This allows probing electrostatic shifts by means of X-ray photoelectron spectroscopy (XPS). For atoms close to the metal surface, the situation can be more complicated, due to the superposition of electrostatic and chemical effects. These aspects are discussed by means of a fictitious system of K atoms on the Au(111) surface at different coverages, that serves as a prototypical simple model to rationalise the impact of chemical and electrostatic effects on core level energies. For this specific interface the effects almost quantitatively compensate, with the charge transferred from the substrate to the adsorbate playing a crucial role.

As discussed above, collective electrostatic effects are largely investigated and exploited for modifying metal/organic interfaces. However, for other classes of materials their potential

is still unexplored. In the last part of the thesis an original way to combine collective electrostatic effects with metal/organic frameworks (MOFs) for organic electronic applications is presented. The approach proposed in this work is based on the introduction of polar apical linkers to modify the potential energy landscape, such that the resulting profile mimics the p-i-n junction commonly present in conventional inorganic semiconductor based solar cells.

Kurzfassung

Aufgrund ihrer hohen Genauigkeit gewinnen computerunterstützte Simulationen von Materialeigenschaften immer mehr an Bedeutung. Dies betrifft sowohl das computerbasiert Design neuartiger Materialien mit speziellen Eigenschaften, als auch die Erklärung von Experimenten. Letzteres profitiert davon, dass Simulationen Einblicke auf (sub)atomarer Skala erlauben.

Im Zuge der vorgelegten Dissertation werden auf Dichtefunktionaltheorie (DFT) basierende Simulationen verwendet, um hybride anorganisch/organische Materialien zu untersuchen. Diese spielen beispielsweise im Bereich der organischen (Opto)elektronik eine zentrale Rolle.

Ein wesentlicher Teil der Arbeit beschäftigt sich dabei mit strukturellen und elektronischen Eigenschaften von Grenzflächen zwischen Metallen und organischen selbstassemblierten Monolagen (SAMs). Diese werden typischerweise mittels Thiolen an Edelmetalloberflächen (beispielsweise Au(111)) gebunden, da sie sich Thiole vergleichsweise einfach herstellen lassen und besonders stabil sind. Als Alternative zu Thiolen wurden auch Selenole vorgeschlagen. Diese besitzen die gleiche elektronische Konfiguration, ergeben aber typischerweise Schichten höherer Qualität. In dem Kontext wurden vergleichende Studien zur Stabilität von thiolat- und selenolatgebundenen SAMs durchgeführt, wobei sowohl die Experimente als auch die Simulationen klar zeigen, dass die stärkere Selen-Au Bindung zu einer Schwächung der Bindung zwischen der Selendockinggruppe und dem Rest des Moleküls führt. Die Simulationen zeigen außerdem, dass sich die experimentellen Ergebnisse nur erklären lassen, wenn man das Vorhandensein von Metalladatomen auf der Oberfläche annimmt.

Für praktische Anwendungen von thiolatgebundenen SAMs in elektronischen Bauelementen ist vor allem deren Fähigkeit relevant, die Austrittsarbeiten von Metallelektroden zu verändern.

Verantwortlich für die Austrittsarbeitsänderung sind dabei sogenannte kollektive elektrostatische Effekte, die in Systemen mit periodisch angeordneten Dipolelementen auftreten und zu einer sprunghaften Verschiebung des elektrostatischen Potentials führen. Im Zuge der vorliegenden Arbeit wurden deshalb verschiedene Metall/SAM Grenzflächen im Hinblick auf ihre elektronische Struktur untersucht, wobei sowohl die polaren Elemente in den adsorbierten Molekülen, als auch die Struktur der Dockinggruppen variiert wurden (hier kommen ein-, zwei- und dreizähnigen Thiole zum Einsatz). Die Simulationsergebnisse wurden dabei konsequent mit experimentellen Daten verglichen. Dadurch konnte ein umfassendes Verständnis der strukturellen und elektronischen Eigenschaften der Grenzflächen inklusive der Auswirkungen der kollektiven elektrostatischen Effekte erzielt werden. Interessanterweise beeinflussen kollektive elektrostatische Effekte nicht nur, wie bereits erwähnt, die Austrittsarbeit von Metallsubstraten, sie verändern auch die Core-level Bindungsenergien der Atome in der SAM. Dies erlaubt eine lokale Bestimmung der elektrostatischen Energie mittels Röntgenphotoelektronenspektroskopie (XPS). Für Atome in unmittelbarer Nähe der Grenzfläche können allerdings Komplikationen auftreten, da sich dort elektrostatische und chemische Verschiebungen (als Folge lokaler Ladungsdichteumverteilungen) überlagern. Um diesen Umstand klar darzustellen, wurde zusätzlich eine K/Au(111) Grenzfläche als prototypisches und einfach zu analysierendes Modellsystem untersucht. Interessanterweise kommt

es für diese Grenzfläche zu einer fast vollständigen Kompensation der elektrostatischen und chemischen Verschiebungen der Core-level Bindungsenergien.

Der letzte Abschnitt der Dissertation zeigt, dass kollektive elektrostatische Effekte nicht nur (wie in der vorherigen Kapiteln gezeigt) die elektronischen Eigenschaften von Grenzflächen massiv beeinflussen können. Sie können auch dazu eingesetzt werden, die elektronischen Eigenschaften von 3D ausgedehnten Materialien zu manipulieren. Dies wird für den periodischen Einbau polarer Linker in so genannte metall-organischen Gerüste (MOFs) gezeigt. Dabei lassen sich Bandverläufe wie in konventionellen, auf p-i-n Übergängen in anorganischen Halbleitern basierten Solarzelle erreichen, ohne dass es nötig ist, die eingesetzten Materialien zu dotieren.

Preface

This work is structured as a so-called semicumulative Ph.D. thesis and as such includes both the scientific published and submitted papers I contributed to and additional data concerning not yet published projects.

An introductory section provides an overview of the investigated materials and their applications, to put into context the work carried out in the thesis. The introduction is followed by a chapter about the adopted methodology, where the basics of density functional theory and the employed modelling approach are presented. In the results section the work carried out during the Ph.D. is presented. In the final section the whole work is summarised, with some concluding remarks and a perspective outlook.

Almost all the projects I contributed to were joint experimental and theoretical investigations. Since reporting only the discussions relative to the modelling parts would have been incomplete and difficult to follow, I have included the whole papers. The papers contained in this thesis are, therefore, not only based on my own work but are the result of the collaboration of several groups, whose contributions will be specified before each paper.

A further paper of which I am coauthor[1] is not included in the thesis.

Contents

1 Introduction

Computational material science is a relatively young interdisciplinary area of research that brings together chemistry, physics, engineering, computer science and material science. A considerably wide variety of computational methods exists, that allow investigating properties and responses of materials at different time and length scales. Specifically, the subject of the present work are quantum-mechanical simulations, whose peculiarity is the explicit modelling of every electron present in the system. Achieving such an atomistic level of understanding is crucial for many technological applications, when, for example, dealing with miniaturisation processes.

In this sense, in the last years computational quantum mechanics based methods have become particularly important for investigating materials, both from a purely theoretical point of view and in combination with the established experimental techniques. Indeed, bringing together experimental and computational methods is a very effective tool to get a complete and detailed characterisation of materials. As already mentioned, calculations allow to explore material properties with atomic resolution, to characterise metastable states that could not be experimentally measured and to model ideal structures, not accessible in the experiments, useful to support and understand the interpretation of experimental data. Moreover, simulations also have a valuable role for the design of new materials and the prediction of their properties, providing a convenient way to identify the most promising candidates for the synthesis. On the other hand, as will be explained in more detail in the following, specific experimental information is needed for the calculations: modelling a material without having any experimental information, such as for instance the size of the unit cell or the packing density, would not be feasible.

The materials investigated in this work can be classified as hybrid inorganic-organic materials, as they consist of a metallic and an organic component. Specifically, the main part of the work will be dealing with metal/self-assembled monolayer (SAM) interfaces, systems of particular interest for the increasingly growing field of organic electronics. The structural and electronics properties of several interfaces will be investigated, putting particular emphasis on the level of insight and understanding that simulations allow achieving.

A minor part of the thesis will regard a different family of hybrid inorganic-organic materials, namely metal organic frameworks (MOFs). For this already widely used class of materials an original and innovative application for the field of organic photovoltaics will be presented based on collective electrostatic effects, a well known phenomenon largely exploited in the applications of the aforementioned metal/SAMs interfaces and explained in detail in the following sections.

2 Systems of interest

2.1 Self-assembled monolayers

The process of self-assembly is the spontaneous and autonomous aggregation of elementary constituents into more complex hierarchical patterns without any external intervention. In the natural world self-assembly occurs ubiquitously, with some of the most notable examples being the formation of folded globular proteins and the droplets that lipids form in aqueous phase[2,3].

On a molecular level, according to the definition of A. Ulman[3] *"SAMs are ordered molecular assemblies formed by the adsorption of an active surfactant on a solid surface, with the order within the two-dimensional system being driven by a spontaneous chemical synthesis at the interface as the supramolecular system reaches the equilibrium"*.

The interaction of the molecules with the substrate can have either a physical or a chemical nature, depending on whether it is driven more by non-covalent forces or by chemical hybridisation of the molecular orbitals with the substrate ones. Subject of this work are chemisorbed organic SAMs, meaning that the constituents of the monolayer are organic molecules covalently bonded to the underlying substrate.

In chemically bonded SAMs three main parts can be identified: a docking group, that provides the anchoring to the substrate, a tail group, that interacts with the outer environment, acting essentially as the new surface, and a spacer or backbone in between, that is responsible for the molecular ordering and the self-assembly process. In figure 2.1 a prototypical cyano substituted biphenylthiolate SAM on the Au(111) surface is shown. The different constituents are indicated: the S atoms act as docking groups, the biphenyl moiety is the backbone and the terminal CN functionality is the tail group.

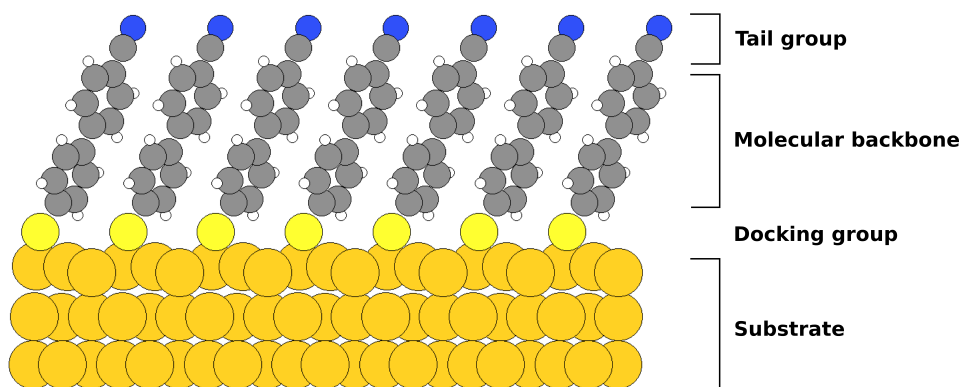The description of the structure already suggests how versatile SAMs are: each compo-

Figure 2.1: Prototypical Au(111)/cyano substituted biphenylthiolate SAM interface with the indication of the different constituents. Au is depicted in dark yellow, S in light yellow, C in grey, N in blue and H in white.

nent can be chosen depending on the purpose it has to serve. For instance, a careful choice of the docking group, responsible for the interaction of the SAM with the surface, allows tuning the strength of such interaction on one side and adapting the SAMs to different substrates on the other. The first section of the results chapter will indeed concern how different docking atoms, specifically S and Se, impact the thermal stability of naphthalene based SAMs on the Au(111) surface. On the other hand, an appropriate tail group can be used to control the interaction of the new surface with the outer environment. Last, the backbone can be conveniently modified to introduce chemical functionalities in the SAM without changing its interaction with the substrate and with the environment. An example of how this can be exploited in practice is given in the second section of the results chapter. By means of appropriately chosen backbones, the SAMs treated there induce different substrate modifications without changing the growth of the materials successively deposited.

Thanks to the in principle unlimited versatility of organic synthesis and to their capability of self-forming, SAMs are an effective mean to customise surface properties. They have therefore been applied in numerous areas of research and technology for many different purposes. Already about 30 years ago the first applications of SAMs to modify the wettability of surfaces[4,5], to prevent their corrosion[6,7] and to change their adhesion properties[8,9] were reported. Somewhat more recent are the first reports of SAMs used to enhance the performances of organic electronic devices[10–12]. More specifically, the application of SAMs to tune the surface potential of the metal electrodes and to improve the growth and the morphology of the active organic elements was reported for organic thin film transistors (OTFTs)[13]. The modification of the surface potential of the electrodes to enhance the injection of charge carriers into the the organic semiconductor was instead reported for organic light emitting diodes (OLEDs)[14]. Since those seminal works, the application of SAMs to modify and tune interface properties in the area of organic electronics has experienced a tremendous growth (see for instance reference 15 and references therein).

The success of SAMs is not only due to their versatility but also to their pretty straightforward preparation: they can be easily prepared either by immersion of the substrate in a solution containing the molecules or by exposing it to the vapour of the species, except for the cases in which reactions in solution with the precursors of the desired SAM are required[16].

Deposition from solution is the simplest and cheapest technique: the previously cleaned substrate just needs to be dipped into the solution containing the molecules forming the SAM for a certain time and the SAM forms spontaneously. The sample then needs to be properly rinsed. Important parameters are the cleanliness of both the substrate and the solution.

In case of gas phase deposition the substrate is placed in an (ultra) high vacuum ((U)HV) chamber, where it undergoes a suitable cleaning procedure. The gas phase molecules are then let diffuse and deposit onto the substrate. Due to the high costs of the equipment, deposition from gas phase is more expensive than from solution, but the employment of a UHV environment allows better controlling both the cleanliness of the substrate and the purity of the SAM. Moreover, many surface science techniques are available for *in situ* analysis in UHV chambers.

2.1.1 Experimental characterisation techniques

SAMs can be experimentally investigated using a wide variety of surface science techniques. In this section an overview of the methods mentioned in this work is given, based on reference 17.

Photoemission spectroscopy (PS) is the most important technique to investigate the band structure of the occupied states, i.e. the binding energies of the electrons. It is based on

the photoelectric effect: photons with a certain energy hit the sample and excite electrons, which are ejected from the sample and detected. The kinetic energy of the ejected electron can then be related to the binding energies in the initial state.

Depending on the incident photon energy, PS can be classified in ultraviolet PS (UPS), with photon energies in the ultraviolet range, and X-ray PS (XPS), where photons have higher energies, in the range of X-rays. UPS allows getting information about the states close to the Fermi energy and can, therefore, be used to determine the work function of a sample, or the work function modification upon absorption of a SAM. On the other side, XPS, making use of more energetic photons, allows probing core level energies. Since these latter are affected by the chemical environment of the considered element, XPS is exploited to identify species on surfaces and is, therefore, also known as electron spectroscopy for chemical analysis (ESCA). When dealing with metal-organic interfaces, besides investigating the chemical identity of the sample, XPS is widely used also to determine the thickness of the organic layer, its packing density and to obtain information about its homogeneity[18]. Moreover, as will be pointed out throughout the present work, recently the use of XPS to follow electrostatic shifts in metal/SAM interfaces has been presented[19].

Another technique based on the adsorption of X-rays is the near-edge X-ray absorption fine structure spectroscopy (NEXAFS), a synchrotron radiation based technique that allows exciting electrons from a deep core level of an atomic element into unoccupied molecular orbitals. NEXAFS can, thus, provide information on the interaction of the adsorbate molecules both with other molecules and with surface atoms. Moreover, NEXAFS allows not only probing the electronic structure of the adsorbate, but also determining the orientation of the molecules with respect to the substrate. A concise description of the working principle of NEXAFS and of its application to the study of surface can be found in reference 20.

Information about the chemical composition of a sample can be obtained also by means of the secondary ion mass spectroscopy (SIMS) technique, where a beam of primary ions, for instance Ar^+, of energies typically ranging between 1 and 10 keV, impacts onto the analysed surface. Due to the high energy, fragments of the molecules on the surface are emitted. The detection of the charged fragments (secondary ions) with a mass spectrometer allows a detailed analysis of the chemical identity of the adsorbed layer.

Another way to measure work functions, more precisely work function changes, is Kelvin probe (KP). In a KP experiment a metallic cantilever with a sharp tip a the end is placed in front of the surface and vibrates against it. The sample and the oscillating tip are electrically connected through an ammeter and a battery that allows applying a variable bias. The physical principle exploited in KP is that when two different materials are in contact, the Fermi levels have to equilibrate. If they are different electrons/holes start to flow from the low/high work function material into the other one. This charge flow gives rise to an oscillating current measured by the ammeter. If a bias is applied that leads to the compensation to the oscillating current to 0, the applied bias is equal to the difference between the work function of the sample and that of the probing electrode. It is then possible to modify the investigated surface and perform the KP measurement again, to get the work function modification.

A direct real space image with atomic resolution of a surface can be obtained by means of scanning tunnelling microscopy (STM). A metal tip is moved across the sample surface and the tunnel current between the surface and the tip is registered as a function of the tip position, allowing, thus, to get information on both the electronic and the geometric structure of the surface.

2.1.2 Self-assembled monolayers in organic electronics

As mentioned in the previous sections, the main application of SAMs is the modification of surface properties. In the field of organic electronics, suitable surface modifications are of crucial importance when bringing together different material, i.e. when forming an interface. According to reference 21, in organic electronic devices three types of interfaces can be identified. How the atomistic structure at these interfaces looks like can dramatically impact the device performance.

Modifications of the dielectric/organic semiconductor (OSC) interface, that can be found for instance in an OTFT, have an impact on the growth of the semiconductor. This latter has in turn a strong influence on the transport properties of the material, on the presence of trap states, detrimental for the device performance, and on the electrostatic potential at the interface, with the possible formation of a built-in field superimposed to the applied gate field.

OSC/OSC interfaces can be found in devices such as organic solar cells or OLEDs and their nature impacts the fundamental processes of such devices, namely exciton dissociation in solar cells and exciton recombination in OLEDs.

The third type is the metal/OSC interface, occurring, for example, between the source and drain electrodes and the active material in an OTFT. Depositing a SAM on the metal surface can, for instance, change the growth of the OSC, and therefore, as already mentioned, its transport properties, and can modify the work function of the metal, having, thus, an impact on the charge injection/extraction processes. The present work mostly focuses on this latter aspect, namely the capability of SAMs to modify the work function of metal surfaces. What is also extensively discussed is how the physical effects responsible for the work function modification also impact other observables, such as XP spectra.

Energetics of metal/SAM interfaces

In this section the basics of the energetic level alignment at metal/SAM interfaces are presented. The discussion is based on references 22 and 23.

The work function (Φ) of a metal is defined as the minimum energy required to extract an electron from the metal surface and bring it to the vacuum level (VL). Φ is therefore a crucial parameter when defining the injection and extraction barriers for electrons and holes at an electrode/OSC interface. Within the Schottky-Mott limit, vacuum level alignment between metal and the organic material is assumed. Consequently, the electron and hole injection barriers EIB and HIB are defined as EIB$= \Phi - A$ and HIB$= I - \Phi$, where A and I are the electron affinity and the ionisation potential of the organic layer, respectively.

In reality, the vacuum level alignment scenario never occurs. Instead, an additional potential step at the metal/organic interface is observed, whose value corresponds to a shift in the VLs at the two sides of the metal/organic system. The occurrence of such potential step is related to the so called collective electrostatic effects [23–25], that appear whenever a two-dimensional periodic arrangement of dipolar units is present.

As instructive example, let us consider a dipolar molecule, such as a CN substituted biphenylthiol, and the electrostatic potential energy of an electron in its vicinity, as done in figure 2.2, panel a. It can be noticed that there is a perturbation in the energy in the proximity of the dipolar units, in particular at the CN moiety, relevantly more polar than the SH one. Such perturbation decays however very rapidly and the energy becomes essentially constant. The scenario changes radically when instead of having an isolated dipolar molecule we have an infinite number of molecules regularly arranged in two dimensions, i.e. a free standing monolayer of dipolar molecules, with all the dipolar units pointing in the same direction. Looking at the electrostatic potential energy of an electron for this case, shown
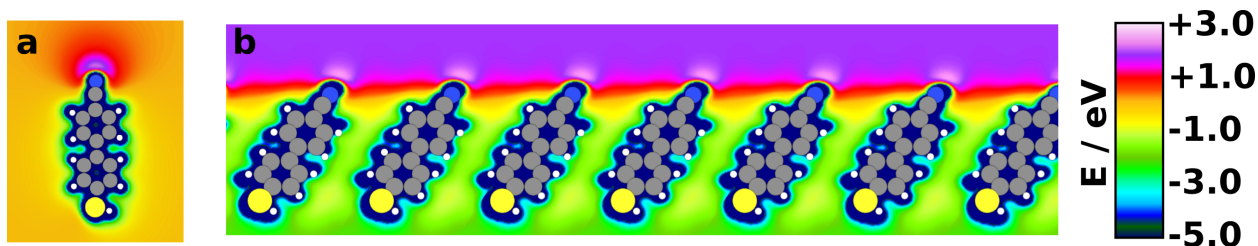
Figure 2.2: Electrostatic potential energy of an electron in the case of an isolated polar molecule (a) and a free standing monolayer (b). The depicted molecule is the same considered in figure 2.1, with the only difference being that in this case the S atom is saturated with a H. The colour coded legend allows intuitively appreciating the difference between the two scenarios. The computational settings used for the calculations are reported at the end of this section.

in figure 2.2, panel b, the situation looks totally different than in the isolated molecule case. A step in the energy, referred to as ΔE^{vac}, occurs and leads to the VLs to be different on the two sides of the dipolar units.

Such shift occurs abruptly and is due to the superimposed fields of the repeated dipole units. The magnitude of ΔE^{vac} can be related to the dipoles μ by the Helmoltz equation:

$$\Delta E^{vac} = \frac{-e}{\varepsilon_0}\frac{\mu_z}{A}. \tag{2.1}$$

e is the elementary charge, ε_0 the vacuum permittivity, A the area per molecule and μ_z the component of the dipole moment perpendicular to the surface.

Equation 2.1 shows that the magnitude of ΔE^{vac} can be tuned both by varying the dipole component perpendicular to the surface, changing either the magnitude or the tilt of the dipolar units with respect to the surface normal, and by varying their density on the surface.

Equation 2.1 is generally valid, meaning that a step in the potential occurs whenever a periodic arrangement of dipolar units is present. When dealing with the adsorption of organic molecules on metal surfaces, such periodically arranged dipoles can occur due to various reasons, as illustrated in the following.

- **Tailing of the electron cloud.** At the surface of a metal, part of the negative electron cloud tails out, leading to the electron density not to go abruptly to zero at the very interface, as schematically shown in panel a of figure 2.3. The presence of a partial negative and a partial positive charge outside, respectively inside, the substrate forms a dipole, shown in blue in figure 2.3. It is called surface dipole and points towards the surface, therefore increasing the energy an electron needs to escape the metal and go to the vacuum. As shown in panel b of figure 2.3, the electrostatic potential energy of an electron $E(x)$ is constant just outside the solid. There the distance x from the solid is much smaller than its extension and the dipole layer can therefore be considered as infinite. The electrostatic potential energy converges then to VL(∞) as a quadratic function of x when this latter becomes larger than the extension of the surface. In this case the dipole layer can be considered as a point dipole. It then becomes clear that the definition of VL needs to be elucidated: the VL in the vicinity of the surface, VL(s), is different than the VL at infinity, VL(∞). What is measured and used to define Φ, and is therefore relevant for the discussions carried out in this work, is VL(s). This latter depends on the tailing of the electron cloud and is therefore different for different surfaces of the same material. All different VL(s)s, however, converge to the same VL(∞).

- **Pauli pushback.** When a molecule approaches the substrate, due to the interaction between the electrons of the molecule and the ones tailing out from the surface, the
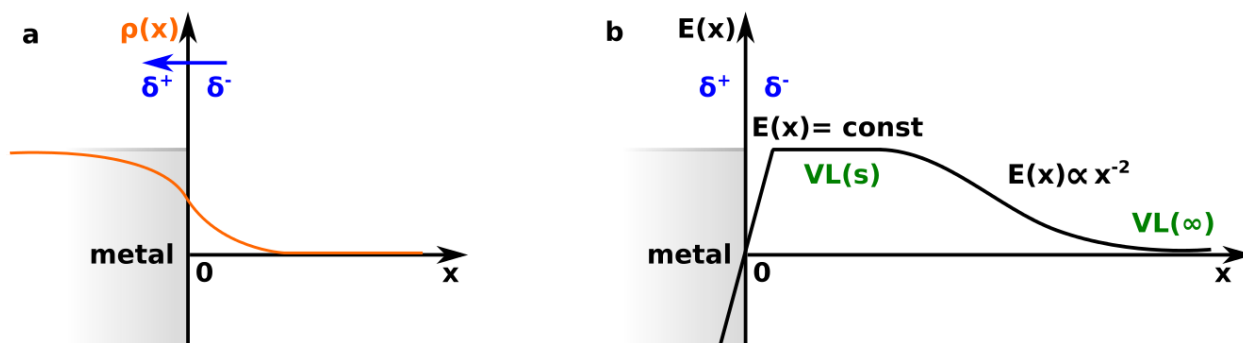
Figure 2.3: a: schematic representation of the density of states $\rho(x)$, orange line, as a function of the distance from the metal/vacuum interface, set at $x = 0$. The hypothetical surface is depicted in grey. In blue the dipole is indicated that arises from the tailing of the electron cloud outside the metal. b: electrostatic potential energy of an electron $E(x)$ as a function of the distance from the metal/vacuum interface, set at $x = 0$. Just outside of the surface, for values of x small relative to the surface extension, the energy stays constant. When x increases and becomes large with respect to the surface extension the energy decays as a quadratic function of x and reaches the value of VL(∞). VL(∞) and VL(s) are respectively the VL at infinite distance from the surface and the VL just outside it. The schematic is based on the illustrations of reference 22.

latter are pushed back into the metal. Therefore, the surface dipole is reduced and Φ decreased. Since the Pauli principle is at the basis of such electronic interaction, the phenomenon is known as Pauli pushback.

- **Charge transfer.** When an electron donor is adsorbed on a substrate with a high Φ, electrons are transferred from the molecule to the substrate, while on the contrary combining an electron acceptor and a low Φ substrate electron transfer occurs from the latter to the molecule. The charge transfer process leads to the formation of a further dipole at the interface. In the high Φ material/donor case the dipole points away from the substrate and, thus, Φ becomes smaller The opposite situation occurs in the low Φ material/acceptor case, where the dipole points towards the surface increasing Φ.

- **Formation of new bonds.** In case of chemisorbed SAMs, a covalent bond is formed between the substrate and the molecules. Upon bond formation, a redistribution of the electron density occurs resulting in the formation of a dipolar layer.

- **Metal induced gap states.** Electrostatic effects can be generated also by the presence of interface states, well known for inorganic semiconductors, due to the hybridisation of the wavefunctions of the metal and the semiconductor.

- **Molecules with permanent dipoles.** As explained above, in the presence of an ordered arrangement of dipolar molecules a step in the electrostatic potential energy of an electron is induced. The step is proportional to the magnitude of the dipole and to its density.

When specifically considering the chemisorption of a SAM, the metal surface, with its electron cloud tailing out, is brought into contact with the molecules. As they reach the substrate, the Pauli pushback effect occurs, followed by the formation of the covalent bonds between the metal surface and the docking groups of the SAM. To this processes several charge rearrangements $\Delta\rho$ at the interface are associated, shown in panel a of figure 2.4 for the prototypical CN substituted biphenylthiolate SAM on Au(111) considered so far.
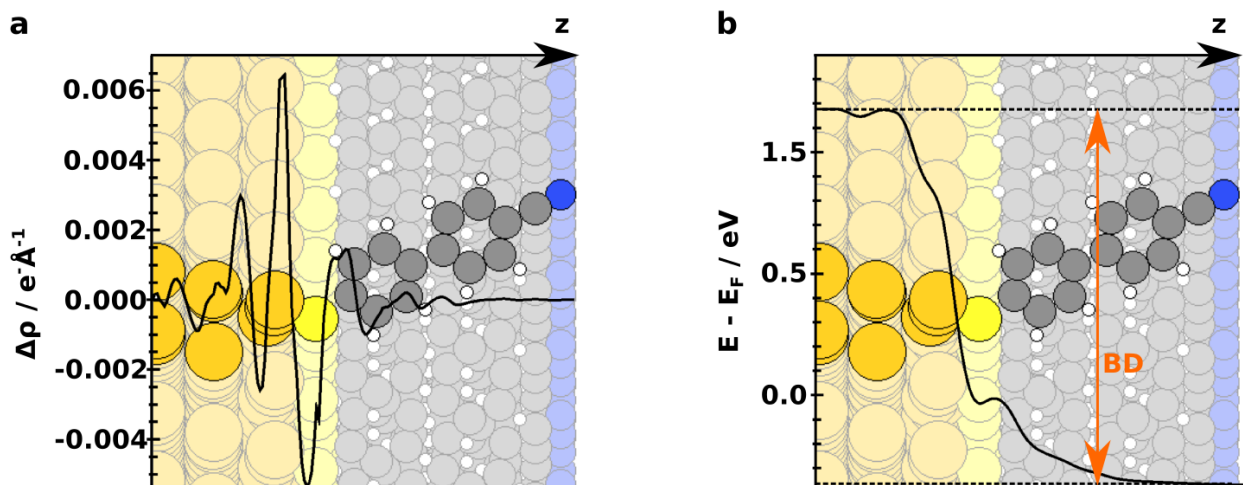
Figure 2.4: a: plane integrated charge rearrangements $\Delta\rho$ at a metal/SAM interface upon SAM adsorption. b: bond dipole (BD) at the metal/SAM interface calculated using the Poisson equation 2.2. The considered systems is the same presented in figure 2.1. The computational settings used for the calculations are reported at the end of this section.

According to the Poisson equation, integrating the charge rearrangements twice it is possible to calculate the potential step occurring at the interface upon adsorption of the SAM, shown in panel b of figure 2.4:

$$\frac{d^2V(z)}{dz^2} = -\frac{\rho(z)}{\varepsilon_0}, \tag{2.2}$$

$V(z)$ is the electrostatic potential of an electron, related to the energy step by $\Delta V = -e\Delta E$. $\rho(z)$ is the charge density and ε_0 is the vacuum permittivity. The magnitude of the step is referred to as bond dipole (BD). The overall work function modification $\Delta\Phi$ upon chemisorption of a SAM on a metal consists then of two contribution, the bond dipole and ΔE^{vac} (see equation 2.1).

Computational details

The data used to produce the plots shown in figures 2.2 and 2.4 were obtained using the code FHI-aims[26] employing the PBE functional[27] and the surface version[28] of the Tkatchenko-Scheffler[29] corrections for the van der Waals interactions. Periodic boundary conditions and the repeated slab approach were applied. Since the calculations were for an instructive purpose only, they were kept cheap using the default FHI-aims light settings to describe all the elements and modelling the Au(111) surface with only three metal layers. The dispersion corrections were turned off between the Au atoms. A $(\sqrt{3} \times \sqrt{3})$ unit cell with one molecule per unit cell was used. The dimensions of the unit cell in the x and y directions were set according to the theoretically calculated Au lattice constant (primitive lattice constant of 4.158 Å, corresponding to a nearest neighbour distance of 2.940 Å). The third dimension was set such as a vacuum region of least 20 Å was included between two consecutive slabs to spatially decouple them. To decouple them also electrostatically a self consistently calculated dipole correction was inserted in the third dimension. A Γ centred $9 \times 5 \times 1$ k-points grid was used. The initial geometry was set up taking the optimised biphenylthiolate (BPT) geometry (see sections 4.2 and 4.3) and adding the CN substituent. Only the position of the latter was then optimised. The total energy criterion for the self-consistency cycle was set to 10^{-6} eV and geometry optimisations were performed until the maximum residual force component per atom was below 0.01 eV/Å.

2.1.3 Metal/SAM interfaces investigated in this work

Most of the systems considered in the present work are interfaces between the Au(111) surface and thiolates.

Thanks to the ease of preparation and the stability of the resulting SAMs, S is the most common docking atom. As alternative to S, Se was proposed[30], that has the same outer valence electron configuration and yields films of higher quality[31–35]. A comparison between the two docking groups in terms of their thermal stability is the topic of section 4.1, where S and Se docked CN substituted naphthalene SAMs on the Au(111) surface are considered. The systems are shown in figure 2.5. The strength of the bonds between substrate and docking group and between docking group and molecular backbone is investigated. The simulated results are compared with the experimental ones obtained from XPS and SIMS measurements. The investigation clarifies the relative stability of the differently docked SAMs and allows understanding the fundamental impact of surface reconstructions. Moreover, the importance of considering also bonds beyond the surface–docking group one when determining the relative stabilities of SAMs is emphasised.
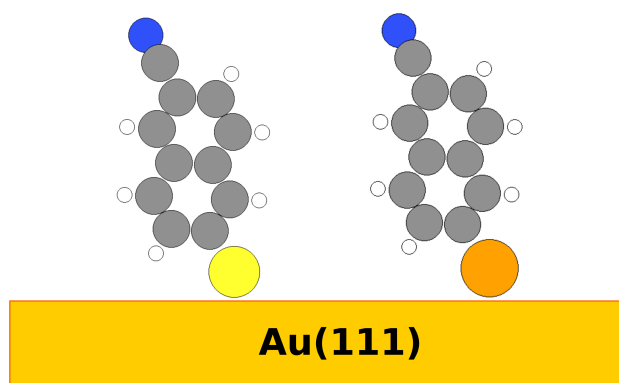
Figure 2.5: S and Se docked CN substituted naphthalene SAMs investigated in section 4.1. C atoms are depicted in grey, H in white, N in blue, S in yellow and Se in orange. The metal substrate is represented by the dark yellow rectangle.

Aromatic thiolates on the Au(111) surface are also the topic of section 4.2, where the structural and the electronic properties of two pyrimidine containing derivatives of biphenylthiolate (BPT) are investigated. The molecules, shown in figure 2.6, are designed following the embedded dipole approach[36,37]: the topmost, respectively the bottom, phenyl ring of BPT are substituted with a polar pyrimidine unit, with the N atoms pointing towards, respectively away from, the substrate. The strategy of embedding the dipolar units in the molecular backbone allows inducing the desired substrate work function modifications without changing the chemistry of the topmost part of the molecules. This approach is particularly convenient when employing such SAM modified metal surfaces as electrodes in organic devices, in order not to affect the deposition of the active material[1].

In section 4.3 the same embedded dipole concept is applied to parent molecules containing two pyrimidine units. The preliminary results of the characterisation of both molecules with two aromatic rings directly bonded to the docking groups and molecules with three aromatic rings and a methylene unit between the backbone and the S docking group are reported. Derivatives of the molecules with three rings, obtained by combining the basic structures with different tail groups, are investigated, too, to predict their potential for work function modifications. The investigated systems are depicted in figure 2.7. Contrary to the monopyrimidine BPT derivatives of section 4.2, the bipyrimidine containing SAMs seem not

Figure 2.6: BPT and embedded dipole derivatives investigated in section 4.2. C atoms are depicted in grey, H in white, N in blue and S in yellow. The metal substrate is represented by the dark yellow rectangle.

Figure 2.7: Embedded dipole derivatives containing two bipyrimidine units investigated in section 4.3. C atoms are depicted in grey, H in white, N in blue and S in yellow. The metal substrate is represented by the dark yellow rectangle.

to form good quality films, as can be inferred from the comparison between simulated and measured results.

S bonded SAMs are considered also in section 4.4, where dithiocarbamates (DTC) are investigated. DTC have the peculiarity of bearing two docking atoms per molecule and have been shown to form robust and stable SAMs on the Au(111) surface and to induce interesting work function modifications[38]. The simulations are performed on two basic systems, shown in figure 2.8, with the purpose of correlating their structure to the observed surface properties modifications. The structural and electronic properties of the systems are analysed, focusing in particular on work function modifications and XP spectra. The atomic insight achieved with the simulations allows understanding and rationalising the experimental measurements. The full characterisation confirms the potential of such novel SAMs as possible alternative to the more common monothiolates.

After the mono- and bidentate S based SAMs of the previous sections, tridentate thiolates are the topic of section 4.5. The great potential of such original SAMs is their capability of bonding to the substrate with all three S atoms, achieving therefore a nearly upright standing orientation, which allows larger work function modifications. Two prototypical triptycene based systems, depicted in figure 2.9, are characterised combining simulations and experimental characterisation techniques. The almost perfect upright standing orientation and the availability of four sites to which tail groups could in principle be attached make such tripodal molecules highly promising candidates for surface modifications in many different applications.
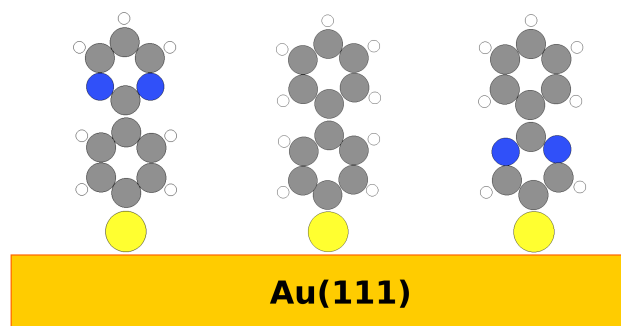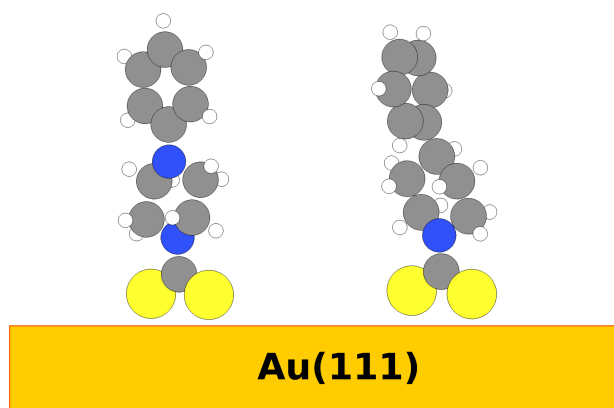
Figure 2.8: DTC SAMs investigated in section 4.4. C atoms are depicted in grey, H in white, N in blue and S in yellow. The metal substrate is represented by the dark yellow rectangle.
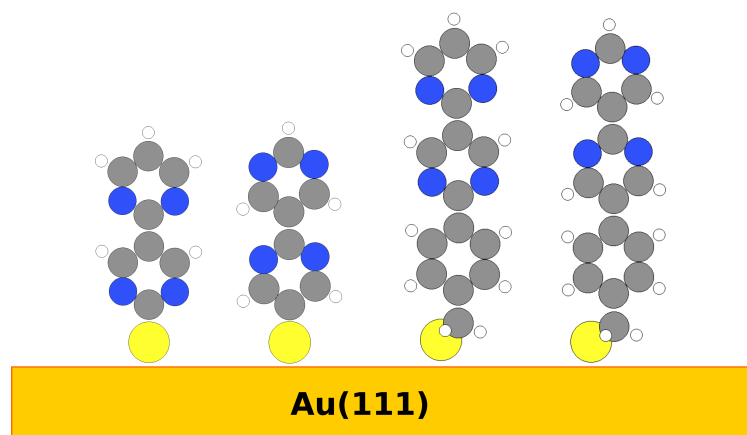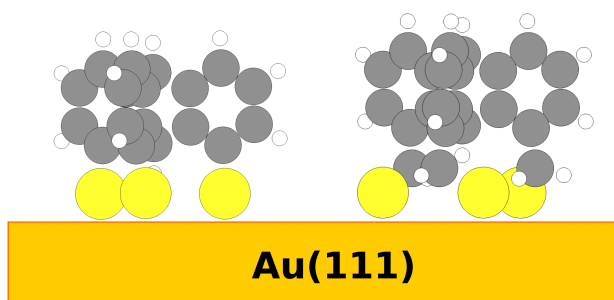

Figure 2.9: Triptycene based SAMs investigated in section 4.5. C atoms are depicted in grey, H in white and S in yellow. The metal substrate is represented by the dark yellow rectangle.

Triptycene based SAMs are investigated also in section 4.6, where the first results of the characterisation of COO bonded triptycenes on the Ag(111) surface are presented. The system is shown in figure 2.10 The main focus of this first analysis is to find a structural model compatible with the experimentally observed STM pictures. This turns out to be particularly challenging, since the arrangement of the molecules on the substrate proposed on the basis of experiments seems not to be compatible with the most stable arrangement found in the simulations.
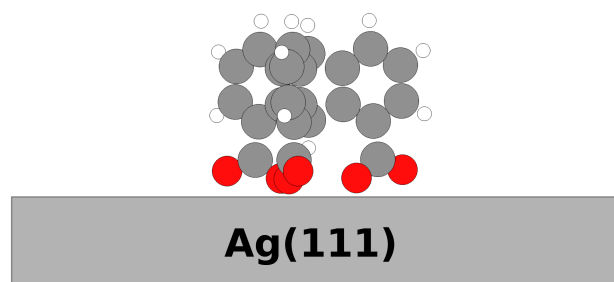
Figure 2.10: Triptycene based SAMs investigated in section 4.6. C atoms are depicted in grey, H in white and O in red. The metal substrate is represented by the grey rectangle.

Topic of section 4.7 is the Au(111)/K interface. The system is chosen as a simple model to perform a *Gedankenexperiment* with the purpose of analysing the interplay of chemical and electrostatic shifts in XPS. This is of particular interest since, as already mentioned, it has recently been shown that collective electrostatic effects do not only induce substrate work function modifications but also affect the core level energies of the adsorbate[19]. XPS has thus been proposed as a suitable and convenient technique to trace such electrostatic

shifts[19,39]. However, there are specific cases, such as the very metal/adsorbate interfaces, in which additional effects can become relevant and mask, or even totally compensate, the effect of electrostatics (see for instance also section 4.4). The delicate interplay between all these different contributions is examined considering a fictitious system of K atoms on the Au(111) surface at different coverages, as shown in figure 2.11. The outcome of the simulations depicts a plausible scenario in which charge transfer processes between substrate and adsorbate play a fundamental role. This emphasises the need of a careful analysis when interpreting the origin of XPS shifts in metal/SAM interfaces.
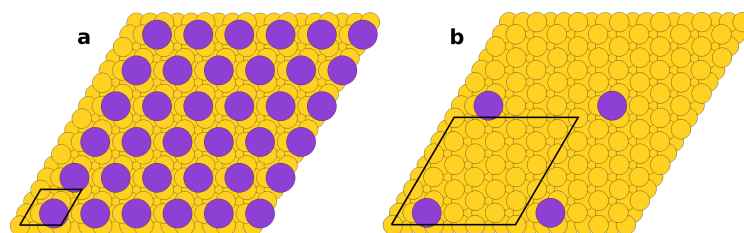
Figure 2.11: K/Au(111) interface at full (panel a) and reduced (panel b) coverage investigated in section 4.7. K atoms are depicted in purple and Au in dark yellow. The black lines enclose the unit cell.

2.2 Metal-organic frameworks

Metal-organic frameworks (MOFs) are hybrid inorganic/organic materials consisting of metal containing nodes, called secondary building units (SBUs), covalently linked by organic ligands, so that the resulting structure is a porous extended system[40].

In figure 2.12 a schematic of the generic MOF structure is shown. The SBUs can contain one or more metal centres and are connected by organic molecules that bear suitable coordinating moieties, such as for instance carboxylates, imidazolates or amines. In three-dimensional MOFs in plane and apical, or pillar, ligands can be identified, as shown in figure 2.13. As it is the case in the figure, the nature of the ligands can be different, with usually the same ligands in plane and a different one in the apical position. MOFs feature an incredible structural and functional flexibility. A wide variety of SBUs can be employed, for instance by changing the metal centres or the coordinating groups. Analogously, the ligands
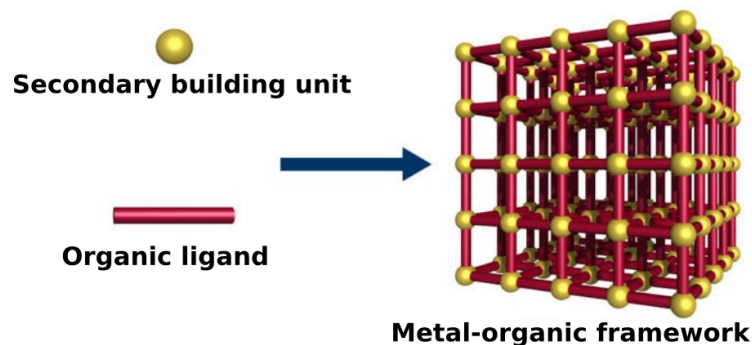
Figure 2.12: Generic MOF structure. Modified from
http://www.ccb.tu-dortmund.de/fb03/en/Fields_of_research/AC/Henke/Research/index.html (visited on the 23.01.2019).
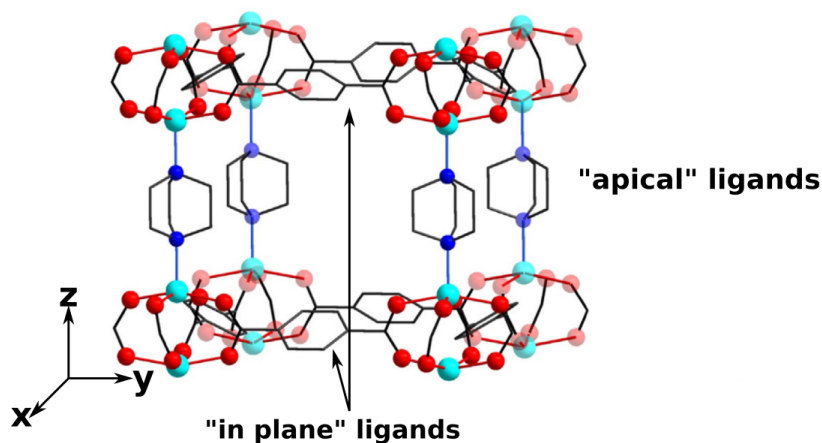
Figure 2.13: Structure of a common MOF with the indication of the "in plane" and the "apical" ligands. Modified from Coordination Chemistry Reviews, Jin-Liang Zhuang, Andreas Terfort, Christof Wöll, Formation of oriented and patterned films of metal-organic frameworks by liquid phase epitaxy: A review., Pages 391-424, Copyright 2016, with permission from Elsevier.

can be modified changing their length or by introducing functional groups. The versatility of MOFs can be further increased by means of post-synthetic modification (PSM), as reported in references 41 and 42 and references therein. Moreover, using the pores as hosts for specific functional moieties can open the way to even more applications, as illustrated in reference 43 and references therein.

It is then obvious that with such a degree of adjustability and tunability, many diverse applications in numerous science and technology fields have been suggested for MOFs. The first ideas were inspired by the porosity of these materials, which explains also why the term porous coordination polymer (PCP) is often used as a synonym for MOF. The first applications proposed for MOFs were gas adsorption, separation and sensing[42,43]. Additionally, MOFs act as catalysts for many reactions, from Lewis acid based catalysis to electrocatalysis. MOFs are also promising candidates for possible biological applications, such as for instance drug delivery or enzyme immobilisation[42].

Beyond these typical applications, alternative ways to exploit the functional MOF pores have recently been explored. For example, the introduction of MOFs as active materials in (opto)-electronic devices is increasingly becoming of interest[44–47]. The integration of MOFs in devices requires their fabrication in form of thin films[48,49]. These can be obtained with several techniques, described in reference 43. The most common one is the direct deposition from solvothermal mother solutions. The advantage of the method is its simplicity: it is sufficient to immerse the substrate in specifically treated solvothermal mother liquors of the desired MOF and let the solvent subsequently evaporate. To suitably modify the surface chemistry of the substrate and regulate nucleation, orientation and structure of the deposited MOFs the use of SAMs has been proposed[50,51]. The significant disadvantage of starting from mother solutions is the low quality of the obtained films: the films are rather inhomogeneous and polycrystalline layers, making them unsuited for the integration as functional materials in devices.

As alternative to the common MOF thin film fabrication procedure, a different approach has been proposed based on a step-by-step liquid-phase epitaxy (LPE) method[46,48,49,52,53].

The first successful application of the LPE technique was the deposition of a multi-layer of $[Cu_3btc_2(H_2O)_n]$ (btc=1,3,5-benzenetricarboxylic acid), also known as HKUST-1, from the Hong-Kong University of Science and Technology, where it was first synthesised. Copper(II)acetate $(Cu(ac)_2)$ and 1,3,5-benzenetricarboxylic acid (H_3btc) were separately dissolved in ethanol and a COOH terminated SAM functionalised Au substrate was cyclically

immersed in the solutions. Each immersion step was followed by rinsing with pure ethanole to remove unreacted components[49].

The general LPE procedure consists then in having a suitably functionalised substrate that is alternatingly immersed in solutions containing the MOF building units or their precursors and rinsing the substrate after each immersion.

This allows the growth of crystalline porous MOF thin films referred to as SURMOFs, standing for *surface grown, crystalline metal-organic framework multilayers*[49]. The LPE method was also successfully applied to the MOF-on-MOF growth, where a Cu containing MOF is used as a template to grow a Zn containing one. This is of particular importance since the latter usually forms pretty amorphous films[53].

Almost all MOFs, due to the nature of their components, behave as poor electrical conductors because of their large band gap. This is unfortunate for their use as active components in electronic devices. While MOFs exhibiting semiconducting properties are still rare, as reported in 54 and references therein, recently some examples of intrinsically conductive MOFs have been presented[55–57], with possible design und synthesis strategies nicely reviewed in reference 58.

These first examples opened the way to further experimental and theoretical investigations of the transport properties of MOFs, in particular focusing on the controlled modification of such properties via band structure engineering. For instance, a computational study has shown the possibility of tuning the band gap and shifting the valence band maximum position by suitably substituting the linkers[59]. Moreover, a strategy to tune the conductivity has been presented[57], via the controlled variation of the distance between the metal centres in the SBU. Also loading the MOF pores with suitable guest molecules has been shown to be a convenient approach for both improving and tuning the electrical conductivity of MOFs[60,61].

2.2.1 MOFs investigated in this work

Along the line of the aforementioned band structure engineering approach, in this work an original application for MOFs is proposed, that takes advantage of the collective electrostatic effects described in section 2.1.2. The idea is to design, and eventually grow via the LPE method illustrated above, SURMOFs in which, by means of the controlled introduction of suitable dipolar linkers, the electrostatic potential energy can be manipulated, in order to obtain convenient potential profiles. The exemplary structure conceived for this purpose is the topic of section 4.8. Bimetallic Zn nodes are employed as SBUs, connected in the x,y plane by terephthalic units. As apical linkers polar 3,5-difluosubstituted 4,4'-bipyridines are used. The investigated system is depicted in figure 2.14. Model structures with an increasing number of polar layers are investigated. The analysis focuses on the electronic properties of the system, in particular on the modifications of the electrostatic potential energy induced by the presence of the repeated polar units. A possible way to exploit such modifications in organic electronic devices is presented.
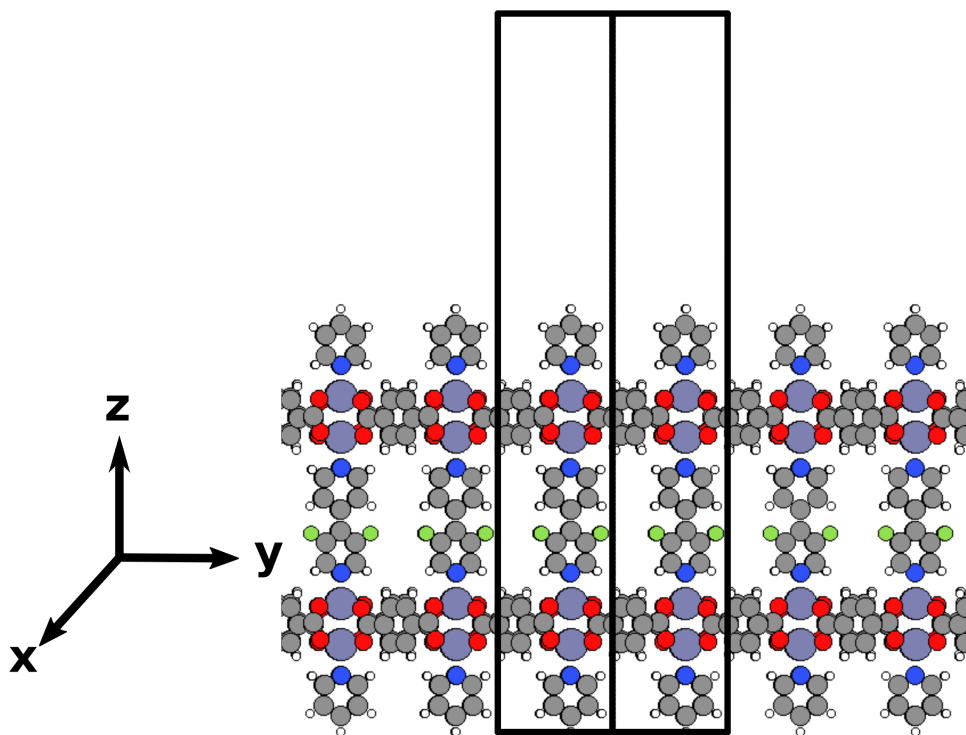
Figure 2.14: Structure of the SURMOF investigated in section 4.8. C atoms are depicted in grey, H in white, N in blue, O in red, F in green and Zn in light blue. The black lines enclose the unit cell used in the simulations.

3 Methodological approach

3.1 Density functional theory

In case of periodic systems consisting of many atoms per unit cell, such as the systems treated in the present thesis, the most common and suitable approach for modelling them is density functional theory (DFT), thanks to its good compromise between accuracy of the results and demand of computational resources. In this chapter the basic theoretical concepts behind DFT are presented, based on references 62–69.

DFT methods are based on the laws of quantum mechanics: a system is fully described by a wavefunction $\Psi = \Psi(\mathbf{r}, t)$ that depends on the coordinates $\mathbf{r}$ of the particles forming the system and on the time t. The properties of such a system can be obtained by applying suitable operators to $\Psi(\mathbf{r}, t)$.

The fundamental equation of quantum mechanics is the Schrödinger equation and most computational approaches are based on the (approximate) solution of its time independent form:

$$\hat{H}\Psi(\mathbf{r}_1, \mathbf{r}_2, ..., \mathbf{r}_N, \mathbf{R}_1, \mathbf{R}_2, ..., \mathbf{R}_M) = E\Psi(\mathbf{r}_1, \mathbf{r}_2, ..., \mathbf{r}_N, \mathbf{R}_1, \mathbf{R}_2, ..., \mathbf{R}_M) \tag{3.1}$$

where $\Psi(\mathbf{r}_1, \mathbf{r}_2, ..., \mathbf{r}_N, \mathbf{R}_1, \mathbf{R}_2, ..., \mathbf{R}_M)$ is the many-body wave function, $\hat{H}$ is the Hamiltonian of an interacting system consisting of M nuclei and N electrons, placed at $\mathbf{R}_I$ and $\mathbf{r}_i$, respectively, in absence of electric or magnetic fields, and E is the total energy of the system. The Hamiltonian is defined as

$$\begin{aligned}
\hat{H} = &-\frac{\hbar^2}{2m_e}\sum_i^N \nabla_i^2 - \frac{\hbar^2}{2}\sum_I^M \frac{1}{M_I}\nabla_I^2 \\
&-\sum_i^N\sum_I^M \frac{Z_I e^2}{|\mathbf{r}_i - \mathbf{R}_I|} + \frac{1}{2}\sum_i^N\sum_{j\neq i}^N \frac{e^2}{|\mathbf{r}_i - \mathbf{r}_j|} + \frac{1}{2}\sum_I^M\sum_{J\neq I}^M \frac{Z_I Z_J e^2}{|\mathbf{R}_I - \mathbf{R}_J|}
\end{aligned} \tag{3.2}$$

where $-\frac{\hbar^2}{2m_e}\sum_i^N \nabla_i^2$ and $-\frac{\hbar^2}{2}\sum_I^M \frac{1}{M_I}\nabla_I^2$ are the kinetic energy of the electrons and the nuclei and $-\sum_i^N\sum_I^M \frac{Z_I e^2}{|\mathbf{r}_i - \mathbf{R}_I|}$, $\frac{1}{2}\sum_i^N\sum_{j\neq i}^N \frac{e^2}{|\mathbf{r}_i - \mathbf{r}_j|}$ and $\frac{1}{2}\sum_I^M\sum_{J\neq I}^M \frac{Z_I Z_J e^2}{|\mathbf{R}_I - \mathbf{R}_J|}$ are the electron-nucleus, electron-electron and nucleus-nucleus interactions, respectively. With the mass of the electrons about 2000 times lower than the mass of the nuclei, the latter move much more slowly than the electrons. Based on this consideration, the well known Born-Oppenheimer approximation significantly simplifies the 3.2: the nuclei are considered fixed while the electrons move in the field generated by the nuclei. The kinetic energy of the nuclei drops therefore out and the nucleus - nucleus interaction becomes simply a constant term. Equation 3.2 can then be rewritten as

$$\hat{H} = -\frac{\hbar^2}{2m_e} \sum_i^N \nabla_i^2 - \sum_i^N \sum_I^M \frac{Z_I e^2}{|\mathbf{r}_i - \mathbf{R}_I|} + \sum_i^N \sum_{j \neq i}^N \frac{e^2}{|\mathbf{r}_i - \mathbf{r}_j|} \tag{3.3}$$

$$= \hat{T} + \hat{V}_{ext} + \hat{V}_{ee},$$

with $\hat{T}$, $\hat{V}_{ext}$ and $\hat{V}_{ee}$ respectively denoting the kinetic energy, the external potential and the electron-electron interaction operators.

The first derivatives of the energy with respect to the nuclear coordinates allow finding the optimum geometry on the Born-Oppenheimer potential energy surface, while the second derivatives are needed to calculate vibrations for non periodic and phonons for periodic structures.

3.1.1 Hohenberg-Kohn theorems

Although simplified with respect to equation 3.2, equation 3.3 still involves $3N$ coordinates, obviously too many considering a common system consisting of hundreds of atoms. A this point, the core idea of DFT comes into play, by means of the two Hohenberg-Kohn theorems[68]. The first theorem, also known as existence theorem, proven in 1964 by Hohenberg and Kohn by *reductio ad absurdum*, states that the external potential v of a system of interacting electrons is uniquely determined by the ground state electron density n_0 of that system, up to an additive constant. Since the electron density n is a scalar object only dependent on the three spatial coordinates, using it to describe all the ground state properties considerably simplifies the theoretical representation.

From the existence theorem and 3.3 it then follows that the total energy E of a system can be written as a *functional* of the electron density n:

$$E[n(\mathbf{r})] = T[n(\mathbf{r})] + E_{ee}[n(\mathbf{r})] + \int d^3 r v(\mathbf{r}) n(\mathbf{r}) \tag{3.4}$$

The second theorem, also known as variational theorem, formulates the Rayleigh-Ritz variational principle in terms of trial densities and can be derived following the *constrained search approach* of Levy and Lieb[70,71]. In case of wave function based approaches, the variational principle states that the ground state energy of a system can be found by minimising $< \Psi | \hat{H} | \Psi >$ over all normalised antisymmetric N-particle wavefunctions:

$$E = \min_{\Psi} < \Psi | \hat{H} | \Psi > . \tag{3.5}$$

The idea of Levy and Lieb for applying the variation principle to densities was to separate the minimisation procedure in two steps. First, a given trial density $n(\mathbf{r})$ is fixed and the minimisation is performed over all the wavefunctions Ψ that yield the same $n(\mathbf{r})$:

$$\min_{\Psi \to n} < \Psi | \hat{H} | \Psi > = \min_{\Psi \to n} < \Psi | \hat{T} + \hat{V}_{ee} | \Psi > + \int d^3 r v(\mathbf{r}) n(\mathbf{r}), \tag{3.6}$$

where the expression is justified by the fact that all wavefunctions that give the same n also give the same external potential $< \Psi | \hat{V}_{ext} | \Psi >$. It is now possible to define a universal functional $F[n]$ as

$$F[n] = \min_{\Psi \to n} < \Psi | \hat{T} + \hat{V}_{ee} | \Psi > = < \Psi_n^{\min} | \hat{T} + \hat{V}_{ee} | \Psi_n^{\min} >, \tag{3.7}$$

with $\Psi_n^{\min}$ being the wavefunction that yields the minimum for the given n. F is a universal functional of the electron density and does not require any information about v. The second step of the procedure consists in minimising over all the N-electron densities:

$$E = \min_n \left\{ F[n] + \int \mathrm{d}^3 r v(\mathbf{r}) n(\mathbf{r}) \right\}, \tag{3.8}$$

with $v(\mathbf{r})$ held fixed during the minimisation. The minimising density is then the ground state density. The number of electrons N is formally held fixed introducing the Lagrange multiplier μ and solving the corresponding Eulero-Lagrange equation:

$$\frac{\delta F}{\delta n(\mathbf{r})} + v(\mathbf{r}) = \mu, \tag{3.9}$$

where the constant μ can be identified as the chemical potential of the system and needs to be adjusted so that the relation $\int \mathrm{d}^3 r n(\mathbf{r}) = N$ is satisfied.

3.1.2 Kohn-Sham approach

The Hohenberg-Kohn theorems prove that the ground state density of a system determines all its properties and that the variational principle is valid also in terms of trial densities. No information is however given about the form of the universal functional. A significant step towards the practical use of DFT came with the so called Kohn-Sham (KS) approach[72]. Kohn and Sham realised that many problems encountered when directly dealing with density functionals, like for example within the Thomas-Fermi approach[73-75], were to be traced back to the way the kinetic energy was treated and that, in this regard, orbital-based approaches such as the Hartree-Fock method give better results. Their idea was to introduce a fictitious auxiliary system of non interacting electrons with the property of having the same ground state density as the real system of interacting electrons. The Hamiltonian of equation 3.3 can then be written as a sum of single particle hamiltonians $\hat{h}_s$, where the subscript s indicates that the non interacting system is considered:

$$\hat{H}_s = \hat{T}_s + \hat{V}_{s,\mathrm{ext}} = \sum_{i=1}^N \hat{h}_s(\mathbf{r}_i). \tag{3.10}$$

The term $\hat{V}_{ee}$ is 0 since being the electrons are non interacting. The Schrödinger equation can be written as

$$\hat{H}_s \Phi = E \Phi, \tag{3.11}$$

where Φ is the many electrons wavefunction of the non interacting system. The Eulero-Lagrange equation for the auxiliary system becomes:

$$\frac{\delta T_s}{\delta n(\mathbf{r})} + v_s(\mathbf{r}) = \mu. \tag{3.12}$$

$T_s[n] = \min_{\Psi \to n} <\Psi|\hat{T}|\Psi> = <\Phi_n^{\min}|\hat{T}|\Phi_n^{\min}>$ is then the kinetic energy of the system of non interacting electrons and $\Phi_n^{\min}$ is the minimising wavefunction. It is now possible to write the universal functional F in terms of T_s:

$$F[n] = T_s[n] + U[n] + E_{xc}[n], \tag{3.13}$$

where $U[n] = \frac{1}{2} \int \mathrm{d}^3 r \int \mathrm{d}^3 r' \frac{n(\mathbf{r}) n(\mathbf{r}')}{|\mathbf{r} - \mathbf{r}'|}$ is the Hartree energy, that describes the classical electrostatic self-repulsion of the electron density, and $E_{xc}[n]$ is the exchange correlation energy, a

key quantity of the KS procedure that includes both the non classical contributions to the energy, namely exchange and correlation energy, and the difference in kinetic energy between the non interacting electron system and the real one. Combining the equations 3.9 and 3.12 the following expression is obtained:

$$v_s(\mathbf{r}) = v(\mathbf{r}) + \frac{\delta U[n]}{\delta n(\mathbf{r})} + \frac{\delta E_{xc}[n]}{\delta n(\mathbf{r})} \tag{3.14a}$$

$$= v(\mathbf{r}) + \int \mathrm{d}^3 r \frac{n(\mathbf{r})}{|\mathbf{r} - \mathbf{r}'|} + v_{xc}(\mathbf{r}), \tag{3.14b}$$

where $v_{xc}(\mathbf{r})$ is the exchange correlation potential.

The KS procedure treats T_s exactly, leaving E_{xc} to be approximated. Such a splitting is reasonable considering that usually T_s represents about the 50 - 60% of the total energy, while E_{xc} amounts to only the 5 - 10%. Moreover, T_s plays a fundamental role for describing the oscillations of the density of the shell structure and the Friedel oscillations, indeed very well treated within DFT. Furthermore, E_{xc} is better suited than T_s to local and semilocal approximations.

Beside the aforementioned advantages, the KS approach has a fundamental downside, that is the appearance of orbitals: neither the KS wavefunctions nor the KS energies have any observable physical meaning. The only exceptions are the relation $n(\mathbf{r}) = \sum_{i=1}^{N} |\phi_i(\mathbf{r})|^2$, where $\phi_i(\mathbf{r})$ are the KS single electron orbitals, and the meaning of the energy of the highest occupied orbital. This latter equals the negative of the lowest vertical ionisation potential. It is very important to point out that if the exact E_{xc} were known, the KS equations would yield the exact density.

3.1.3 E_{xc} approximations

As mentioned in the previous section, the form of the exchange correlation functional is not known and needs to be approximated. The simplest approximation is the Local Density Approximation (LDA)[67], in which E_{xc} is defined as:

$$E_{xc}^{LDA} = \int \mathrm{d}^3 r n(\mathbf{r}) e_{xc}[n(\mathbf{r})] \tag{3.15}$$

were e_{xc} is the exchange correlation energy per particle of a uniform electron gas with density n. The LDA is obviously exact for uniform densities and gives good results for slowly varying ones. This latter condition is satisfied by some simple crystalline metals like Na, but is generally pretty rare in nature. However, the LDA performs surprisingly well for many systems. On the other hand, as expected, it fails for systems in which the electron-electron interactions vary strongly.

The most logical way to improve the LDA is to include in the E_{xc} expression the dependence not only on the electron density but also on its gradient:

$$E_{xc}^{GGA} = \int \mathrm{d}^3 r n(\mathbf{r}) e_{xc}[n(\mathbf{r}), \nabla n(\mathbf{r})] \tag{3.16}$$

Such an approach is known as Generalised Gradient Approximation (GGA). While there is solely one way to define E_{xc} within LDA, there are instead in principle many different ways to define it in the framework of GGA. For instance, the Perdew-Burke-Ernzerhof (PBE)[27] GGA functional, the most used functional in solid state physics, is based on the idea of keeping all the good properties of the LDA and improving the aspects in which the LDA

fails. While improving many energy related properties (e.g. total energies and energy differences), GGA functionals still suffer from several drawbacks, like, for instance, the systematic underestimation of the band gap and the overestimation of the delocalisation of the electrons. Further, more sophisticated strategies to go beyond the LDA are including in the expression of E_{xc} the second derivative of the electron density (meta-GGA) and the exact exchange energy density (hyper-GGA). A particular case of hyper-GGAs are so called hybrid functionals, in which the exchange contribution to the exchange correlation energy includes a fraction of the exact Hartree Fock (HF) exchange and a fraction of GGA exchange. The E_{xc} is defined as follows:

$$E_{xc}^{hyb} = aE_x^{HF} + (1-a)E_x^{GGA} + E_c^{GGA} = E_{xc}^{GGA} + a(E_x^{HF} - E_x^{GGA}), \qquad (3.17)$$

where the constant a can be either theoretically estimated or empirically fitted. For example, in the very commonly used hybrid functional PBE0[76], the value of a has been calculated to be 0.25 using perturbation theory.

Including a fraction of the HF exact exchange allows at least partially solving the aforementioned GGA main problems. This however drastically increases the computational cost of the calculations. A way to make such calculations more efficient in terms of time was proposed by Heyd, Scuseria and Ernzerhof, who suggested the screened hybrid functional HSE[77–81]. The idea is to accelerate the spatial decay of the HF exchange interaction by dividing the exchange contribution into short-range (SR) and long-range (LR) components. A screening parameter ω is introduced that defines the separation range:

$$E_{xc}^{HSE} = aE_x^{HF,SR}(\omega) + (1-a)E_x^{PBE,SR}(\omega) + E_x^{PBE,LR}(\omega) + E_c^{PBE}, \qquad (3.18)$$

where $E_x^{HF,SR}$ is the short range HF exchange, $E_x^{PBE,SR}$ and $E_x^{PBE,LR}$ are respectively the short and long range components of the PBE exchange, E_c^{PBE} is the PBE correlation and $a = 0.25$. For $\omega = 0$ HSE equals the conventional hybrid functional PBE0[76], while for $\omega = \infty$ the GGA functional PBE[27]. A commonly employed functional belonging to the HSE family is HSE06[82], with $\omega = 0.11$ bohr^{-1}, that gives pretty accurate predictions of many properties like band gaps, lattice constants of solids, ionisation potentials and electron affinities.

3.1.4 Long range interactions

As already mentioned, the majority of quantum mechanical simulations are presently performed using the DFT approach[72,83]. The reason is the suitability of DFT for describing many diverse systems and its good compromise between accuracy and computational resources. However, DFT approximated methods[1] present a relevant drawback, namely they do not describe long range electronic interactions responsible for van der Waals (vdW) forces[84,85]. Van der Waals forces, known also as dispersion forces, play an important role in many systems and are responsible for electrostatic interactions.

Being the dispersion contribution totally related to electronic correlation[86], the addition of an (empirical) pairwise energy term of the form $C_6\mathbf{r}^{-6}$, in which $\mathbf{r}$ is the interatomic distance and C is a dispersion coefficient[87–89] has been suggested as the most immediate approach to account for them. A common way to write the correction term E_{vdW} is

$$E_{vdW} = -\frac{1}{2} \sum_{A,B} f_{\text{damp}}(\mathbf{r}_{AB}, \mathbf{r}_A^0, \mathbf{r}_B^0) C_{6AB}\mathbf{r}_{AB}^{-6}, \qquad (3.19)$$

---

[1]It is worthwhile to again point out that density functional theory is in principle correct, while the necessary approximations due to the E_{xc} being unknown suffer from the limitations and problems described in the text.

where $\mathbf{r}_A^0$ and $\mathbf{r}_B^0$ are the van der Waals radii of the atoms A and B, respectively, $\mathbf{r}_{AB}$ is the distance between the atoms A and B and C_{6AB} is the corresponding C_6 coefficient. $f_{\mathrm{damp}}(\mathbf{r}_{AB}, \mathbf{r}_A^0, \mathbf{r}_B^0)$ is a short range damping function with the purpose of preventing E_{vdW} from diverging for small values of $\mathbf{r}_{AB}$.

Within the Tkatchenko Scheffler (TS) approach[29], used throughout this thesis, C_6 coefficients and vdW radii are calculated based on the ground state charge density and, therefore, depend on the local chemical environment of the atoms.

In order to improve the description of long range interactions for organic molecules adsorbed on metallic surfaces, such as the majority of the systems investigated in the present thesis, the vdW$^{\mathrm{surf}}$ method has been developed[28]. Within such approach, screening from substrate electrons is taken into account for the calculation of C_6 coefficients and vdW radii by combining the above described TS method and the Lifshitz-Zaremba-Kohn theory for vdW interactions between a solid surface and an atom[90,91].

3.1.5   Charge partitioning schemes

Many systems considered in the present work are analysed in terms of their electrostatic properties. These latter are strictly related to how the electrons are distributed within the molecules. It is therefore conceptually very useful to assign atomic partial charges, although they are not physical observables. Several different approaches have been developed to assign partial charges, based either on the partitioning of the wave function in terms of the basis functions, like within the Mulliken[92] and the Löwdin[93] methods, on fitting the electrostatic potential (ESP charges[94]), or on the partitioning of the electron density, like in the Bader[95–97] and in the Hirshfeld[98] partitioning schemes.

The two latter approaches are preferable, since they are based on properties of the electron density itself and not on the basis set used to represent the wave function. As only the electron density is involved, the results are expected to be insensitive to the level of theory used for generating the wave function. Bader and Hirshfeld schemes are therefore used to assign atomic partial charges in the present work. The idea behind both approaches is to divide the molecular volume into subsections belonging to each atom and to integrate the electron density within each subsection. The atomic partial charge is then obtained adding the positive charge of the nucleus of the specific atom. The difference between Hirshfeld and Bader charges is the way the molecular volume is divided.

Within the Hirshfeld scheme the atomic densities are used to partition the molecular density: a so called promolecular density is defined, which is the sum of the atomic densities placed at the nuclear positions, and at each point in space the atomic density is calculated using weighting factors obtained according to the atomic contributions to the promolecular density.

A more rigorous way to divide the molecular volume is the Bader Atoms In Molecules (AIM) method, that performs a topological analysis of the electron density taken as a function of the three spatial coordinates. Maxima in the electron density occur at, or in the close vicinity of, the nuclei. These latter are the source of positive charge and act as attractors of the electron density. Thus, at each point in space the gradient of the electron density points in the direction of the strongest local attractor, while in the opposite direction the gradient goes to zero. The collection of all such points forms the volume associated with a specific attractor, i.e. the atomic volume associated to each atom.

Since as already mentioned partial charges are no physical observables, all partitioning schemes are to some extent ambiguous and it is not possible to define the best approach. Moreover, there is no reference value to which the population analysis can be compared. Results obtained within different schemes can then be quantitatively and qualitatively dif-

ferent. Therefore only partial charges calculated with the same method and the same level of theory can be reasonably compared.

3.2 Computational details

Almost all the calculations presented in this work have been performed using the Fritz Haber Institute *ab initio* molecular simulations (FHI-aims) package[26]. FHI-aims is an all-electron code, meaning that all the electrons of the simulated systems are accounted for in the calculations. It supports both periodic and open boundary conditions. The Vienna *ab-initio* simulations package[99–102] (VASP), a plane wave code which describes the core electrons using pseudopotentials and implements the projector augmented wave (PAW) method as described by Blöchl[103], has been used to perform the Bader charge partitioning analysis for the systems treated in section 4.7. Some reference calculations on isolated gas phase molecules have been also performed using the code Gaussian 09, RevD.01[104]. Gaussian is the most used code in computational chemistry. It is an all-electron code and is mostly used to perform calculations, up to very high levels of theory, on isolated molecules or clusters, for which it provides reliable results to compare to.

Specific informations regarding employed functionals and basis set and the level of accuracy of the performed calculations are given for each investigated system in the corresponding sections in chapter 4.

Before running any calculation, a suitable geometry needs to be set up. The systems investigated in this work are surfaces, that is, they are periodic in two directions, while in the third direction the periodicity is broken. To model such systems the so called repeated slab approach is used: in the z direction a vacuum region of about 20-25 Å and a dipole correction are introduced. The former has the purpose of quantum-mechanically decoupling two consecutive slabs, while the latter is needed to compensate possible dipoles arising from the slab. It has the form of a discontinuity in the electrostatic potential, to recover its original value at the bottom of the next repeated unit. This is graphically shown in figure 3.1.

The metal slab is usually modelled using five layers of metal atoms, where the number can change depending on the purpose of the calculation and the required accuracy. For instance, for some expensive calculations presented in chapter 4 only three layers of metal were used. Although in FHI-aims it is possible to optimise both the atomic positions and the unit cell edges, the dimensions of the unit cell in the x and y directions are set according to the theoretically calculated substrate lattice constant. Moreover, the three bottom layers (for a five layers substrate) are kept fixed in all the calculations, to mimic the bulk, while the two topmost ones are relaxed in case of geometry optimisations. These precautions are adopted to avoid spurious relaxations in the bulk.

As mentioned in the introduction, setting up a unit cell for such systems without having any information about how it should look like is not feasible. In passing we note that in this regard structure search methods based on machine learning techniques are being developed for metal/organic interfaces (see for instance references 105 and 106 and references therein). Nevertheless, at the present stage they are still unsuited for molecules with many degrees of freedom such the ones considered in this work. Some experimental support is therefore necessary and useful input is usually taken from techniques such as STM or XPS. Important pieces of information are, for instance, the shape of the unit cell and the density of the adsorbed molecules. With that knowledge it is then possible to proceed with a partial screening of the potential energy surface, testing significant high symmetry docking positions of the adsorbate molecules, their conformation and their arrangement with respect
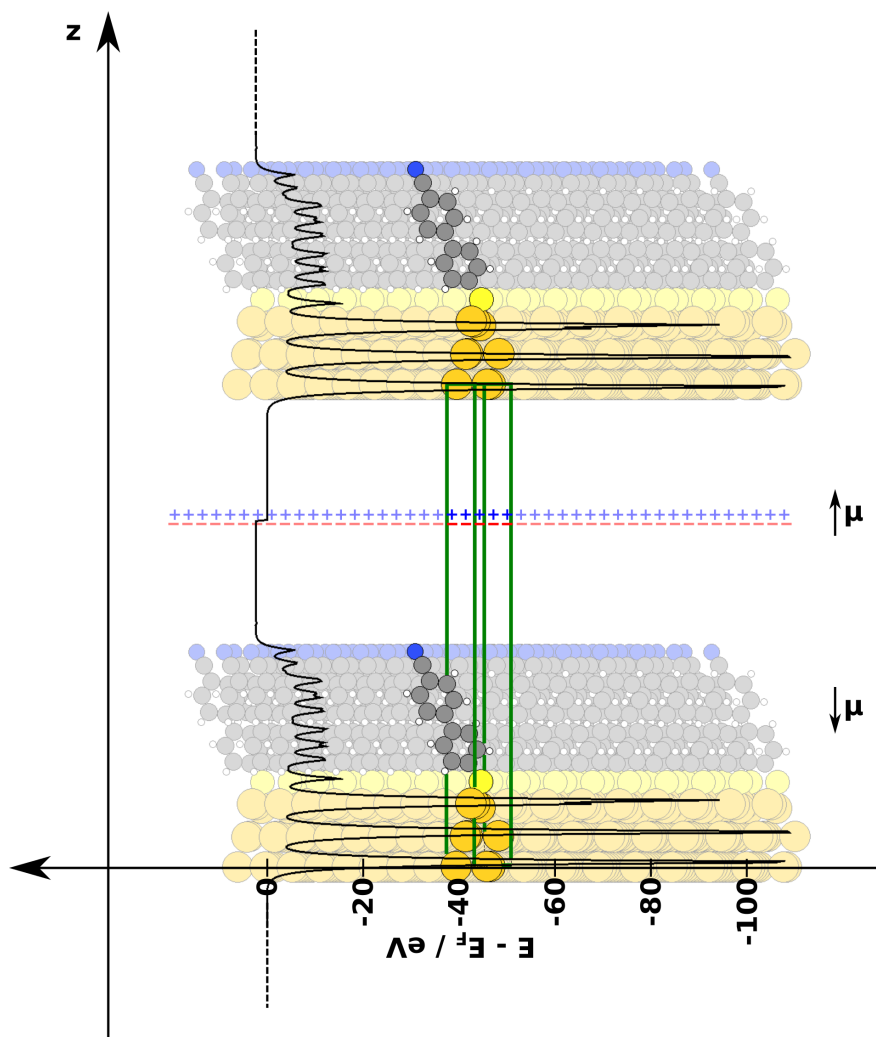
Figure 3.1: Illustration of the repeated slab approach combined with periodic boundary conditions. The unit cell used in the simulations is depicted in green and the x,y plane averaged electrostatic potential energy of an electron is plotted (black line). The vacuum region in the z direction and the discontinuity in the electrostatic potential energy due to the introduction of the dipole correction are also shown. The illustrated system is the same as the one considered in figure 2.1. The computational settings used for the calculations are reported at the end of section 2.1.2.

to the neighbouring ones. The disadvantages of the approach are obvious: only commensurate adsorbates, i.e. with the lattice spacing of the adsorbate layer being correlated by an integer value to the periodicity of the substrate, and perfectly ordered structures can be modelled. The main consequences of such limitations are that the simulated structures do not always reflect the real ones and when comparing calculated and measured properties often the discrepancies are caused exactly by this issue, as it will be extensively discussed in chapter 4. Keeping the methodological restrictions in mind helps interpreting the data and understanding why sometimes experimental and calculated results disagree, see for instance sections 4.4 and 4.5.

4 Results

4.1 Relative thermal stability of thiolate- and selenolate-bonded aromatic monolayers on the Au(111) surface

As discussed in the introduction, self-assembled monolayers (SAMs) of organic molecules are largely exploited in the field of organic electronics to modify the properties of metal electrodes. S docked SAMs on the Au(111) surface are the most frequent system. Recently, however, Se based SAMs have been proposed as alternative to the more common S based ones[30–35]. In this section the relative thermal stability of CN substituted naphthalene based thiolates and selenolates on the Au(111) surface is investigated. Such a comparison is of fundamental interest. The detailed knowledge of the atomistic structure at the interface and of the impact of the docking atom is essential for the practical applications of such systems. The investigation is performed combining experimental X-ray photoelectron spectroscopy (XPS) and secondary ion mass spectrometry (SIMS) results and state-of-the-art density functional theory (DFT) calculations.

The results of the investigation have been published in the *Journal of Physical Chemistry C*, see reference 107. The original paper is here reprinted with permission from Ossowski, J.; Nascimbeni, G.; Żaba, T.; Verwüster, E.; Rysz, J.; Terfort, A.; Zharnikov, M.; Zojer, E.; Cyganik, P. Relative Thermal Stability of Thiolate- and Selenolate-Bonded Aromatic Monolayers on the Au(111) Substrate. *J. Phys. Chem. C* **2017**, *121*, 28031-28042. Copyright 2017 American Chemical Society. A reduced version of the supporting information is included. The full supporting information, containing additional SIMS data, is available at DOI: 10.1021/acs.jpcc.7b09685. This work was a collaboration between the groups of Piotr Cyganik, Michael Zharnikov, Andreas Terfort and Egbert Zojer. Jakub Ossowski, Tomasz Żaba, Jakub Rysz and Piotr Cyganik performed SIMS experiments. Michael Zharnikov performed XPS measurements. The molecules were synthesised in the group of Andreas Terfort. Egbert Zojer, Elisabeth Verwüster and I contributed the simulation part. Piotr Cyganik, Michael Zharnikov and Egbert Zojer coordinated the work. The data were discussed and interpreted jointly by all the authors. A first draft of the paper was written by Piotr Cyganik. All the other authors contributed in writing the sections concerning their results and revising the draft. I performed all the calculations presented in the work, did the figure 7 and wrote a draft of the computational part, that was revised and corrected by Egbert Zojer and incorporated in the manuscript by Egbert Zojer and me. I wrote the computational section of the supporting information and prepared all the figures presented there. The text was revised and corrected by Egbert Zojer.

4.1.1 Original paper

Relative Thermal Stability of Thiolate- and Selenolate-Bonded Aromatic Monolayers on the Au(111) Substrate

Jakub Ossowski,[†] Giulia Nascimbeni,[‡] Tomasz Żaba,[†] Elisabeth Verwüster,[‡] Jakub Rysz,[†] Andreas Terfort,[§] Michael Zharnikov,[||] Egbert Zojer,*,[‡] and Piotr Cyganik*,[†]

[†]Smoluchowski Institute of Physics, Jagiellonian University, Łojasiewicza 11, 30-348 Kraków, Poland
[‡]Institute of Solid State Physics, NAMI Graz, Graz University of Technology, Petergasse 16, 8010 Graz, Austria
[§]Institute of Inorganic and Analytical Chemistry, Goethe University, Max-von-Laue Str. 7, 60438 Frankfurt, Germany
[||]Applied Physical Chemistry, Heidelberg University, Im Neuenheimer Feld 253, 69120 Heidelberg, Germany

S *Supporting Information*

ABSTRACT: The thermal stability of self-assembled monolayers (SAMs) is of fundamental importance for the majority of their applications. It strongly depends on the type of chemical group used for bonding the molecules forming the SAMs to the selected substrate. Here, we compare the impact of using S and Se bonding groups on the thermal stability of aromatic model SAMs based on naphthalene, containing a polar substituent, and formed on a Au(111) substrate. Using a combination of secondary ion mass spectrometry (SIMS) and X-ray photoelectron spectroscopy (XPS) while heating the samples, we show that the thermal stability of S-bonded SAMs is higher although the bonding between Se and the Au substrate is stronger. This seeming contradiction is found to result from a higher stability of the S−C compared to the Se−C bond. The latter forms the weakest link in the SAMs with Se anchor and, thus, controls its thermal stability. These conclusions are supported by state-of-the art dispersion-corrected density functional theory (DFT) calculations. Notably, full qualitative agreement between the experiments and simulations is obtained only when including Au adatoms in the setup of the unit cells, as these reinforce the bonding between the docking groups and the metal surface. This is an indication for the occurrence of such surface reconstructions also for SAMs consisting of comparably large aromatic molecules.
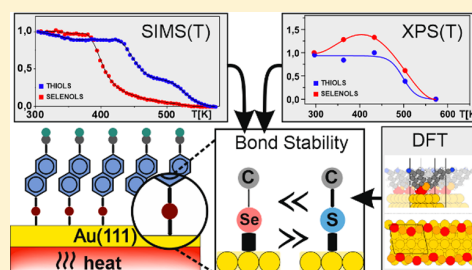
I. INTRODUCTION

Self-assembled monolayers (SAMs)[1−3] are considered as prototypical systems for investigating physical and chemical properties of organic nanostructures and their potential application in nanotechnology.[4,5] The key to SAMs functionality is the comparably strong chemical bonding between the SAM-forming molecules and the respective substrate on which the monolayer is formed. So far, the overwhelming majority of studies analyzing fundamental properties and applications of SAMs have been conducted on molecules containing sulfur as head groups covalently bonded to the Au(111) substrates.[3,6] In recent years it has, however, been demonstrated that selenium, which has the same valence electron configurations as sulfur, is a promising alternative for docking molecules to noble-metal substrates.[7]

One of the advantages of selenium-based SAMs on Au(111) is their better structural quality. Scanning tunneling microscopy (STM) studies of purely aromatic[8−10] as well as hybrid aromatic–aliphatic[11,12] selenolate SAMs on Au(111) demonstrated the formation of layers, which were superior to their thiolate analogues in terms of structural perfection, domain size, and long-range order. It has been proposed that the main reason which limits structural quality of SAMs with aromatic backbones is the stress originating from the misfit between the

structure favored by the aromatic backbones and the template provided by the Au(111) substrate.[13] The release of this stress leads to the formation of defects and limits the achievable domain size. One of the ways to circumvent this problem is the application of hybrid aromatic−aliphatic molecules, where insertion of flexible aliphatic chains between docking group and aromatic backbone provides pathways to reduce stress without breaking the structure preferred by the aromatic moieties.[13] This approach, however, also affects other properties of the films; it, for example, results in a significant reduction in the conductance of the monolayer. Thus, solving the stress problem via the application of another headgroup atom, i.e., selenium instead of sulfur, with no further modification of the molecular backbone is an attractive alternative solution for improving film quality, especially as this substitution does not change the conductance of the monolayer.[14]

The substitution of the headgroup also affects the stability of the molecule−metal bond, which is fundamental for most applications of SAMs. Despite several studies addressing the relative strength of S−Au and Se−Au bonds in SAMs, this issue
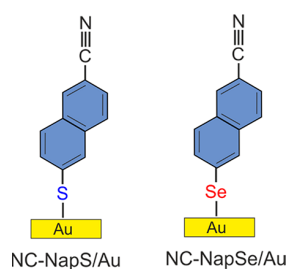
is still not fully clarified. Several conceptually different experimental approaches were used for the analysis including thermal desorption,[9,15] electrochemical desorption,[15,16] ion-induced desorption,[14,17−19] competitive adsorption,[20] X-ray photoelectron spectroscopy (XPS),[21,22] and exchange reactions.[14,23,24] With one exception[24] all these experiments geared at determining stability were done by comparing SAMs with molecular backbones based on benzene,[7,13,15,19] such as BS(Se), (C_6H_4−S(Se)), biphenyl and its derivatives[9,16,20,21] (such as BPnS(Se), CH_3−(C_6H_4)$_2$−(CH_2)$_n$−S(Se), $n = 2$−6), or recently naphthalene[14] (NC−NapS(Se), NC−$C_{10}H_6$−S(Se)). The majority of these reports indicates a higher stability of the Se−Au bond[14,16−18,20,22−24] with, however, two publications[9,21] claiming a higher stability of the S−Au bond. Interestingly, experiments arriving at contradicting conclusions (i.e., a higher stability of either S−Au[9,21] or Se−Au[15,16,20]) were exclusively performed on benzene-based systems comparing benzenethiol (BS) and benzeneselenol (BSe) SAMs.

In this context it is important to consider that for a meaningful comparison of the relative molecule−substrate bonding strength the studied SAMs not only need to have the same molecular backbones but they also should represent well-defined films with very similar molecular packing. Only under such conditions the impact of differences in intermolecular interactions can be minimized, and the bonding of the headgroup to the substrate becomes the main factor determining film stability. Notably, for the BS/Au(111) and BSe/Au(111), STM analysis[9] indicates the formation of structures with packing densities differing by as much as ~40%. Moreover, high-resolution XPS (HRXPS) analysis[15] reveals coadsorption of the headgroup atoms (S or Se) and unbounded molecules in these SAMs. Therefore, in our opinion, a precise comparison of the stability of S−Au and Se−Au bonds using the BS/Au(111) and BSe/Au(111) SAMs is not reliable. Similar considerations apply also to investigations of the thermal stability of these SAMs, where again contradicting results have been obtained, suggesting either a lower[9] or higher[15] thermal stability of BSe/Au(111) compared to BS/Au(111).

Considering that the thermal stability of SAMs is one of the most important factors determining their range of applications, a systematic investigation of this property for SAMs differing only in the used docking atom, but otherwise having similar structures and packing densities (where the latter ought to be sufficiently high), is in high demand. Accordingly, we provide a detailed analysis of the thermal stability of the NC-NapS/Au(111) and NC-NapSe/Au(111) (see Figure 1 for chemical structures). They serve as well-defined model systems with no coadsorption of docking group atoms or unbound molecules

seen in HRXPS.[14] Moreover, they form well-ordered high-density structures displaying similar packing densities as found by STM.[14]

Our experimental studies rely on X-ray photoelectron spectroscopy (XPS) and secondary ion mass spectrometry (SIMS) performed on samples during heating cycles. They are supported by dispersion-corrected density functional theory (DFT) calculations, describing the stability of chemical bonds close to the metal−molecule interface for different bonding scenarios (i.e., flat Au(111) surfaces and surfaces in the presence of a varying number of adatoms). We find that a larger bonding energy between the metal and the docking group does not necessarily yield higher thermal stability. Moreover, full qualitative agreement between the experiments and calculations is achieved only when considering surface reconstructions for both SAMs.

II. EXPERIMENTAL SECTION

SAM Preparation. The Au(111) substrates were prepared by evaporating 150 nm of gold onto single crystal silicon (100) wafer substrates (ITME, Warsaw) primed with a 5 nm chromium adhesion layer (base pressure of ~10^{-7} mbar, rate 0.5 nm/s). The synthesis of the NC-NapS(Se) molecules is described in ref 14. Following a previously developed procedure,[14] SAMs were prepared by immersion of the Au(111) substrates into 1 mM solutions of the respective precursors in pure ethanol at 60 °C for 24 h. After immersion, samples were rinsed with pure ethanol, blown dry with nitrogen, and immediately transferred to the experimental setups (XPS or S-SIMS).

XPS. XPS measurements were performed with a dedicated spectrometer equipped with a hemispherical energy analyzer (VG SCIENTA R3000). The spectra were taken using a monochromatized Al Kα source ($E = 1486.6$ eV; MX-650 VG Scienta). The base pressure in the analytical chamber was 5×10^{-9} mbar. The acquisition of all spectra was carried out in normal emission geometry with an energy resolution of 1.15 eV. The binding energy (BE) scale was referenced to the Au 4f$_{7/2}$ peak at 84.0 eV. To monitor the thermal stability, the sample temperature was linearly ramped at a rate of 5 K/min. Upon reaching the desired temperature, the system was left to stabilize for 5 min, and then the measurement of the chosen signal was carried out. Because of the poor signal-to-noise ratio and the resulting long acquisition time, S and Se core-level spectra were collected in independent experiments. All spectra were fitted by symmetric Voigt functions, and a Shirley-type background was subtracted. For fitting S 2p$_{3/2,1/2}$ and Se 3p$_{3/2,1/2}$ doublets, two peaks with the same fwhm, a fixed branching ratio (2:1), and defined spin−orbit splitting (~1.2 eV[25] and ~5.40 eV,[26] respectively), verified by fits, were used.

S-SIMS. The SIMS experiments were performed using a time-of-flight SIMS (TOF SIMS V system, ION TOF GmbH, Germany). The instrument was operated at a base pressure of 6×10^{-10} mbar. The primary 30 keV Bi$^+$ ion beam was scanned over a 500 μm × 500 μm area (128 × 128 data points) during data acquisition. The secondary ions were extracted into a reflectron TOF mass spectrometer before reaching a multi-channel plate (MCP) detector. For the thermal stability analysis, the sample temperature was linearly ramped from room temperature up to 725 K at a rate (β) of 3.75 K/min. The SIMS measurements were performed at selected temperatures without interrupting the sample heating. As discussed in the Supporting Information (Figure S1), SIMS experiments were

Figure 1. Schematic structures of the SAMs used in this study along with their acronyms.

also performed at room temperature to prove the absence of ion-beam-induced damage of the investigated samples. These experiments confirmed the prevalence of static conditions during the SIMS measurements (S-SIMS). Before analysis, all spectra were normalized to the respective total counts.

Simulations. To analyze the bonding between the adsorbates and substrate, we calculated the energies associated with breaking S(Se)/Au and S(Se)/C bonds for a variety of adsorbate configurations using dispersion-corrected DFT. All calculations were performed using the FHI-aims code,[27] employing the PBE functional.[28] To include long-range van der Waals interactions, the latter was augmented by the Tkatchenko−Scheffler[29,30] scheme parametrized specifically to treat adsorption on metallic surfaces (PBE+vdWsurf).[31] The dispersion corrections between the substrate Au atoms were turned off. To model bonded monolayers on substrates and clean metal surfaces, periodic boundary conditions and the repeated slab approach were employed representing the substrate by five layers of Au. Periodic replicas of the slab were decoupled by an at least 20 Å wide vacuum gap and a self-consistently determined dipole layer to account for the electrostatic asymmetry.[32] The bottom three Au layers were kept fixed in the geometry optimizations to avoid spurious relaxations at the bottom surface of the slab. As the observed energy differences between SAMs bonded by S and Se atoms in many cases are very small, it has been crucial to carefully converge the k-point sampling, the basis set (avoiding artifacts due to basis-set superposition errors), and other numerical parameters with more details given in the Supporting Information. In short, Au atoms were described using the default FHI-aims "tight" settings, while for all the other atoms the default tight settings were augmented by adding a further basis function and tightening numerical settings (for more details see the Supporting Information). $6 \times 3 \times 1$, $9 \times 5 \times 1$, and $4 \times 4 \times 1$ Monkhorst−Pack k-point grids[33] were used for the rectangular $(4 \times \sqrt{3})$, rectangular $(3 \times \sqrt{3})$, and oblique $(3 \times \sqrt{7})$ unit cell, respectively. The convergence criterion for the total energy in the self-consistency cycle was set to 10^{-6} eV, and the optimizations were performed until the maximum residual force component per atom was below 0.01 eV/Å.

The primarily analyzed quantities derived from the simulations are the bonding energies (bond-breaking energies) between the docking atoms S or Se (X) and the Au surface or the first C atom (Y), E_{X-Y}. They are defined as the differences in total energy between the isolated molecular fragments, $E_{mol\text{-}fragment,X-Y}$, plus the energy of the Au(111) surface (in some cases containing adatoms and/or adsorbed S/Se atoms), $E_{surf,X-Y}$, and the energy of the adsorbed SAM on the Au substrate (i.e., the undisturbed, bonded SAM), $E_{SAM\text{-}bonded}$:

$$E_{X-Y} = E_{mol\text{-}fragment,X-Y} + (E_{surf,X-Y} - E_{SAM\text{-}bonded})/2$$

The factor of 1/2 accounts for the two molecules in the unit cell (vide infra) such that average energies per molecule are obtained. $E_{surf,X-Y}$ and $E_{SAM\text{-}bonded}$ ($E_{mol\text{-}fragment,X-Y}$) have been obtained using periodic (open) boundary conditions. Note that for calculating those energies, the geometries of all subsystems were fully relaxed. To assess the impact of vibrational degrees of freedom, we also calculated the vibrational eigenmodes of the bonded layer and of the individual fragments after bond-breaking for the unreconstructed rectangular $(4 \times \sqrt{3})$ unit cell employing finite displacements (for details see the Supporting Information). These calculations allowed an assessment of the impact of zero-point energies and the thermal occupation of

vibrational modes. As the vibrational energies had only a minor impact on the overall energetics and in view of the massive computational efforts associated with such calculations, we considered vibrational effects only for a single adsorption motifs, as discussed below.

III. RESULTS

Thermal Stability Analysis by XPS. To monitor the evolution of NC-NapS/Au and NC-NapSe/Au structure with temperature, signals corresponding to Au, C, S, and Se were monitored by XPS (Figures 2−4) at several different
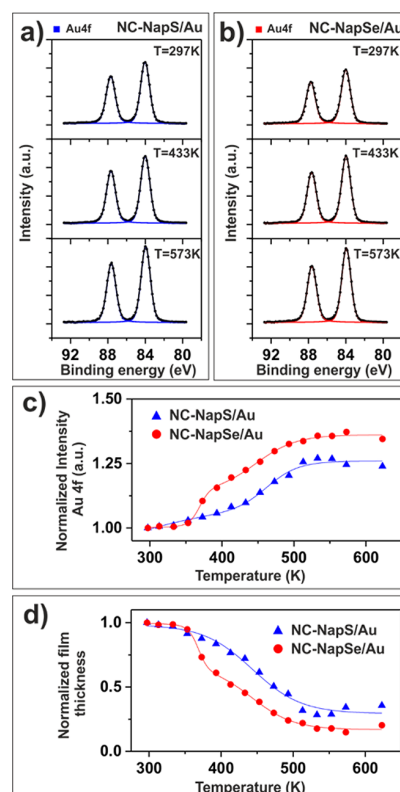
Figure 2. XPS data analysis. (a, b) Selected Au 4f spectra obtained at different temperatures for the NC-NapS/Au and NC-NapSe/Au SAMs, respectively. (c) Au 4f signal intensities normalized to the room temperature values as a function of the sample temperature measured for NC-NapS/Au (blue points) and NC-NapSe/Au (red points). (d) The normalized film thickness as a function of temperature (relative to the value at room temperature) measured for NC-NapS/Au (blue points) and NC-NapSe/Au (red points). The color-coded lines in (c) and (d) are guides to the eye.

temperatures ranging from 297 K (24 °C, room temperature) up to 623 K (350 °C). In Figures 2a and 2b selected Au 4f$_{7/2,5/2}$ spectra obtained for NC-NapS/Au and NC-NapSe/Au at temperatures of 297, 433, and 573 K are presented. The temperature dependence of the integrated Au 4f$_{7/2,5/2}$ intensity (normalized to the room temperature value) is shown in Figure 2c for the two SAMs. It reveals a substantial difference between NC-NapS/Au and NC-NapSe/Au. Starting from 350 K (77 °C), a pronounced increase of the Au 4f$_{7/2,5/2}$ signal for the NC-NapSe/Au SAM is observed, and it becomes noticeably higher than that for the NC-NapS/Au system. For the latter a somewhat steeper increase of the signal is observed only above

450 K (177 °C), but the overall signal remains lower than that for NC-NapSe/Au. Above ca. 525 K (252 °C) the signal saturates for both types of SAMs. Notably, for NC-NapSe/Au the saturation level corresponds to ca. 1.35 of the room temperature signal, while for the NapS/Au the ratio is only 1.25.

The increase of the Au $4f_{7/2,5/2}$ signal reflects a temperature-induced reduction in the effective SAM thickness. Assuming the standard exponential dependence of the Au 4f signal on the thickness of the adsorbate layer due to attenuation, one can determine relative changes in the effective film thickness as a function of temperature using the equation

$$\frac{d_T}{d_{T_0}} = 1 - \frac{\lambda}{d_{T_0}} \ln\left(\frac{I_{Au}(T)}{I_{Au}(T_0)}\right) \tag{1}$$

Here, d_T is the effective film thickness at elevated temperature T, d_{T_0} is the equivalent quantity at room temperature, λ is the electron mean free path, $I_{Au}(T)$ is the Au 4f intensity at temperature T, and $I_{Au}(T_0)$ is the Au 4f intensity at room temperature. Setting λ to 3.15 nm (in accordance with ref 34) and using for d_0 the values obtained in our previous HRXPS studies[14] on these SAMs (1.17 nm for NC-NapSe/Au and 1.05 nm for NC-NapS/Au), the corresponding $\frac{d_T}{d_0}(T)$ values were calculated from the measured $\frac{I_{Au}(T)}{I_{Au}(T_0)}$ ratios. The resulting evolution is presented in Figure 2d. It reproduces the trend inferred from the intensity ratios, indicating a more pronounced decrease of the effective film thickness with temperature for the Se-bonded SAM.

Selected C 1s spectra for the NC-NapS/Au and NC-NapSe/Au are shown in Figures 3a and 3b, respectively, together with the temperature-dependent evolution of the peak intensities in Figure 3c. The spectra acquired at room temperature exhibit an intense peak at a BE of 284.5 eV accompanied by a shoulder at higher BE (286.0 eV). Following previous HRXPS study,[14] the intense peak is assigned to the naphthalene backbone, while the high binding energy shoulder is associated with the nitrile carbon. For both types of SAMs, the integrated C 1s intensity, normalized to the value at room temperature, decreases with increasing temperature, followed by a saturation around 525 K (252 °C) (Figure 3c). This is the inverse of the behavior of the Au $4f_{7/2,5/2}$ signal discussed previously. Above ca. 350 K (77 °C) the normalized C 1s intensity is consistently lower for the NC-NapSe/Au layer compared to NC-NapS/Au, which is inverse to the trend observed for the Au $4f_{7/2,5/2}$ signal.

Interestingly, a qualitatively different behavior is observed for the S $2p_{3/2,1/2}$ and Se $3p_{3/2,1/2}$ spectra presented in Figure 4. The analysis of the integrated and normalized S $2p_{3/2,1/2}$ signal in Figure 4c shows a roughly constant value between room temperature and ca. 450 K (177 °C), which is followed by a drop below the detection limit of XPS for temperatures exceeding 550 K (277 °C). In contrast, for the Se $3p_{3/2,1/2}$ signal, an increase by ca. 25% is observed up to a temperature of ca. 400 K (127 °C), which is again followed by a sharp drop at higher temperatures.

Thermal Stability Analysis by S-SIMS. SIMS is a useful, complementary technique to study the thermal stability of SAMs.[35] Here, we recorded the emission intensities of characteristic secondary ions associated with the SAMs as a function of the (linearly increasing) sample temperature (a heating rate of 3.75 K/min). Two types of secondary ions were
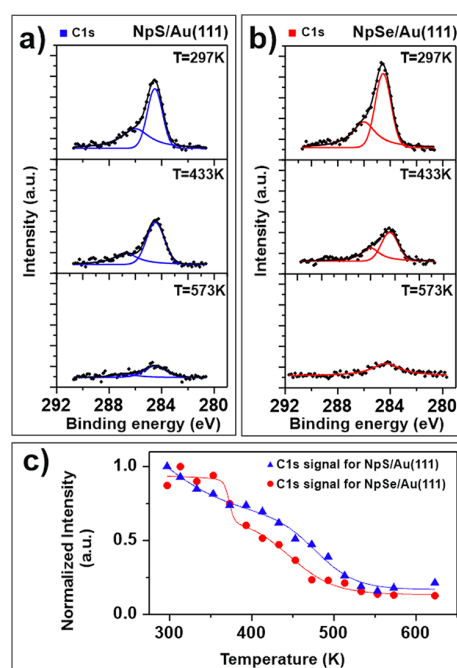
Figure 3. XPS data analysis. (a, b) Selected C 1s spectra obtained at different temperatures for NC-NapS/Au and NC-NapSe/Au, respectively (all spectra have the same vertical scale). (c) C 1s signal intensities normalized to the room temperature values as a function of the sample temperature measured for NC-NapS/Au (blue points) and NC-NapSe/Au (red points). The color-coded lines in (c) are guides to the eye.
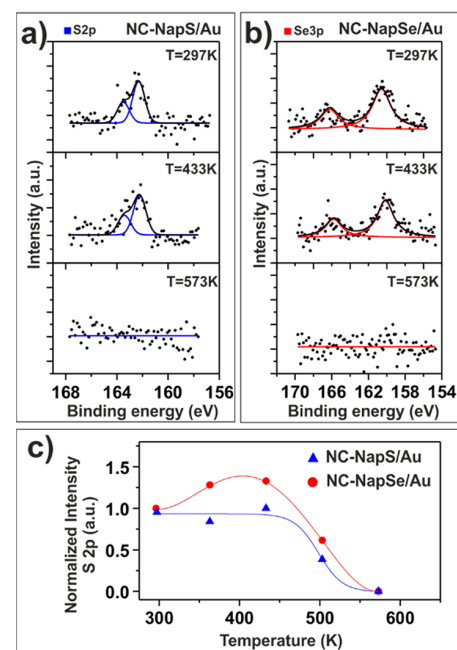
Figure 4. XPS data analysis. (a, b) Selected S 2p and Se 3p spectra obtained at different temperatures for NC-NapS/Au and NC-NapSe/Au, respectively. (c) S 2p and Se 3p signal intensities normalized to the room temperature values as a function of the sample temperature measured for NC-NapS/Au (blue points) and NC-NapSe/ (red points), respectively. The color-coded lines in (c) are guides to the eye.

analyzed, namely "organic" ions, such as M_2Au^- (where M denotes the complete NC-NapS or NC-NapSe molecules), and "inorganic" ions, such as $AuS(Se)^-$, $AuS(Se)_2^-$, and $Au_2S(Se)^-$. To ensure that the measured intensity changes analyzed in the thermal SIMS experiments are not related to primary ion beam damage during the data acquisition, separate reference experiments monitoring the intensity of the analyzed signals at room temperature for 110 scans were conducted (see Figure S1 in the Supporting Information). These data show that during the entire measurement time needed for the thermal analysis (65 scans in Figure 5 and 95 scans in Figure 6) all signals remain constant. From this behavior one can conclude that all experiments were conducted in the static SIMS (S-SIMS) mode.

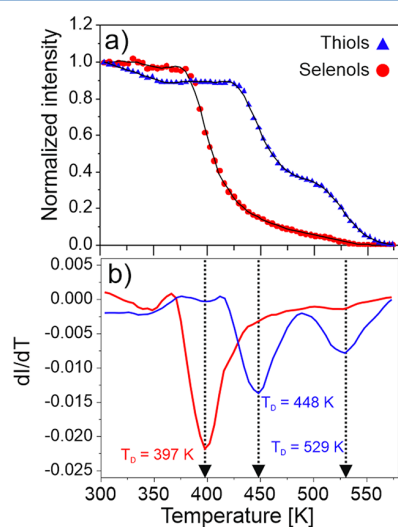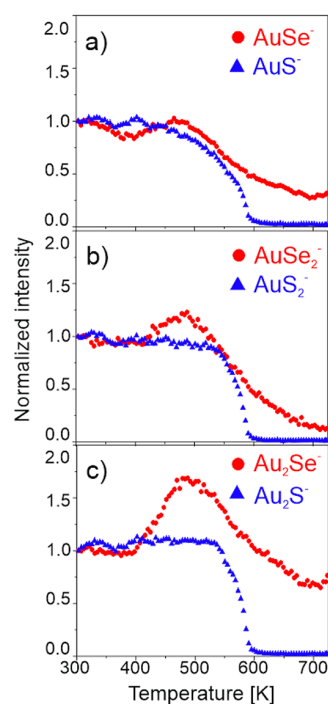**Figure 5.** S-SIMS data analysis. (a) shows M_2Au^- secondary ion intensities normalized to the room temperature values as a function of the sample temperature measured for NC-NapS/Au (blue points) and NC-NapSe/Au (red points). Solid lines in (a) show the spline function fitted to the data points to enable the data processing. (b) Derivatives of the experimental curves in a (calculated from the aforementioned spline functions) for NC-NapS/Au (blue line) and NC-NapSe/Au (red line). The desorption temperatures (T_D) corresponding to the minima of the derivatives are indicated.

The signal for the "organic" M_2Au^- secondary ion provide information on changes in the coverage for a given SAM as a function of the temperature ramping. In fact, metal−organic secondary ions like M_2Au^- are well-known "fingerprints" for SAM formation and desorption analysis in SIMS.[35−41] The "inorganic" secondary ion group can be used to trace the stability of the bonding between the headgroup atom and the substrate.

Figure 5a shows changes in the emission intensity of the M_2Au^- secondary ions as a function of temperature in the range between room temperature and 570 K (297 °C). To enable a direct comparison of both types of SAMs, the data presented in Figure 5a are normalized to the values measured at room temperature. For both types of SAMs, an approximately constant signal intensity is observed up to a certain temperatures, which is followed by an intensity drop to zero at the higher temperatures. The character of the signal decrease is, however, substantially different between NC-NapS/Au and NC-NapSe/Au. While for the Se-bonded SAM a single sharp

Figure 6. S-SIMS data analysis. (a) AuS^- and $AuSe^-$ secondary ion intensities normalized to the room temperature values as a function of the sample temperature measured for NC-NapS/Au (blue points) and NC-NapSe/Au (red points) SAMs. (b) Equivalent data for the AuS_2^- and $AuSe_2^-$ secondary ions, and (c) displays them for the Au_2S^- and Au_2Se^- secondary ions.

drop is observed, which starts already below 400 K (127 °C), the signal for the S-bonded SAM decreases in two steps, which both occur at significantly higher temperatures. To determine the temperatures characteristic of the observed drops of the M_2Au^- signal, the first derivative of the normalized intensity as a function of temperature was calculated (Figure 5b). This derivative yields a single characteristic temperature of 397 K (124 °C) for the NC-NapSe/Au, indicative of a single thermal desorption process. In contrast, for the NC-NapS/Au, two minima at 448 K (175 °C) and 529 K (256 °C) are obtained, indicative of two successive desorption processes which set in at significantly higher temperatures. We note here that such a two-step desorption process is not visible in the temperature-dependent XPS data (Figures 2 and 3) which are acquired with a much slower procedure (27 min per each temperature step in XPS in contrast to only 1 min in SIMS) and with much lower resolution (16 points for the whole temperature range in XPS, in contrast to 74 points in SIMS). Provided that the change in the SIMS signal intensity is proportional to the surface coverage, Θ, of the NC-NapS/Au, the first desorption process reduces the coverage by ca. 60%. Assuming first-order kinetics of all observed processes, one can estimate the value of the corresponding desorption energy E_D using the Redhead formula:[42]

$$E_D = kT_P\left[\ln\left(\frac{\nu_T T_P}{\beta}\right) - 3.64\right] \quad (2)$$

where k is the Boltzmann constant, T_P is the peak temperature (i.e., the temperature where the change in the surface coverage Θ is most pronounced and $d\Theta/dT$ becomes a minimum), ν_T is

the frequency factor (which is usually approximated as ca. 10^{13} s^{-1}),[9,15,43,44] and β = 3.75 K/min is the heating rate. For the NC-NapSe/Au, T_P = 397 K yields a value of E_D = 1.20 eV; for the NC-NapS/Au the two characteristic temperatures of T_P = 448 K (175 °C) and T_P = 529 K (256 °C) correspond to E_D = 1.35 eV and E_D = 1.61 eV, respectively.

The analysis of the "inorganic" signals corresponding to the $AuS(Se)^-$, $AuS(Se)_2^-$, and $Au_2S(Se)^-$ secondary ions is presented in Figure 6. All three signals exhibit significant differences for the NC-NapS/Au and NC-NapSe/Au. First, for NC-NapS/Au an abrupt drop of the signals is observed above ca. 500 K (227 °C) reaching zero above ca. 600 K (327 °C). In contrast, for NC-NapSe/Au an increase of the signals is observed in the region between ca. 400 K (127 °C) and 450 K (177 °C), which is especially pronounced for the $AuSe_2^-$ and Au_2Se^- ions. Additionally, for NC-NapSe/Au a significant intensity of all signals is observed even at 725 K (452 °C), i.e., at the upper temperature limit of our experiments.

Simulations. To further analyze the bonding between the docking groups and the substrate, as well as bonding between the docking groups and the molecular backbone, we calculated the energies associated with the breaking of these bonds for a variety of adsorbate configurations. These simulations follow the approach usually applied for computing stabilities of adsorbate layers, namely comparing the energy differences between SAMs adsorbed on the substrate and molecules detached from the surface. What they do not take into account are the details of the desorption process. Unfortunately, a meaningful simulation of the dynamics of molecular desorption for system as complex as the present ones is currently intractable by computational techniques, which provide the accuracy required for the present problem (see below). One of the reasons for that is that thermally initiated desorption most likely occurs from the rims of islands or from disordered regions of the adsorbate layer. The simulation would require the consideration of huge supercells. Therefore, we restrict the following analysis to bond-breaking energies (for further details see Experimental Section). In this context it is however, worthwhile mentioning that calculations on phenyl thiolates and selenolates at low coverage by Cometto et al.[15] suggest that energy differences and activation barriers are intimately related for systems like the present one.

Notably, in the simulations considering a translational periodicity of the substrate and the adsorbate, we need to consider adsorbate unit cells that are also commensurate with the periodicity of the unreconstructed Au(111) surface. Moreover, even with state-of-the-art resources, simulations like the present ones are limited to a few hundred atoms in the unit cell. These aspects prevented us from directly adopting the large $(2\sqrt{3} \times \sqrt{37})$ unit cell identified experimentally[14] for the NC-NapS/Au SAM or the $(2 \times 1.5\sqrt{3})$ adsorbate unit cell reported for the NC-Nap-Se/Au SAM, which is non-commensurate with the Au substrate. Consequently, we identify computationally affordable unit cells commensurate with the periodicity of the unreconstructed Au(111) surface, in which the SAMs display packing densities similar to the ones obtained in the respective experiments. Therefore, in our simulations we considered three different unit cells containing two molecules arranged in a herringbone pattern, as identified for the related anthraceneselenolates[10,45] on the Au(111) substrate (see Figure 7). The first is the commensurate rectangular $(3 \times \sqrt{3})$ unit cell, which has the same area per molecule (0.215 nm^2) as the incommensurate rectangular $(2 \times$
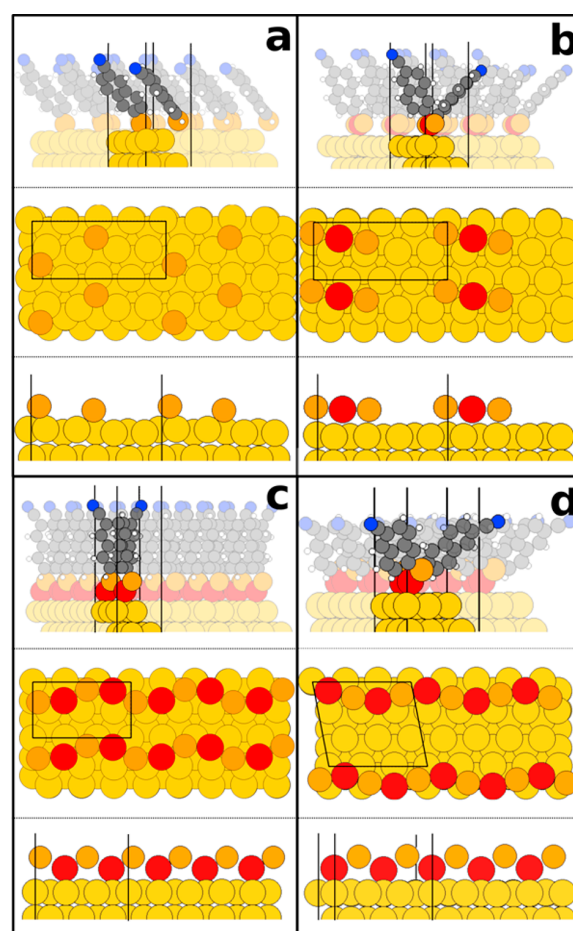
Figure 7. Top and side views of exemplary unit cells of the NC-NapS and NC-NapSe adsorbates on Au(111) after geometry optimization. All unit cells contain two molecules in herringbone arrangement, and in the bottom two panels of each plot, the molecular backbones are not displayed to more clearly show the relative positions of the gold adatoms and the docking groups. (a) Rectangular $(4 \times \sqrt{3})$ surface unit cell with unreconstructed Au surface; (b) rectangular $(4 \times \sqrt{3})$ surface unit cell containing one gold adatom; (c) rectangular $(3 \times \sqrt{3})$ surface unit cell containing two gold adatoms; (d) oblique $(3 \times \sqrt{7})$ unit cell containing two adatoms. Au atoms are yellow and adatoms red; docking atoms (S or Se) are orange, C atoms gray, H atoms white, and N atoms blue.

$1.5\sqrt{3})$ unit cell observed[14] in previous STM experiments on the NC-NapSe/Au interface as the closest approximation to the real structure (bearing in mind the finite experimental resolution). The molecules in that unit cell are tightly packed with the area per molecule slightly smaller than in some of the reported naphthalene crystal structures.[14] In spite of considerable efforts, this very tight packing prevented convergence of the self-consistent field cycles in the absence of reconstructions of the Au(111) surface. Therefore, we also considered a larger commensurate rectangular $(4 \times \sqrt{3})$ surface unit cell with an area per molecule of 0.287 nm^2. Notably, the $(4 \times \sqrt{3})$ surface unit cell is also the one found for anthraceneselenolate SAMs on Au(111).[10] Finally, we also tested an even larger commensurate oblique $(3 \times \sqrt{7})$ cell with an area per molecule of 0.323 nm^2. This served to evaluate the impact that an increased molecular tilt angle, occurring at lower coverages, has on binding energies. In passing, we note that the above

31

Table 1. Bond-Breaking Energies (E_{S-C}, E_{Se-C}, E_{Au-S}, E_{Au-Se}) and Respective Differences ($\Delta E_{S/Se-C}$, $\Delta E_{Au-S/Se}$) for All Studied Systems Together with the Average Tilt Angles of Each Conformation and the Order of the Bonding Energies

unit cell recon	rectangular (4 × √3)			rectangular (3 × √3)		oblique (3 × √7)
	none	1 ad	2 ad	1 ad	2 ad	2 ad
E_{S-C} (eV)	3.003	3.286	3.252	3.144	3.044	3.223
E_{Se-C} (eV)	2.696	2.888	2.883	2.772	2.725	2.880
$\Delta E_{S/Se-C}$ (eV)	−0.307	−0.398	−0.369	−0.372	−0.319	−0.343
E_{Au-S} (eV)	2.544	2.892	3.104	2.748	3.214	3.358
E_{Au-Se} (eV)	2.625	2.912	3.120	2.798	3.313	3.413
$\Delta E_{Au-S/Se}$ (eV)	0.081	0.020	0.016	0.050	0.099	0.055
av tilt (deg)	47	38	38	14	19	57
order	S−C > Se−C ≥ Au−Se ≥ Au−S	S−C > Au−Se ≥ Au−S ≥ Se−C	S−C > Au−Se ≥ Au−S ≥ Se−C	S−C > Au−Se ≥ Se−C ≥ Au−S	Au−Se > Au−S > S−C > Se−C	Au−Se > Au−S > S−C > Se−C

areas per unit cell are reported for the experimental Au(111) lattice constant of 0.286 nm while in the simulations the equilibrium lattice constant for the employed methodology has been used (0.294 nm) in order to avoid spurious relaxations of the surface atoms during the geometry optimizations.

In addition to varying the size of the unit cells, we also considered several adatom motifs discussed in the literature.[6,46] This is insofar relevant in the present context, as reconstructions of the Au(111) surface are expected to modify the bonding between the docking atom (S or Se) and the substrate, which in turn also changes the bonding between S(Se) and the adjacent C atom.[14,17,18] Moreover, the existence and nature of surface reconstructions have been intensively (and sometimes controversially) discussed for short-chained thiolates. Still, very little is known regarding comparably large conjugated backbones like the anthracenes considered here. Thus, the comparison between the calculated and measured trends discussed in the following will also provide valuable insight into the nature of surface reconstructions in such systems. In particular, we considered the following:

(i) A flat unreconstructed Au(111) surface (see Figure 7a; calculated only for the rectangular (4 × √3) surface unit cell due to the above-described convergence problems): There we find the molecules bonded to the substrate with the S/Se atoms in the fcc-hollow sites shifted toward the bridge.

(ii) A reconstructed surface with one adatom per unit cell located on a bridge site as suggested in ref 6 (see Figure 7b; calculated for the rectangular (3 × √3) and (4 × √3) unit cells): There the docking atoms coordinate with the adatom and with an atom of the regular surface, which shifts them to a position between fcc-hollow and on-top.

(iii) A reconstructed surface with two adatoms per unit cell[6,46] (see Figure 7c,d; calculated for the rectangular (3 × √3), the rectangular (4 × √3), and the oblique (3 × √7) surface unit cells): For the rectangular (3 × √3) and oblique (3 × √7) unit cells, each docking atom is coordinated with two adatoms, the S and Se atoms are lifted from the surface, and docking atoms and adatoms form an alternating chain on the surface. Conversely, for the optimized structure in the rectangular (4 × √3) unit cell the second adatom appears not to interact very strongly with the adjacent docking atom (see Supporting Information).

The relative stabilities of the adatom structures are discussed in detail in the Supporting Information where also structures of all calculated systems are shown.

The bond-breaking energies calculated for all considered systems are summarized in Table 1 with the energy differences between S and Se docking atoms plotted in bold. In all studied configurations, $\Delta E_{S/Se-C}$ is negative; i.e., the bonding energy between S and C is always higher than between Se and C, independent of the considered unit cell or adatom structure. Conversely, $\Delta E_{Au-S/Se}$ is always positive, indicating that the binding energy between Se and Au is consistently larger than between S and Au (albeit differences here are comparably small). These observed opposing trends for bonding between the docking atom and the substrate and the backbone support the notion that strengthening one of the bonds weakens the other.[14,17,18]

Interestingly, the relative strength of the bonds between the docking atom and either the metal substrate or the nearest C atom strongly depends on the number of adatoms per unit cell. For an unreconstructed surface, the bonds of both S and Se to C (i.e., to the molecular backbone) are stronger than those to Au. Adding adatoms, however, reinforces the bonds between the docking atoms and the substrate. For only one adatom per unit cell, this results in nearly identical bonding energies for the Se−C and Au−S bonds. With two adatoms per unit cell the bonding strength to the substrate increases further and for the rectangular (3 × √3) and oblique (3 × √7) unit cells, the Au−Se becomes the strongest of the considered bonds. Concomitantly, the Se−C bond becomes the weakest (notably, for all analyzed cells with two adatoms). The particularly large bonding energies to the substrate for two adatoms in the rectangular (3 × √3) and oblique (3 × √7) unit cells can be tentatively attributed to the formation an alternating chain of adatoms and docking atoms lifted from the surface (see structures in Figure 7). For such a situation one obtains a bonding energy order of $E_{Au-Se} > E_{Au-S} > E_{S-C} > E_{Se-C}$. This order prevails independent of the molecular tilt angle, which in our calculations varies from 19° (in the rectangular (3 × √3) structure) to 57° (in the oblique (3 × √7) structure).

The biggest impact of the vibrational contributions to bond-breaking energies is expected for the Au−S/Se bonds, as then the masses of the leaving fragments differ considerably; moreover, even when the SAM is still intact, a vibration involving the Au−S(Se) bond is expected to most strongly depend on the docking atom considering the significant differences in the oscillating masses. Thus, we only tested the impact of vibrational energies on breaking the bond between the two docking atoms (S or Se) and the (unreconstructed) Au surface. Here we found only a small increase in the bonding

asymmetry between S−Au and Se−Au from 0.085 eV (when disregarding vibrations) to 0.098 eV (when including the zero-point energy) and to 0.120 eV (when considering the thermal occupation of vibrational modes at room temperature). A more detailed discussion of vibrational contributions can be found in the Supporting Information.

As another possible scenario, we tested the desorption of molecules as dithiols, as this has been discussed in several publications on aliphatic thiolates.[43,47−50] A comprehensive study of all possible leaving fragments goes beyond the scope of the present article, but it should be mentioned that the binding energy of a dithiol (i.e., the energy difference of the dithiol minus 2 times the energy of the individual radicals) is 0.080 eV larger than that of the diselenols (2.239 eV for dithiols and 2.160 for diselenols). This would make it energetically less costly to break Au−S bonds compared to Au−Se bonds provided that dimer desorption is a favorable process also for the present systems.

A final "word of warning" concerns the impact of disorder: As mentioned earlier, desorption is not to be expected from perfectly packed films, but from rims of islands and disordered portions of the films; thus, calculating surfaces with perfect lateral periodicity can only approximate the real situation. Still, it is interesting to see that aspects like molecular tilt (potentially varying significantly in disordered areas) have only a comparably minor impact on bonding strengths. In contrast, the actual structure of the substrate (i.e., the presence of adatoms) and, thus, the local bonding partners of the docking atoms are crucial for the interface energetics.

IV. DISCUSSION

The key conclusion that can be drawn from the above experiments is that the Se-bonded SAMs are thermally less stable than their thiolate counterparts. This can, for example, be inferred from the faster decrease of the nominal film thickness with heating that is observed in the XPS experiments on Se-bonded films. It is also consistent with the larger film thickness at saturation range above 525 K (252 °C) observed for S-bonded SAMs (Figure 2): The saturation of the signals at high temperatures is consistent with previous observations on biphenylthiol-based SAMs[51,52] and can be attributed to the binding of the carbonaceous fragments to defects and steps on the gold substrate.[53] The saturation level is primarily determined by the amount of material still present on the surface. Therefore, the higher saturation levels for the S-bonded SAM is another aspect testifying to its increased thermal stability.

A more quantitative picture is obtained from the S-SIMS experiments (employing a much faster annealing procedure than for XPS). The temperature evolution of the M_2Au^+ signal not only confirms the higher thermal stability of the thiol-bonded monolayer but also allows extracting activation energies. For the NC-NapSe/Au desorption takes place in a single step with an estimated activation energy of $E_D = 1.20$ eV. In contrast, for the NC-NapS/Au desorption occurs in two steps. The first and major step (∼60% reduction in coverage) corresponds to an activation energy of $E_D = 1.35$ eV, which is noticeably higher than the activation energy for selenolate desorption. Like the single desorption step for the NC-NapSe/Au, it is attributed to desorption of molecules from the initial high density structures of both SAMs, i.e., presumably from the rims of islands of upright-standing molecules. The second step for the NC-NapS/Au at $E_D = 1.61$ eV corresponds to

desorption from a low density (∼40% of initial coverage) structure. It is tentatively associated with an adsorbate film consisting of strongly tilted molecules,[54] with the backbones interacting with the surface by van der Waals interactions (in addition to the headgroup−substrate bond).[55,56] This leads to an overall increase of the binding energy per molecule.

The observation of a more strongly bonded phase at low coverages in NC-NapS/Au is insofar important, as it strongly supports our statement in the Introduction that for understanding the fundamental reasons for the thermal stability of molecule−metal interface one has to compare desorption from equivalent (typically high density) phases with similar structures. As this is the case for NC-NapS/Au and NC-NapSe/Au, with microscopically and spectroscopically well-characterized structure,[14] this justifies an estimation of the difference in desorption energies between NC-NapS/Au and NC-NapSe/Au. It amounts to $\Delta E_D = 0.15$ eV. Notably, even for well-defined samples like the present ones, this value is associated with a non-negligible error bar, as choosing a frequency factor of 10^{16} s^{-1} Hz (as it has been done in refs 35 and 43), in contrast to the 10^{13} s^{-1} Hz used above (to be consistent with refs 9, 15, and 57), increases that difference to $\Delta E_D = 0.20$ eV.

The obtained value of $\Delta E_D = 0.15$ eV is very close to the desorption-energy difference of $\Delta E_D = 0.12$ eV, which has been derived from thermal desorption spectroscopy (TDS) data for phenylthiol (BS) and phenylselenol (BSe) SAMs on Au employing the Redhead formula with the same frequency factor of 10^{13} s^{-1} as used here.[9] Interestingly, in those systems, a two-step desorption has been observed for both docking groups, and consistent with what has been stated above, the quoted value corresponds to desorption from the high-density phase. In contrast, recent *ex situ* studies in nitrogen atmosphere of the BS/Au and BSe/Au surface coverage changes as a function of thermal annealing[15] yielded, for high density phases, a much smaller difference in desorption energies of only 0.03 eV.

What still needs to be clarified is the reason for the reduced thermal stability of the Se-docked SAMs in spite of the typically observed stronger bonding of that group to the metal surface (refs 14, 16−18, 20, 22, and 23; Table 1). This question can be addressed on the basis of the S 2p/Se 2p XPS spectra and the $AuSe(S)_2^-$ and $Au_2Se(S)^-$ S-SIMS data, where the S-SIMS experiments benefit from a much higher signal-to-noise ratio. Moreover, XPS and S-SIMS provide complementary information. The XPS signal intensities are determined by two competing trends: On the one hand, the S/Se signal drops due to the desorption of the S and Se atoms from the surface (potentially with attached molecular backbones). This process dominates, when the Se/S−Au bonds are broken. On the other hand, an increase of the S 2p/Se 2p XPS signals is possible, when the Se/S−C bond breaks and the docking atoms remain on the substrate, as then the attenuation of the photoelectron signal is reduced due to a decreased effective thickness of the hydrocarbon film. Following these arguments, the initial increase of the Se 3p signal for the NC-NapSe/Au sample in the temperature range between 350 and 450 K (Figure 4c) is a clear indication for an efficient scission of the bond between Se and the adjacent C atom of the molecular backbone. Conversely, the S 2p signal remains constant in the given temperature range. As the C 1s signal drops upon heating the sample (to about 50% at 450 K, Figure 3c), this indicates that also for the NC-NapS/Au system the S−C scission occurs

accompanied by a breaking of the S−Au bond. We note at this point that efficient breaking of the S−C bond during thermal annealing of thiols has been reported earlier for both aromatic and aliphatic SAMs formed on different metal substrates such as Au,[51,52,58] Cu,[59] and Ni.[60] The data obtained here for NC-NapS/Au and NC-NapSe/Au systems show that temperature-induced Se−C bond scission is more effective than the S−C bond breaking.

S-SIMS provides information on the desorbing ions without being affected by signal attenuation effects. Still, the AuSe⁻, AuSe$_2^-$, and Au$_2$Se⁻ signals increase significantly at temperature above 400 K, i.e., at a temperature corresponding to the onset of the desorption process for the NC-NapSe/Au (see Figure 5). This indicates a much higher efficiency of Se−C bond scission than for the Au−Se bond at an elevated temperature. In contrast, the AuS⁻, AuS$_2$, and Au$_2$S⁻ signals remain constant, supporting the assumption of a much more balanced efficiency for S−C and Au−S bond breaking.

The above conclusions are in agreement with the results of a recent study on the same SAMs as investigated here, probing the relative stability of S−C and Se−C bonds by ion-induced desorption.[14] There, as an explanation for the comparably weak bonding between the Se and the C atoms, it has been suggested that a higher involvement of the headgroup atom in the chemical bonding with the Au(111) substrate reduces its involvement in the chemical bonding to the molecular backbone.[14] Ion-desorption experiments for a homologues series of biphenyl substituted aliphatic SAMs (Au(Ag)−S(Se)−(CH$_2$)$_n$−C$_6$H$_4$−C$_6$H$_4$−CH$_3$, $n = 2$−6) have, in fact, suggested that this effect is rather general and leads to an oscillation in stability of consecutive chemical bonds in molecular adsorbates.[17,18]

Overall, the current thermal stability experiments in conjunction with former SIMS[14,17,18] and exchange[23] experiments imply the following sequence of bonds stabilities: Au−Se > Au−S > C−S > C−Se. Notably, especially the S-SIMS data provide further insight into the interface properties. They, for example, hint toward a possible existence of adatoms: The observed increase of the signal of the "inorganic" ions is much more pronounced for AuSe$_2^-$ and Au$_2$Se⁻ secondary ions compared to AuSe⁻, which indicates that AuSe$_2^-$ and Au$_2$Se⁻ signals more directly follow the changes in Se concentration on Au surface. Assuming that Au and Se atoms in these secondary ions reflect the original bonding geometry at the molecule−metal interface, this observation would be consistent with the adsorption model involving adatoms,[6,38−40] in which the headgroup atom forms chemical bonds with two Au adatoms (forming Au$_2$Se⁻) and the Au adatom binding with two headgroup atoms (forming AuSe$_2^-$).

Information on the fate of the docking atom can be gained from the S-SIMS data at higher temperatures: For the AuS⁻, AuS$_2^-$, and Au$_2$S⁻ signals a sharp drop is observed down to the zero level at 600 K (327 °C), where also the signal from the molecules traced by the M$_2$Au⁺ emission has vanished completely. This suggests a complete removal of the S atoms from the surface. The drop in the AuSe⁻, AuSe$_2^-$, and Au$_2$Se⁻ signals is more gradual, and even at the highest tested temperature (725 K) the associated signal does not reach the zero level. This hints toward a particularly strong bonding of the Se atoms to the Au substrate preventing their complete desorption, which is fully consistent with literature reports on the formation of Au−Se alloys at temperatures above 613 K.[61]

Comparing the experimentally determined data to the results of the calculations, several interesting observations can be made: (i) Consistent with the current thermal experiments and former bonding stability analysis,[14,17,18] the Se−C bond is weaker than the S−C bond for all considered unit cells and surface reconstructions. In line with the arguments from refs 14, 17, and 18 that strengthening the bond between the docking atom and one partner weakens the bond to the other partner, this results in the Se−Au bond being stronger than the S−Au one. (ii) Whether or not the links to C or to the Au atoms are the weakest elements of the SAM depends on the presence of adatoms. These strengthen the bonds to the (reconstructed) Au surface and, consequently, weaken the bonds to the C backbone. As a result, the Se−C bond represents the weakest link also in the simulations, but only when adatoms are considered (typically for two adatoms per unit cell, but in the case of a rectangular $(4 \times \sqrt{3})$ unit cell also for one). Finally, and most importantly, the sequence of bonds stability which has been deduced from the experiments, i.e., Au−Se > Au−S > C−S > C−Se, is observed exclusively for rectangular $(3 \times \sqrt{3})$ and oblique $(3 \times \sqrt{7})$ unit cells containing two adatoms. Note that the latter unit cell is contained here only for comparative reasons to show that the adatoms rather than details of the molecular arrangement determine the order in bond strength. Its comparably large molecular footprint (0.323 nm^2) is not compatible with experimental values for the NC-NapSe/Au (0.215 nm^2) and NC-NapS/Au (0.239 nm^2). This suggests the rectangular $(3 \times \sqrt{3})$ unit cell with two adatoms per unit cell as the most likely scenario (at least among the ones considered here), which is also supported by the observation that for that unit cell we calculate the highest SAM-formation energy per surface area (see Table S4 in the Supporting Information).

Finally, we note that the experimentally obtained difference in desorption energies for NC-NapS/Au and NC-NapSe/Au (0.15 eV) is smaller than the difference in the S−C and Se−C bond stability (0.32 eV) calculated for the rectangular $(3 \times \sqrt{3})$ unit cell with two adatoms. Besides the uncertainty of the experimental value linked to the choice of the frequency factor (see above), a possible explanation for that is that in the calculations we consider the breaking up of the continuous SAM into individual molecules and a substrate still containing the surface reconstructions, while the actual thermal desorption of molecules happens from the rim of molecular islands with modified molecule−molecule and molecule−substrate interactions. This is also almost certainly the reason for very large absolute values of the calculated bond-breaking energies. Moreover, as described in the Results section, also the nature of the actually leaving species does have some impact on the exact energetics of the process. Independent of these complications, the simulations clearly support the qualitative picture that arises from the thermal stability experiments.

V. SUMMARY AND CONCLUSIONS

Two independent sets of experiments based on the XPS and S-SIMS techniques were performed for probing the influence of the bonding group (S or Se) on the thermal stability of prototypical aromatic SAMs on the Au(111) substrate. Both types of experiments unequivocally demonstrated a higher thermal stability of thiolate-bonded SAMs with the quantitative analysis by SIMS showing ca. 0.15 eV higher desorption energy for that system.

This is insofar surprising, as most experiments suggest a lower stability of the S−Au compared to the Se−Au bond. The

apparent contradiction is resolved by showing that not Se−Au but Se−C is the actual weak link in the studied SAMs, i.e., that the lower thermal stability of the selenolate-bonded layers is a consequence of a preferential scission of the bond between the docking group and the backbone. The experimental studies are augmented by state-of-the-art DFT simulations which confirm the main trends seen experimentally. Interestingly, to fully reproduce the order of the bond strengths suggested by the experiments (Au−Se > Au−S > C−S > C−Se), it is necessary to include two adatoms per surface unit cell in the simulations. This hints toward the prevalence of such reconstructions not only in S-bonded but also in Se-bonded monolayers. The obtained order in the bond strengths supports the notion that a higher involvement of the bonding atom in the chemical linking to the substrate weakens its bond to the molecular backbone. From a design point of view, the present results show that for obtaining SAMs with higher thermal stability, one cannot simply follow the strategy of selecting a docking group with a particularly high bonding strength to the substrate but needs to finely balance the strength of the bonding between docking group and the substrate and between docking group and molecular backbone.

◼ ASSOCIATED CONTENT

ⓢ Supporting Information

The Supporting Information is available free of charge on the ACS Publications website at DOI: 10.1021/acs.jpcc.7b09685.

> Additional details regarding the S-SIMS analysis as well as the theoretical approach including a description of the chosen starting geometries, the optimization procedure, the simulations of vibrational properties, and the overview of calculated SAM-formation energies (PDF)

◼ AUTHOR INFORMATION

Corresponding Authors

*E-mail: piotr.cyganik@uj.edu.pl (P.C.).
*E-mail: egbert.zojer@tugraz.at (E.Z.).

ORCID ⊙

Andreas Terfort: 0000-0003-2369-5151
Michael Zharnikov: 0000-0002-3708-7571
Egbert Zojer: 0000-0002-6502-1721
Piotr Cyganik: 0000-0001-6131-4618

Notes

The authors declare no competing financial interest.

◼ ACKNOWLEDGMENTS

◼ REFERENCES

(1) Ulman, A. Formation and Structure of Self-Assembled Monolayers. *Chem. Rev.* **1996**, *96*, 1533−1554.

(2) Schreiber, F. Self-Assembled Monolayers: From 'Simple' Model Systems to Biofunctionalized Interfaces. *J. Phys.: Condens. Matter* **2004**, *16*, R881−R900.

(3) Love, J. C.; Estroff, L. A.; Kriebel, J. K.; Nuzzo, R. G.; Whitesides, G. M. Self-Assembled Monolayers of Thiolates on Metals as a Form of Nanotechnology. *Chem. Rev.* **2005**, *105*, 1103−1170.

(4) Casalini, S.; Bortolotti, C. A.; Leonardi, F.; Biscarini, F. Self-Assembled Monolayers in Organic Electronics. *Chem. Soc. Rev.* **2017**, *46*, 40−71.

(5) Xiang, D.; Wang, X.; Jia, C.; Lee, T.; Guo, X. Molecular-Scale Electronics: From Concept to Function. *Chem. Rev.* **2016**, *116*, 4318−4440.

(6) Häkkinen, H. The Gold−Sulfur Interface at the Nanoscale. *Nat. Chem.* **2012**, *4*, 443−455.

(7) Romashov, L. V.; Ananikov, V. P. Self-Assembled Selenium Monolayers: From Nanotechnology to Materials Science and Adaptive Catalysis. *Chem. - Eur. J.* **2013**, *19*, 17640−17660.

(8) Shaporenko, A.; Cyganik, P.; Buck, M.; Ulman, A.; Zharnikov, M. Self-Assembled Monolayers of Semifluorinated Alkaneselenolates on Noble Metal Substrates. *Langmuir* **2005**, *21*, 8204−8213.

(9) Käfer, D.; Bashir, A.; Witte, G. Interplay of Anchoring and Ordering in Aromatic Self-Assembled Monolayers. *J. Phys. Chem. C* **2007**, *111*, 10546−10551.

(10) Bashir, A.; Käfer, D.; Müller, J.; Wöll, C.; Terfort, A.; Witte, G. Selenium as a Key Element for Highly Ordered Aromatic Self-Assembled Monolayers. *Angew. Chem., Int. Ed.* **2008**, *47*, 5250−5253.

(11) Cyganik, P.; Szelagowska-Kunstman, K.; Terfort, A.; Zharnikov, M. Odd-Even Effect in Molecular Packing of Biphenyl-Substituted Alkaneselenol Self-Assembled Monolayers on Au(111): Scanning Tunneling Microscopy Study. *J. Phys. Chem. C* **2008**, *112*, 15466−15473.

(12) Dendzik, M.; Terfort, A.; Cyganik, P. Odd-even Effect in the Polymorphism of Self-Assembled Monolayers of Biphenyl-Substituted Alkaneselenolates on Au(111). *J. Phys. Chem. C* **2012**, *116*, 19535−19542.

(13) Cyganik, P.; Buck, M.; Wilton-Ely, J. D.; Wöll, C. Stress in Self-Assembled Monolayers: ω-biphenyl Alkane Thiols on Au(111). *J. Phys. Chem. B* **2005**, *109*, 10902−10908.

(14) Ossowski, J.; Wächter, T.; Silies, L.; Kind, M.; Noworolska, A.; Blobner, F.; Gnatek, D.; Rysz, J.; Bolte, M.; Feulner, P.; Terfort, A.; Cyganik, P.; Zharnikov, M. Thiolate versus Selenolate: Structure, Stability and Charge Transfer Properties. *ACS Nano* **2015**, *9*, 4508−4526.

(15) Cometto, F. P.; Patrito, E. M.; Paredes Olivera, P.; Zampieri, G.; Ascolani, H. Electrochemical, High-Resolution Photoemission Spectroscopy and vdW-DFT Study of the Thermal Stability of Benzenethiol and Benzeneselenol Monolayers on Au(111). *Langmuir* **2012**, *28*, 13624−13635.

(16) Sato, Y.; Mizutani, F. Formation and Characterization of Aromatic Selenol and Thiol Monolayers on Gold: In-Situ IR Studies and Electrochemical Measurements. *Phys. Chem. Chem. Phys.* **2004**, *6*, 1328−1331.

(17) Ossowski, J.; Rysz, J.; Krawiec, M.; Maciazek, D.; Postawa, Z.; Terfort, A.; Cyganik, P. Oscillations in the Stability of Consecutive Chemical Bonds Revealed by Ion-Induced Desorption. *Angew. Chem., Int. Ed.* **2015**, *54*, 1336−1340.

(18) Ossowski, J.; Rysz, J.; Terfort, A.; Cyganik, P. Relative Stability of Thiolate and Selenolate SAMs on Ag(111) Substrate Studied by Static SIMS. Oscillation in Stability of Consecutive Chemical Bonds. *J. Phys. Chem. C* **2017**, *121*, 459−470.

(19) Wyczawska, S.; Cyganik, P.; Terfort, A.; Lievens, P. Ion-Beam-Induced Desorption as a Method for Probing the Stability of the

Molecule-Substrate Interface in Self-Assembled Monolayers. *Chem-PhysChem* **2011**, *12*, 2554−2557.

(20) Huang, F. K.; Horton, R. C.; Myles, D. C.; Garrell, R. L. Selenolates as Alternatives to Thiolates for Self-Assembled Monolayers: A SERS Study. *Langmuir* **1998**, *14*, 4802−4808.

(21) Yokota, K.; Taniguchi, M.; Kawai, T. Control of the Electrode-Molecule Interface for Molecular Devices. *J. Am. Chem. Soc.* **2007**, *129*, 5818−5819.

(22) Weidner, T.; Shaporenko, A.; Müller, J.; Höltig, M.; Terfort, A.; Zharnikov, M. Self-Assembled Monolayers of Aromatic Tellurides on (111)-Oriented Gold and Silver. *J. Phys. Chem. C* **2007**, *111*, 11627−11635.

(23) Szelagowska-Kunstman, K.; Cyganik, P.; Schüpbach, B.; Terfort, A. Relative Stability of Thiol and Selenol Based SAMs on Au(111) - Exchange Experiments. *Phys. Chem. Chem. Phys.* **2010**, *12*, 4400−4406.

(24) Hohman, J. N.; Thomas, J. C.; Zhao, Y.; Auluck, H.; Kim, M.; Vijselaar, W.; Kommeren, S.; Terfort, A.; Weiss, P. S. Exchange Reactions between Alkanethiolates and Alkaneselenols on Au{111}. *J. Am. Chem. Soc.* **2014**, *136*, 8110−8121.

(25) Moulder, J. F.; Stickle, W. E.; Sobol, P. E.; Bomben, K. D. *Handbook of X-ray Photo-electron Spectroscopy*; Perkin-Elmer Corp.: Eden Prairie, MN, 1992.

(26) Kondoh, H.; Nakai, I.; Nambu, A.; Ohta, T.; Nakamura, T.; Kimura, R.; Matsumoto, M. Dissociative and Non-Dissociative Adsorption of Selenophene on Au(111) Depending on the Preparation Method. *Chem. Phys. Lett.* **2001**, *350*, 466−472.

(27) Blum, V.; Gehrke, R.; Hanke, F.; Havu, P.; Havu, V.; Ren, X.; Reuter, K.; Scheffler, M. Ab Initio Molecular Simulations with Numeric Atom-Centered Orbitals. *Comput. Phys. Commun.* **2009**, *180*, 2175−2196.

(28) Perdew, J. P.; Burke, K.; Ernzerhof, M. Generalized Gradient Approximation Made Simple. *Phys. Rev. Lett.* **1996**, *629*, 453−462.

(29) Tkatchenko, A.; Scheffler, M. Accurate Molecular van der Waals Interactions from Ground-State Electron Density and Free-Atom Reference Data. *Phys. Rev. Lett.* **2009**, *102*, 073005.

(30) Freysoldt, C.; Eggert, P.; Rinke, P.; Schindlmayr, A.; Scheffler, M. Screening in Two Dimensions: GW Calculations for Surfaces and Thin Films Using the Repeated-Slab Approach. *Phys. Rev. B: Condens. Matter Mater. Phys.* **2008**, *77*, 235428.

(31) Ruiz, V. G.; Liu, W.; Zojer, E.; Scheffler, M.; Tkatchenko, A. Density-Functional Theory with Screened van der Waals Interactions for the Modeling of Hybrid Inorganic-Organic Systems. *Phys. Rev. Lett.* **2012**, *108*, 146103.

(32) Neugebauer, J.; Scheffler, M. Adsorbate-Substrate and Adsorbate-Adsorbate Interactions of Na and K Adlayers on Al(111). *Phys. Rev. B: Condens. Matter Mater. Phys.* **1992**, *46*, 16067.

(33) Monkhorst, H. J.; Pack, J. D. Special points for Brillouin-Zone Integrations. *Phys. Rev. B* **1976**, *13*, 5188−5192.

(34) Lamont, C. L. A.; Wilkes, J. Attenuation Length of Electrons in Self-Assembled Monolayers of n-Alkanethiols on Gold. *Langmuir* **1999**, *15*, 2037−2042.

(35) Rading, D.; Kersting, R.; Benninghoven, A. Secondary Ion Emission from Molecular Overlayers: Thiols on Gold. *J. Vac. Sci. Technol., A* **2000**, *18*, 312−319.

(36) Cooper, E.; Leggett, G. Static Secondary Ion Mass Spectrometry Studies of Self-Assembled Monolayers: Influence of Adsorbate Chain Length and Terminal Functional Group on Rates of Photooxidation of Alkanethiols on Gold. *Langmuir* **1998**, *14*, 4795−4801.

(37) Tarlov, M. J.; Newman, J. G. Static Secondary Ion Mass Spectrometry of Self-Assembled Alkanethiol Monolayers on Gold. *Langmuir* **1992**, *8*, 1398−1405.

(38) Arezki, B.; Delcorte, A.; Chami, A. C.; Garrison, B. J.; Bertrand, P. Gold-Thiolate Cluster Emission from SAMs under keV Ion Bombardment: Experiments and Molecular Dynamics Simulations. *Nucl. Instrum. Methods Phys. Res., Sect. B* **2003**, *212*, 369−375.

(39) Arezki, B.; Delcorte, A.; Garrison, B. J.; Bertrand, P. Understanding Gold-Thiolate Cluster Emission from Self-assembled Monolayers upon Kiloelectronvolt Ion Bombardment. *J. Phys. Chem. B* **2006**, *110*, 6832−6840.

(40) Nie, H. Y. Revealing Different Bonding Modes of Self-Assembled Octadecylphosphonic Acid Monolayers on Oxides by Time-of-Flight Secondary Ion Mass Spectrometry: Silicon vs Aluminum. *Anal. Chem.* **2010**, *82*, 3371−3376.

(41) Zhou, C.; Jones, J. C.; Trionfi, A.; Hsu, J. W. P.; Walker, A. Electron Beam-Induced Damage of Alkanethiolate Self-Assembled Monolayers Adsorbed on GaAs (001): A Static SIMS Investigation. *J. Phys. Chem. C* **2010**, *114*, 5400−5409.

(42) Redhead, P. A. Thermal Desorption of Gases. *Vacuum* **1962**, *12*, 203−211.

(43) Stettner, J.; Winkler, A. Characterization of Alkanethiol Self-Assembled Monolayers on Gold by Thermal Desorption Spectroscopy. *Langmuir* **2010**, *26*, 9659−9665.

(44) Käfer, D.; Witte, G.; Cyganik, P.; Terfort, A.; Wöll, C. A Comprehesive Study of Self-Assembled Monolayers of Anthracene Thiol on Gold: Solvents Effects, Structure and Stability. *J. Am. Chem. Soc.* **2006**, *128*, 1723−1732.

(45) Track, A. M.; Rissner, F.; Romaner, L.; Käfer, D.; Bashir, A.; Rangger, G. M.; Hofmann, O. T.; Bučko, T.; Witte, G.; Zojer, E. Simultaneously Understanding the Geometric and Electronic Structure of Anthraceneselenolate on Au(111): A Combined Theoretical and Experimental Study. *J. Phys. Chem. C* **2010**, *114*, 2677−2684.

(46) Forster-Tonigold, K.; Groß, A. A Systematic DFT Study of Substrate Reconstruction Effects due to Thiolate and Selenolate Adsorption. *Surf. Sci.* **2015**, *640*, 18−24.

(47) Kondoh, H.; Kodama, C.; Sumida, H.; Nozoye, H. Molecular Processes of Adsorption and Desorption of Alkanethiol Monolayers on Au(111). *J. Chem. Phys.* **1999**, *111*, 1175−1184.

(48) Hayashi, T.; Wakamatsu, K.; Ito, E.; Hara, M. Effect of Steric Hindrance on Desorption Processes of Alkanethiols on Au(111). *J. Phys. Chem. C* **2009**, *113*, 18795−18799.

(49) Stettner, J.; Frank, P.; Griesser, T.; Trimmel, G.; Schennach, R.; Gilli, E.; Winkler, A. A Study on the Formation and Thermal Stability of 11-MUA SAMs on Au(111)/Mica and on Polycrystalline Gold Foils. *Langmuir* **2009**, *25*, 1427−1433.

(50) Voets, J.; Gerritsen, J. W.; Grimbergen, R. F. P.; van Kempen, H. Chain-Length-Dependent Structure of Alkanethiols Forming Dimers on Au(111). *Surf. Sci.* **1998**, *399*, 316−323.

(51) Turchanin, A.; El-Desawy, M.; Gölzhäuser, A. High Thermal Stability of Cross-Linked Aromatic Self-Assembled Monolayers: Nanopatterning via Selective Thermal Desorption. *Appl. Phys. Lett.* **2007**, *90*, 053102.

(52) Turchanin, A.; Käfer, D.; El-Desawy, M.; Wöll, C.; Witte, G.; Gölzhäuser, A. Molecular Mechanisms of Electron-Induced Cross-Linking in Aromatic SAMs. *Langmuir* **2009**, *25*, 7342−7352.

(53) Whelan, C. M.; Barnes, C. J.; Gregoire, C.; Pireaux, J. J. The influence of step sites on the bonding of benzenethiol on Au surfaces. *Surf. Sci.* **2000**, *454−456*, 67−72.

(54) Verwüster, E.; Hofmann, O. T.; Egger, D. A.; Zojer, E. Electronic Properties of Biphenylthiolates on Au(111): The Impact of Coverage Revisited. *J. Phys. Chem. C* **2015**, *119*, 7817−7825.

(55) Liu, W.; Tkatchenko, A.; Scheffler, M. Modeling Adsorption and Reactions of Organic Molecules at Metal Surfaces. *Acc. Chem. Res.* **2014**, *47*, 3369−3377.

(56) Ramalho, J. P. P.; Gomes, J. R. B.; Illas, F. Accounting for van Der Waals Interactions between Adsorbates and Surfaces in Density Functional Theory Based Calculations: Selected Examples. *RSC Adv.* **2013**, *3*, 13085−13100.

(57) Lavrich, D. J.; Wetterer, S. M.; Bernasek, S. L.; Scoles, G. Physisorption and Chemisorption of Alkanethiols and Alkyl Sulfides on Au(111). *J. Phys. Chem. B* **1998**, *102*, 3456−3465.

(58) Chandekar, A.; Sengupta, S. K.; Whitten, J. E. Thermal Stability of Thiol and Silane Monolayers: A Comparative Study. *Appl. Surf. Sci.* **2010**, *256*, 2742−2749.

(59) Gölzhäuser, A.; Panov, S.; Schertel, A.; Mast, M.; Wöll, C.; Grunze, M. Growth of Pyromellitic Dianhydride on an Amino-Terminated Surface. *Surf. Sci.* **1995**, *334*, 235−247.

36

(60) Rufael, T. S.; Huntley, D. R.; Mullins, D. R.; Gland, J. L. Methyl Thiolate on Ni(ll1): Multiple Adsorption Sites and Mechanistic Implications. *J. Phys. Chem.* **1995**, *99*, 11472−11480.

(61) Cranton, G.; Heyding, R. The Gold/Selenium System and Some Gold Seleno-Tellurides. *Can. J. Chem.* **1968**, *46*, 2637−2640.

4.1.2 Supporting information

Details of the starting geometries and of the optimisation procedure

In all the considered unit cells, rectangular $(4 \times \sqrt{3})$, with 8 Au atoms per layer, rectangular $(3 \times \sqrt{3})$, with 6 Au atoms per layer, and oblique $(3 \times \sqrt{7})$, with 9 Au atoms per layer), two molecules were arranged in herringbone fashion. In the unreconstructed rectangular $(4 \times \sqrt{3})$ unit cell the docking groups were placed in *fcc*-hollow sites and the CN-Naphthalene backbones were positioned to the left with respect to the Au–S(e) bond, according to the most favourable arrangement found in reference 108. The dimensions in the x and y directions were defined according to the calculated Au lattice constant, which amounts to 2.940 Å. The optimised structure is shown in figure 4.1.

Figure 4.1: Top (left) and side (right) view of the optimised geometry of the unreconstructed rectangular $(4 \times \sqrt{3})$ unit cell. Au atoms are depicted in dark yellow, S in light yellow, N in blue, C in grey and H in white. The dashed black line represents the unit cell. NC-NapS Au(111) is shown. For NC-NapSe/Au(111) the docking configuration and the molecular orientation are similar.

The initial geometries for the reconstructed rectangular $(4 \times \sqrt{3})$ unit cell were set up starting from the optimised unreconstructed one. For the one adatom per unit cell case, the Au adatom was placed in bridge position between the two docking groups, resulting in a reconstruction motif in which the adatom is coordinated to both docking groups[109,110]. The latter are coordinated to the adatom and to one atom of the regular Au surface. The structure was then optimised and in the final geometry such reconstruction motif was maintained (see figure 4.2), with the adatom in bridge position and the two docking groups occupying two bridge positions, in one case slightly shifted towards *hcp*-hollow and in the other case slightly shifted towards ontop.

Figure 4.2: Top (left) and side (right) view of the optimised geometry of the rectangular $(4 \times \sqrt{3})$ unit cell with one adatom per unit cell. Au adatoms are depicted in red, Au atoms in dark yellow, S in light yellow, N in blue, C in grey and H in white. The dashed black line represents the unit cell. NC-NapS/Au(111) is shown. For NC-NapSe/Au(111) the docking configuration and the molecular orientation are similar.

For the reconstructed surface with two adatoms per unit cell another Au adatom was placed in bridge position, resulting in it being coordinated to only one of the docking groups (see figure 4.3).
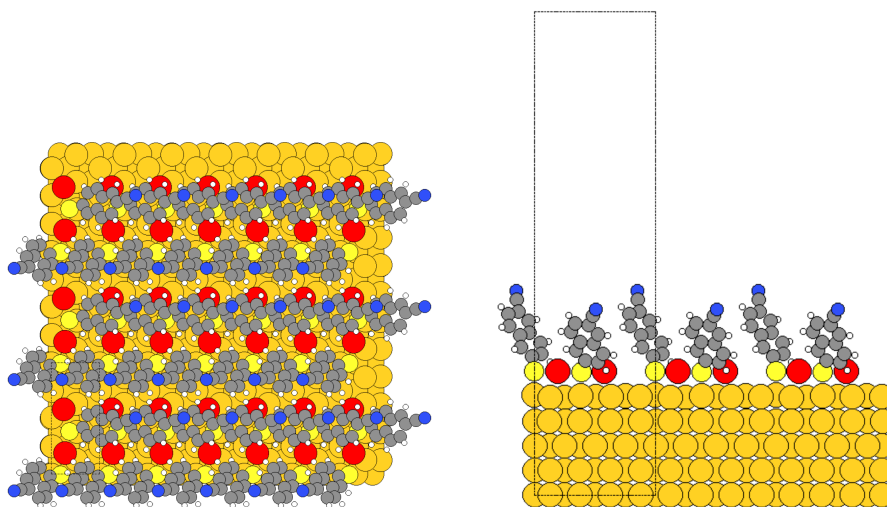
Figure 4.3: Top (left) and side (right) view of the starting geometry of the rectangular $(4 \times \sqrt{3})$ unit cell with two adatoms per unit cell. Au adatoms are depicted in red, Au atoms in dark yellow S in light yellow, N in blue, C in grey and H in white. The dashed black line represents the unit cell. NC-NapS/Au(111) is shown. For NC-NapSe/Au(111) the docking configuration and the molecular orientation are similar.

During the optimisation, the second adatom shifted towards the closest hollow position, while the other adatom and the docking groups adopted essentially the same configuration they display for the one adatom/unit cell case (see figure 4.4).
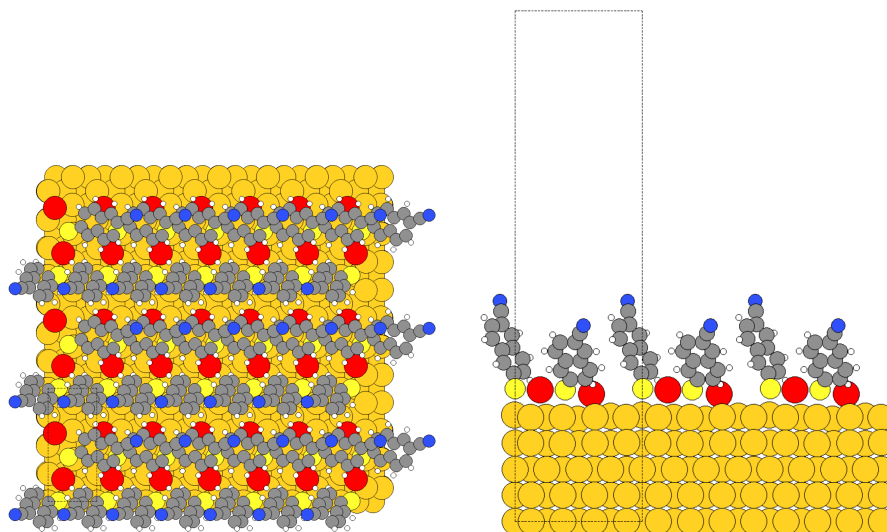
Figure 4.4: Top (left) and side (right) view of the optimised geometry of the rectangular $(4 \times \sqrt{3})$ unit cell with two adatoms/unit cell. Au adatoms are depicted in red, Au atoms in dark yellow S in light yellow, N in blue, C in grey and H in white. The dashed black line represents the unit cell. NC-NapS/Au(111) is shown. For NC-NapSe/Au(111) the docking configuration and the molecular orientation are similar.

The rectangular $(3 \times \sqrt{3})$ unit cell turned out to be too small for the two molecules to fit without accounting for surface reconstructions. The one adatom/unit cell starting geometry was set up by placing the molecules and the docking group in the same configuration they adopted in the rectangular $((4 \times \sqrt{3})$ unit cell with one adatom per unit cell. The structure was then optimised and in the resulting geometry the adatom was coordinated to both docking groups; the docking groups were coordinated to the adatom and to an atom of the regular Au(111) surface, similar to what obtained for the rectangular $(4 \times \sqrt{3})$ unit cell (see figure 4.5).
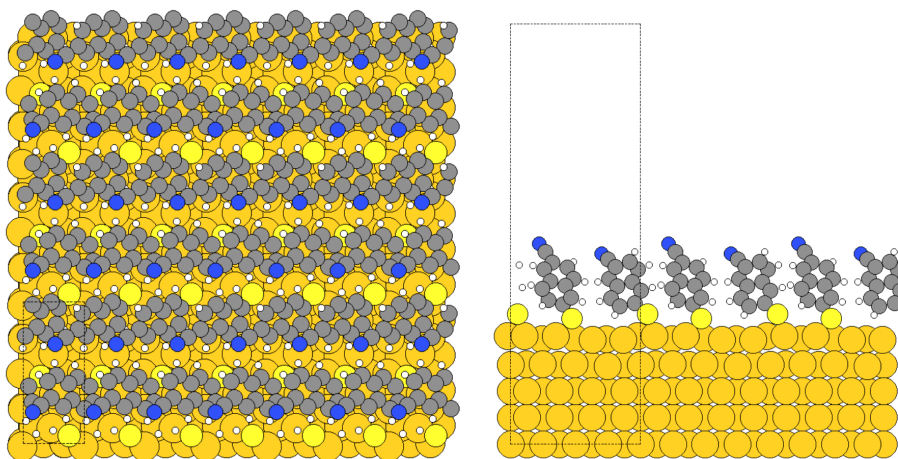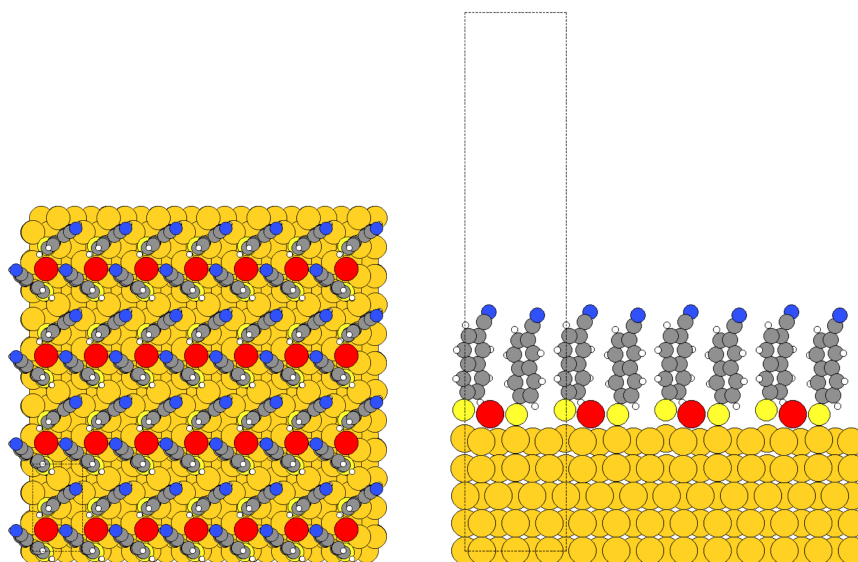

Figure 4.5: Top (left) and side (right) view of the optimised geometry of the rectangular $(3 \times \sqrt{3})$ unit cell with one adatom per unit cell. Au adatoms are depicted in red, Au atoms in dark yellow S in light yellow, N in blue, C in grey and H in white. The dashed black line represents the unit cell. NCNapS/ Au(111) is shown. For NC-NapSe/Au(111) the docking configuration and the molecular orientation are similar.

From the optimised geometry, the unit cell with 2 adatoms was built by placing another Au adatom in bridge position. The reconstruction motif, in which every adatom is coordinated to two docking group and all the docking groups are coordinated to two adatoms, was maintained also in the optimised geometry (see figure 4.6).
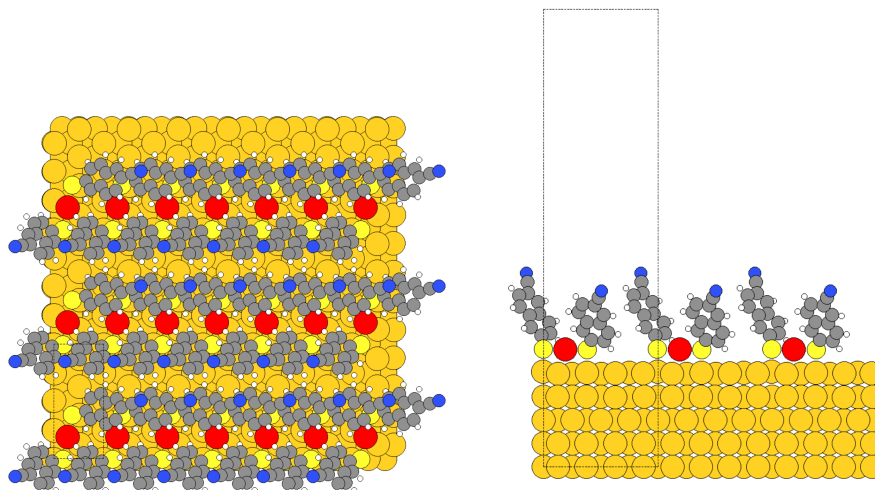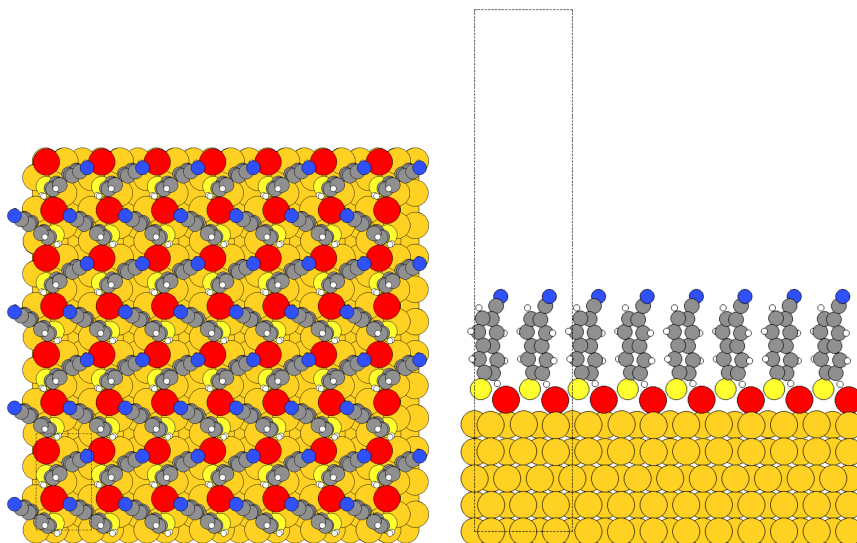

Figure 4.6: Top (left) and side (right) view of the optimised geometry of the rectangular $(3 \times \sqrt{3})$ unit cell with two adatoms/unit cell. Au adatoms are depicted in red, Au atoms in dark yellow S in light yellow, N in blue, C in grey and H in white. The dashed black line represents the unit cell. NC-NapS/Au(111) is shown. For NC-NapSe/Au(111) the docking configuration and the molecular orientation are similar.

The latter result was used to build the oblique $(3 \times \sqrt{7})$ unit cell with two adatoms/unit cell, by increasing the dimensions of the unit cell. During the optimisation the tilt angle of the molecules increased relevantly, while the reconstruction motif was essentially maintained (see figure 4.7).
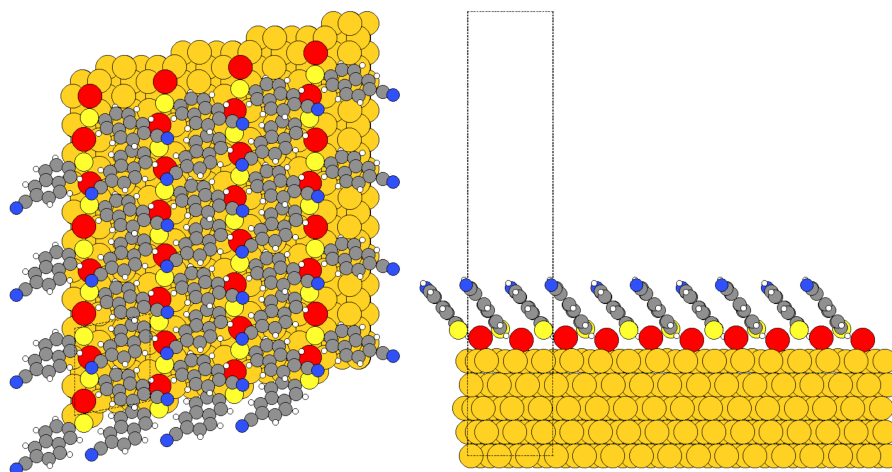
Figure 4.7: Top (left) and side (right) view of the optimised geometry of the oblique $(3 \times \sqrt{7})$ unit cell with two adatoms per unit cell. Au adatoms are depicted in red, Au atoms in dark yellow S in light yellow, N in blue, C in grey and H in white. The dashed black line represents the unit cell. NC-NapS/Au(111) is shown. For NC-NapSe/Au(111) the docking configuration and the molecular orientation are similar.

Details of the computational methods

The following self consistency cycle criteria were set: sc_accuracy_rho 1×10^{-5}, sc_accuracy_etot 1×10^{-6}, sc_accuracy_forces 1×10^{-4} and sc_accuracy_eev 1×10^{-3}. The occupation of the Kohn-Sham eigenstates was defined setting a width of 0.1 eV and 0.01 eV for the Gaussian broadening function for the periodic systems and for the isolated molecules, respectively. On the sub-fragments spin polarised calculations were performed, to account for the bond breaking process.

As already mentioned in the main paper, the Au atoms were described using the default FHI-aims tight basis set, while for all the other species such default tight settings were modified by adding a further basis function (namely third tier hydro 4 f for H atoms, third tier hydro 2 p for C atoms, second tier hydro 4 p for for S atoms, second tier hydro 5 g for Se atoms and third tier hydro 3 s for N atoms), by setting the onset radius of the cutoff potential to 4.1 Å, by setting the value of the radial_multiplier tag to 3 and by setting the outer_grid tag to 590 and uncommenting the relative division line. The choice of these particular settings and of the k-point grids reported in the main text were made according to thorough convergence tests, such that the differences between the bonding energies calculated with the aforementioned settings and with more accurate ones were below 10 meV.

To calculate the Au lattice constant, single point calculations were performed for Au bulk in an *fcc* unit cell (containing 4 Au atoms) as a function of the lattice constants using the numerical settings described above (i.e., the ones used also in all other simulations). The total energy was plotted as a function of the lattice constant (in steps of 0.0025 Å) and the curve was fitted with a quadratic function. The value of the lattice constant corresponding to the minimum of the curve was taken as the optimised one. $12 \times 12 \times 12$ and a $24 \times 24 \times 24$ k-points grids were tested with the obtained values agreeing to within three digits after the comma. The obtained value for the lattice constant was 4.158 Å, corresponding to a nearest neighbour distance of 2.940 Å.

Details of the frequency calculations

The vibrational contribution was calculated within the finite differences approach and were considered for breaking the bond between the metal surface and the docking group for the unreconstructed rectangular $(4 \times \sqrt{3})$ unit cell only: considering the different mass of S and Se, the Au–S(e) bond should be the one most affected by the vibrational contribution. Considering that calculating vibrations using the finite differences approach is computationally particularly expensive, the slab type calculations were performed modelling the metal with only 3 layers of Au instead of 5 and by modifying the default FHI-aims tight basis set for the Au atoms commenting the "h" basis function of the first tier. These settings were chosen after performing tests to guarantee that the energy difference between the Au–S and the Au–Se bond for the chosen geometry also with the revised settings were converged converged below 10 meV.

Table 4.1: Au–S(e) bond-breaking energies. E_{elec}: electronic energy. ZPE: vibrational contribution at 0 K (zero point energy). $E_{298.15K}$: vibrational contribution at 298.15 K. The E_{elec} values differ from the ones given in the main paper since for calculating vibrations reduced computational settings were employed (see above).

	E_{elec} / eV	E_{elec} + ZPE / eV	E_{elec} + $E_{298.15}$ / eV
Au–S	2.490	2.430	2.496
Au–Se	2.575	2.528	2.616

For the isolated gas phase radicals the frequencies were calculated in FHI-aims. The displacement was set to 0.015 Å and the zero point energy (ZPE) and the vibrational energy at 298.15 K were taken directly from the output file basic.vib.out. The displacement was chosen after testing several values in a range between 0.0001 and 0.025 Å: the differences in terms of vibrational energy were widely below 5 meV. Moreover, the vibrational energy was also calculated in Gaussian 09, RevD.01[104] (PBEPBE/6-311++g(d,p)). The difference between the vibrational energies calculated with the two codes was again below 5 meV.

For the periodic systems (the thiol(selenol) SAM/Au(111) and the clean Au(111) surface) the phonon frequencies were calculated combining FHI-aims and the GPL utility phonopy[111] (version 20111113). The displacement was set to 0.015 Å and the calculation was performed in the unit cell specified in the geometry.in input file (i.e.: the tag phonon supercell was set to 1 1 1). The zero point energy and the vibrational energy at 298.15 K were directly taken from the phonopy generated phonopy-FHI-aimsfree_energy.dat file. For the calculation of the phonon free energy, the k-point density was set to 60, as the obtained energy values were converged to within 10 meV with respect to the ones obtained using denser grids.

Before calculating the phonon frequencies, the geometry was optimised keeping the 2 bottom Au layers fixed to their bulk optimised positions. As already mentioned in the main text, this is usually done to avoid spurious bulk relaxations. However, in principle frequency calculations should be performed on optimised structures. For this reason, the fully optimised geometry (without fixing any Au layer) was tested, too. The difference in terms of bond energy differences turned out not to be particularly relevant, as shown in table 4.2.

Table 4.2: Au–S(e) bond-breaking energies accounting for the vibrational contribution at 0 and 298.15 K obtained keeping the two bottom Au layers fixed (2 fixed) or fully optimising the Au atomic positions (all opt). E_{elec}: electronic energy. ZPE: vibrational contribution at 0 K (zero point energy). $E_{298.15K}$: vibrational contribution at 298.15 K.

	E_{elec} + ZPE / eV, 2 fixed	E_{elec} + ZPE / eV, all opt	E_{elec} + $E_2$98.15 / eV, 2 fixed	E_{elec} + $E_{298.15K}$ / eV, all opt
Au–S	2.430	2.339	2.496	2.561
Au–Se	2.528	2.416	2.616	2.669

Accounting for the reconstruction energy

The energy needed for for the reconstruction of the metal surface was evaluated within the approach described by Otálvaro et al.[112], that assumes that the adatoms are supplied from the Au bulk. With the same notation used in the main text, the formation energy becomes:

$$E_{X-Y} = E_{mol-fragment} + (E_{clean} + n_a \times E_{bulk} - E_{SAM-bonded})/2, \quad (4.1)$$

where $E_{mol-fragment}$ is the energy of the isolated molecular fragment, E_{clean} is the energy of the unreconstructed surface, na is the number of adatoms in the unit cell, E_{bulk} is the total energy per bulk atom and $E_{SAM-bonded}$ is the energy of the SAM adsorbed on the Au surface.

In table 4.3 the formation energy values including the reconstruction energy are compared. Table 4.4 contains the same energies per surface area. Such a comparison could in principle give information also about the relative stability of the different reconstruction motifs, i.e. larger bond energies correspond to more stable structures. For systems in contact with a solution (or a gas phase) the primarily relevant quantity is the formation energy per area. This quantity is largest for the $(3 \times \sqrt{3})$ unit cells containing two adatoms. For a

fully quantitative analysis of the situation providing information also on temperature, concentration, and pressure ranges at which certain phases form it would, however be necessary to include the chemical potential of the SAM-forming molecules in solution, the interaction of the solvent with the surface and the vibrational energy contributions of all constituents. Obtaining all that information would be extremely challenging if at all possible with contemporary computational tools and certainly goes beyond the scope of the present manuscript.

Table 4.3: Au–S(e) SAM formation energies of all the considered unit cells including the energy needed for the surface reconstruction according to the model described by Otálvaro *et al*[112].

Unit cell	Bond	Bond energy / eV
rectangular $(4 \times \sqrt{3})$ unit cell	Au–S	2.544
	Au–Se	2.625
rectangular $(4 \times \sqrt{3})$ unit cell, 1 adatom/unit cell	Au–S	2.543
	Au–Se	2.563
rectangular $(4 \times \sqrt{3})$ unit cell, 2 adatoms/unit cell	Au–S	2.309
	Au–Se	2.336
rectangular $(3 \times \sqrt{3})$ unit cell, 1 adatom/unit cell	Au–S	2.424
	Au–Se	2.473
rectangular $(3 \times \sqrt{3})$ unit cell, 2 adatoms/unit cell	Au–S	2.511
	Au–Se	2.609
rectangular $(4 \times \sqrt{3})$ unit cell, 2 adatoms/unit cell	Au–S	2.696
	Au–Se	2.751

Table 4.4: Au–S(e) SAM-formation energies per area area of all the considered unit cells including the energy needed for the surface reconstruction according to the model described by Otálvaro *et al*[112].

Unit cell	Bond	Bond energy / eV
rectangular $(4 \times \sqrt{3})$ unit cell	Au–S	8.498
	Au–Se	8.767
rectangular $(4 \times \sqrt{3})$ unit cell, 1 adatom/unit cell	Au–S	8.492
	Au–Se	8.557
rectangular $(4 \times \sqrt{3})$ unit cell, 2 adatoms/unit cell	Au–S	7.712
	Au–Se	7.801
rectangular $(3 \times \sqrt{3})$ unit cell, 1 adatom/unit cell	Au–S	10.790
	Au–Se	11.011
rectangular $(3 \times \sqrt{3})$ unit cell, 2 adatoms/unit cell	Au–S	11.179
	Au–Se	11.618
rectangular $(3 \times \sqrt{7})$ unit cell, 2 adatoms/unit cell	Au–S	7.861
	Au–Se	8.021

4.2 Understanding the properties of tailor-made self-assembled monolayers with embedded dipole moments for interface engineering

As already mentioned, SAMs are often used to modify metal electrodes in organic electronic devices. One of the main purposes is the modification of the work function of the substrate. As explained in chapter 2, dipolar units play a fundamental role for the work function modification, The most intuitive way to introduce dipolar units in a SAM is its functionalisation by means of a polar tail group, such as the CN group of the S and Se based SAMs investigated in section 4.1. This strategy presents however some disadvantages. The tail group could for instance affect the growth of the active material subsequently deposited on the SAM covered metal. Moreover, chemical reactions could occur between the tail group and the active material.

To overcome this issue the alternative embedded dipole approach has been proposed[36,37]. The dipolar units are inserted within the backbone of the SAM, without therefore changing the chemistry of the upper part of the molecules. The systems presented in this section are a successful example of the application of such approach. Two derivatives of biphenylthiol (BPT) on the Au(111) obtained by substituting one of the phenyl rings with a dipolar pyrimidine unit embedded in two opposite direction are investigated. It has recently been shown that SAMs of that molecules can significantly reduce the contact resistance in p- and n-type organic thin film transistors containing pentacene and C60 as active layers[1]. In this section the synthesis of the molecules and the compete characterisation of the SAMs is presented. The latter is performed combining ellipsometry, infrared reflection absorption spectroscopy (IRRAS), scanning tunnelling microscopy (STM), near edge X-ray absorption fine structure (NEXAFS) contact angle goniometry and X-ray photoelectron spectroscopy (XPS) experiments and state-of-the-art density functional theory (DFT) calculations.

The results have been published in the *Journal of Physical Chemistry C*, see reference 113. The original paper is here reprinted with permission from Gärtner, M.; Sauter, E.; Nascimbeni, G.; Petritz, A.; Wiesner, A.; Kind, M.; Abu-Husein, T.; Bolte, M.; Stadlober, B.; Zojer, E.; Terfort, A.; Zharnikov, M. Understanding the Properties of Tailor-Made Self-Assembled Monolayers with Embedded Dipole Moments for Interface Engineering. *J. Phys. Chem. C* **2018**, *122*, 28757-28774. Copyright 2018 American Chemical Society. A reduced version of the supporting information is included. The full supporting information is available at DOI: 10.1021/acs.jpcc.8b09440. It contains additional experimental data regarding the synthesis of the molecules, with details of the characterisation techniques and NMR spectra, single crystal diffraction data ad optimised geometries in the xyz format. The work was a collaboration between the groups of Andreas Terfort, Michael Zharnikov and Egbert Zojer. Michael Gärtner and Andreas Terfort synthesised the molecules, performed the X-ray diffraction and IR and IRRAS analysis and registered STM images. Eric Sauter and Michael Zharnikov prepared the SAMs, did the ellipsometry and the contact angle goniometry measurements and performed Kelvin probe (KP), XPS and NEXAFS experiments. Egbert Zojer and I contributed the simulation part. Andreas Terfort, Michael Zharnikov and Egbert Zojer coordinated the work. The data were discussed and interpreted jointly by all the authors. A first draft of the paper was written by Michael Zharnikov. All the other authors contributed in writing the sections concerning their results and revising the draft. I performed all the calculations presented in the work, prepared figures 9 and 10 and wrote a draft of the computational part, that was then revised and corrected by Egbert Zojer and incorporated in the manuscript by Egbert Zojer and me. I wrote the computational section of the supporting information and prepared all the figures presented there. The text was revised and corrected

by Egbert Zojer.

4.2.1 Original paper

Understanding the Properties of Tailor-Made Self-Assembled Monolayers with Embedded Dipole Moments for Interface Engineering

Michael Gärtner,[†,⊥] Eric Sauter,[‡,⊥] Giulia Nascimbeni,[§,⊥] Andreas Petritz,[∥] Adrian Wiesner,[†] Martin Kind,[†] Tarek Abu-Husein,[†] Michael Bolte,[†] Barbara Stadlober,[∥] Egbert Zojer,[*,§] Andreas Terfort,[*,†] and Michael Zharnikov[*,‡]

[†]Institut für Anorganische und Analytische Chemie, Johann Wolfgang Goethe Universität Frankfurt, Max-von-Laue-Straße 7, D-60438 Frankfurt am Main, Germany

[‡]Angewandte Physikalische Chemie, Universität Heidelberg, Im Neuenheimer Feld 253, D-69120 Heidelberg, Germany

[§]Institute of Solid State Physics, NAWI Graz, Graz University of Technology, Petersgasse 16, 8010 Graz, Austria

[∥]MATERIALS-Institute for Surface Technologies and Photonics, Joanneum Research Forschungsgesellschaft, Franz-Pichler-Straße 30, 8160 Weiz, Austria

Ⓢ *Supporting Information*

ABSTRACT: Self-assembled monolayers (SAMs) are frequently used for interfacial dipole engineering in organic electronics and photovoltaics. This is mostly done by the attachment of dipolar tail groups onto the molecular backbone of the SAM precursors. The alternative concept of embedded dipoles involves the incorporation of polar group(s) into the backbone. This allows one to decouple the tuning of the electrostatic properties of the SAM from the chemical identity of the SAM−ambient interface. Here we present design and synthesis of particularly promising SAM precursors utilizing this concept. These precursors feature the thiol-docking group and a short heteroaromatic backbone, consisting of a nonpolar phenyl ring and a polar pyrimidine group, embedded in two opposite orientations. Packing density, molecular orientation, structure, and wetting properties of the SAMs on Au substrates are found to be nearly independent of their chemical structure, as shown by a variety of complementary experimental techniques. A further important property of the studied SAMs is their good electrical conductivity, enabling their application as electrode modifiers for low-contact resistances in organic electronic devices. Of particular interest are also the electronic properties of the SAMs, which were monitored by Kelvin probe and high-resolution X-ray photoelectron spectroscopy measurements. To obtain a fundamental understanding of these properties at an atomistic level, the experiments were combined with state-of-the-art band structure calculations. These not only confirm the structural properties of the films but also explain how the C 1s core-level binding energies of the various atoms are controlled by their chemical environments in conjunction with the local distribution of the electrostatic potential within the monolayer.
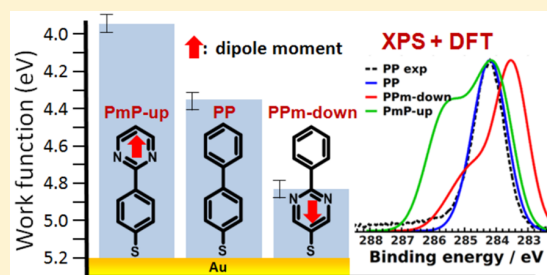
1. INTRODUCTION

Interfacial engineering in organic electronics is an important subject of current research.[1−3] The most essential aspects within this topic are (a) the optimization of the charge carrier injection barrier by minimizing the energetic gap between the electrode Fermi level and the transport levels of the organic semiconductor (OSC) and (b) the surface-mediated growth of the active layer at the electrodes and in the channel. Both aspects can be addressed by modifying the electrodes or gate dielectrics with self-assembled monolayers (SAMs),[4−7] which are two-dimensional (2D) polycrystalline films of semirigid molecules that are chemically bound to a substrate by suitable docking groups.[8,9]

A particularly important advantage of using SAMs is that they allow the optimization of charge carrier injection barriers at the electrode/OSC interface via the adjustment of the electrode work function (WF). Typically, the WF of an electrode increases when perfluorinated molecules are chemisorbed, whereas it decreases for the corresponding nonfluorinated, H-terminated derivatives.[10,11] An additional tuning of the WF can then be achieved by attachment of polar tail groups like −CN, −F, −CF₃, −NH₂, or −NO₂ to the SAM backbone, which is probably the most frequently used

approach in this regard.[11−15] This strategy, however, has significant drawbacks, such as (i) a strong influence of the nature of the polar tail groups on OSC growth and (ii) the risk of a possible modification of the (chemical) structure of the tail-group substituents as a consequence of the interaction with the eventually deposited OSC. These problems can be avoided by embedding the polar groups into the backbone of the SAM constituents. This permits an independent adjustment of the dipole moment and the interfacial chemistry at the SAM/OSC interface and prevents direct contact between the dipolar groups and the OSC. First examples of such SAMs comprised aliphatic backbones with embedded polar ester groups at varying orientations.[16,17] The embedded dipole concept has recently also been used to explain the electronic properties of partially fluorinated aliphatic SAMs.[18] As an alternative, pyrimidine groups have been embedded into an aromatic backbone.[19] Both for aliphatic and aromatic SAMs, the inclusion of the embedded dipoles results in only minor changes of the resulting monolayer structure as compared to the parent, nonsubstituted films.[16,17,19] The SAMs not only allow increasing or decreasing the substrate work function (for dipole-down and dipole-up orientations, respectively) but enable also a continuous tuning of the WF between the ultimate values of the single-component SAMs by combining up- and down-constituents in mixed monolayers,[7,20−22] in analogy to what has been observed also for mixtures of fluorinated and nonfluorinated alkanethiolate SAMs.[23,24]

The initial design of the prototypical SAMs with embedded dipoles, however, disregarded an important aspect, namely, the electrical resistance caused by the organic monolayer, which reduces the efficiency of charge carrier injection at electrode−SAM−OSC interfaces. This is, on the one hand, a consequence of the transport properties of aliphatic SAMs, which are inferior to their aromatic counterparts.[25−27] On the other hand, the prototypical (first generation) aromatic SAMs with embedded dipoles tested in recent years relied on comparably long backbones consisting of three rings and a methylene linker connecting the backbone to the thiolate docking group (see Figure S1 in the Supporting Information).[19] The latter has been introduced primarily to improve molecular packing and lateral order in the SAMs.[28−30] Significantly, both long backbones and methylene linkers are detrimental to charge transport through the SAMs, as the conductance of molecular monolayers typically decreases exponentially with film thickness,[25−27,31] while the introduction of the methylene linker electronically decouples the metal substrate from the conjugated segment.[32−34]

Bearing the above considerations in mind, we designed a set of molecules (second generation) that exploits the concept of embedded dipoles in a fashion much more suitable for applications in organic electronic devices (Figure 1). As polar element (yellow in Figure 1), a pyrimidine ring (Pm) with a dipole moment of 2.3 D[35] was used. It was built into a biaryl system in two different orientations. To make sure that in all cases the same tail group (green in Figure 1) is exposed at the SAM/OSC interface, a phenyl ring (P) was employed as second aryl element. As anchoring group, the thiol group (orange in Figure 1) is directly attached to the aromatic system in a way that no other heteroatoms are close to it, as it has been shown that the presence of heteroatoms, such as N or O, often hampers the formation of high quality SAMs.[36−38] As reference, 4-biphenyl thiol (PP), with a nonpolar backbone, was used. In some sense, PP can be considered as "parent"
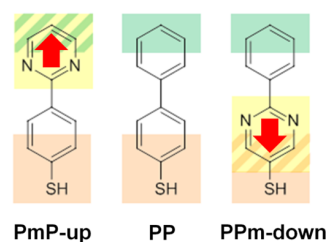
Figure 1. SAM-forming molecules used in this project along with their acronyms (P = phenyl, Pm = pyrimidine, up/down = direction of dipole moment (red arrows) with respect to the anchoring group). The structure of this series was optimized for the application of the corresponding SAMs in organic electronics and photovoltaics. Chemically similar parts of the molecular building blocks are marked by different colors (see text for details) with mixed colors reflecting the possible influence of the adjacent nitrogen atoms at the respective interface upon monomolecular assembly. Note that common acronyms for PP are also BPT (biphenylthiol) or BP0 and that, consequently, BP0-up and BP0-down has been used by us before for PmP-up and PPm-down.[39] We, however, feel that the acronyms used in this work better reflect the molecular identity of the system and are also more easily adapted to more complex molecular structures (containing, e.g., multiple pyrimidine units).

molecule for PmP-up and PPm-down, where one of the phenyl rings is substituted by pyrimidine.

We have shown recently that SAMs consisting of PmP-up and PPm-down molecules can reduce or increase, respectively, contact resistances in p- and n-type transistors comprising established organic semiconductors (pentacene and C_{60}).[39] In the same study we also extensively characterized the properties of the pentacene layers grown on top of the SAM-modified electrodes, showing that there is only little difference in their structure and morphology for different dipole orientations. In the present work, we focus on the characteristics of the SAMs themselves, describing the synthesis of the precursors and studying their structural properties by ellipsometry, infrared reflection−absorption spectroscopy (IRRAS), scanning-tunneling microscopy (STM), near edge X-ray absorption fine structure (NEXAFS) spectroscopy, and contact angle goniometry. Moreover, X-ray photoelectron spectroscopy (XPS) reveals the integrity of the SAMs. In conjunction with dispersion-corrected density-functional theory (DFT) based simulations, the current study also provides insight into the electronic structure within the SAMs, correlating core-level binding energies with local shifts in the local electrostatic potential. The latter also gives rise to SAM-induced work function changes, which are quantified by the Kelvin Probe (KP) technique. Finally, we briefly review the charge-transport characteristics through the SAMs and their application as electrode modifiers in p- and n-type transistors.

2. EXPERIMENTAL SECTION

Chemicals and Synthesis Procedure. Solvents and chemicals necessary for the synthesis of the SAM precursors (Figure 1) were purchased from different vendors (see the Supporting Information) and used as received. PP was synthesized according to a literature procedure.[40] To synthesize PPm-down, a triisopropylsilylsulfide group was introduced to 5-bromo-2-phenylpyrimidine by a cross coupling reaction with triisopropylsilylthiol, Pd(dppf)Cl$_2$ as catalyst and LiHMDS as base. By reaction with HCl in MeOH, the TIPS-group was cleaved to release the free thiol. For the synthesis of

48

PmP-up, 4-bromophenyl(triisopropylsilyl)sulfide was first converted to the corresponding Grignard reagent and coupled with 2-chloropyrimidine catalyzed by Pd(dppf)Cl$_2$ followed by deprotection with HCl in MeOH. A detailed description of the synthesis procedures and the characterization data for the intermediates and final products are given in the Supporting Information.

X-ray Diffraction Analysis. The bulk structures of the single crystals of PPm-down and PmP-up were determined by X-ray diffraction. The data were collected on a STOE IPDS II two-circle diffractometer with a Genix Microfocus tube with mirror optics using Mo Kα radiation (λ = 0.71073 Å). The data were scaled using the frame-scaling procedure in the X-AREA program system.[41] The structures were solved by direct methods using the program SHELXS[42] and refined against F^2 with full-matrix least-squares techniques again employing SHELXL.[42] The CCDC deposition numbers are CCDC-1865408 (PmP-up) and CCDC-1865409 (PPm-down). PmP-up: The H atom bonded to S is disordered over two equally occupied positions. Nevertheless, it was freely refined. PPm-down: The coordinates of the H atom bonded to S were refined. Its U-value was set to 1.5U_{eq}(S).

SAM Preparation. The PPm-down, PmP-up, and PP SAMs were prepared on gold substrates. The substrates were purchased from Georg Albert PVD-Beschichtungen (Silz, Germany). They were prepared by thermal evaporation of 30 nm of gold (99.99% purity) onto polished single-crystal silicon (100) wafers (Silicon Sense) that had been precoated with a 9 nm titanium adhesion layer. The films were polycrystalline, exposing mostly (111) oriented surfaces of individual crystallites. The RMS value for these substrates was estimated as 0.8 nm (5 × 5 μm^2 scan area); in our experience, this value does not change noticeably upon the SAM formation.

Substrates for scanning tunneling microscopy (STM) measurements were purchased from Phasis (Geneva) or prepared by e-beam evaporation of gold (200 nm) onto high-quality mica at 400 °C in ultrahigh vacuum (UHV). Before evaporation, the mica substrates were annealed for 3 h at 400 °C. First 150 nm of gold were deposited at a high evaporation rate (30−60 Å/s) followed by 50 nm at a lower rate (0.5 Å/s). A shutter was used to protect the substrate while adjusting the evaporation rate. After evaporation, the substrates were annealed for 1 h at 400 °C.

The SAMs were formed by immersion of the substrates into solutions of the SAM precursors in either tetrahydrofuran (THF; Sigma-Aldrich) or ethanol (Sigma-Aldrich) for 24 h (also for a longer time, in the case of the STM experiments; see Section 3.5) under nitrogen and at room temperature. After immersion, the samples were carefully rinsed with pure solvent and dried under a flow of N$_2$. The SAMs prepared from both solvents did not show any significant differences with only one exception (see Section 3.4); therefore, mostly the data for the THF preparation are shown. Note that THF provides a better solubility of the thiols compared to ethanol and also, in the given case, a better reproducibility of the monolayers. However, in our previous study dealing with the device applications of the PPm-down and PmP-up SAMs we used the ethanol preparation, because of specific technical reasons.[39]

In addition, reference SAMs of hexadecanethiolate (HDT) and perdeuterated dodecanethiolate on the same Au(111) substrates were prepared according to the literature procedures.[43,44] HDT was purchased from Sigma-Aldrich; the

perdeuterated dodecanethiol was synthesized from the respective bromoalkane using standard procedures.

Characterization. *General Comments.* The SAMs were experimentally characterized by ellipsometry, contact angle goniometry, STM, IRRAS, synchrotron-based XPS, NEXAFS spectroscopy, KP measurements, and electric conductance measurements. In all cases, the characterization was performed at room temperature. XPS and NEXAFS spectroscopy experiments were conducted under UHV conditions with special care taken to minimize potential modification of the SAMs induced by the primary X-rays.[45−47] The SAMs were also characterized computationally by means of quantum mechanical simulations to analyze the experimental data and to support their interpretation. Note that a limited characterization of the PPm-down and PmP-up SAMs prepared from EtOH on "technical" gold substrates also used for device fabrication (for details see ref 39) has already been performed within the previous device study (contact angle goniometry, work function, and electric conductance).[39]

Ellipsometry. Ellipsometry measurements on the SAMs were carried out with a Sentech SE 400 ellipsometer equipped with a He/Ne laser (wavelength 632.8 nm, beam diameter 1−2 mm). The angle of incidence was 70° with respect to the sample surface normal. The complex refractive indices of the substrates, necessary for the data evaluation, were measured separately after a hydrogen plasma treatment for 2 min.[48] For the refractive indices of the monolayers, the extinction coefficients were assumed to be zero, while the real part was assumed to be 1.55, a value that according to our experience is well applicable in the case of mainly aromatic molecules.

Contact Angle Goniometry. Advancing and receding contact angles of Millipore water were measured on freshly prepared samples with a custom-made, computer-controlled goniometer. The measurements were performed under ambient conditions with the needle tip in contact with the drop. At least three measurements at different locations on each sample were made. The averaged values are reported. Deviations from the average were less than ±2°.

IRRAS. All IR spectra were obtained using a Thermo Nicolet 6700 Fourier transform IR spectrometer with a narrow-band mercury cadmium telluride semiconductor detector at a resolution of 4 cm^{-1}. The optical path was purged with dried and CO$_2$-free air during the measurement. Neat substances were measured using a single-reflection diamond attenuated total reflection unit and the infrared reflection absorption spectra of the SAMs were recorded at an angle of 80° relative to the sample surface normal with p-polarized radiation against a reference SAM of perdeuterated dodecanethiolate on Au.

IR spectra of isolated molecules were calculated using density functional theory (Gaussian 09 program package[49] with the BP86 functional[50,51] and the SVP basis set[52]), helping to assign the vibrational modes and to identify the directions of their transition dipole moments (TDMs). The spectra were not scaled.

STM. A Bruker Multimode 8 Nanoscope with a MultiMode V SPM Control Station was used for STM experiments. A low-current STM Converter (Model MMSTMLCE) allowed carrying out measurements in the pA regime. Therefore, a usual measurement current was 5−50 pA at a sample bias of about 200 mV. The scanner had a maximum range of 1.4 μm × 1.4 μm. Probes were manufactured by cutting Pt−Ir (80:20) wires with a diameter of 0.25 mm. The tip quality was assessed

49

by measuring highly oriented pyrolytic graphite (HOPG). Only monolayers deposited onto gold on mica substrates (vide infra) were measured.

XPS. XPS measurements were performed at the HE-SGM beamline (bending magnet) of the synchrotron storage ring BESSY II in Berlin, Germany, using a custom-made experimental station.[53] Primary photon energies (PE) of 350 and 580 eV were used. The spectra acquisition was carried out in normal emission geometry with a Scienta R3000 electron energy analyzer. The energy resolution was ~0.3 and ~0.6 eV at PEs of 350 and 580 eV, respectively.

The binding energy (BE) scale of the spectra was referenced to the Au $4f_{7/2}$ emission at 84.0 eV.[54] When necessary, the spectra were fitted by symmetric Voigt functions and either a linear or Shirley-type background. To fit the S $2p_{3/2,1/2}$ doublets, we used two peaks with the same full width at half-maximum (fwhm), a standard[54] spin−orbit splitting of ~1.2 eV (verified by a fit), and a branching ratio of 2 (S $2p_{3/2}$/ S $2p_{1/2}$).

The effective thicknesses of the SAMs and their packing densities were calculated using standard procedures,[43,55] based on the C 1s/Au 4f and S 2p/Au 4f intensity ratios, respectively. For the thickness evaluation, a standard expression for the attenuation of the photoemission signal was assumed[56] and the literature values for attenuation lengths, relying on the measurements of alkanethiolate SAMs, were used, viz. 11.5 and 15.75 Å for kinetic energies of 295 and 490 eV, respectively.[57] The spectrometer-specific coefficients were determined by using the PP SAM as a direct reference, relying on the well-known thickness of this monolayer (1.09 ± 0.02 nm).[44] This SAM also served as a reference for the evaluation of packing densities, relying on the packing density (4.63 × 10^{14} molecules/cm²) corresponding to the ($\sqrt{3} \times \sqrt{3}$)R30° molecular lattice, which is the dominant structural phase of the PP SAMs formed after long immersion time.[58,59] This value was additionally verified by referencing the PP SAM to the even better defined HDT monolayer on Au(111) also having an overall packing density of 4.63 × 10^{14} molecules/cm².[60] The packing density of the PP SAM was found to be nearly identical to that of HDT, being only slightly (~4%) lower, which is presumably related to the specific morphology of the PP monolayer (small domains and a certain polymorphism).[59]

NEXAFS Spectroscopy. The NEXAFS spectra were collected at the same beamline as the XPS data. They were measured at the carbon and nitrogen K-edges in the partial electron yield (PEY) mode with retarding voltages of −150 and −300 V, respectively. Linearly polarized synchrotron light with a polarization factor of ~89% was used as the primary X-ray source. The incidence angle of the X-rays was varied between the normal (90°) and grazing (20°) incidence geometry to monitor the linear dichroism reflecting the molecular orientation in the SAMs.[61] The energy resolution was ~0.3 eV at the C K-edge and ~0.45 eV at the N K-edge. The PE scale was referenced to the pronounced π* resonance of HOPG at 285.38 eV.[62] The spectra were corrected for the PE dependence of the incident photon flux and reduced to the standard form with zero intensity in the pre-edge region and the unity jump in the far postedge region.

KP Measurements. Work function measurements were carried out using a UHV Kelvin Probe 2001 system (KP technology Ltd., U.K.). The pressure in the UHV chamber was ~10^{-9} mbar. As reference, we used a HDT SAM with the work function value set to 4.3 eV according to literature.[17] The latter

value was additionally verified by its referencing to the work function of freshly sputtered gold set to 5.2 eV.[63]

Electrical Conductance Measurements. The measurements were performed with a custom-made two-terminal tunneling junction setup, based on the Keithley 2635A source meter.[64] The gold substrate and a sharp tip of eutectic GaIn (EGaIn)[65] served as bottom and top electrodes.[65] Tunneling junctions were formed by contacting grounded SAM/Au samples with the EGaIn tips and applying a potential. The voltage was varied between −0.6 and +0.6 V in steps of 0.05 V. At least 10 I−V curves measured at several different places were recorded for each sample; the average values were calculated.

Quantum Mechanical Simulations. The computational study was performed using the FHI-aims code[66] employing the PBE functional.[67] To account for long-range van der Waals interactions, we employed the surface version[68] of the Tkatchenko−Scheffler dispersion correction.[69] The system was modeled using periodic boundary conditions and the repeated slab approach. The metallic substrate was described with five Au layers, holding the three bottom ones fixed during all calculations and turning off the dispersion corrections between the Au atoms. Two molecules arranged in a herringbone fashion were put in a $(3 \times \sqrt{3})rect$ unit cell, whose dimensions in the x- and y-directions were defined according to the calculated Au lattice constant and held fixed in all calculations. The systems were optimized using the FHI-aims default "tight" setting and a $9 \times 5 \times 1$ Γ centered k-points grid. The total energy criterion for the self-consistency cycle was set to 10^{-6} eV and geometry optimizations were continued until the maximum residual force component per atom was below 0.01 eV/Å.

The C 1s XP spectra were simulated within the initial state approach, to avoid artifacts arising from combining periodic boundary conditions and explicit excitations in each unit cell.[70] The spectra were modeled following the procedure described in ref 70 using an image potential model to account for the screening due to the highly polarizable metal substrate and weighting the contribution of every atom to account for the finite escape depth of the photoelectrons.

Further information regarding the initial geometry, the numerical settings and the simulation of the XP spectra can be found in the Supporting Information.

3. RESULTS AND DISCUSSION

3.1. Synthesis. As mentioned in Section 2, the new pyrimidine-containing molecules were obtained via palladium-catalyzed cross-coupling reactions from literature-known starting materials (Scheme 1).[71,72] The use of the triisopropylsilyl (TIPS) moiety as protective group for the sulfur atoms was a key to this procedure, as this group is compatible with the Pd chemistry.[72,73]

It is worth mentioning that the TIPS derivatives of thiophenols, in contrast to aliphatic TIPS-protected thiols, are not very stable against the typical conditions of column chromatography or gradient sublimation. Therefore, the intermediates **2** and **4** were not isolated, but the crude products were directly deprotected following a literature known procedure.[19] The resulting thiols (PPm-down and PmP-up) are very prone to oxidation during the typical workup procedures, resulting in only moderate yields.

3.2. X-ray Diffraction Analysis. Despite the proneness of PPm-down and PmP-up to oxidation, it was nevertheless

Scheme 1. Synthesis of Dipolar SAM Precursors 2-Phenylpyrimidine-5-thiol (PPm-down) and 2-(4-Mercaptophenyl)pyrimidine (PmP-up)
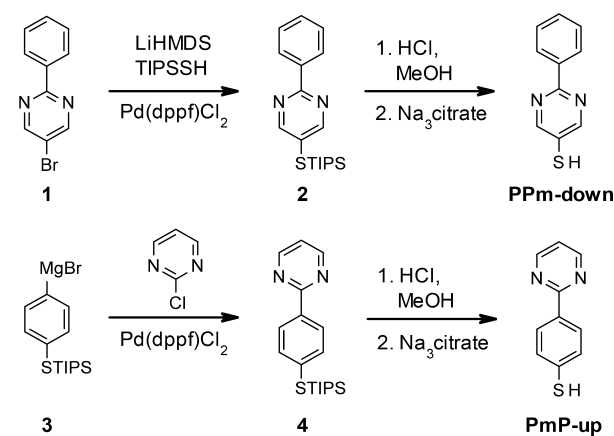
possible to obtain single crystals of both compounds and to determine the respective bulk structure by X-ray diffraction (see the Supporting Information, in particular Figures S9 and S11). Both structures have two features in common, viz. an antiparallel arrangement of the molecules compensating the molecular dipole moments and a close-to-coplanar orientation of the aromatic rings within individual molecules. Although for PmP-up the torsion is less than 1°, for PPm-down an angle of about 17° could be determined. This is presumably due to sterical interactions and the specific packing motif mentioned above. The frequently observed coplanarity of 2-phenyl-pyrimidines[74] provides a good electronic coupling between the π-systems of individual rings, which is expected to be advantageous for the electric conductivity in the respective SAMs, provided that the bulk arrangement is mimicked in the monolayers (apart from the antiparallel orientation not observed in the monolayers; see below).

Despite the above similarities, there are certain differences in the packing of the molecules (see the Supporting Information), presumably because in the case of PPm-down an interaction between the π-system of the phenyl ring and the thiol proton of a neighboring molecule occurs, resulting in the formation of distinguished pairs. For PmP-up, this interaction would need to occur with the pyrimidine ring, which has a lower electron density.

Note that although the X-ray diffraction analysis of the single crystals provides important reference data for the SAMs, such as a close-to-coplanar orientation of the aromatic rings within individual molecules, the antiparallel molecular arrangement observed in the crystals does not occur in the SAMs. There, the molecules are bonded by the anchoring group (thiolate in the present case) to the substrate and thus are arranged in a parallel fashion.

3.3. Ellipsometry. The ellipsometric thicknesses of the PP, PPm-down, and PmP-up SAMs were estimated as 1.11 ± 0.02, 0.93 ± 0.02, and 1.10 ± 0.03 nm, respectively. As all the molecules mentioned above have a similar length of ~ 1.0 nm and the length of S—Au bond is estimated as 0.24 nm,[75,76] it can be assumed that all three thiols form dense monolayers with similar packing densities, even though the PPm-down SAM might be not as closely packed as the two other monolayers. A simple comparison of the derived layer thickness to the sum of the molecular length and the length

of the S—Au bond permits a rough estimation of the molecular tilt angles (β) relative to the surface normal, which amount to $\sim 26°$ (PP), $\sim 41°$ (PPm-down), and $\sim 26°$ (PmP-up).

3.4. Wetting Properties. The wetting properties of the PmP-up, PPm-down, and PP SAMs are important in the context of OSC growth on SAM-modified electrodes[39] and as a fingerprint of the decoupling of the SAM-OSC (SAM/ambient) interface and the dipole engineering.

Advancing (θ_{adv}) and receding (θ_{rec}) water contact angles (WCA) for the PmP-up, PPm-down, and PP SAMs prepared from THF and ethanol solutions are presented in Figure 2a,b,
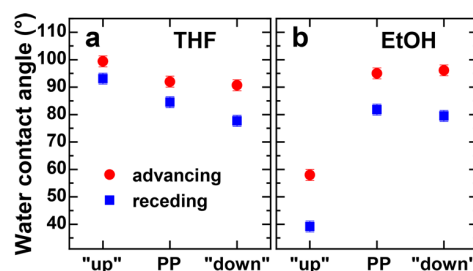
Figure 2. Advancing (red circles) and receding (blue squares) water contact angles for the PmP-up ("up"), PPm-down ("down") and PP SAMs prepared from THF (a) and ethanol (b).

respectively. For the THF preparation, both θ_{adv} and θ_{rec} show similar values for the different monolayers, verifying the general notion of a decoupling the SAM-OSC (SAM/ambient) interface and the dipole engineering. There is, however, a weak, systematic dependence of the WCA on the molecular dipole moment, which means that the influence of the molecular dipole cannot be completely neglected within the given two-rings molecular architecture. Note that generally the relation between molecular dipole and surface energy represents an interesting issue (see, e.g., ref 15).

For the ethanol preparation, θ_{adv} and θ_{rec} are only similar for the PPm-down and PP SAMs (showing also a good correlation with the WCA values for the THF case), whereas the values for the PmP-up monolayers are noticeably lower, which agrees with the previous measurement performed in context of device applications of these SAMs and is mostly related to the polar component of the surface energy.[39] The reasons for this behavior are unclear at the moment, because we could not observe any other distinct differences between the films prepared from THF and ethanol.

Note that the WCA values for the reference PP SAMs are higher than those published in literature (θ_{adv} and θ_{rec}, viz. 73° and 69°),[40] indicative of the very high quality of our films.

3.5. STM. Molecular packings in the PP, PPm-down, and PmP-up SAMs were characterized by STM. Representative large scale and high-resolution STM images of these monolayers are shown in Figure 3. For the PmP-up SAM, well-ordered structures could be obtained in a straightforward manner after an immersion time of 24 h. The domains have a size of about 20 nm and expose the well-known ($\sqrt{3} \times \sqrt{3}$)R30° superstructure corresponding to a packing density of 4.63×10^{14} molecules/cm². The situation was more complex for the PPm-down monolayers, for which domains were only observed after immersion times of at least 7 days. The domains with a size of about 4−5 nm were still quite disordered after this time, consistent with the lower apparent film thickness

51
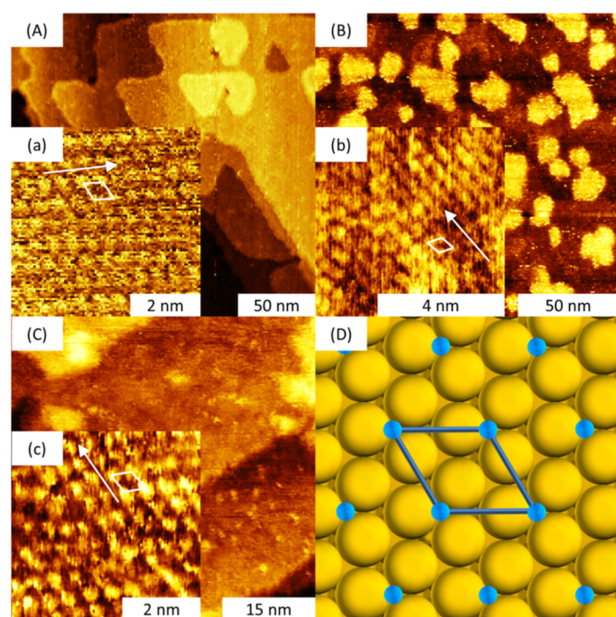
Figure 3. Large scale (A−C) and high magnification (a−c) STM images of the dominant ($\sqrt{3} \times \sqrt{3}$)R30° phase in the PmP-up (A, a), PP (B, b) and PPm-down (C, c; after 8 days of immersion) SAMs along with a scheme of the respective molecular arrangement (D; for the sketch we arranged the sulfur on top of a 3-fold hollow site). In panels a−c, the unit cell and the $\langle 11\bar{2} \rangle$ direction (white arrows) are marked. Parameters: (A) 1.0 pA, 200 mV; (a) 12.0 pA, 220 mV; (B) 1.5 pA, 200 mV; (b) 20.0 pA, 60 mV; (C) 5.0 pA, 200 mV; (c) 40.0 pA, 200 mV.

determined in the ellipsometry experiments. When the immersion time was prolonged to 12 days, the average domain size increased to 8 nm and the order within the domains improved. A ($\sqrt{3} \times \sqrt{3}$)R30° unit cell could be observed.

Note that the PmP-up, PPm-down, and PP SAMs do not induce pronounced etch pits on Au(111) as typical for some thiol-based monolayers (see e.g. ref 77) but rather form Au islands as seen in the large scale images in Figure 3. Such a behavior is frequently observed if the anchoring S atom is directly attached to the aromatic system (see, e.g., ref 59).

Note also that the ($\sqrt{3} \times \sqrt{3}$)R30° structure was recorded as the dominant structural phase for the reference PP SAMs as well but it was difficult to obtain well-resolved images of this arrangement. In accordance with literature data,[59] this issue is presumably related to the small size of the crystalline domains and some polymorphism. This can generally be explained by a mismatch of the optimal molecular packing and the underlying (111) lattice of the gold substrate;[78] in particular, the preferred packing of bulk biphenyl deviates slightly different from a hexagonal arrangement.[79]

In addition to the ($\sqrt{3} \times \sqrt{3}$)R30° structure, a (2 × 2) phase was also observed in all three monolayers. Such a structure, in fact, has been reported previously for the PP SAMs prepared on Au(111) by vapor deposition.[80] This phase is characterized by a ∼25% lower packing density compared to the ($\sqrt{3} \times \sqrt{3}$)R30° structure. In view of the XPS data (vide infra), however, it is believed to be the minority phase and the ($\sqrt{3} \times \sqrt{3}$)R30° structure is considered as reference structure throughout the entire paper. In passing, we note that the STM data do not provide information on the relative orientation of neighboring molecules, i.e., it cannot be deduced whether the

molecules pack in a cofacial or in a herringbone structure, where the latter, due to the presence of two symmetry-inequivalent molecules, would require a larger unit cell than ($\sqrt{3} \times \sqrt{3}$)R30°. This issue will be addressed later when modeling the structural properties of the investigated SAMs.

3.6. XPS. S 2p, N 1s, and C 1s XP spectra of the PmP-up, PPm-down, and PP SAMs are presented in Figure 4; the complementary Au 4f and O 1s spectra are compiled in Figure S12 in the Supporting Information.
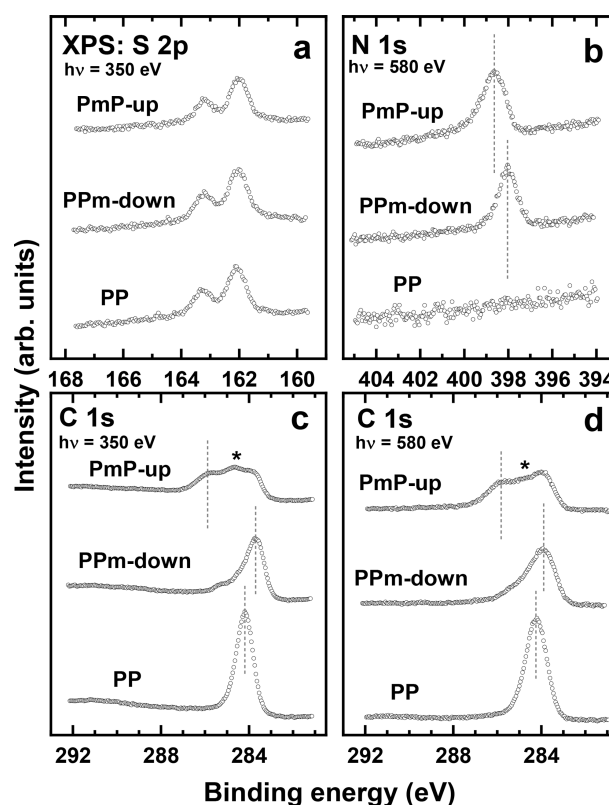
Figure 4. S 2p (a), N 1s (b), and C 1s (c,d) XP spectra of the PmP-up, PPm-down, and PP SAMs. The spectra were acquired at photon energies of 350 eV (a,c) and 580 eV (b,d). The vertical dashed lines are guides to the eye. A feature with a strongly photon-energy-dependent intensity between the two major peaks in the C 1s spectra of PmP-up is marked by *.

The S 2p XP spectra of all three films in Figure 4a exhibit a single S $2p_{3/2,1/2}$ doublet at ∼162.0 eV (S $2p_{3/2}$). The BE is representative of the thiolate species bound to noble metal substrates,[46] indicative of the distinct SAM character of all the studied films. The intensity of the doublet is similar over the series, being only slightly weaker for PmP-up/Au. This suggests a similar packing density of all three SAMs. This conclusion is supported by the similar intensities of the Au 4f signal, determined via the attenuation by the SAM overlayer (Figure S12a in the Supporting Information).

The N 1s XP spectra of PmP-up/Au and PPm-down/Au are presented in Figure 4b. These spectra exhibit a single N 1s peak assigned to the nitrogen atoms in the pyrimidine ring of the SAM precursors. In contrast, the spectrum of PP/Au does not show any N 1s signal, in accordance with the chemical composition of the SAM. The BEs of the N 1s peak, however, are distinctly different for the PPm-down and PmP-up SAMs,
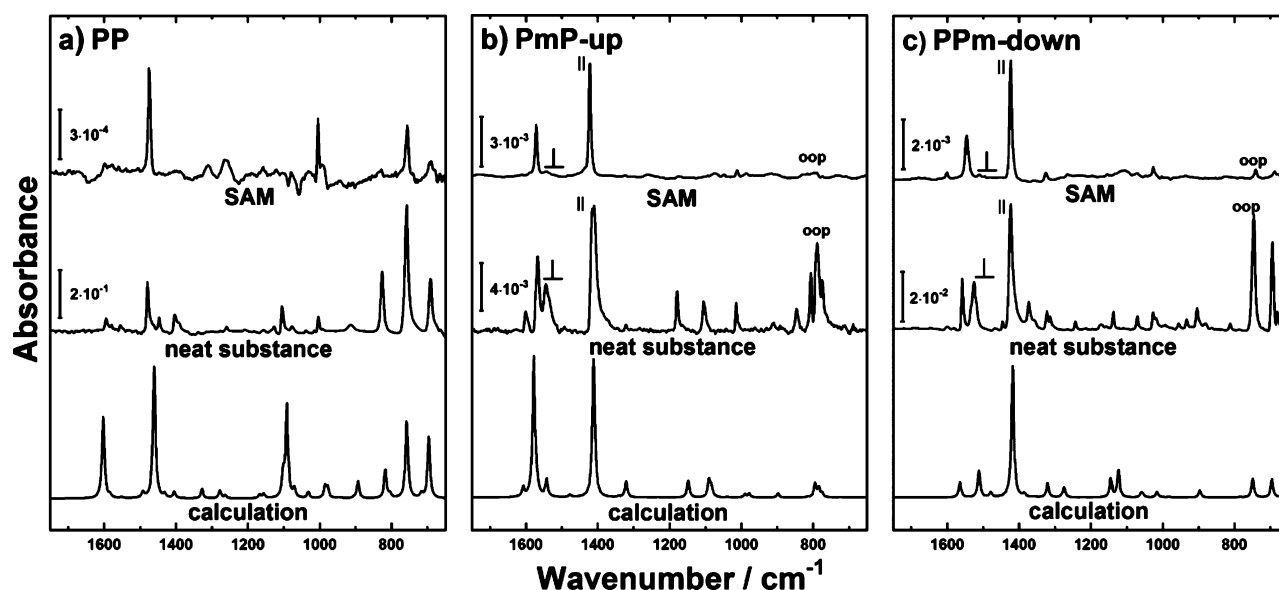
Figure 5. IRRA spectra of PP (a), PmP-up (b), and PPm-down (c) SAMs (upper curves) along with the IR spectra of the neat substances (middle curves) and the DFT calculated spectra (bottom curves). Absorbance scale bars are given for the experimental spectra while the calculated spectra are displayed in arbitrary units. The modes, which were used for the calculation of the tilt and twist angles, are labeled as ∥, ⊥, and oop. Note that the selected ⊥ mode, which only has reasonable intensity for the PmP-up and PPm-down case, is partly merged with a ∥ mode appearing at a higher wavenumber.

Table 1. Positions (given in cm⁻¹) of the Most Important Vibrational Modes in the IR Spectra of the PPm-down and PmP-up Molecules and Corresponding SAMs, Together with the Respective Theoretical Values (DFT)[a]

no.	mode[b,c]	TDM[d]	PPm-down			PmP-up		
			DFT	neat[e]	SAM[e]	DFT	neat[e]	SAM[e]
1	γ CH ring twist	oop	696	695 s	688 w			
2	γ CH ring twist	oop	749	747 s	741 w	794	789 s	790 w
3	ν CC, δ NCN	∥				979	1014 m	1012 w
4	δ CH	∥				1148	1179 m	1175 vw
5	ν CC, δ NCN	∥				1321	1322 w	1324 w
6	ν CC CN, δ CH	⊥	1386	1373 m				
7	ν CN$^{(s)}$	∥	1418	1424 vs	1424 vs	1412	1410 vs	1422 vs
8	ν CN$^{(as)}$	⊥	1512	1526 m	1511 w	1542	1544 m	1544 w
9	δ CH, ν CN	∥	1565	1558 m	1546 m	1578	1567 s	1572 m
10	ν SH		2604	2535 m		2617	2578 vw	

[a]The assignment of the vibrational modes was carried out on the basis of the DFT calculations, which also provided the orientations of the respective TDMs. [b]Due to the differences in the molecular structure of PPm-down and PmP-up, the equivalents of some strong bands in the spectrum of one of the molecules have very low intensities in the spectrum of the other molecules and can become almost invisible. Where this applies, we refrain from displaying their wavenumbers. [c]ν, stretch mode; δ, in plane bending mode; γ, out of plane bending mode; s, symmetric; as, asymmetric. [d]∥, parallel to the molecular backbone; ⊥, perpendicular to the main molecular backbone and in the plane of the aromatic ring; oop, perpendicular to the aromatic plane. [e]vs, very strong; s, strong; m, medium; w, weak; vw, very weak.

being 398.05 and 398.65 eV, respectively. This difference cannot stem exclusively from the different screening of the photoemission hole by the substrate, resulting in a slightly lower N 1s BE value for PPm-down/Au, because the respective effect is not that strong and can be estimated as 0.05−0.1 eV in the given case.[81] Rather, it is a consequence of electrostatically induced XPS shifts,[16,17,70,82,83] as shall be discussed in Section 3.10.

The C 1s XP spectra of PmP-up/Au and PPm-down/Au are presented in Figure 4c,d. They are distinctly different and cannot be explained by a mere superposition of a pyrimidine spectrum and a phenylene spectrum, as both SAMs consist of these two rings. Rather, the spectra are again strongly influenced by electrostatic effects, associated with the periodic arrangement of the dipole moments of the embedded pyrimidine moieties.[17,70,82,83] These effects will be discussed in detail below, when analyzing the electronic structure of the SAMs (Section 3.10), relying on a comparison of our experiments with DFT simulations and on an analysis of literature data on related compounds. They are also mostly responsible for the larger apparent width of the XPS features for PmP-up. Beyond that, a direct comparison between calculated and measured spectra for both systems (see the Supporting Information) yields a minor additional broadening for PmP-up, hinting toward a slightly reduced order in these films.

Along with the qualitative analysis of the XPS data, their quantitative evaluation was performed (see Section 2 for

details), yielding the same packing density of about 4.5×10^{14} molecules/cm^2 for both monolayers together with effective thicknesses of 0.93 ± 0.05 and 1.00 ± 0.05 nm for the PPm-down and PmP-up SAMs, respectively. Significantly, the values for the PPm-down and PmP-up SAMs are close to (albeit slightly lower than) those of PP/Au (1.09 nm and 4.6×10^{14} molecules/cm^2, corresponding to the $(\sqrt{3} \times \sqrt{3})R30°$ structure; see Section 2). This suggests a similar molecular packing with some disorder due to the presence of the dipolar pyrimidine groups (or the occurrence of (2×2) structures as a minority phase, as discussed in Section 3.5).

3.7. IRRAS. IRRAS offers a means to characterize the molecular identity as well as the orientation of surface bound species. In Figure 5, the IR spectra of the bulk PP, PPm-down, and PmP-up materials as well as the IRRA spectra of the corresponding SAMs are displayed, along with the results of DFT calculations on isolated molecules.

In Table 1, the most prominent vibrational modes for the PPm-down and PmP-up monolayers are compiled and assigned, based on the DFT calculations. Additionally, the TDMs of these modes with respect to the molecular backbone and the molecular plane (assuming a close-to-planar conformation) are given as "∥" (parallel), "⊥" (perpendicular, in-plane), and "oop" (perpendicular, out-of-plane). From Figure 5 and Table 1, it is evident that in the IRRA spectra those bands are attenuated whose TDMs are perpendicular to the molecular axes, while the other bands stay intense. According to the surface selection rules for metal substrates,[84] this indicates an almost upright molecular orientation in all studied SAMs. Apart from this qualitative conclusion, the tilt angle β (deviation of the direction of the molecular backbone from the surface normal; see Figure 6) for the PmP-up and PPm-down molecules on the gold substrate were estimated using the method established by Parikh and Allara.[85] This method compares the relative intensities of three IR bands (each with an independent TDM) from the IR spectra of the
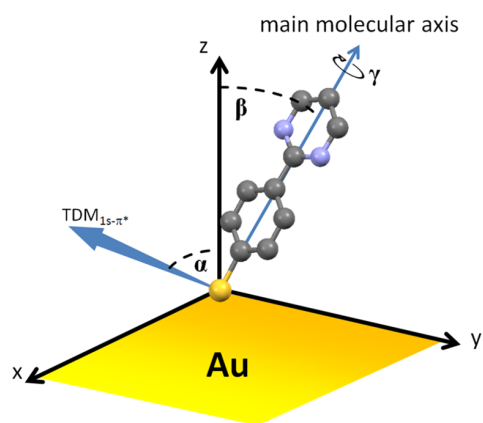
Figure 6. Exemplary illustration of PmP-up in a coordinate system along with β (tilt angle of the main molecular axis with respect to the surface normal), γ (molecular twist angle), and α (tilt angle of the π^* orbitals: see Section 3.8). Both aromatic rings are considered to be coplanar, consistent with the results of the simulations (see below) and X-ray diffraction analysis for the single crystals (see Section 3.2). The twist angle is defined such that it is zero when the tilt occurs perpendicular to the molecular plane. The transition dipole moment of the 1s-π^* resonance lies then in the plane spanned by the z-axis and the main molecular axis.

SAM and the neat substance. For the PmP-up and PPm-down monolayers the intensities of bands 2 (oop), 7 (∥) and 8 (⊥) were compared. This yields tilt angles of $24° \pm 11°$ and $14° \pm 10°$, respectively. Note that the given approach in principle allows also evaluating the twist angle γ (rotation around the molecular axis; see Figure 6) but the low intensities of the ⊥ and oop bands in the IRRA spectra cause very large error bars for this parameter, so that we refrain from presenting the respective results. Note also that the low intensities of these bands prevent the evaluation of the tilt and twist angles for PP. Complementary data on molecular orientation were obtained using NEXAFS spectroscopy (vide infra).

3.8. NEXAFS Spectroscopy. C and N K-edge NEXAFS data for the PmP-up and PPm-down SAMs are presented in Figures 7 and 8, respectively; the reference data for PP/Au are
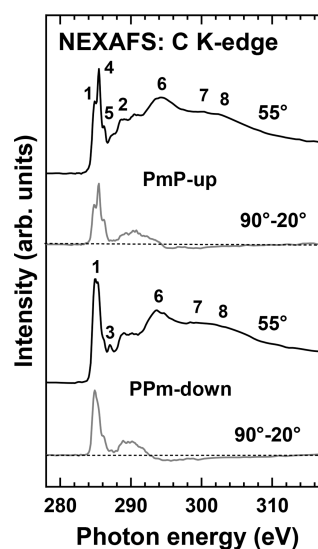
Figure 7. C K-edge NEXAFS spectra of the PmP-up and PPm-down SAMs acquired at an X-ray incidence angle of 55° (black lines), along with the respective difference between the spectra collected under the normal (90°) and grazing (20°) incidence geometry (gray lines). Individual absorption resonances are marked by numbers (see text for the assignments). The horizontal dashed lines correspond to zero.

compiled in Figure S13 in the Supporting Information. In Figures 7 and 8, two kinds of spectra are depicted. First, there are spectra acquired at an X-ray incidence angle of 55° (magic angle), which are representative of the electronic structure of the films (unoccupied molecular orbitals) and are not affected by orientational effects.[61] Second, there are curves corresponding to the difference between the spectra collected under the normal (90°) and grazing (20°) incidence geometry. These curves are useful fingerprints of orientational order and molecular orientation,[61] showing the extent of the resonance intensity change upon variation of the angle between the electric field vector of the primary X-ray beam and the TDMs of the relevant molecular orbitals.

Let us first consider the 55° spectra, starting with the C K-edge ones. Within the generally acceptable building block scheme in X-ray absorption spectroscopy,[61] the spectra of PmP-up/Au and PPm-down/Au can be understood as superpositions of the component spectra of phenyl and pyrimidine rings. Generally, the spectrum of phenyl and oligophenyl SAMs is dominated by the strong π_1^* resonance at

54
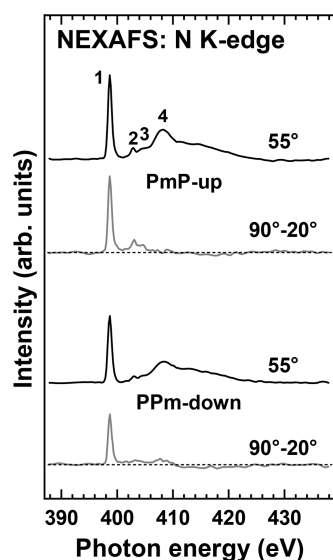
Figure 8. N K-edge NEXAFS spectra of the PmP-up and PPm-down SAMs acquired at an X-ray incidence angle of 55° (black lines), along with the respective difference between the spectra collected under the normal (90°) and grazing (20°) incidence geometry (gray lines). Individual absorption resonances are marked by numbers (see text for the assignments). The horizontal dashed lines correspond to zero.

~285.0 eV (**1**), accompanied by the respective π_2^* peak (**2**) at ~288.8 eV and several broader σ^* resonances (**6–8**) at higher excitation energies (see Figure S13 in the Supporting Information).[44,61,86,87] In addition, in oligophenyl SAMs a R*/C−S* resonance (**3**) at ~287.0 eV is frequently observed.[44] The spectrum of pyrimidine is dominated by a complex feature, with maxima at 284.7−285.1 eV (close to **1**; low intensity), 285.4 eV (**4**; high intensity), and 285.86 eV (**5**; high intensity), containing contributions from several π^* resonances.[88,89] The spectrum exhibits also a variety of comparably weak π^* and Rydberg resonances as well as broader σ^* resonances at higher excitation energies.[88,89]

The above features are indeed observed in the 55 °C K-edge NEXAFS spectra of PmP-up/Au and PPm-down/Au in Figure 7, with the weights modulated by the attenuation effects for the PEY signal[90] and a certain decrease in intensity of absorption resonances for the moieties located far away from the SAM-ambient interface.[44] Accordingly, the spectrum of PPm-down/Au, having the phenyl ring in the top position and the pyrimidine ring in the bottom position (Figure 1), is dominated by the features of the phenyl moiety, with just a "broadening" of the most intense π_1^* resonance (**1**) due to the admixture of the pyrimidine resonances **4** and **5**. In contrast, the spectrum of PmP-up/Au, having the pyrimidine ring in the top position and phenyl ring in the bottom position (Figure 1), is dominated by the pyrimidine resonances **4** and **5** forming a complex absorption structure in the pre-edge region, with a contribution of the π_1^* resonance (**1**) of the phenyl ring. At the same time, both for PPm-down/Au and PmP-up/Au, the post-edge region is dominated by the σ^* resonances of phenyl (compare with the data for PP/Au in Figure S13 in the Supporting Information) which are generally more distinct than those of pyrimidine.

The 55° N K-edge NEXAFS spectra of PPm-down/Au and PmP-up/Au in Figure 8 exhibit the characteristic features of pyrimidine.[88,89] The spectra are dominated by a strong π^*

resonance at ~398.5 eV (**1**) accompanied by a mixed π^*-Rydberg feature at 402.7 eV (**2**) and Rydberg features at higher excitation energies (**3** and **4**). The intensity of the resonances is somewhat lower for PPm-down/Au, which is related to the stronger attenuation of the PEY signal for the pyrimidine ring in the bottom position as well as to the slightly lower coverage as compared to PmP-up/Au (see Sections 3.3 and 3.6).

Although the 55° NEXAFS spectra allow the verification of the chemical identity of the PPm-down and PmP-up SAMs, the difference 90°−20° spectra in Figures 7 and 8 give insight into the molecular orientation in the films. In these spectra, pronounced difference peaks at the positions of the absorption resonances are observed, indicative of a high orientational order. Further, the peaks associated with the π^* resonances are positive, whereas those related to the σ^* resonances are negative. Considering that the TDMs of the π^* and σ^* orbitals are directed perpendicular and parallel to the ring planes, respectively, the signs of the difference peaks mean a largely upright molecular orientation in the SAMs, in qualitative agreement with the ellipsometry, IR spectroscopy, and XPS results (see Sections 3.3, 3.6, and 3.7).

In addition to the above-described qualitative analysis, a quantitative evaluation of the entire set of the NEXAFS data for PPm-down/Au and PmP-up/Au was performed, relying on the most prominent π^* resonances at the C and N K-edge and using the standard theoretical framework for the vector-like orbitals, suitable in the given case.[61] Within the respective evaluation procedure, the intensity of a particular π^* resonance was derived from the spectra, plotted as a function of the X-ray incidence angle, and fitted by the theoretical curves for a vector-like orbital with the average tilt angle of the π^* orbital with respect to the surface normal, α (see Figure 6), being the only parameter.[44,91] The derived values of this parameter for the C and N K-edge resonances are compiled in Table 2. The

Table 2. Average Tilt Angles of the π^* Orbitals in the PmP-up and PPm-down SAMs, Calculated on the Basis of the C K-Edge and N K-Edge NEXAFS Data[a]

monolayer	tilt angle (α) from the C K-edge data	tilt angle (α) from the N K-edge data	average value
PmP-up/Au	65.6°	69.1°	67.5°
PPm-down/Au	65.9°	65.8°	66°

[a]The accuracy of the values is ±3°.

very similar values obtained evaluating the C and N K-edge resonances suggest that the two rings are coplanar or close-to-coplanar in the SAMs, because the derived angles are predominantly (C K-edge) or exclusively (N K-edge) representative of the orientation of the phenyl and pyrimidine rings, respectively. Furthermore, it is consistent with the simulations discussed in the following section and with the very small, respectively, vanishing inter-ring torsions seen in the single crystal data for the precursor materials in Section 3.2.

On the basis of the average tilt angles of the π^* orbitals, average molecular tilt angles with respect to the surface normal, β, can be calculated using $\cos \alpha = \sin \beta \times \cos \gamma$, where γ is the molecular twist angle (see Section 3.7). The latter angle cannot be determined from the NEXAFS data (except for specially derivatized molecules)[72]. Thus, it is usually derived from bulk structures, IR data, or from simulations. In the present case, we will rely on the latter (see next section), taking the level of agreement between the experimental and theoretical values of

55

α as a criterion for the reliability of the simulations. Provided that this agreement is satisfactory, molecular tilt and twist angles can then be directly determined from the simulated structures.

3.9. Modeling the Structural Properties of the SAMs.

The optimized geometries of the PmP-up and PPm-down SAMs are shown in Figure 9. As mentioned in the
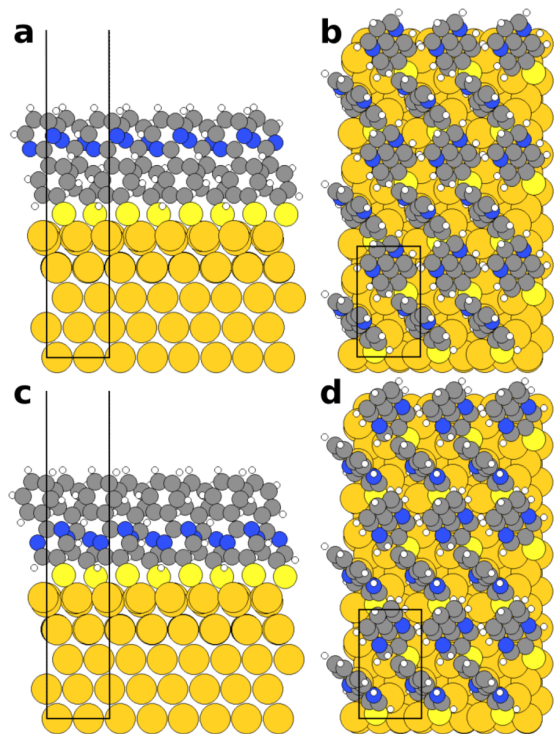
Figure 9. DFT-optimized structures of the PmP-up (a,b) and PPm-down (c,d) SAMs. Color code: H, white; C, gray; N, blue; S, light yellow; and Au, dark yellow.

methodology section, all SAMs were modeled using a $(3 \times \sqrt{3})rect$ unit cell containing two molecules, which yields the same packing density as the $(\sqrt{3} \times \sqrt{3})R30°$ structure $(4.6 \times 10^{14}$ molecules/cm^2, in line with the value observed experimentally). It, however, allows for a herringbone arrangement of the molecules. To determine the actual film structure, we then compared the energetics of the herringbone and cofacial arrangements of the molecules and found the former to be more stable in both studied systems (by 0.12 eV per molecule for PmP-up/Au and by 0.11 eV for PPm-down/Au). The individual molecules assume a planar conformation (with inter-ring torsions below 3° for PmP-up/Au and 7° for PPm-down/Au) consistent with the experimental results discussed above. A detailed analysis of the intermolecular interactions causing this specific intra- and intermolecular

arrangement is provided in ref 92 for the reference PP/Au system.

From the simulated geometries, the structural parameters can be directly obtained and compared to the experimental ones. The derived tilt angles of the π^* orbitals, α, the molecular tilt angles, β, and the molecular twist angles, γ, are reported in Table 3, where the subscripts 1 and 2 refer to the symmetry inequivalent molecules in the unit cell. For α also, the value averaged over the two molecules, α_{av}, is given. To be consistent with the NEXAFS evaluation, it is obtained via $\cos^2\alpha_{av} = (\cos^2\alpha_1 + \cos^2\alpha_2)/2$, because the tilt angle enters the equation for the intensity of an absorption resonance associated with a vector-like orbital as $\cos^2\alpha$.[61]

The calculated average tilt angles of the π^* orbitals agree very well with the values obtained in the NEXAFS experiments (see Table 2), which underlines the reliability of the theoretical modeling and makes the respective β-values reasonable estimates for the molecular tilt in the studied SAMs. The calculated tilt angle for the PPm-down SAM is somewhat larger than for the PmP-up monolayer. This agrees with the ellipsometry (Section 3.3) and XPS (Section 3.6) data, which suggest higher effective thickness in the PmP-up case (corresponding to a smaller molecular tilt). The non-negligible differences in the α-values between the two molecules in the unit cell are not due to different tilts, but result from strongly different twists (caused by different directions into which the molecules tilt). Therefore, they can be considered as a consequence of the herringbone-arrangement of the molecules.

3.10. Electronic Properties of the SAMs: Simulated XP Spectra.

As a first step to analyze the electronic structure of the SAMs, we calculated their XP core-level spectra. They are shown in the top panel of Figure 10 for a signal damping consistent with a primary photon energy of 580 eV. As simulations within the initial-state approach rely on the calculation of the Kohn–Sham orbital energies of the core levels, they provide information only on the relative energetics of the different atoms.[93−96] Therefore, the values have been rigidly shifted to higher binding energies (BEs) by 18.94 eV (a value we typically observe for SAMs), such that the experimental and calculated spectra of the "parent" PP SAM are aligned.

The overall shape of the spectra agrees well with the experiments (see Figure 4c,d). The spectrum of the PP SAM is characterized by a single peak with a binding energy of 284.2 eV (in general agreement with the experimental data).[46,97] Also for PPm-down/Au, the spectrum is clearly dominated by a single feature, which, however, is shifted to lower binding energies by about 0.6 eV. Moreover, there is a pronounced tail at the high binding-energy side of the spectrum with a shoulder at about 284.8 eV. In contrast, in the 580 eV spectrum of PmP-up/Au two more clearly separated main features, split by 1.4 eV, can be identified, with the more intense feature essentially coinciding with the main peak for the PP SAM. Interestingly,

Table 3. DFT Calculated Average Tilt Angles of the π^* Orbitals α, Molecular Tilt Angles β and Molecular Twist Angles γ in the PmP-up and PPm-down SAMs[a]

monolayer	α_{av}	α_1	α_2	β_1	β_2	γ_1	γ_2
PmP-up/Au	69.5°	75.8°	64.6°	29.6°	25.6°	60.2°	7.7°
PPm-down/Au	66.5°	75.7°	59.5°	31.5°	30.8°	61.8°	7.2°

[a]1 and 2 denote the values for the two symmetry inequivalent molecules in the unit cell. The value of α_{av} is obtained employing the averaging described in the main text. The twist angle is defined such that it is zero when the tilt occurs perpendicular to the molecular plane.[72]
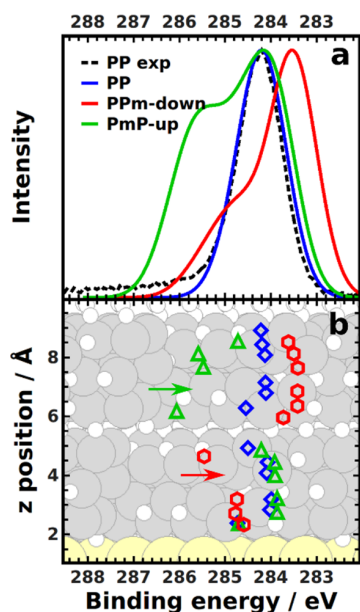
Figure 10. (Top) DFT calculated XP spectra for the PP (blue), the PPm-down (red), and the PmP-up (green) SAMs. The spectra have been aligned to the experimental spectrum of PP and a damping consistent with a primary photon energy of 580 eV was assumed (for details see main text and the Supporting Information). (Bottom) Atom-resolved, (shifted) core-level binding energies of individual C atoms in the PP (blue diamonds), PPm-down (red hexagons), and PmP-up (green triangles) SAMs. The energies are averaged over equivalent atoms in the two molecules contained in the unit cell. The PP SAM shown in the background serves to identify the z-position (vertical axis) of individual C atoms. The z-axis is perpendicular to the substrate with its origin corresponding to the position of the image plane (i.e., 0.9 Å above the average z-position of the topmost Au layer, see the Supporting Information). The average positions of the N atoms in the PPm-down and PmP-up SAMs are indicated by red and green arrows, respectively. For both spectra and energies of the individual levels, screening effects by the substrate according to the electrostatic model described in the Supporting Information have been considered.

for smaller primary photon energies (350 eV) in the experiments, a third feature appears between the two peaks of the 580 eV spectra (see Figure 4c,d), which is also seen in the corresponding simulations, albeit with a reduced relative intensity (see the simulated spectrum of PmP-up/Au for 350 eV contained in the Supporting Information, Figure S14).

A distinct advantage of the calculated XP spectra is that it is straightforward to decompose them into contributions from individual C atoms. This is done based on the bottom panel of Figure 10, which shows the core level energies for all C atoms of the three systems considered here. For the case of PP/Au, the core-levels of most of the C atoms are located at comparable energies. The small, continuous shift to higher BEs by increasing the distance to the substrate is attributed to differences in screening. Only the positions of the C atom bonded to the thiolate and of the two C atoms forming the bridge between the two rings are somewhat shifted to even higher BEs. This can be attributed to their different chemical environments (chemical shifts), and especially for the lowest C atom, also to particularly large screening effects by the substrate.

The situation becomes much more complex for the pyrimidine containing systems. There, one encounters a superposition of strong chemical shifts (due to C atoms bonded to the N atoms)[98] and electrostatic shifts due to the pyrimidine dipoles. The origin of the latter shifts are so-called collective electrostatic effects caused by a parallel alignment of dipoles.[99−101] This results in a sharp step in the electrostatic energy at the position of the dipole layer, which shifts the core-level energies relative to the Fermi level for all atoms further away from the substrate than that dipole layer. As the Fermi level of the substrate serves as the reference energy for the XPS experiment, the consequence is a change in the respective core-level binding energies.[70] Notably, this shift is not related to any change in the local charge density around the said atoms, as it is observed for chemically identical species solely separated by a dipole layer;[16,17] it is also not related to the evanescent field of the dipole assembly as the decay length of that field is extremely short.[99]

For PPm-down/Au, such electrostatic shifts caused by the pyrimidine dipoles result in a reduction of the BEs of the C atoms of the upper ring compared to the PP/Au reference system despite the identical atomic charges on the outermost rings found for both systems (see the Supporting Information). In contrast, the BEs of the C atoms in the bottom pyrimidine ring are increased compared to PP/Au (with the exception of the atom bonded to S). This is due to chemical shifts, as all these atoms are bonded to electronegative N atoms. These chemical shifts reach a maximum for the topmost C atom of that ring, which is bonded to two N atoms. Consequently, the low-lying C atoms are responsible for the high-BE tail in the spectra, which is consistent with the experimental observation that the intensity of that tail decreases for primary photon energies of 350 eV.

For PmP-up/Au, the core-level energies of the bottom ring are hardly shifted relative to the PP/Au reference, as these C atoms do not experience any extra electrostatic shifts (the only dipoles between them and the metal are those associated with the dipoles of the thiolate groups present in all monolayers). Additionally, compared to PPm-down/Au, none of the respective C atoms experiences a chemical shift. Conversely, the core-levels of the C atoms in the pyrimidine ring are strongly shifted to higher BEs. This can be understood as a superposition of a chemical shift (due to the bonding to the N atoms) and an electrostatic shift (originating from the pyrimidine dipole). As both shifts go in the same direction for PmP-up/Au, the associated BEs are particularly large, which explains the pronounced high-BE peak observed for this system both in the experiments and in the simulations. Interestingly, the core-level of the topmost C atom in the PmP-up SAM is found at a smaller BE, as it is not directly bonded to the nitrogen atoms. Therefore, we hold this atom responsible for the peak at 284.6 eV visible in the experimental 350 eV spectrum (see Figure 4c; where the features of the lower-lying C atoms are attenuated due to the very small escape depth of the photoelectrons).

The above-described different combinations of chemical and electrostatic shifts in PmP-up/Au and PPm-down/Au explain both the different lineshapes of the XP spectra and the different binding energies of the main peak.

The above-discussed electrostatic shifts are also responsible for the different core-level BEs of the N atoms. Qualitatively consistent with the experiments, we calculated the N 1s energy of PPm-down/Au to be 0.5 eV smaller than for PmP-up/Au.

57

As the chemical environments of the N atoms are essentially identical in both systems, the reason for the shift is that the N atoms are located on different "sides" of the primary components of the differently oriented pyrimidine dipoles.

3.11. Electronic Properties of the SAMs: Measured and Calculated SAM-Induced Work Function Changes.
The parallel alignment of the pyrimidine dipoles also causes a shift in the sample work function. This is shown for the PmP-up, PPm-down, and PP SAMs in Figure 11a,b for films grown
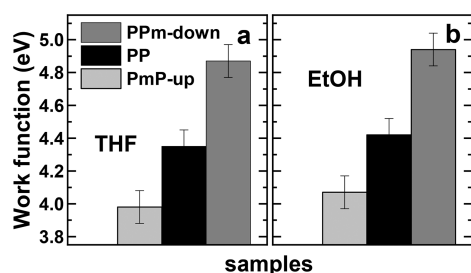
Figure 11. Work function values for the PmP-up, PPm-down, and PP SAMs prepared from THF (a) and ethanol (b) measured with a Kelvin probe on high-quality, commercial Au substrates (see Section 2). The gray scale code is given in the panels.

from THF and ethanol, respectively. Significantly, the THF values are only slightly smaller than the ethanol ones. This suggests that the ability of the PmP-up and PPm-down films to manipulate charge carrier injection barriers in organic electronics assemblies does not depend significantly on the solvent applied for their preparation. Also, the values presented here for SAMs prepared from ethanol on high-quality, commercial gold substrates (see Section 2) are very close to those for "technical gold substrates" (a RMS value of 1.8 nm over a scan area of $4 \times 4 \ \mu m^2$) treated analogous to electrodes in patterned device structures (see ref 39 for details); viz. the value for PmP-up/Au is identical and that for PPm-down/Au is only slightly higher (by ∼0.1 eV). This means that the dipole engineering by the PmP-up and PPm-down SAMs is sufficiently robust with respect to the character of the substrate.

In line with the orientation of the dipole moment of the embedded pyrimidine group, the work functions of PPm-down/Au and PmP-up/Au are higher (by +0.52 eV) and lower (by −0.37 eV), respectively, than for PP/Au (THF preparation). The measured WF shifts are very close to those observed for the previously reported terphenylmethane-thiol-based SAMs, also containing a single pyrimidine unit per molecule (see Figure S1 in the Supporting Information), viz. +0.56 eV and −0.42 eV.[19] The slightly larger shifts in the latter systems can in part be explained by a somewhat smaller molecular inclination, which results in a larger projection of the dipole moment onto the surface normal, which defines the SAM-induced change of the work function.

The work function difference between PPm-down/Au and PmP-up/Au is ∼0.9 eV, where we expect that the work function can be adjusted continuously within this range by mixing PPm-down and PmP-up molecules in a single SAM, as it has been demonstrated for a variety of different mixed SAMs[7,23,102−104] including systems with embedded dipoles.[20−22]

The experimental trend is confirmed by the simulations with a decrease of the work function for PmP-up/Au and an increase for PPm-down/Au (compared to the reference PP SAM). The absolute magnitude of the effect (±0.65 eV) is, however, overestimated, which is in line with what we have observed for a variety of other systems, especially other pyrimidine-containing compounds.[19] This is in part a consequence of the simulations assuming a densely packed periodic structure, with the entire film in a $(3 \times \sqrt{3})rect$ arrangement. Such a model does not account for disordered regions like grain boundaries[19] or the patches of lower-coverage domains with molecules arranged in a (2×2) pattern, as recorded in the STM measurements (see Section 3.5). Additionally, we observe that both the dipole moment of the pyrimidine unit and the bond-dipole associated with the thiolate docking group depend on the used methodology (i.e., there is an inevitable systematic error associated with using a specific functional like PBE; see the Supporting Information for more details). Interestingly, the calculated work function changes for PPm-down/Au and PmP-up/Au relative to PP/Au are identical in the simulations, while they somewhat differ in the experiments. This could again be a consequence of disorder within the experimentally studied SAM, as discussed in the Supporting Information.

3.12. Electrical Conductance.
Besides the changes of the electrode work function, also the electrical conductance of the monolayer is a crucial parameter for the application of the SAMs as interfacial layers between the electrode and the active layer in organic electronic devices. Semilogarithmic current–density versus voltage plots for Au/SAM//EGaIn junctions with the PmP-up, PPm-down, and PP (reference) SAMs are presented in Figure 12; they agree well with the analogous data
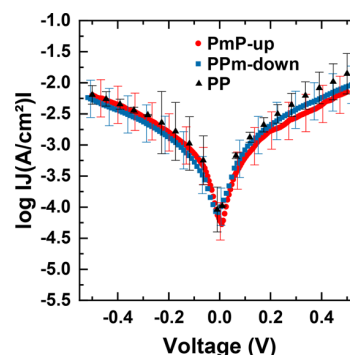
Figure 12. Semilogarithmic current-density versus voltage plots for Au/SAM//EGaIn junctions with the PmP-up (red circles), PPm-down (blue squares), and PP (black triangles) SAMs.

measured within the previous device study.[39] The currents are higher by about 1 order of magnitude than those observed for the analogous terphenylmethanethiol-based molecules with embedded pyrimidine group (see Figure S1 in the Supporting Information).[39,105] This indicates superior electric transport properties of the PmP-up and PPm-down monolayers, making these SAMs particularly promising for applications in organic electronics and photovoltaic devices. Such a stronger coupling in the absence of a methylene spacer has been found in various experiments[106,107] and is also consistent with the massively broadened transmission functions calculated for thiol-bonded vs methylthiol-bonded SAMs.[108,109]

An interesting side aspect are quite similar current values for the SAMs with opposite directions of the dipole moment. This is consistent with the observation for terphenylmethanethiol-
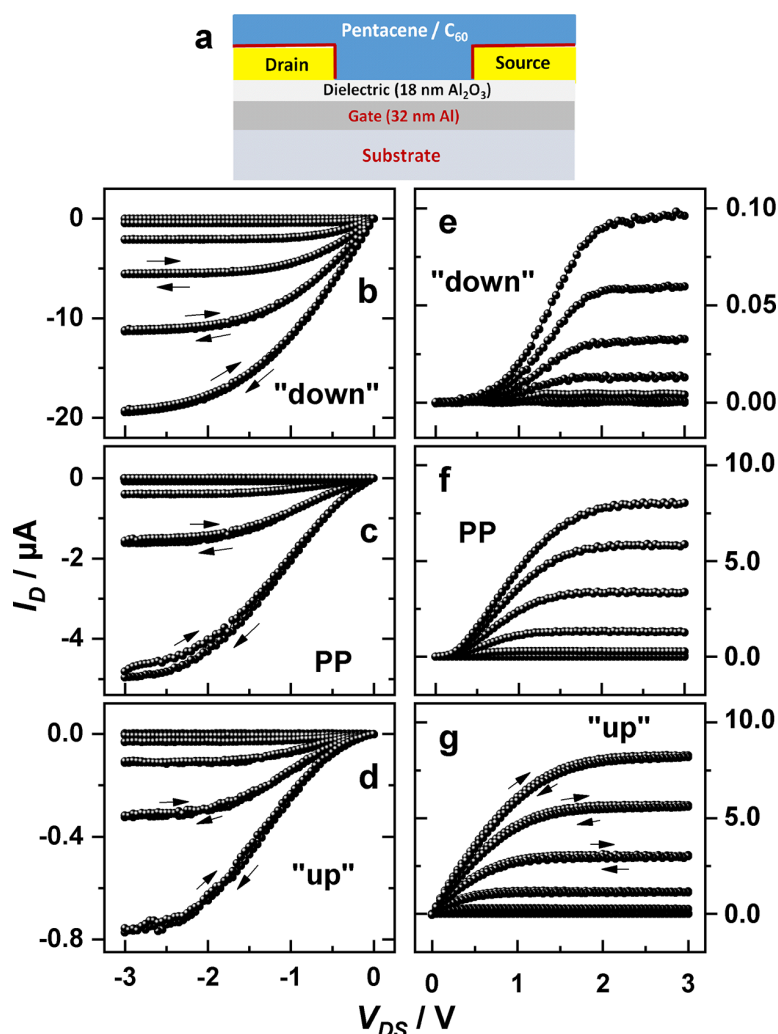
Figure 13. Schematic of the bottom gate, bottom contact OTFTs (a) featuring SAM-modified source and drain gold electrodes (50 nm) and either pentacene or C_{60} as OSC. The SAMs are indicated by the red line. The description of the fabrication process and the technical details can be found elsewhere.[39] Panels b−d show typical output characteristics of p-type pentacene OTFTs with the electrodes modified by the PPm-down (b, "down"), PP (c), and PmP-up (d, "up") SAMs; panels e−g contain typical output characteristics of n-type C_{60} OTFTs with the electrodes modified by the PPm-down (e, "down"), PP (f), and PmP-up (g, "up") SAMs. The curves were acquired at several different V_{GS} values varied in 0.5 steps from 0.5 to −2.5 V (b), from 1 to −2 V (c), from 1.2 to −1.8 V (d), from 3.4 to 6.4 V (e), and from 2.1 to 5.1 V (f,g). The different V_{GS} ranges for the different OTFTs are a consequence of the different onset voltages (V_{on}) observed in the different devices. In this way, the values of $V_{GS}-V_{on}$ (defining the output current of OTFTs) are varied similarly for either p-type or n-type devices. Accordingly, the output characteristics become directly comparable. The OTFTs were fabricated either on glass (p-type) or polycarbonate plastic film (n-type). Adapted from ref 39.

based SAMs containing central pyrimidine units at varying orientation, where a careful statistical analysis of the current− voltage curves yielded a rectification of only ∼1.2.[110] Also, alkyl SAMs including polar groups either into the backbones or as tail groups did not yield significant rectification ratios.[111] What is somewhat surprising for the present systems is that increasing the coupling to the Au electrode by skipping the methylene linker does not have a distinct impact on rectification, considering that asymmetries of the coupling to the two electrodes have been predicted to yield more sizable rectification ratios in related systems.[112]

3.13. Applications in Organic Thin Film Transistors. Because of their structural and electrostatic properties, the PmP-up and PPm-down SAMs can be used in organic electronics and photovoltaics, providing energy level adjust- ment at the interfaces between the electrodes and OSC or

between the electrodes and buffer layers. The application of these monolayers in organic thin film transistors (OTFTs) and related electronic circuits on solid (glass) and flexible (polycarbonate plastic film) substrates is described in detail in our recent dedicated study.[39] To illustrate the potential of the PmP-up and PPm-down SAMs, Figure 13 shows the output curves of both p-type (pentacene as OSC) and n-type (C_{60} as OSC) OTFTs featuring SAM-modified Au source and drain electrodes. The curves in Figure 13 show a clear effect of the embedded dipoles. For pentacene-based devices, the currents increase by a factor of ∼25 when employing PPm- down SAMs compared to the PmP-up case, while the trend is reversed for the C_{60} devices with the ratio here even exceeding a factor of 60. This can be associated with the contact resistance changing by more than 2 orders of magnitude[39] for electrodes modified with the two SAMs. Generally, PPm-down

Table 4. Basic Parameters of the PP, PmP-up, and PPm-down SAMs Derived from the Experimental Data and Theoretical Simulations

monolayer	effective thickness [nm]		packing density [molecules cm^{-2}]	molecular tilt angle [°]				twist angle [°]
method	XPS	ellipsometry	XPS	ellipsometry	NEXAFS	IR	theory	theory
PP	1.09 ± 0.05	1.11 ± 0.02	4.6 × 10^{14}	26 ± 10	19 ± 3[b]	n.d.	27.1/24.7	56.1/13.1.
PmP-up	1.0 ± 0.05	1.10 ± 0.03	4.5 × 10^{14}	26 ± 10	29 ± 3[a]	24 ± 11	29.6/25.6	60.2/7.7
PPm-down	0.93 ± 0.05	0.93 ± 0.02	4.5 × 10^{14}	41 ± 10	31.5 ± 3[a]	14 ± 10	31.5/30.8	61.8/7.2

[a]The NEXAFS-derived tilt angles for PmP-up/Au and PPm-down/Au were calculated from the average values given in Table 2, assuming the twist angles from Table 3 and the same tilt angles of both nonequivalent molecules in the unit cell. For the simulations, the tilt and twist angles for both nonequivalent molecules in the unit cell are given. [b]The NEXAFS-derived tilt angle for PP/Au was calculated assuming a twist angle of 32° taken from the bulk crystal data.[79,113]

favors hole and PmP-up favors electron injection. This is fully consistent with the changes in the respective injection barriers[39] arising from the work function modifications described in Section 3.11.

3.14. Summary of the Results. The basic structural parameters of the PP, PPm-down, and PmP-up monolayers derived by ellipsometry, XPS, STM, IR, and NEXAFS spectroscopy experiments as well as by the quantum mechanical simulations are compiled in Table 4. The values obtained with the different techniques correlate well with each other, even though there is a certain scattering of individual parameters. The effective thicknesses and packing densities of the PP, PPm-down, and PmP-up SAMs are similar, suggesting similar molecular packing. The packing density values correlate well with the packing density of the ($\sqrt{3} \times \sqrt{3}$)R30° structure, which was indeed directly observed by STM (Figure 3), even though the imaging was not easy and a certain polymorphism was recorded. The molecular conformation in the PPm-down and PmP-up monolayers is essentially planar, as suggested by the bulk crystallography (Figures S9 and S11 in the Supporting Information) and the NEXAFS spectroscopy data and additionally confirmed by the DFT simulations (Figure 9). The simulations favor a herringbone molecular arrangement (Figure 9), which requires a ($3 \times \sqrt{3}$)$rect$ unit cell, which however has the same packing density and is compatible with the ($\sqrt{3} \times \sqrt{3}$)R30° structure. The simulations also shed light on the molecular orientation in the PPm-down and PmP-up SAMs (Table 3) with a very good agreement with the results of the NEXAFS spectroscopy (Table 2) and with the IR-derived value for PmP-up/Au. The particularly small tilt calculated from the IR data for PPm-down/Au appears less realistic and is presumably related to a low intensity of specific vibrational modes used for the evaluation (see Section 3.7). Insights into the electronic structure of the SAMs could be gained from comparing calculated and measured XPS data (Figures 4 and 10) revealing a superposition of electrostatic and chemical shifts of the core-level binding energies. We also observed a good correlation between the KP data (Figure 11) and calculated electrostatic properties of the PPm-down and PmP-up SAMs. The electric conductance of these monolayers is found to be rather high (Figure 12), which is a sizable advantage for their applications in organic electronics and photovoltaics. The potential of the PmP-up and PPm-down SAMs in organic electronics is illustrated by representative experimental data for the bottom gate, bottom contact OTFTs, featuring SAM-modified source and drain gold electrodes (Figure 13).

4. CONCLUSIONS

On the basis of the concept of the embedded dipoles in molecular self-assembly on solid substrates, we designed and synthesized optimal molecules for controlling the energy level alignment at interfaces between electrodes and organic semiconductor layers. The molecules, PmP-up and PPm-down, feature the thiol docking group and a short heteroaromatic backbone consisting of a nonpolar phenyl ring and a polar pyrimidine group. The latter is "embedded" in two opposite orientations in a way that its nitrogen atoms are buried with respect to the SAM−substrate and SAM−ambient interfaces. This decouples these interfaces from the dipole engineering. The resulting dipolar systems have significant inherent flexibility and are relatively easy to modify as the key functionality of the SAM is maintained when changing, for example, the docking group (now thiol to bind to noble metals) or when adjusting the tail-group polarity and reactivity (now inert C—H).

In view of the popularity of gold as substrate when studying SAMs and as electrode material in organic electronics, we fabricated and characterized in detail PmP-up, PPm-down, as well as reference nonpolar PP monolayers on Au(111) substrates, putting particular emphasis on the electronic properties. The results of a variety of complementary spectroscopic and microscopic techniques consistently suggest the formation of densely packed and well-defined SAMs, with all molecules bonded to the substrate via the thiolate docking group in an almost upright geometry. Packing density, molecular orientation, structure, and wetting properties of these SAMs were found to be nearly independent of their electrostatic properties (with only one exception; see Section 3.4). The latter correlate precisely with the molecular architecture and the orientation of the embedded dipolar group. More insights into the electrostatic properties of the SAMs can be obtained by comparing XP spectra with calculated core-level binding-energies, which reveals pronounced shifts due to collective electrostatic effects on top of chemical shifts. Concomitantly, depending on the pyrimidine orientation, the SAMs studied here can change the Au work function by ~0.9 eV. Moreover, currents through the studied SAMs measured in EGaIn junctions are relatively high. These aspects place the PmP-up and PPm-down SAMs as ideal systems for model studies in the context of interfacial dipole engineering but also as highly suitable functional blocks for device applications. The latter is illustrated by realizing highly promising p- and n-type transistors using Au as electrode material, while optimizing the level alignment through chemisorbing SAMs containing suitably oriented pyrimidine groups.

■ ASSOCIATED CONTENT

ⓢ Supporting Information

The Supporting Information is available free of charge on the ACS Publications website at DOI: 10.1021/acs.jpcc.8b09440.

Crystallographic data (PDF)

Exact description of the procedures for the synthesis of the SAM precursors; additional spectroscopic data; computational details (PDF)

■ AUTHOR INFORMATION

Corresponding Authors

*E-mail: egbert.zojer@tugraz.at.
*E-mail: aterfort@chemie.uni-frankfurt.de.
*E-mail: Michael.Zharnikov@urz.uni-heidelberg.de.

ORCID ⦿

Egbert Zojer: 0000-0002-6502-1721
Andreas Terfort: 0000-0003-2369-5151
Michael Zharnikov: 0000-0002-3708-7571

Author Contributions

[1]M.G., E.S., and G.N. have provided equivalent contributions.

Notes

The authors declare no competing financial interest.

■ REFERENCES

(1) Koch, N. Energy Levels at Interfaces between Metals and Conjugated Organic Molecules. *J. Phys.: Condens. Matter* **2008**, *20*, 184008.

(2) Liu, C.; Xu, Y.; Noh, Y.-Y. Contact Engineering in Organic Field-Effect Transistors. *Mater. Today* **2015**, *18*, 79−96.

(3) Casalini, S.; Bortolotti, C. A.; Leonardi, F.; Biscarini, F. Self-Assembled Monolayers in Organic Electronics. *Chem. Soc. Rev.* **2017**, *46*, 40−71.

(4) Kymissis, I.; Dimitrakopoulos, C. D.; Purushothaman, S. High-Performance Bottom Electrode Organic Thin-Film Transistors. *IEEE Trans. Electron Devices* **2001**, *48*, 1060−1064.

(5) Bock, C.; Pham, D. V.; Kunze, U.; Käfer, D.; Witte, G.; Wöll, Ch. Improved Morphology and Charge Carrier Injection in Pentacene Field-Effect Transistors with Thiol-Treated Electrodes. *J. Appl. Phys.* **2006**, *100*, 114517.

(6) Acton, O.; Dubey, M.; Weidner, T.; O'Malley, K. M.; Kim, T.-W.; Ting, G. G.; Hutchins, D.; Baio, J. E.; Lovejoy, T. C.; Gage, A. H.; et al. Simultaneous Modification of Bottom-Contact Electrode and Dielectric Surfaces for Organic Thin-Film Transistors Through Single-Component Spin-Cast Monolayers. *Adv. Funct. Mater.* **2011**, *21*, 1476−1488.

(7) Kim, J.; Rim, Y. S.; Liu, Y.; Serino, A. C.; Thomas, J. C.; Chen, H.; Yang, Y.; Weiss, P. S. Interface Control in Organic Electronics Using Mixed Monolayers of Carboranethiol Isomers. *Nano Lett.* **2014**, *14*, 2946−2951.

(8) Ulman, A. Formation and Structure of Self-Assembled Monolayers. *Chem. Rev.* **1996**, *96*, 1533−1554.

(9) Love, J. C.; Estroff, L. A.; Kriebel, J. K.; Nuzzo, R. G.; Whitesides, G. M. Self-Assembled Monolayers of Thiolates on Metals as a Form of Nanotechnology. *Chem. Rev.* **2005**, *105*, 1103−1169.

(10) De Boer, B.; Hadipour, A.; Mandoc, M. M.; Van Woudenbergh, T.; Blom, P. W. M. Tuning of Metal Work Functions with Self-Assembled Monolayers. *Adv. Mater.* **2005**, *17*, 621−625.

(11) Hamadani, B. H.; Corley, D. A.; Ciszek, J. W.; Tour, J. M.; Natelson, D. Controlling Charge Injection in Organic Field-Effect Transistors Using Self-Assembled Monolayers. *Nano Lett.* **2006**, *6*, 1303−1306.

(12) Heimel, G.; Romaner, L.; Brédas, J. L.; Zojer, E. Interface Energetics and Level Alignment at Covalent Metal-Molecule Junctions: π-Conjugated Thiols on Gold. *Phys. Rev. Lett.* **2006**, *96*, 196806.

(13) Heimel, G.; Romaner, L.; Zojer, E.; Bredas, J.-L. The Interface Energetics of Self-Assembled Monolayers on Metals. *Acc. Chem. Res.* **2008**, *41*, 721−729.

(14) Lange, I.; Reiter, S.; Pätzel, M.; Zykov, A.; Nefedov, A.; Hildebrandt, J.; Hecht, S.; Kowarik, S.; Wöll, C.; Heimel, G.; et al. Tuning the Work Function of Polar Zinc Oxide Surfaces using Modified Phosphonic Acid Self-Assembled Monolayers. *Adv. Funct. Mater.* **2014**, *24*, 7014−7024.

(15) Lee, H. Ju; Jamison, A. C.; Lee, T. R. Surface Dipoles: A Growing Body of Evidence Supports Their Impact and Importance. *Acc. Chem. Res.* **2015**, *48*, 3007−3015.

(16) Cabarcos, O. M.; Shaporenko, A.; Weidner, T.; Uppili, S.; Dake, L. S.; Zharnikov, M.; Allara, D. L. Physical and Electronic Structure Effects of Embedded Dipoles in Self-Assembled Monolayers: Characterization of Mid-Chain Ester Functionalized Alkanethiols on Au{111}. *J. Phys. Chem. C* **2008**, *112*, 10842−10854.

(17) Cabarcos, O. M.; Schuster, S.; Hehn, I.; Zhang, P. P.; Maitani, M. M.; Sullivan, N.; Giguère, J.-B.; Morin, J.-F.; Weiss, P. S.; Zojer, E.; et al. Effects of Embedded Dipole Layers on Electrostatic Properties of Alkanethiolate Self-Assembled Monolayers. *J. Phys. Chem. C* **2017**, *121*, 15815−15830.

(18) Bruce, R. C.; You, L.; Förster, A.; Pookpanratana, S.; Pomerenk, O.; Lee, H. Ju; Marquez, M. D.; Ghanbaripour, R.; Zenasni, O.; Lee, T. R.; Hacker, C. A. Contrasting Transport and Electrostatic Properties of Selectively Fluorinated Alkanethiol Monolayers with Embedded Dipoles. *J. Phys. Chem. C* **2018**, *122*, 4881−4890.

(19) Abu-Husein, T.; Schuster, S.; Egger, D. A.; Kind, M.; Santowski, T.; Wiesner, A.; Chiechi, R.; Zojer, E.; Terfort, A.; Zharnikov, M. The Effects of Embedded Dipoles in Aromatic Self-Assembled Monolayers. *Adv. Funct. Mater.* **2015**, *25*, 3943−3957.

(20) Hehn, I.; Schuster, S.; Wächter, T.; Abu-Husein, T.; Terfort, A.; Zharnikov, M.; Zojer, E. Employing X-ray Photoelectron Spectroscopy for Determining Layer Homogeneity in Mixed Polar Self-Assembled Monolayers. *J. Phys. Chem. Lett.* **2016**, *7*, 2994−3000.

(21) Sauter, E.; Gilbert, C.-O.; Boismenu-Lavoie, J.; Morin, J.-F.; Zharnikov, M. Mixed Aliphatic Self-Assembled Monolayers with Embedded Polar Group. *J. Phys. Chem. C* **2017**, *121*, 23017−23024.

(22) Sauter, E.; Gilbert, C.-O.; Morin, J.-F.; Terfort, A.; Zharnikov, M. Mixed Monomolecular Films with Embedded Dipolar Groups on Ag(111). *J. Phys. Chem. C* **2018**, *122*, 19514−19523.

(23) Wu, K.-Y.; Yu, S.-Y.; Tao, Y.-T. Continuous Modulation of Electrode Work Function with Mixed Self-Assembled Monolayers and Its Effect in Charge Injection. *Langmuir* **2009**, *25*, 6232−6238.

(24) Venkataraman, N. V.; Zürcher, S.; Rossi, A.; Lee, S.; Naujoks, N.; Spencer, N. D. Spatial Tuning of the Metal Work Function by Means of Alkanethiol and Fluorinated Alkanethiol Gradients. *J. Phys. Chem. C* **2009**, *113*, 5620−5628.

(25) Holmlin, R. E.; Haag, R.; Chabinyc, M. L.; Ismagilov, R. F.; Cohen, A. E.; Terfort, A.; Rampi, M. A.; Whitesides, G. M. Electron Transport through Thin Organic Films in Metal-Insulator-Metal

Junctions Based on Self-Assembled Monolayers. *J. Am. Chem. Soc.* **2001**, *123*, 5075–5085.

(26) Adams, D. M.; Brus, L.; Chidsey, C. E. D.; Creager, S.; Creutz, C.; Kagan, C. R.; Kamat, P. V.; Lieberman, M.; Lindsay, S.; Marcus, R. A.; et al. Charge Transfer on the Nanoscale: Current Status. *J. Phys. Chem. B* **2003**, *107*, 6668–6697.

(27) Branchi, B.; Simeone, F. C.; Rampi, M. A. Active and Non-Active Large-Area Metal–Molecules–Metal Junctions. In Unimolecular and Supramolecular Electronics II; Metzger, R. M., Ed.; *Top Curr. Chem. 313*; Springer: Heidelberg, 2012; pp 85–120.

(28) Yang, G.; Liu, G. New Insights for Self-Assembled Monolayers of Organothiols on Au(111) Revealed by Scanning Tunneling Microscopy. *J. Phys. Chem. B* **2003**, *107*, 8746–8759.

(29) Shaporenko, A.; Brunnbauer, M.; Terfort, A.; Grunze, M.; Zharnikov, M. Structural Forces in Self-Assembled Monolayers: Terphenyl-Substituted Alkanethiols on Noble Metal Substrates. *J. Phys. Chem. B* **2004**, *108*, 14462–14469.

(30) Azzam, W.; Bashir, A.; Terfort, A.; Strunskus, T.; Wöll, Ch. Combined STM and FTIR Characterization of Terphenylalkanethiol Monolayers on Au(111): Effect of Alkyl Chain Length and Deposition Temperature. *Langmuir* **2006**, *22*, 3647–3655.

(31) Simmons, J. G. Generalized Formula for the Electric Tunnel Effect Between Similar Electrodes Separated by a Thin Insulating Film. *J. Appl. Phys.* **1963**, *34*, 1793–1803.

(32) Heimel, G.; Romaner, L.; Bredas, J.-L.; Zojer, E. Odd-Even Effects in Self-Assembled Monolayers of ω-(Biphenyl-4-yl)-alkanethiols: A First-Principles Study. *Langmuir* **2008**, *24*, 474–482.

(33) Bowers, C. M.; Rappoport, D.; Baghbanzadeh, M.; Simeone, F. C.; Liao, K.-C.; Semenov, S. N.; Żaba, T.; Cyganik, P.; Aspuru-Guzik, A.; Whitesides, G. M. Tunneling across SAMs Containing Oligophenyl Groups. *J. Phys. Chem. C* **2016**, *120*, 11331–11337.

(34) Wächter, T.; Weinhardt, L.; Terfort, A.; Zharnikov, M. Pyridine as a Resonantly Addressable Group to Study Electron Transfer Dynamics in Self-Assembled Monolayers. *J. Phys. Chem. C* **2018**, *122*, 12534–12548.

(35) Blackman, G. L.; Brown, R. D.; Burden, F. R. The Microwave Spectrum, Dipole Moment, and Nuclear Quadrupole Coupling Constants of Pyrimidine. *J. Mol. Spectrosc.* **1970**, *35*, 444–454.

(36) Pergolese, B.; Muniz-Miranda, M.; Bigotto, A. SERS Study of the Adsorption of 2-mercaptobenzoxazole on Gold Colloidal Nanoparticles. *J. Mol. Struct.* **2009**, *924–926*, 559–561.

(37) Cui, B.; Chen, T.; Wang, D.; Wan, L. J. In situ STM Evidence for the Adsorption Geometry of Three N-heteroaromatic Thiols on Au(111). *Langmuir* **2011**, *27*, 7614–7619.

(38) Partes, C.; Yildirim, C.; Schuster, S.; Kind, M.; Zharnikov, M.; Terfort, A.; et al. Self-Assembled Monolayers of Pseudo-C2v-Symmetric, Low-Band Gap Areneoxazolethiolates on Gold Surfaces. *Langmuir* **2016**, *32*, 11474–11484.

(39) Petritz, A.; Krammer, M.; Sauter, E.; Gärtner, M.; Nascimbeni, G.; Schrode, B.; Fian, A.; Gold, H.; Cojocaru, A.; Karner-Petritz, E.; et al. Embedded Dipole Self-Assembled Monolayers for Contact Resistance Tuning in p- and n-Type Organic Thin Film Transistors and Flexible Electronic Circuits. *Adv. Funct. Mater.* **2018**, *28*, 1804462.

(40) Kang, J. F.; Ulman, A.; Liao, S.; Jordan, R.; Yang, G. H.; Liu, G. Y. Self-Assembled Rigid Monolayers of 4′-substituted-4-mercaptobiphenyls on Gold and Silver Surfaces. *Langmuir* **2001**, *17*, 95–106.

(41) X-AREA: Diffractometer Control Program System; Stoe & Cie: Darmstadt, Germany, 2002.

(42) Sheldrick, G. M. A Short History of SHELX. *Acta Crystallogr., Sect. A: Found. Crystallogr.* **2008**, *64*, 112–122.

(43) Chesneau, F.; Zhao, J.; Shen, C.; Buck, M.; Zharnikov, M. Adsorption of Long-Chain Alkanethiols on Au(111) - A Look from the Substrate by High Resolution X-Ray Photoelectron Spectroscopy. *J. Phys. Chem. C* **2010**, *114*, 7112–7119.

(44) Frey, S.; Stadler, V.; Heister, K.; Eck, W.; Zharnikov, M.; Grunze, M.; Zeysing, B.; Terfort, A. Structure of Thioaromatic Self-Assembled Monolayers on Gold and Silver. *Langmuir* **2001**, *17*, 2408–2415.

(45) Heister, K.; Zharnikov, M.; Grunze, M.; Johansson, L. S. O.; Ulman, A. Characterization of X-Ray Induced Damage In Alkanethiolate Monolayers by High-Resolution Photoelectron Spectroscopy. *Langmuir* **2001**, *17*, 8–11.

(46) Zharnikov, M. High-Resolution X-Ray Photoelectron Spectroscopy in Studies of Self-Assembled Organic Monolayer. *J. Electron Spectrosc. Relat. Phenom.* **2010**, *178–179*, 380–393.

(47) Sauter, E.; Yildirim, C.; Terfort, A.; Zharnikov, M. Adjustment of the Work Function of Pyridine and Pyrimidine Substituted Aromatic Self-Assembled Monolayers by Electron Irradiation. *J. Phys. Chem. C* **2017**, *121*, 12834–12841.

(48) Raiber, K.; Terfort, A.; Benndorf, C.; Krings, N.; Strehblow, H. H. Removal of Self-Assembled Monolayers of Alkanethiolates on Gold by Plasma Cleaning. *Surf. Sci.* **2005**, *595*, 56–63.

(49) Frisch, M. J.; Schlegel, H. B.; Scuseria, G. E.; Robb, M. A.; Cheeseman, J. R.; Scalmani, G.; Barone, V.; Mennucci, B.; Petersson, G. A.; Nakatsuji, H.; et al. *Gaussian 09*, Revision A. 02; Gaussian: Wallingford, CT, 2009.

(50) Perdew, J. Density-Functional Approximation for the Correlation Energy of the Inhomogeneous Electron Gas. *Phys. Rev. B: Condens. Matter Mater. Phys.* **1986**, *33*, 8822–8824.

(51) Becke, A. D. Density-Functional Exchange-Energy Approximation with Correct Asymptotic Behavior. *Phys. Rev. A: At., Mol., Opt. Phys.* **1988**, *38*, 3098–3099.

(52) Weigend, F.; Ahlrichs, R. Balanced Basis Sets of Split Valence, Triple Zeta Valence and Quadruple Zeta Valence Quality for H to Rn: Design and Assessment of Accuracy. *Phys. Chem. Chem. Phys.* **2005**, *7*, 3297–3305.

(53) Nefedov, A.; Wöll, C. *Advanced Applications of NEXAFS Spectroscopy for Functionalized Surfaces, in Surface Science Techniques*; Bracco, G., Holst, B., Eds.; Springer Series in Surface Science; Springer-Verlag, Berlin, 2013; Vol. *51*, pp 277–306.

(54) Moulder, J. F.; Stickle, W. E.; Sobol, P. E.; Bomben, K. D. *Handbook of X-ray Photoelectron Spectroscopy*, Chastian, J., Ed.; Perkin-Elmer Corp.: Eden Prairie, MN, 1992.

(55) Thome, J.; Himmelhaus, M.; Zharnikov, M.; Grunze, M. Increased Lateral Density in Alkanethiolate Films on Gold by Mercury Adsorption. *Langmuir* **1998**, *14*, 7435–7449.

(56) Ratner, M.; Castner, D. *Electron Spectroscopy for Chemical Analysis, in Surface Analysis - The principal techniques*; Vickerman, J., Ed.; Wiley: Chichester, 1997.

(57) Lamont, C. L. A.; Wilkes, J. Attenuation Length of Electrons in Self-Assembled Monolayers of n-Alkanethiols on Gold. *Langmuir* **1999**, *15*, 2037–2042.

(58) Leung, T. Y. B.; Schwartz, P.; Scoles, G.; Schreiber, F.; Ulman, A. Structure and Growth of 4-Methyl-4′-Mercaptobiphenyl Monolayers on Au(111): A Surface Diffraction Study. *Surf. Sci.* **2000**, *458*, 34–52.

(59) Azzam, W.; Fuxen, C.; Birkner, A.; Rong, H.-T.; Buck, M.; Wöll, C. Coexistence of Different Structural Phases in Thioaromatic Monolayers on Au(111). *Langmuir* **2003**, *19*, 4958–4968.

(60) Schreiber, F. Self-Assembled Monolayers: From 'Simple' Model Systems to Biofunctionalized Interfaces. *J. Phys.: Condens. Matter* **2004**, *16*, R881–R900.

(61) Stöhr, J. *NEXAFS Spectroscopy; Springer series in surface sciences*; Springer: Berlin, 2003.

(62) Batson, P. E. Carbon-1s Near-Edge-Absorption Fine-Structure in Graphite. *Phys. Rev. B: Condens. Matter Mater. Phys.* **1993**, *48*, 2608–2610.

(63) Ford, W. E.; Gao, D.; Knorr, N.; Wirtz, R.; Scholz, F.; Karipidou, Z.; Ogasawara, K.; Rosselli, S.; Rodin, V.; Nelles, G.; et al. Organic Dipole Layers for Ultralow Work Function Electrodes. *ACS Nano* **2014**, *8*, 9173–9180.

(64) Querebillo, C.; Terfort, A.; Allara, D.; Zharnikov, M. Static Conductance of Nitrile-Substituted Oligophenylene and Oligo-(phenylene ethynylene) Self-Assembled Monolayers Studied by Mercury-Drop Method. *J. Phys. Chem. C* **2013**, *117*, 25556–25561.

(65) Chiechi, R. C.; Weiss, E. A.; Dickey, M. D.; Whitesides, G. M. Eutectic Gallium-Indium (EGaIn): A Moldable Liquid Metal for

Electrical Characterization of Self-Assembled Monolayers. *Angew. Chem.* **2008**, *120*, 148−150.

(66) Blum, V.; Gehrke, R.; Hanke, F.; Havu, P.; Havu, V.; Ren, X.; Reuter, K.; Scheffler, M. Ab Initio Molecular Simulations with Numeric Atom-Centered Orbitals. *Comput. Phys. Commun.* **2009**, *180*, 2175−2196.

(67) Perdew, J. P.; Burke, K.; Ernzerhof, M. Generalized Gradient Approximation Made Simple. *Phys. Rev. Lett.* **1996**, *77*, 3865−3868.

(68) Ruiz, V. G.; Liu, W.; Zojer, E.; Scheffler, M.; Tkatchenko, A. Density-Functional Theory with Screened van der Waals Interactions for the Modeling of Hybrid Inorganic-Organic Systems. *Phys. Rev. Lett.* **2012**, *108*, 146103.

(69) Tkatchenko, A.; Scheffler, M. Accurate Molecular van der Waals Interactions from Ground-State Electron Density and Free-Atom Reference Data. *Phys. Rev. Lett.* **2009**, *102*, 073005.

(70) Taucher, T. C.; Hehn, I.; Hofmann, O. T.; Zharnikov, M.; Zojer, E. Understanding Chemical versus Electrostatic Shifts in X-Ray Photoelectron Spectra of Organic Self-Assembled Monolayers. *J. Phys. Chem. C* **2016**, *120*, 3428−3437.

(71) Hughes, G.; Wang, C.; Batsanov, A. S.; Fearn, M. J.; Frank, S.; Bryce, M. R.; Perepichka, I. F.; Monkman, A. P.; Lyons, B. P. New Pyrimidine- and Fluorene-Containing Oligo(arylene)s: Synthesis, Crystal Structures, Optoelectronic Properties and a Theoretical Study. *Org. Biomol. Chem.* **2003**, *1*, 3069−3077.

(72) Ballav, N.; Schüpbach, B.; Dethloff, O.; Feulner, P.; Terfort, A.; Zharnikov, M. Direct Probing Molecular Twist and Tilt in Aromatic Self-Assembled Monolayers. *J. Am. Chem. Soc.* **2007**, *129*, 15416−15417.

(73) Kreis, M.; Bräse, S. A General and Efficient Method for the Synthesis of Silyl-Protected Arenethiols from Aryl Halides or Triflates. *Adv. Synth. Catal.* **2005**, *347*, 313−319.

(74) Barone, V.; Commisso, L.; Lelj, F.; Russo, N. Conformational Behaviour of Phenylpyrimidines. A Quantum Mechanical Study. *Tetrahedron* **1985**, *41*, 1915−1918.

(75) Kondoh, H.; Iwasaki, M.; Shimada, T.; Amemiya, K.; Yokoyama, T.; Ohta, T.; Shimomura, M.; Kono, S. Adsorption of Thiolates to Singly Coordinated Sites on Au(111) Evidenced by Photoelectron Diffraction. *Phys. Rev. Lett.* **2003**, *90*, 066102−1.

(76) Roper, M. G.; Skegg, M. P.; Fisher, C. J.; Lee, J. J.; Dhanak, V. R.; Woodruff, D. P.; Jones, R. G. Atop Adsorption Site of Sulphur Head Groups in Gold-Thiolate Self-Assembled Monolayers. *Chem. Phys. Lett.* **2004**, *389*, 87−91.

(77) Lüssem, B.; Müller-Meskamp, L.; Karthäuser, S.; Homberger, M.; Simon, U.; Waser, R. Electrical and Structural Characterization of Biphenylethanethiol SAMs. *J. Phys. Chem. C* **2007**, *111*, 6392−6397.

(78) Shaporenko, A.; Cyganik, P.; Buck, M.; Terfort, A.; Zharnikov, M. Self-Assembled Monolayers of Aromatic Selenolates on Noble Metal Substrates. *J. Phys. Chem. B* **2005**, *109*, 13630−13638.

(79) Charbonneau, G.-P.; Delugeard, Y. Structural Transition in Polyphenels. III. Crystal Structure of Biphenyl at 110 K. *Acta Crystallogr., Sect. B: Struct. Crystallogr. Cryst. Chem.* **1976**, *32*, 1420−1423.

(80) Matei, D. G.; Muzik, H.; Gölzhäuser, A.; Turchanin, A. Structural Investigation of 1,1′-Biphenyl-4-thiol Self-Assembled Monolayers on Au(111) by Scanning Tunneling Microscopy and Low-Energy Electron Diffraction. *Langmuir* **2012**, *28*, 13905−13911.

(81) Heister, K.; Johansson, L. S. O.; Grunze, M.; Zharnikov, M. A Detailed Analysis of the C 1s Photoemission of N-Alkanethiolate Films on Noble Metal Substrates. *Surf. Sci.* **2003**, *529*, 36−46.

(82) Cabellos, J. L.; Mowbray, D. J.; Goiri, E.; El-Sayed, A.; Floreano, L.; de Oteyza, D. G.; Rogero, C.; Ortega, J. E.; Rubio, A. Understanding Charge Transfer in Donor-Acceptor/Metal Systems: A Combined Theoretical and Experimental Study. *J. Phys. Chem. C* **2012**, *116*, 17991−18001.

(83) El-Sayed, A.; Borghetti, P.; Goiri, E.; Rogero, C.; Floreano, L.; Lovat, G.; Mowbray, D. J.; Cabellos, J. L.; Wakayama, Y.; Rubio, A.; et al. Understanding Energy-Level Alignment in Donor − Acceptor/Metal Interfaces from Core-Level Shifts. *ACS Nano* **2013**, *7*, 6914−6920.

(84) Greenler, R. G. Infrared Study of Adsorbed Molecules on Metal Surfaces by Reflection Techniques. *J. Chem. Phys.* **1966**, *44*, 310−315.

(85) Parikh, A. N.; Allara, D. L. Quantitative Determination of Molecular Structure in Multilayered Thin Films of Biaxial and Lower Symmetry from Photon Spectroscopies. I. Reflection Infrared Vibrational Spectroscopy. *J. Chem. Phys.* **1992**, *96*, 927−945.

(86) Horsley, J.; Stöhr, J.; Hitchcock, A. P.; Newbury, D. C.; Johnson, A. L.; Sette, F. Resonances in the K Shell Excitation Spectra of Benzene and Pyridine: Gas Phase, Solid, and Chemisorbed States. *J. Chem. Phys.* **1985**, *83*, 6099−6107.

(87) Yokoyama, T.; Seki, K.; Morisada, I.; Edamatsu, K.; Ohta, T. X-Ray Absorption Spectra of Poly-p-Phenylenes and Polyacenes: Localization of π* Orbitals. *Phys. Scr.* **1990**, *41*, 189−192.

(88) Bolognesi, P.; O'Keeffe, P.; Ovcharenko, Y.; Coreno, M.; Avaldi, L.; Feyer, V.; Plekan, O.; Prince, K. C.; Zhang, W.; Carravetta, V. Pyrimidine and Halogenated Pyrimidines Near Edge X-ray Absorption Fine Structure Spectra at C and N K-Edges: Experiment and Theory. *J. Chem. Phys.* **2010**, *133*, 034302.

(89) Lin, Yi-S; Lin, H.-Ru; Liu, W.-L.; Lee, Y. T.; Tseng, C.-M.; Ni, C.-K.; Liu, C.-L.; Tsai, C.-C.; Chen, J.-L.; Hu, W.-P. Measurement and Prediction of the NEXAFS Spectra of Pyrimidine Andpurine and the Dissociation Following the Core Excitation. *Chem. Phys. Lett.* **2015**, *636*, 146−153.

(90) Zharnikov, M.; Frey, S.; Heister, K.; Grunze, M. An Extension of the Mean Free Path Approach to X-ray Absorption Spectroscopy. *J. Electron Spectrosc. Relat. Phenom.* **2002**, *124*, 15−24.

(91) Zharnikov, M.; Kuller, A.; Shaporenko, A.; Schmidt, E.; Eck, W. Aromatic Self-Assembled Monolayers on Hydrogenated Silicon. *Langmuir* **2003**, *19*, 4682−4687.

(92) Verwüster, E.; Wruss, E.; Zojer, E.; Hofmann, O. T. Exploring the Driving Forces behind the Structural Assembly of Biphenylthiolates on Au(111). *J. Chem. Phys.* **2017**, *147*, 024706.

(93) Vackář, J.; Hyťha, M.; Šimůnek, A. All-Electron Pseudopotentials. *Phys. Rev. B: Condens. Matter Mater. Phys.* **1998**, *58*, 12712−12720.

(94) Methfessel, M.; Fiorentini, V.; Oppo, S. Connection between Charge Transfer and Alloying Core Level Shifts Based on Density-Functional Calculations. *Phys. Rev. B: Condens. Matter Mater. Phys.* **2000**, *61*, 5229−5236.

(95) Morikawa, Y.; Hayashi, T.; Liew, C. C.; Nozoye, H. First-Principles Theoretical Study of Alkylthiolate Adsoprtion on Au(111). *Surf. Sci.* **2002**, *507-510*, 46−50.

(96) Bagus, P. S.; Ilton, E. S.; Nelin, C. J. The Interpretation of XPS Spectra: Insights into Materials Properties. *Surf. Sci. Rep.* **2013**, *68*, 273−304.

(97) Shaporenko, A.; Terfort, A.; Grunze, M.; Zharnikov, M. A detailed analysis of the photoemission spectra of basic thioaromatic monolayers on noble metal substrates. *J. Electron Spectrosc. Relat. Phenom.* **2006**, *151*, 45−51.

(98) Bolognesi, P.; O'Keeffe, P.; Feyer, V.; Plekan, O.; Prince, K.; Coreno, M.; Mattioli, G.; Amore Bonapasta, A.; Zhang, W.; Carravetta, V.; et al. Inner Shell Excitation, Ionization and Fragmentation of Pyrimidine. *J. Phys.: Conf. Ser.* **2010**, *212*, 012002.

(99) Natan, A.; Kronik, L.; Haick, H.; Tung, R. T. Electrostatic Properties of Ideal and Non-Ideal Polar Organic Monolayers: Implications for Electronic Devices. *Adv. Mater.* **2007**, *19*, 4103−4117.

(100) Heimel, G.; Rissner, F.; Zojer, E. Modeling the Electronic Properties of π-Coniugated Self-Assembled Monoayers. *Adv. Mater.* **2010**, *22*, 2494−2513.

(101) Monti, O. L. A. Understanding Interfacial Electronic Structure and Charge Transfer: An Electrostatic Perspective. *J. Phys. Chem. Lett.* **2012**, *3*, 2342−2351.

(102) Rissner, F.; Egger, D. A.; Romaner, L.; Heimel, G.; Zojer, E. The Electronic Structure of Mixed Self-Assembled Monolayers. *ACS Nano* **2010**, *4*, 6735−6746.

(103) Chen, C.-Y.; Wu, K.-Y.; Chao, Y.-C.; Zan, H.-W.; Meng, H.-F.; Tao, Y.-T. Concomitant Tuning of Metal Work Function and Wetting

63

Property with Mixed Self-Assembled Monolayers. *Org. Electron.* **2011**, *12*, 148−153.

(104) Vetushka, A.; Bernard, L.; Guseva, O.; Bastl, Z.; Plocek, J.; Tomandl, I.; Fejfar, A.; Baše, T.; Schmutz, P. Adsorption of Oriented Carborane Dipoles on a Silver Surface: Adsorption of Oriented Carborane Dipoles on a Silver Surface. *Phys. Status Solidi B* **2016**, *253*, 591−600.

(105) Kovalchuk, A.; Abu-Husein, T.; Fracasso, D.; Egger, D. A.; Zojer, E.; Zharnikov, M.; Terfort, A.; Chiechi, R. C. Transition Voltages Respond to Synthetic Reorientation of Embedded Dipoles in Self-Assembled Monolayers. *Chem. Sci.* **2016**, *7*, 781−787.

(106) Xiao, X.; Xu, B.; Tao, N. J. Measurement of Single Molecule Conductance: Benzenedithiol and Benzenedimethanethiol. *Nano Lett.* **2004**, *4*, 267−271.

(107) Danilov, A.; Kubatkin, S.; Kafanov, S.; Hedegård, P.; Stuhr-Hansen, N.; Moth-Poulsen, K.; Bjørnholm, T. Electronic Transport in Single Molecule Junctions: Control of the Molecule-Electrode Coupling through Intramolecular Tunneling Barriers. *Nano Lett.* **2008**, *8*, 1−5.

(108) Obersteiner, V.; Egger, D. A.; Zojer, E. Impact of Anchoring Groups on Ballistic Transport: Single Molecule vs Monolayer Junctions. *J. Phys. Chem. C* **2015**, *119*, 21198−21208.

(109) Van Dyck, C.; Geskin, V.; Cornil, J. Fermi Level Pinning and Orbital Polarization Effects in Molecular Junctions: The Role of Metal Induced Gap States. *Adv. Funct. Mater.* **2014**, *24*, 6154−6165.

(110) Kovalchuk, A.; Egger, D. A.; Abu-Husein, T.; Zojer, E.; Terfort, A.; Chiechi, R. C. Dipole-Induced Asymmetric Conduction in Tunneling Junctions Comprising Self-Assembled Monolayers. *RSC Adv.* **2016**, *6*, 69479−69483.

(111) Yoon, H. J.; Bowers, C. M.; Baghbanzadeh, M.; Whitesides, G. M. The Rate of Charge Tunneling Is Insensitive to Polar Terminal Groups in Self-Assembled Monolayers in AgTSS(CH2)nM(CH2)-mT//Ga2O3/EGaIn Junctions. *J. Am. Chem. Soc.* **2014**, *136*, 16−19.

(112) Zhang, G.-P.; Hu, G.-C.; Song, Y.; Li, Z.-L.; Wang, C.-K. Modulation of Rectification in Diblock Co-oligomer Diodes by Adjusting Anchoring Groups for Both Symmetric and Asymmetric Electrodes. *J. Phys. Chem. C* **2012**, *116*, 22009−22014.

(113) Trotter, J. The Crystal and Molecular Structure of Biphenyl. *Acta Crystallogr.* **1961**, *14*, 1135−1140.

4.2.2 Supporting information

Previous embedded dipole system
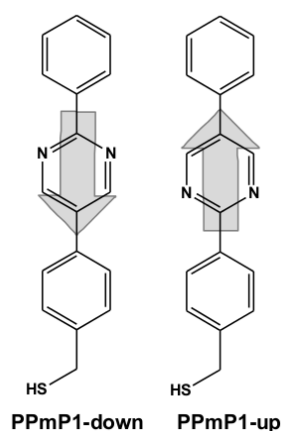
Figure 4.8: Schematic drawing of the terphenyl-4-methanethiol-based molecules with the central phenylene ring substituted by a 2,5-pyrimidine group in the two opposite orientations, along with their acronyms[114]. The directions of the dipole moment associated with the embedded pyrimidine group are shown (the direction from the negative charge to the positive charge is considered as positive). The molecules are named accordingly. An upright molecular geometry is assumed.

Additional experimental data
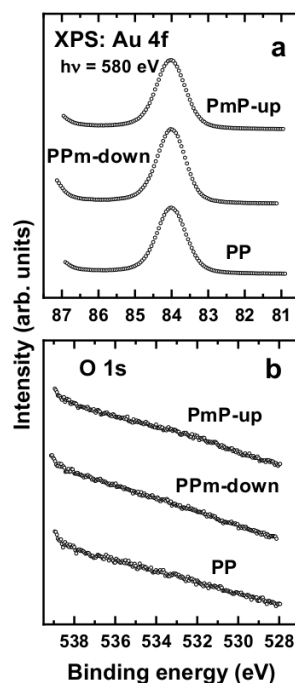
Figure 4.9: Au $4f_{7/2}$ (a) and O 1s (b) XPS spectra of the PmP-up, PPm-down, and PP SAMs. The spectra were acquired at a photon energy of 580 eV. Similar intensities of the Au signal for all SAMs suggest similar packing densities of thereof, in agreement with the numerical evaluation of the XPS data (see section 3.6). The O 1s XP spectra of the PP and PPm-down SAMs do not exhibit any oxygen signal, which suggest that these monolayers were contamination-free. There is a very weak O signal for the PmP-up SAM, most likely originating from a minor, oxygen-containing contamination.
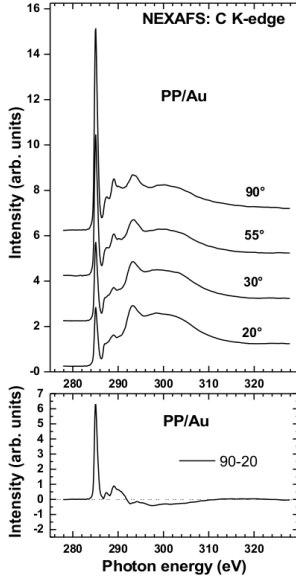
Figure 4.10: C K-edge NEXAFS spectra of the reference PP SAMs acquired at different X-ray incidence angles (top panel), along with the respective difference between the spectra collected under normal (90°) and grazing (20°) incidence (bottom panel). The horizontal dashed lines correspond to zero.

Computational details

Unit cell used in the simulations. The dimensions of the unit cell in the x and y directions were defined according to the theoretically calculated Au lattice constant (4.158 Å, corresponding to a nearest neighbour distance of 2.940 Å) and held fixed in all the calculations. In the z direction a vacuum region of at least 20 Å and a self-consistently calculated dipole correction[115] were inserted, in order to spatially and electrostatically decouple the slabs.

The S docking groups were placed in *fcc*-hollow sites in the initial geometry and found to be shifted towards bridge in the final one, consistent with the typically observed favourable docking position for thiolate SAMs on Au(111). The default FHI-aims default tight basis set was used for all the elements and the following self-consistency cycle criteria were used: sc_accuracy_rho=1×10^{-5} e$^-$, sc_accuracy_etot=1×10^{-6} eV, sc_accuracy_forces=1×10^{-4} eV/Å, sc_accuracy_eev=1×10^{-3} eV, sc_accuracy_potjump=1×10^{-4} eV.

Simulation of the XP spectra. The C 1s core level energies were taken directly from the atom projected density of states FHI-aims output files and an electrostatic image charge model[116,117] was used to include the screening of the core hole by the metal surface:

$$\epsilon_{C1s,screened} = \epsilon_{C1s} + 27.211 \frac{1}{4\varepsilon \cdot 1.889716 \cdot (z - z_0)}. \qquad (4.2)$$

ε is the dielectric constant of the SAM, set to 3.9[118], z is the z coordinate of the C atom and z_0 is the image plane position (both given in Å). The conversion factor 14.340, given by the product of the conversion factors between Hartree and eV and Bohr and Å, is used to obtain the energy in eV. The position of the image plane was set to 0.9 Å above the average z-position of the Au atoms of the topmost layer[119,120]. As described in reference 19, such approach does not account for either the direct screening effects within the SAM or its finite thickness. The screened energies thus obtained were convoluted with Gaussian functions, with a variance of 0.25 eV for the 580 eV spectra. The contribution of every

atom was weighted to account for the finite escape depth of the photoelectrons[121]. This was done multiplying the Gaussian functions by an exponential attenuation function containing a suitable damping factor (attenuation length) appropriate to the primary kinetic energy of the photoelectrons:

$$w_i(d) = w_0 e^{\frac{-d}{\lambda}}. \tag{4.3}$$

w_0 is a scaling constant that does not change the shape of the spectrum, $w_i(d)$ is the individual weight of the i-th atom, that depends on the vertical distance d between the atom and the topmost C atom in the SAM and on a damping factor λ. According to reference 121, λ is defined as $\lambda = 0.3 E_{kin}^{\beta}$, where E_{kin} is the kinetic energy of the escaping electron and β is an empirical attenuation factor. E_{kin} is given by the difference between the energy of the incident photon (580 or 350 eV in our cases) and the calculated binding energy of the C 1s electron. The value of β was set to 0.51 to obtain the best match between the experimental and simulated spectra. This is done as we are not aware of experimentally determined damping factors for the aromatic SAMs considered here. A simulation of the damping factor for systems as complex as the present one would also go far beyond current computational possibilities.

Impact of the choice of β on the shape of the spectra. As mentioned in the previous section, the value of β was changed until the best agreement between the shapes of the simulated and calculated spectra was obtained.

Using the relation between β and the attenuation length λ, it would be possible to obtain β using the experimental value of λ. Such values have been reported for alkylthiol SAMs[121] and when using those values (as is done for evaluating the SAM thickness from XPS data, as reported in the main manuscript in section 2) for calculating β, a value of 0.64 is obtained. However, when using that value to simulate the XP spectra, the agreement between theory and experiments becomes worse (see figure 4.11). A possible reason for this can be differences in the attenuation factors between aliphatic and aromatic SAMs.
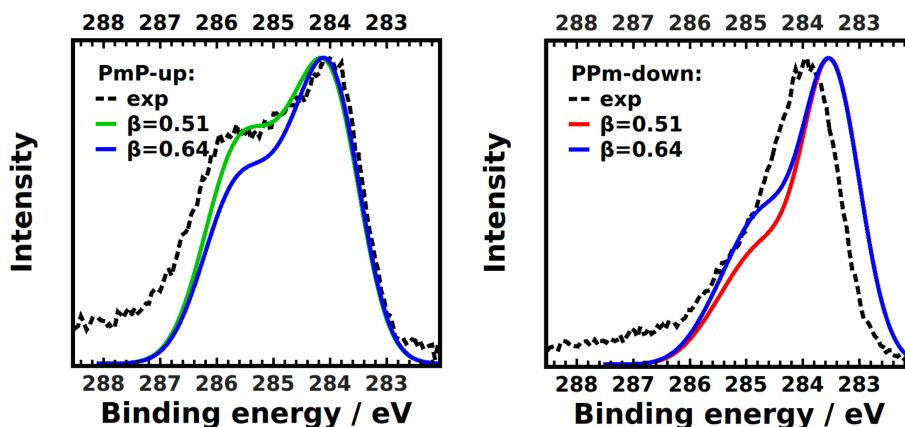
Figure 4.11: Impact of the choice of the β values for the PmP-up (left panel) and the PPm-down (right panel) SAMs. The same shift as for the PP SAM (18.94 eV) has been used for the simulated spectra.

Hirshfeld charges. To better understand the interplay between chemical and electrostatic shifts in the PPm-down SAM, the Hirshfeld charges of the C atoms in the topmost ring and of the topmost C atom in the bottom ring have been calculated and compared to the PP case. The results are shown in figure 4.12. Although partial charges are no physical observables and partitioning schemes can be ambiguous, the values in figure 4.12 show that the C in the

topmost rings have the same partial charges in both SAMs (i.e., for such atoms, we do not expect a chemical shift), while for the topmost C atom in the bottom ring the situation is clearly different due to the two neighbouring N atoms in the PPm-down SAM.
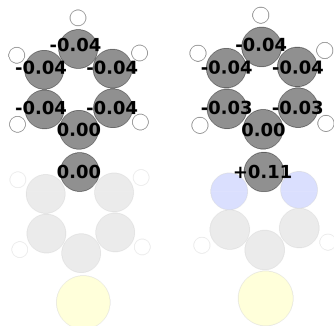
Figure 4.12: Hirshfeld charges on the C atoms in the topmost ring and of the topmost C atom in the bottom ring in the PPm-down and PP SAMs. The values are averaged over the two inequivalent molecules in the unit cell.

PmP-up C1s 350 eV XP spectrum. The simulated PmP-up C1s XP spectrum at 350 eV is shown in figure 4.13, where the calculated Kohn-Sham energies are used, i.e. no additional shift is applied. When applying the same damping factor and variance used for the 580 eV spectra (0.51 and 0.25 eV, respectively) only two peaks are observed (green line in panel a). By changing the width of the Gaussian functions it is however possible to see a third peak appearing between the two main ones, as shown by the dotted orange line. The occurrence of a third signal qualitatively agrees with the experimental observations (see main paper), although the intensities do not match.
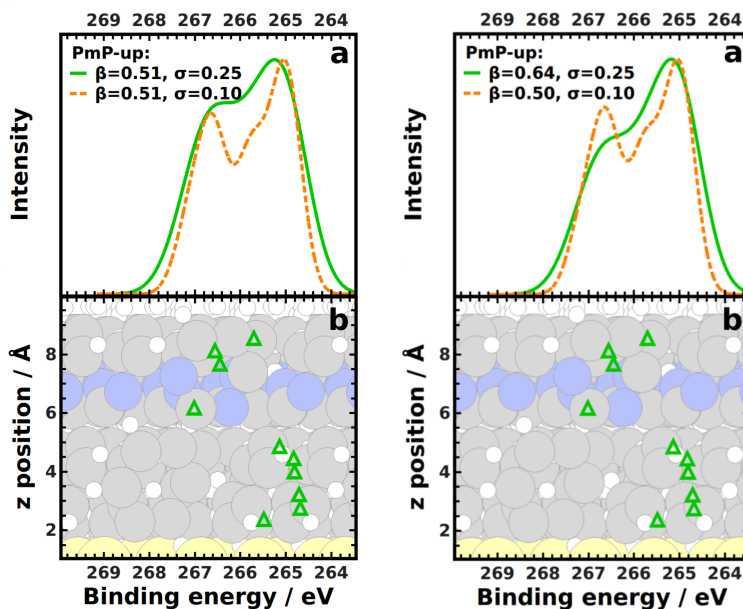
Figure 4.13: a: DFT calculated 350 eV XP spectra for the PmP-up SAM. The green line shows the spectrum obtained with the same values of β and σ used for the 580 eV spectra reported in the main paper. The orange dotted line shows the spectrum obtained by setting σ to 0.10 eV, in order to resolve the central peak. b: core-level binding energies of individual C atoms averaged over equivalent atoms in the two molecules contained in the unit cell. For both spectra and energies of the individual levels, screening effects by the substrate according to the electrostatic model described above have been considered. No additional shifts were applied.

The atomically resolved C contributions to the spectrum shown in panel b allow assigning the central peak to the topmost C atom. The assignment is consistent with the fact that at lower photon energies the relative intensity of the signal coming from the topmost atoms of the SAM is stronger.

Possible impact of the lateral disorder on the work function change. An interesting property of pyrimidine containing molecules is that their dipoles crucially depend on the local environment of the N atoms due to the interplay of their π-donating and σ-accepting character. Consequently, we indeed see somewhat varying differences between the long-axes dipole moments for isolated PPm-down and PmP-up molecules and the PP parent system (see table 4.5). Interestingly, most of this difference disappears when packing the molecules into perfectly ordered (hypothetical) free-standing monolayers in the same geometry the molecules adopt on the surface (i.e., with only the positions of the H atoms saturating the thiolates optimised). This can be inferred from the reduced differences in the values of ΔE_{vac} (i.e. the step in the electrostatic potential energy induced by the periodic arrangement of the dipolar units) between the PPm-down/PmP-up monolayers and that of the PP film (see table 4.5). Notably, this is not caused by the minor distortion of the molecular structure in the SAM, as can be concluded from the dipoles of the isolated molecules calculated in the geometry they adopt in the SAM. The coupling between thiol and pyrimidine dipoles is, however, reduced by the much faster decay length of the electric fields of dipoles in SAMs compared to isolated molecules[24] resulting in a reduced coupling between thiol and pyrimidine dipoles in the SAM. Moreover, there are larger depolarisation effects for larger molecular dipoles. For the SAM-induced work function change, the asymmetry between the PPm-down/PmP-up disappears completely as a consequence of different bond dipoles (i.e. the step in the electrostatic potential energy due to the charge rearrangements taking place at the metal/SAM interface upon absorption). This suggests that in the pyrimidine-containing SAMs lateral disorder might impact the final work function change. In the absence of suitable structural models for disordered layers, this assessment, however, remains highly speculative.

Table 4.5: Dipole moments and energetic shifts relative to the PP reference are given in parentheses. μ is the long molecular axis component of the dipole of the gas phase optimised molecule, while μ_{SAM} is the z component (component perpendicular to the surface) of the dipole in the geometry the molecules assume when packed in the SAM. ΔE_{vac} is the step in electrostatic energy in a hypothetical free-standing SAM with the S atoms saturated by hydrogens. BD is the bond dipole reflecting the charge rearrangements upon replacing the S–H bonds by S–Au bonds and $\Delta \Phi$ is the work function change, equal to the sum of ΔE_{vac} and BD.

	μ / D	μ_{SAM} / D	ΔE_{vac} / eV	BD / eV	$\Delta \Phi$ / eV
PmP-up	+1.70 (+1.28)	+1.25 (+1.00)	-0.93 (-0.71)	-1.16 (+0.06)	-2.09 (-0.65)
PP	+0.42	+0.25	-0.22	-1.22	-1.44
PPm-down	-1.21 (-1.63)	-1.1 (-1.35)	+0.53 (-0.75)	-1.32 (+0.10)	-0.79 (+0.65)

An alternative explanation for the experimentally observed asymmetry between PPM-down/Au and PmP-up/Au could be a somewhat smaller tilt angle in the experimentally studied PP SAMs compared to the pyrimidine-containing compounds (as suggested by the larger XPS-derived film thicknesses and by the NEXAFS data, while not being supported by all of the other measurements). This would result in a relatively larger work function reduction in the PP/Au layers. A consequence of this shift in the reference work function would be that the additional work function reduction by PmP-up/Au would appear smaller than the reduced work function reduction by PPm-down/Au.

Impact of different methodologies on the calculated properties. As mentioned in the main text when discussing the comparison of the calculated and measured work function (changes), the method employed to compute the properties can have a sometimes relevant impact on the calculated results. This is shown for the dipole moment (property that directly impacts the calculated work function change) of a PmP isolated molecule without the thiol group, shown in figure 4.14, in table 4.6. The methods compared are Hartree-Fock (HF), the Local Spin Density Approximation (LSDA), the General Gradient Approximation (GGA) with the PBE functional and the Hybrid Functional HSE06. The calculations were performed with FHI-aims using the default really tight settings.
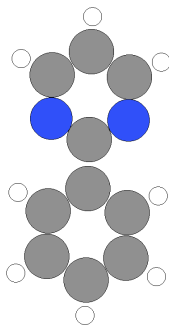
Figure 4.14: PmP isolated molecule without thiol group used for testing different methods. C atoms are depicted in grey, H in white and N in blue.

Table 4.6: Dipole moment of an isolated PmP molecule calculated using different methodologies. The acronyms are explained in the text.

Method	Dipole moment / D
HF	1.74
LSDA	1.52
PBE	1.44
HSE06	1.58

4.3 Third generation self-assembled monolayers with embedded dipole moments.

The embedded dipole approach presented in section 4.2 was applied also to a third generation of SAMs containing a further dipolar pyrimidine element. The systems described in this section are conceptual derivatives of the SAMs considered in section 4.2 and of the SAMs investigated in reference 114, respectively referred to as second and first generation SAMs. The parent systems and their nomenclature are depicted in figure 4.15.

The third generation molecules, depicted in figure 4.16, were synthesized by Michael Gärtner in the group of Professor Andreas Terfort at the University of Frankfurt and deposited on the substrate by Eric Sauter in the group of Professor Michael Zharnikov at the University of Heidelberg. Eric Sauter and Professor Zharnikov also performed the experimental XPS and work function measurements reported in this work. In the following, the calculated XP spectra and work function changes, $\Delta\Phi$, will be discussed and compared to the experimental ones. The systems were modelled assuming the same unit cell and molecular arrangement described in the previous section for the second generation SAMs.

First generation molecules **Second generation molecules**

PPP1   **PPmP1-up**   **PPmP1-down**   **PP**   **PmP-up** **PmP-down**
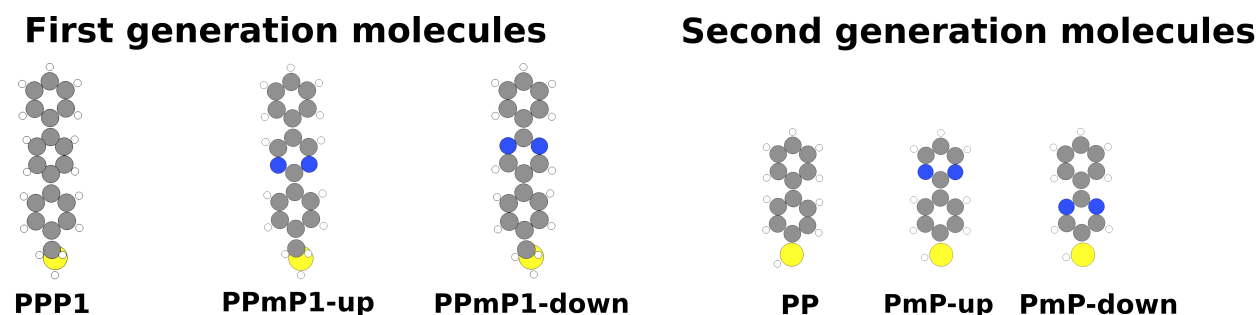
Figure 4.15: First and second generation molecules with their nomenclature. P stays for phenyl ring, Pm for pyrimidine ring, the number 1 indicates the presence of a methyl unit between the molecular backbone and the docking group and the indication up/down gives the direction of the dipole of the pyrimidine rings. PPP1 and PP are taken as references systems for the first and second generation molecules, respectively. C atoms are depicted in grey, H in white, N in blue and S in light yellow.

Third generation molecules

PmPm-up **PmPm-down**   **PmPmP1-up** **PmPmP1-down**
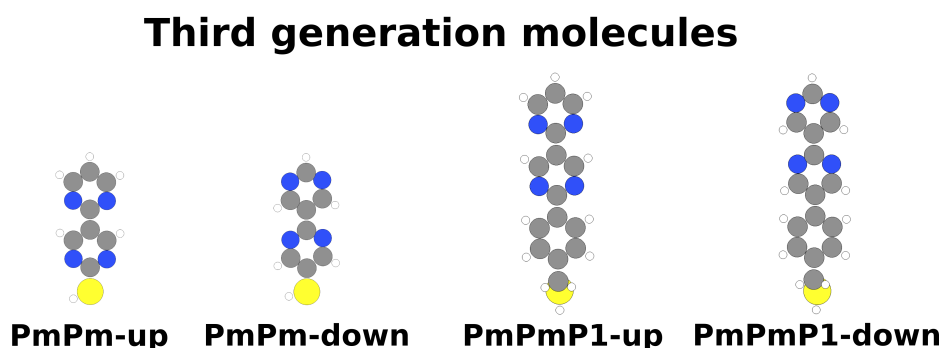
Figure 4.16: Third generation molecules with their nomenclature. P stays for phenyl ring, Pm for pyrimidine ring, the number 1 indicates the presence of a methyl unit between the molecular backbone and the docking group and the indication up/down gives the direction of the dipole of the pyrimidine rings. PPP1 and PP (depicted in figure 4.15) are taken as references systems for the PmPm and the PmPmP1 molecules, respectively. C atoms are depicted in grey, H in white, N in blue and S in light yellow.

4.3.1 Computational methods

The simulations were performed using the FHI-aims code[26] and employing the PBE functional[27]. Van der Waals interactions were accounted for via the Tkatchenko-Scheffler scheme[29] in its parametrisation for surfaces[28]. The dispersion corrections were turned off between the metal atoms. The interfaces were modelled using periodic boundary conditions and the repeated slab approach. Two molecules arranged in a herringbone fashion were placed in a $(3 \times \sqrt{3})rect$ unit cell. The dimensions of the unit cell in the x and y direction were set according to the theoretically calculated Au lattice constant (4.158 Å, corresponding to a nearest neighbour distance of 2.940 Å). The dimension in the z direction was set such that a vacuum region of at least 20 Å was inserted between two consecutive replicas of the slab, to spatially decouple them. To decouple them also electrostatically, a self-consistently determined dipole correction was introduced in the z direction. The metal substrate was modelled using 5 layers of Au. The three bottom metal layers were kept fixed in all the calculations, while the two topmost ones were let relax. The calculations were performed using a $9 \times 5 \times 1$ Γ centred k-points grid and describing all the elements using the default FHI-aims tight basis set. For the flipped and exchanged arrangements tested for the PmPmP1- SAMs the default FHI-aims light basis set was employed, the k-point grid was scaled according to the larger dimensions of the unit cell and only three layers of Au were used, keeping the bottom one fixed. The total energy criterion for the self-consistency cycle was set to 10^{-6} eV and geometry optimisations were performed until the maximum residual force component per atom was below 0.01 eV/Å.

As explained in detail in the methodology parts of sections 4.2 and 4.4 the C1s XP spectra were simulated within the initial state approach using an image potential model[116,117] to account for the screening due to the highly polarisable metal substrate and weighting the contribution of every atom to account for the finite escape depth of the photoelectrons. The expressions used to include screening effects and damping can be found in the supporting information of the paper included in section 4.2. Where not otherwise stated, the dielectric constant of the SAMs was set to 3.9, for sake of consistency with the calculations performed in section 4.2, and the variance of the gaussian functions used to artificially broad the simulated spectra was set to 0.15 eV. The value of the damping factor β was tuned until the best agreement between the simulated and the experimental spectra was obtained and is specified in the corresponding section for each spectrum.

4.3.2 PmPm- SAMs

Work function change

The calculated $\Delta\Phi$ values (given with respect to a calculated work function of 5.12 eV for a clean Au(111) surface) are -2.62 eV and +0.95 eV for the PmPm-up and for the PmPm-down SAMs, respectively. The experimental Φ values for the PmPm-up and the PmPm-down SAMs are 4.33 and 4.9 eV. Considering a measured Φ of about 5.2 eV for a clean Au surface, the experimental values correspond to $\Delta\Phi$ of about -0.9 and -0.3 eV for the PmPm-up and PmPm-down SAMs, respectively. The calculated values largely overestimate the measured ones, in the PmPm-down case even the sign of the variation is different. Although a certain overestimation in the simulations is usually expected, in this case it is far too large. For the PmPm-up SAM, this could in part be ascribed to the low packing density observed in experiments: the measured density is 3.6E14 molecules/cm^2, somewhat lower than the one observed for the parent molecules of the previous section (4.5E14) and the one used in the simulations (4.45E14). To account for that, for the PmPm-up SAM also a (2×4) unit cell with two molecules per unit cell was tested, that gives a coverage of 3.37E14 molecules/cm^2,

thus closer to the experimental one. The calculation was however stopped because during the optimisation the molecules tilted by more than 50°, inconsistent with the much smaller tilt angles estimated on the basis of the experimental measurements (see table 4.7).

Structural parameters

In table 4.7 the calculated structural parameters are reported and compared to the available experimental data. The tilt angle of the molecules with respect to the surface normal β, the tilt angle of the π^* orbitals with respect to the surface normal α and the molecular twist angle γ (rotation around the molecular axis) are reported for the two inequivalent molecules in the unit cell. The average value of α was obtained via $\cos^2\alpha_{av} = (\cos^2\alpha_1 + \cos^2\alpha_2)/2$, to be consistent with the NEXAFS evaluation, as explained in section 4.2. A graphical representation of the α, β and γ angles is given in figure 6 of section 4.2.

Regarding the structural parameters, both simulations and experiments give larger tilt angles for the PmPm SAMs than for the PP one, as was already the case for the monopyrimidine SAMs (see section 4.2). Quantitatively, the experimental and calculated values differ quite a lot, with the calculated values of the tilt angles overestimating the measured ones by more than 10°. The qualitative trend of the PmPm-down SAM being more tilted than the PmPm-up one is reproduced both in simulations and in experiments. Interestingly, the down SAM was more tilted than the up one also in the second generation molecules of section 4.2. As already mentioned, for the PmPm-up SAM the experimental packing density is relevantly lower than for the PmPm-down SAM, while in the simulations the same coverage of 4.45E14 molecules/cm² is used for both SAMs, corresponding to 2 molecules in a ($\sqrt{3}$ x 3)*rect* unit cell (see previous section).

Table 4.7: Tilt angle of the π^* system α and its average over the two inequivalent molecules in the unit cell (α_{av}), molecular tilt angle (β) and molecular twist angle (γ) for the PmPm-up and PmPm-down SAMs. The values for the 2 inequivalent molecules in the unit cell are given. For the tilt angle of the π^* system α and the molecular tilt angle β also the experimental values exp. α and the minimum values consistent with NEXAFS data exp. β are reported (for further details about the tilt angle evaluation see the results chapter of section 4.4).

	α / °	α_{av} / °	exp. α / °	β / °	exp. β / °	γ / °
			PmPm-up			
Mol. 1	74.91	65.2	69.5	32.29	17.5	63.92
Mol. 2	57.78			32.21		1.00
	α / °	α_{av} / °	exp. α / °	β / °	exp. β / °	γ / °
			PmPm-down			
Mol. 1	74.54	65.0	76.0	33.89	22.8	61.44
Mol. 2	57.62			32.42		2.55

C1s X-ray photoelectron spectra

In figure 4.17 the simulated and experimental XPS of the PmPm-up and PmPm-down SAM are shown. The PP SAM spectrum is also reported as reference. The shape of the PmPm down spectrum is decently reproduced, while, regarding the position, the shift with respect to the PP spectrum is larger in the experiments (about 1 eV, with the PP peak lying at smaller binding energies) than in the simulations (about 0.5 eV). The disagreement is much more evident in the PmPm-up case: in experiments the most intense peak is essentially

at the same position as the PmPm-down peak. In the simulated PmPm-up SAM XPS instead, the peak at smaller binding energies is shifted by about 0.9 eV to larger energies with respect to the PmPm-down spectrum. Moreover, also the peak intensities do not agree: the experimental spectrum has a main peak and a consistent shoulder at the higher binding energy side, while the simulated spectrum gives two peaks with essentially the same intensity. The experimentally observed main peak and the shoulder are shifted by more than 1 eV, the simulated peaks are shifted by less than 1 eV. The shape of the spectrum could probably be improved by varying the damping parameter (see computational details and the methodology parts of the previous and the next sections.).
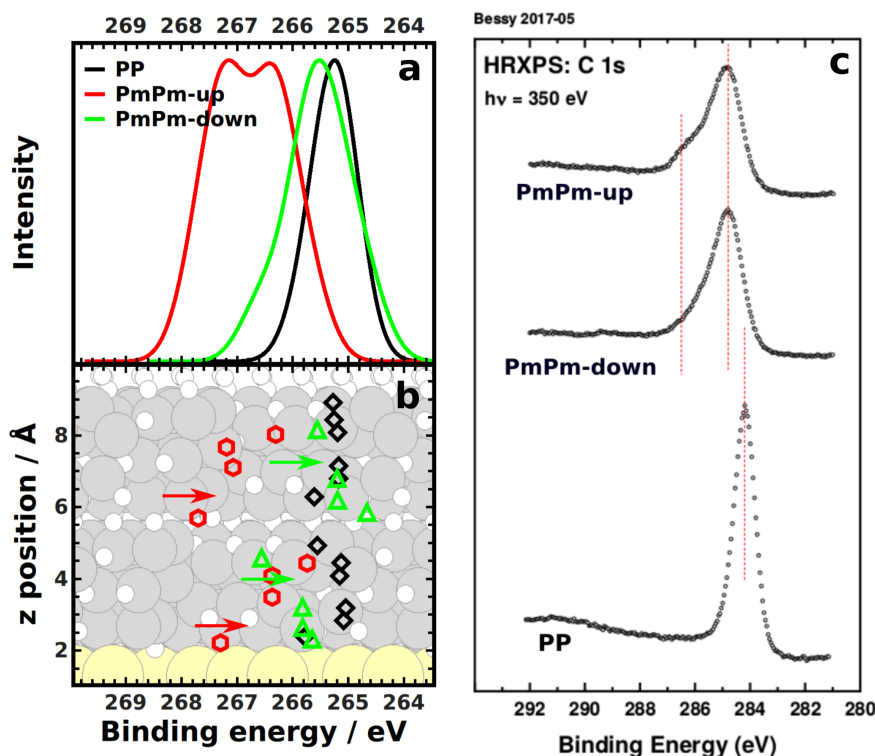
Figure 4.17: Panel a: simulated C1s XPS of the PP, PmPm-up and PmPm-down SAMs for a photon energy of 350 eV. The spectra are reported as calculated, without any artificial shift to align them to the experimental ones (see discussions in sections 4.2 and 4.4). In panel b the atomic contributions to the C1s spectra are resolved. In the background the PP SAM is shown, in order to assign the black PP symbols to the C atoms in the molecular backbone. Red and green arrows indicate the position of N atoms in the PmPm-up, respectively PmPm-down, SAM. The positions of C atoms in the different SAMs do not match because of the non negligible difference in the tilt angles. In panel c the experimental C1s XP spectra registered at a photon energy of 350 eV are shown. The vertical red dashed lines are guides to the eyes.

"Fictitious" reduced coverage for the PmPm-up SAM

The most relevant discrepancy concerns the PmPm-up SAM XPS. Prof. Zharnikov observed that in the simulated spectra both chemical and electrostatic effects are included, whereas in experiments, according to the measured work function, the latter effect seems actually not to occur. Following this consideration, a "fictitious" reduced coverage situation was simulated: instead of using a larger unit cell and relaxing the molecules, as in the case of the (2×4) unit cell mentioned above, the optimised $(3 \times \sqrt{3})rect$ unit cell was doubled to obtain a $(3 \times 2\sqrt{3})rect$ one and all the molecules but one were removed. The final coverage was thus 25% of the initial one. The system was not optimised, since the relaxation would lead to a sever tilt of the molecule. XP spectra were simulated, testing also different values

of the damping parameter β and the dielectric constant of the SAM ε (see computational details and the methodology parts of the sections 4.2 and 4.4). The simulated spectra are reported in figure 4.18.
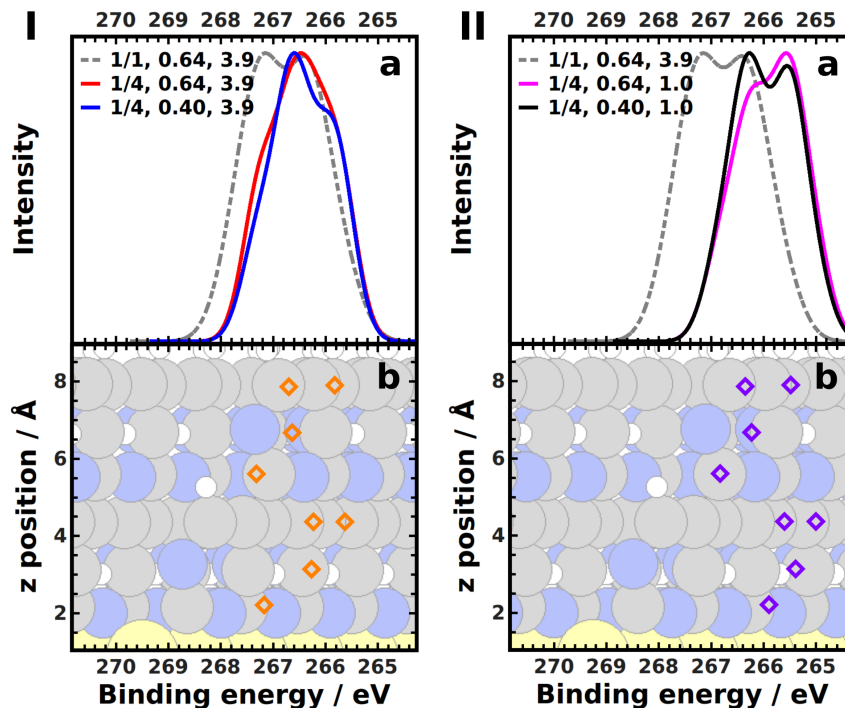
Figure 4.18: Simulated C1s XPS of the PmPm-up SAM at full (1/1) and 1/4 reduced coverage for a photon energy of 350 eV. Panels I: comparison of full coverage (grey dashed line) and reduced coverage XPS calculated using $\varepsilon = 3.9$ and $\beta = 0.64$ (red line) and 0.40 (blue line). Panels II: comparison of full coverage (grey dashed line) and reduced coverage XPS calculated using $\varepsilon = 1.0$ and $\beta = 0.64$ (black line) and 0.40 (magenta line). In panels a the spectra are reported, without any artificial shift to align them to the experimental ones (see discussions in the previous section and in section 4.4). In panels b the atomic contributions to the C1s spectra are resolved. In the background the PmPm-up SAM is shown, in order to assign the symbols to the C atoms in the molecular backbone.

In panels I $\varepsilon = 3.9$ is used, that is the same value used in the full coverage case and for the second generation molecules of previous section 4.2. The situation with respect to the full coverage case does not actually improve with any of the used damping factors. The value 0.64 was calculated according to the experimental escape depth while 0.40 is a test value to obtain an appreciable difference in the shape of the spectrum. Indeed, using 0.40 a main peak and a shoulder at smaller binding energies can be resolved. The spectrum shifts by about 0.5 eV to smaller binding energies with respect to the full coverage case, thus improving the agreement with experiments. However, the simulated spectrum lies still at too large energies, when compared to the experimental one. A further discrepancy regards the shape of the spectrum: the shoulder lies at smaller binding energies in the simulated spectrum, while in the experimental one it lies at larger binding energies. In panels II the reduced coverage XPS is calculated using a different value of the dielectric constant ε, since at reduced coverages it is reasonable to assume that the value would be smaller. $\varepsilon = 1$ was used, even if the choice might not be the most appropriate one. $\varepsilon = 1$ would

actually be suited for a much more reduced coverage modelling an isolated molecule on the surface, like for instance 1/16 (see the reduced coverage calculations performed in section 4.4). $\varepsilon = 1$ was nevertheless used to test how large the impact of ε is. Indeed, using $\varepsilon = 1$ the simulated spectra get shifted towards smaller binding energies by about 1 eV, improving the agreement with experiments, in which the main PmPm-up and PmPm-down peaks lie essentially at the same energy. Moreover, the XPS with $\beta = 0.64$ shows a main peak and a shoulder at larger binding energies, as observed in experiments. The relative intensities are however not satisfactorily captured, since in experiments the shoulder is much less intense than the main peak, while in the simulations this is not the case. These aspects altogether seem to indicate that the experimental PmPm-up spectrum is consistent with the lower packing density measured for this SAM. However, there are several other aspects that need to be clarified, not only when comparing simulated and measured results but also within the latter. For instance, the PmPm-up SAM shows a reduced packing density but also a smaller tilt angle than the PmPm-down SAM, which is somehow counterintuitive considering that having more space the molecules should tilt more.

So far, no conclusive explanation could be found and the discrepancies observed between calculated and measured results for the PmPm- SAMs were attributed to the bad quality of the films formed by the molecules with two pyrimidine rings. Probably the backbone dipoles are too large in order for the parallel arrangement to be favourable (for the isolated gas phase PmPm-down and PmPm-up thiols the PBE calculated dipoles are 4.27 and 3.37 D, respectively). To rationalise the lower packing density observed for the PmPm-up SAM, a non favourable interaction of the bottom N atoms with the underlying metal substrate has been hypothesised.

4.3.3 PmPmP1- SAMs

Work function change

The calculated work function changes, given with respect to a calculated work function of 5.12 eV for a clean Au(111) surface, are -2.58 eV and +1.06 eV for the PmPmP1-up and for the PmPmP1-down SAMs, respectively. The experimental Φ values for the PmPmP1-up and the PmPmP1-down SAMs are 3.70 and 5.03 eV, that correspond to $\Delta\Phi$ values of -1.50 and -0.17 eV, respectively. Also in this case, the calculated values largely overestimate the measured ones. For the PmPmP1-down SAM, similar to the PmPm-down case discussed above, the sign of the work function modification in experiment and in the simulations is different.

Structural parameters

In table 4.8 the calculated structural parameters are reported and compared to the available experimental data. The values of the PPP1 SAM are given as reference. The calculated values show an overall nice agreement with the experimental ones. With respect to the PmPm-SAMs, the PmPmP1 SAMs have smaller tilt angles. For both the SAMs the experimental packing density is about 4.4E14 molecules/cm², fully comparable with the coverage of 4.45E14 molecules/cm² used in the simulations.

Table 4.8: Tilt angle of the π^* system α and its average over the two inequivalent molecules in the unit cell (α_{av}), molecular tilt angle (β) and molecular twist angle (γ) for the PPP1, the PmPmP1-up and the PmPmP1-down SAMs. The values for the 2 inequivalent molecules in the unit cell are given. For the tilt angle of the π^* system α and the molecular tilt angle β also the experimental values exp. α and the minimum values consistent with NEXAFS data exp. β are reported (for further details about the tilt angle evaluation see the results chapter of section 4.4).

	α / °	α_{av} / °	exp. α / °	β / °	exp. β / °	γ / °
			PPP1			
Mol. 1	78.07			16.60		43.68
Mol. 2	76.00	77.00	81.9	15.38		24.13
			PmPmP1-up			
	α / °	α_{av} / °	exp. α / °	β / °	exp. β / °	γ / °
Mol. 1	87.27			24.80		83.34
Mol. 2	67.73	74.30	73.5	23.17	19.0	15.59
			PmPmP1-down			
	α / °	α_{av} / °	exp. α / °	β / °	exp. β / °	γ / °
Mol. 1	87.38			25.11		83.81
Mol. 2	69.09	75.30	75.5	23.54	18.0	26.68

PmPmP1-up C1s X-ray photoelectron spectra

In figure 4.19 the simulated and the experimental PmPmP1-up C1 XP spectra at a photon energy of 580 eV are compared. The C1s XPS of the PPP1 SAM is also shown as reference. The simulated spectra are shifted by 19 eV to larger binding energies, in order to make the simulated PPP1 spectrum lie on top of the experimental one (the shift of the simulated spectra is discussed in sections 4.2 and 4.4). Position and intensities of the main peaks do not agree very well, in particular in the simulated spectrum two equally intense peaks can be identified at the high energy site, whereas in the experimental spectrum only one peak is visible, with the other one being probably hidden under the tail of the most intense one.

Regarding the positions, the experimental main peak lies at about 285 eV, while in the simulated spectrum the central peak lies at 285.5 eV and the peak at highest binding energies lies at 286 eV. The shoulder at lower binding energies lies instead in both spectra at about 284.1 eV, showing nice agreement also in terms of intensity. This is consistent with the fact that this signal comes from the lowermost phenyl ring (as also confirmed by panel b of figure 4.19) and that the simulated spectra are all shifted taking the experimental PPP1 as reference. Energetically, the shoulder should essentially lie at the same position of the PPP1 signal (if the SAMs have comparable packing densities), and this is indeed the case. Concerning the other peaks, the intensity of the simulated ones does not really agree with experiments, in particular the central peak should be the most intense one and the peak at 286 eV should be much less intense. In the simulated spectra the relative intensities of the peaks are governed by the damping parameter β. In this case $\beta = 0.47$ has been used, since no more suitable value could be found that allowed better reproducing the experimentally observed relative intensities. Regarding the peak positions, the main peak in the experimental spectrum is shifted by about 0.6-0.7 eV to larger binding energies with respect to the PPP1 SAM, while in the simulations the central peak is shifted by 1.3 eV.
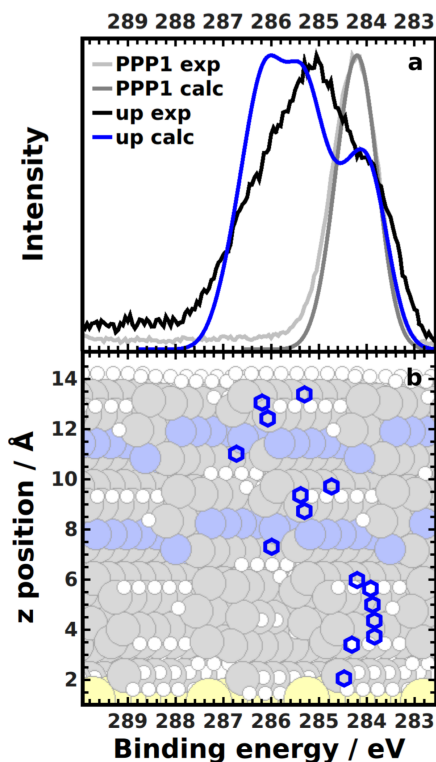
Figure 4.19: C1s XP spectrum of the PmPmP1-up SAM at a photon energy of 580 eV. In panel a the experimental spectrum is compared to the simulated one. The experimental and simulated PPP1 SAM XPS are also drawn for comparison. In panel b the energetic positions of the C atoms of the PmPmP1-up SAM are given (average over the 2 inequivalent molecules in the unit cell), in order to identify which atoms contribute to which peaks in the overall spectrum. As mentioned in the test, the simulated spectra are shifted by 19 eV to larger binding energies (value needed to make the simulated and experimental PPP1 SAM XPS lie on top of each other).

As extensively discussed in sections 4.2 and 4.4, the work function changes should reflect the shifts observed in XPS. According to the experimental data, the work function of PmPmP1-up SAM is by 0.7 eV lower than the work function of the reference system PPP1 SAM (4.4 eV). The calculations predict instead for the PmPmP1-up SAM a work function lower by 1.28 eV than in the PPP1 SAM case ($\Delta\Phi = -1.3$ eV), thus largely overestimating the experimental value. However, both in experiments and simulations these values are fully consistent with the shifts between the PPP1 and the PmPmP1-up peaks observed in XPS.

To clarify why the experimental shift is so much smaller than the calculated one, and considering that the coverage used in the calculations is compatible with the experimental coverage obtained analysing both XPS and STM results, some explanations were proposed, with valuable input from Professor Christian Slugovc from the Institute for Chemistry and Technology of Materials of the Graz University of Technology. Some molecules could for instance orient in the opposite direction due to the unfavourable interaction between the parallel dipolar units. The inversion of the orientation could in principle take place with two mechanisms, shown in figure 4.20. The occurrence of flipped molecules was thought actually to be pretty unlikely, since the presence of an -SH group should produce a distinct signal in the S2p XPS, not seen in the present case. Alternatively, some molecules could undergo some sort of exchange reactions via homolytic breaking of the S—C bond and formation of a radical intermediate.

To test the effect of the possible presence of flipped or exchanged molecules, a twice as big unit cell was set up with 4 molecules/unit cell and one of the molecule was flipped, respectively exchanged, resulting therefore in a 1:3 mixed arrangement. To make the simulations
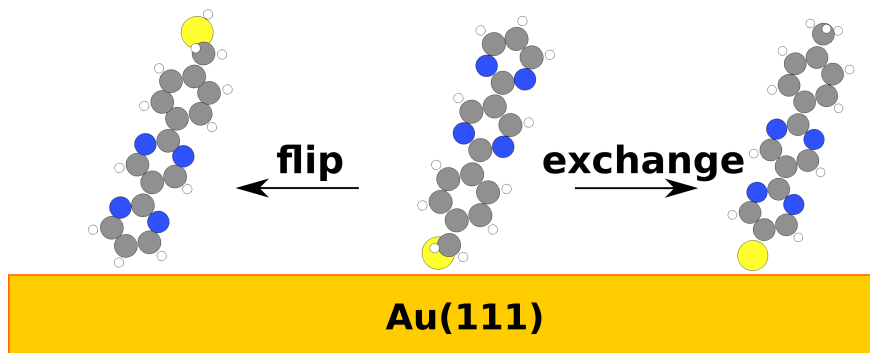
Figure 4.20: Hypothetic flip and exchange reactions for the PmPmP1-up SAM.

cheaper, the mixed arrangements were calculated using only 3 layers of Au and light settings (see computational details). In table 4.9 the total energies per molecule for the regular, 1:3 exchanged and 1:3 flipped arrangements are given.

Table 4.9: Total energies per molecule for the regular, 1:3 exchanged and 1:3 flipped PmPmP1-up SAMs. For the 1:3 flipped case the energy of half of a H_2 molecule is subtracted because of stoichiometry. All the structures are optimised using 3 Au layers and light settings.

	Energy / eV (light, 3 Au layers)
PmPmP1-up	$-4\,853\,443.202$
PmPmP1-up exchanged	$-4\,853\,443.152$
PmPmP1-up flipped	$-4\,853\,443.173$

The 1:3 exchanged arrangement is less favourable than the regular one by 0.050 eV/molecule. The 1:3 flipped arrangement is higher in energy than the regular one, too, but only by 0.029 eV/molecule. Keeping in mind that the used settings might not be properly converged, such small energy differences do not allow conclusive considerations regarding the stability. For that, further more accurate calculations are needed. Moreover, for the flipped case there are at least two relevant conformations of the S–H bond that should be tested: they differ in the orientation of the H atom, downwards oriented in one case, upwards oriented in the other. Nevertheless, the purpose of the test on the mixed arrangements was not finding the overall most stable arrangement, but rather understanding their possible impact on the work function change $\Delta\Phi$ and XP spectra. The $\Delta\Phi$ values obtained for the different arrangements are reported in table 4.10, where PPP1 and PPmP1-up are also given for comparison.

Table 4.10: $\Delta\Phi$ calculated for the different PmPmP1-up arrangements using the FHI-aims default light basis set for all the elements and only 3 layers of Au to describe the metal substrate (see text for more details). As reference, also the values for PPmP1-up and PPP1, calculated using the FHI-aims default tight settings and 5 layers of Au, are given.

	$\Delta\Phi$ / eV
PmPmP1-up	-2.62 (light, 3 Au layers)
PmPmP1-up exchanged	-2.04 (light, 3 Au layers)
PmPmP1-up flipped	-1.78 (light, 3 Au layers)
PPmP1-up	-1.88
PPP1	-1.30

As expected, introducing a percentage of flipped or exchanged molecules reduces $\Delta\Phi$. In particular, considering the flipped case, the $\Delta\Phi$ is even smaller than the one induced by the PPmP1-up SAM, with only one pyrimidine ring in the backbone. Please note that the values could change when refining the optimisation, but the change is not expected to be so dramatic. More interesting is the fact that actually the core level energies of the S atoms in the 1:3 flipped arrangement are all within 0.1 eV, even if one of the S belongs to a thiol. This might be due to superimposed chemical and electrostatic effects and means that the possible occurrence of a flipped molecule might not be immediately detectable from the S2p XPS. Regarding the C1s XPS, the calculated spectrum for the flipped arrangement is plotted and compared to the regular arrangement in figure 4.21.

Figure 4.21: C1s XP spectrum of the PmPmP1-up SAM. The calculated XPS for the regular (blue curve) and the 1:3 flipped arrangement (orange curve) are compared to the experimental spectrum registered at a photon energy of 580 eV (black line). As mentioned in the text the simulated spectra are shifted by 19 eV to larger binding energies (value needed to make the simulated and experimental PPP1 SAM XPS lie on top of each other, see figure 4.19).

Consistent with the smaller electrostatic shift, the spectrum of the flipped arrangement is shifted towards lower binding energies with respect to the regular case. In terms of agreement to experiments, the shift with respect to PPP1 is now underestimated, which could mean that in case of real occurrence of flipped molecules, their density would be lower than 1:3. This would, of course, impact also the intensities, that now do not really compare very well to the experimental spectrum. Moreover, it should be noted that the spectrum of the flipped arrangement is obtained using a smaller variance (0.10 eV) than the spectrum of the regular case (0.15 eV). The smaller value was used to resolve the three peaks, taking a larger value only one broader peak centred at about 284.6 eV is obtained. The XP spectrum for the exchanged arrangement is shown, too, although that arrangement is somewhat higher in energy, and is shown in figure 4.22.

Obviously also the XPS of the exchanged arrangement is shifted towards smaller binding energies than the regular case. Also in this case the simulated and experimental intensities somewhat disagree. This can be rationalised considering that in the simulations even the mixed structures are highly ordered, while in reality the degree of disorder is expected to be much higher and it is very unlikely that exactly the 1:3 ratio occurs. What could instead be interesting would be to try a larger unit cell, lowering this way the density of
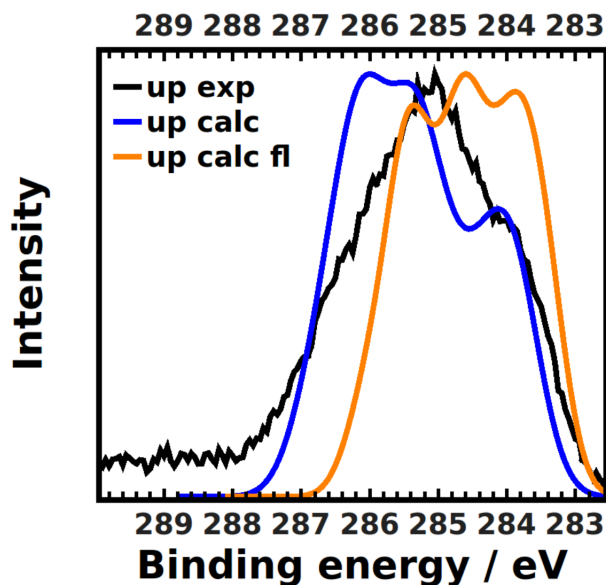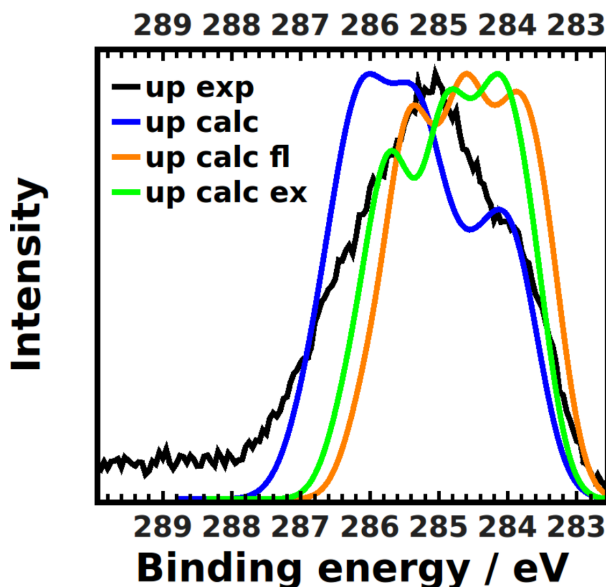
Figure 4.22: C1s XP Spectrum of the PmPmP1-up SAM. The calculated XPS for the regular (blue curve), 1:3 flipped (orange curve) and 1:3 exchanged (green curve) arrangements are compared to the experimental spectrum registered at a photon energy of 580 eV (black line). As mentioned in the text the simulated spectra are shifted by 19 eV to larger binding energies (value needed to make the simulated and experimental PPP1 SAM XPS lie on top of each other), see figure 4.19).

flipped/exchanged molecules, not only to see the impact on the XP spectra but also to look at the S core level energies: in the 1:3 flipped case they are all very close, using a different ratio the situation might change due to the different electrostatic effects.

The presented models show that the occurrence of flipped or exchanged molecules, although clearly not in a 1:3 ratio, could provide a plausible explanation for the smaller measured $\Delta\Phi$.

Regarding the N binding energies, according to the calculations, in the exchanged and flipped case the N core level energies should lie at about 0.35 eV smaller energies than in the regular case.

PmPmP1-down C1s X-ray photoelectron spectra

In figure 4.23 the simulated and the experimental 580 eV PmPmP1-down XP spectra are compared. As done for the PmPmP1-up SAM, the simulated spectrum is shifted by 19 eV to larger binding energies and the experimental and calculated PPP1 SAM XPS are given as reference.

In both the experimental and simulated spectra only one peak is visible. The experimental peak is broad and asymmetric, while the simulated one is almost symmetric, with only a tail at larger binding energies. Regarding the position, the simulated spectrum lies essentially on top of the PPP1 one (this can be again explained with superimposed electrostatic and chemical effects), while the experimentally measured one lies at about 284.8 eV, that is at 0.6 eV larger binding energy than PPP1.

The measured Φ is 5.03 eV, that is 0.63 eV higher than for PPP1 (4.4 eV). The calculated $\Delta\Phi$ is 1.06. Considering that the theoretical $\Delta\Phi$ for the PPP1 SAM is -1.30 eV, the calculated values are again way larger than the measured ones. Contrary to what done for PmPmP1-up, it is now not really possible to correlate $\Delta\Phi$ and XPS shifts: essentially all the C atoms mainly contributing to the spectrum, namely the highest ones, experience both the electrostatic effect that lower their binding energies (increasing of the surface Φ) and the

81
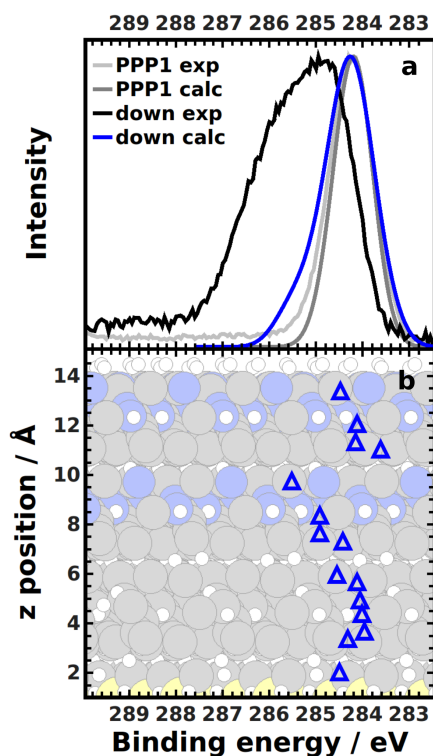
Figure 4.23: C1s XP spectrum of the PmPmP1-down SAM. In the panel a the experimental spectrum registered at a photon energy of 580 eV is compared to the simulated one. The experimental and simulated PPP1 SAM XPS are also drawn for comparison. In panel b the energetic positions of the C atoms constituting the PmPmP1-down SAM are given (average over the 2 inequivalent molecules in the unit cell), in order to identify which atoms are contributing to which peaks in the overall spectrum. As mentioned in the text the simulated spectra are shifted by 19 eV to larger binding energies (value needed to make the simulated and experimental PPP1 SAM XPS lie on top of each other).

chemical effect of being bonded to N atoms, that leads to larger binding energies. This superposition of effects is also the reason why the PmPmP1-down peak lies at the same position of the PPP1 one.

Also for the PmPmP1-down SAM the 1:3 exchanged and flipped arrangements were tested. The total energies per molecule of the different arrangements are reported in table 4.11.

Table 4.11: Total energies per molecule for the regular, 1:3 exchanged and 1:3 flipped PmPmP1-down SAMs. For the 1:3 flipped case the energy of half of a H_2 molecule is subtracted because of stoichiometry. All the structures are optimised using 3 Au layers and light settings.

	Energy / eV (light, 3 Au layers)
PmPmP1-down	$-4\,853\,443.013$
PmPmP1-down exchanged	$-4\,853\,443.040$
PmPmP1-down flipped	$-4\,853\,443.033$

Contrary to the PmPmP1-up case, now the flipped and exchanged arrangements are more favourable than the regular one. However also in this case, since the energy differences are really tiny, namely 0.027 eV for the exchanged and 0.020 eV for the flipped arrangement, a refinement of the settings is needed. Moreover, in this case the terminal H atom of the flipped molecule has the opposite orientation it has in the PmPmP1-up case. This impact of the H

orientation needs to be more accurately tested. What is instead worthwhile noticing is that, for all the three arrangements, the PmPmP1-up SAMs have lower total energies than the PmPmP1-down SAMs (0.189, 0.112 and 0.140 eV/molecule for the regular, 1:3 exchanged and 1:3 flipped arrangement, respectively). This is probably due to the fact that the dipoles of the molecules in the PmPmP1-down SAMs are larger: according to the calculations the dipoles of isolated gas phase PmPmP1-up and PmPmP1-down thiolates are 3.37 and 5.34 D, respectively. The repulsion between the parallel arranged PmPmP1-down molecules in the SAM is therefore stronger, lowering thus the stability of the structure with respect to the SAM formed by the molecules with the opposite dipole orientation.

In table 4.12 the calculated $\Delta\Phi$ for the PmPmP1-down arrangements is reported.

Table 4.12: $\Delta\Phi$ calculated for the different PmPmP1-down arrangements using the FHI-aims default light basis set for all the elements and only 3 layers of Au to describe the metal substrate (see text for more details). As reference, the values for PPmP1-down and PPP1, calculated using the FHI-aims default tight settings and 5 layers of Au, are given.

	$\Delta\Phi$ / eV
PmPmP1-down	1.13 (light, 3 Au layers)
PmPmP1-down exchanged	0.18 (light, 3 Au layers)
PmPmP1-down flipped	0.55 (light, 3 Au layers)
PPmP1-down	−0.50
PPP1	−1.30

Also in this case, introducing flipped or exchanged molecules lowers the calculated $\Delta\Phi$. For every arrangement, the PmPmP1-down SAM gives a positive $\Delta\Phi$, meaning that the SAM increases the Φ of the Au substrate. On the contrary, the adsorption of the PPmP1-down SAM reduces the work function of the substrate. In experiments, instead, also the PmPmP1-down SAM decreases the Φ of the clean Au surface: according to the measured data, the Φ of the PmPmP1-down modified Au(111) surface is 5.03 eV, about 0.17 eV lower than the 5.2 eV usually measured for a clean Au(111) surface. Coming back to the possible occurrence of exchanged or flipped molecules, the S and N core level energies for the considered PmPmP1-down arrangements were calculated: in this case, this allows excluding the presence of flipped molecules (at least at this density), for which the S signal would lie at 1.9 eV smaller binding energies than the docking S atom. As already mentioned, the H orientation could have an impact on the binding energy of the thiol S and needs to be tested. Regarding the N binding energies, in the flipped and exchanged cases they are predicted to be about 0.55 eV larger than in the regular arrangement. How the mixed arrangements would modify the C1s XP spectrum is shown in figure 4.24.

The presence of flipped or exchanged molecules, that lead to the 25% of the dipoles pointing in the opposite direction that the other ones, induces a shift of the spectrum towards larger binding energies (the spectrum of the flipped arrangement is plotted, too, even if it can be excluded from the S binding energies). The spectra of the mixed arrangements are broader than in the regular case (please note than for all these simulated spectra the same variance has been used used, 0.15 eV). This improves the agreement with the experimental spectrum in terms of shape, however in terms of position the spectrum still lies at too small binding energies.

Even if no full agreement between experimental and calculated spectra could be found, also in this case the introduction of some disorder in the system improves the comparison, as it has already been the case for the PmPmP1-up SAM.
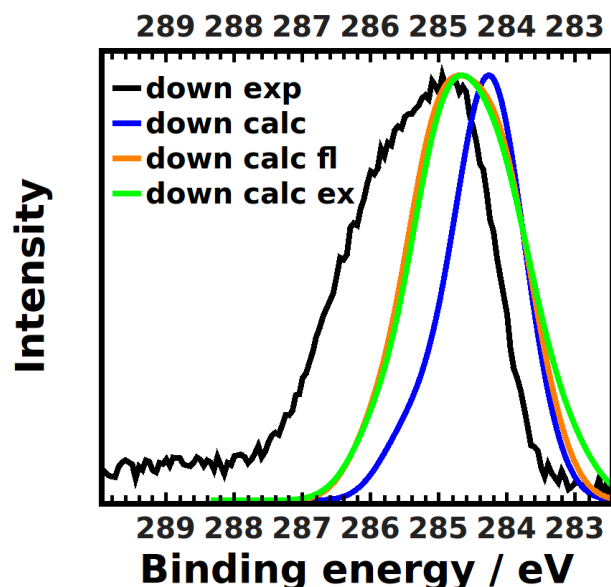
Figure 4.24: C1s XP spectrum of the PmPmP1-down SAM.The calculated XPS for the regular (blue curve), 1:3 flipped (orange curve) and 1:3 exchanged (green curve) arrangements are compared to the experimental spectrum registered at a photon energy of 580 eV (black curve). The simulated spectra are shifted by 19 eV to larger binding energies (value needed to make the simulated and experimental PPP1 SAM XPS lie on top of each other (see figure 4.23).

4.3.4 Substituted PmPmP1- SAMs

From the perspective of tuning the work function of metal substrates within an even larger range, several derivatives of the PmPmP1 SAMs were designed and calculated. The derivatives were conceptually obtained functionalising the topmost pyrimidine ring by the addition of a tail group. The systems are shown in figure 4.25.

With the PmPmP1-up SAM NH_2, $N(CH_3)_2$ and C_5H_4 (pyrrolidine ring) groups were combined, the PmPmP1-down SAM was instead substituted using F, CF_3, SF_5 and CN groups. The calculated work function modifications are reported in table 4.13.

According to the simulations, using the PmPmP1 derivatives it would be possible to tune the work function of a Au(111) surface over a range of almost 8 eV. As previously discussed, however, much smaller modifications are to be expected for the real systems. This is due, on one side, to the systematic overestimation of work function modifications in
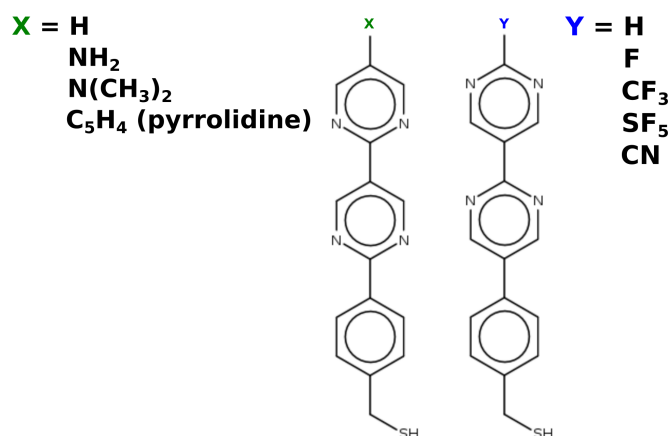
Figure 4.25: PmPmP1 SAMs derivatives considered in this work.

Table 4.13: Calculated work function change ($\Delta\Phi$) for the investigated PmPmP1- SAMs derivatives.

		$\Delta\Phi$ / eV
	H	−2.58
X=	NH$_2$	−3.01
	N(CH$_3$)$_2$	−4.00
	C$_5$H$_4$	−4.03
	H	1.06
	F	2.16
Y=	CF$_3$	2.62
	SF$_5$	2.93
	CN	3.53

PBE calculations, as pointed out throughout the whole work. On the other side, simulations describe a perfectly ordered situation that in reality might not occur or might be disturbed by the presence of imperfections or defects. The calculated results give, nevertheless, an indication of possible derivatives that could be synthesised and experimentally tested. A further interesting aspect is that the derivatisation using a polar tail group allows modifying the work function of the substrate beyond pinning effects. This can be understood looking at the densities of states (DOS) plotted in figure 4.26 for the PPP1, PmPmP1-up and PmPmP1-down SAM. As can be seen comparing the PPP1 and the PmPmP1-up SAMs, embedding in the backbone an upwards pointing dipole shifts the states localised on the molecules to smaller energies. Comparing the PPP1 and the PmPmP1-down SAMs, the opposite effect is observed: for a downwards pointing dipole the states shift upwards in energy. While in the PmPmP1-up case the highest occupied and the lowest unoccupied states localised on the molecule are still far from the Fermi level, in the PmPmP1-down case the highest occupied molecular state gets pinned at the Fermi level. The consequence of Fermi level pinning is that also by increasing the molecular dipole, for instance by introducing a further pyrimidine ring, it would not be possible to further modify the work function of the substrate, since the highest occupied molecular state can not be shifted above the Fermi level. However, the values of table 4.13 confirm that introducing the polar tail groups it is still possible to induce larger work function modifications, also for the PmPmP1-down derivatives. The reason for that is discussed in detail reference 122. What counts for the work function modification is the position of the dipole layer: if this latter is localised within the pinning induced charge rearrangement region it does not have any impact on the work function of the pinned system. However, if the dipoles are localised above that region, they will have an additive effect. This is indeed what happens for the systems considered in this section, with the dipolar units introduced as tail substituents.

4.3.5 Conclusions

In this section a new generation of SAMs with embedded dipole moments for electrode work function modification has been presented. The investigated systems are thiolate SAMs with an aromatic backbone containing two pyrimidine rings as polar elements. The position of the N atoms determines the direction in which the dipole points. The new generation of molecules is conceptually derived from the systems investigated in section 4.2 of the present thesis and from the SAMs treated in reference 114. The derivatives of the SAMs discussed in section 4.2 consist of two pyrimidine rings directly bonded to the docking group (PmPm- SAMs), while the derivatives of the system investigated in reference 114 are longer,
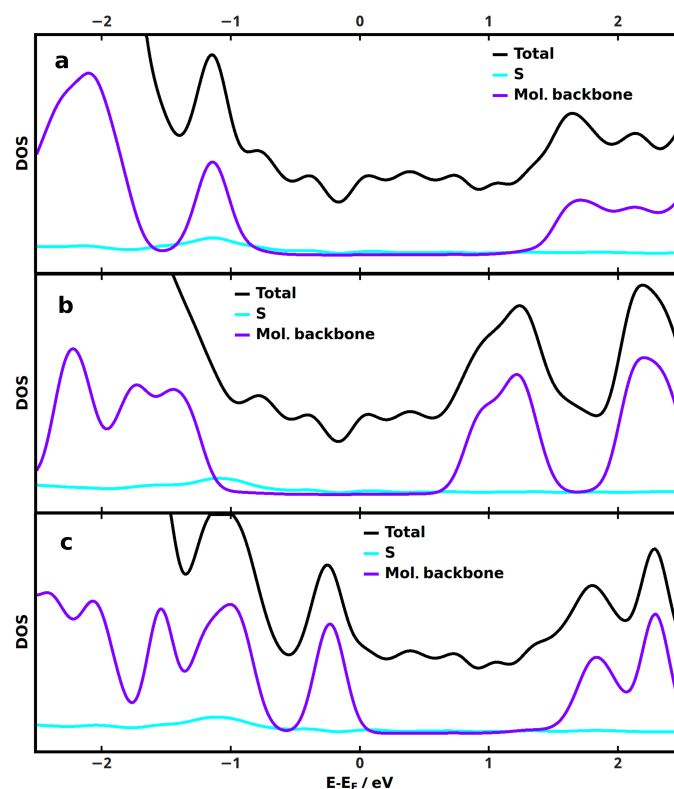
Figure 4.26: Density of states (DOS) around the Fermi level for the PPP1 (panel a), PmPmP1-up (panel b) and PmPmP1-down (panel c) SAMs. The total DOS (black lines) and the DOS projected onto the docking groups (light blue lines) and the molecular backbones (purple lines) are plotted.

containing a further phenyl ring and a methyl spacer between the aromatic backbone and the docking groups (PmPmP1- SAMs). According to the calculations, the expected work function modification induced by the PmPm- SAMs were -2.62 and +0.95 for the up and the down SAM, respectively. In the case of the PmPmP1 SAMs the calculated values were in a similar range, being -2.58 and +1.06 eV for the PmPmP1-up and the PmPmP1-down SAMs, respectively. The measured $\Delta\Phi$ values were instead much smaller, being -0.9 and -0.3 for the PmPm-up and PmPm-down SAMs and -1.50 and -0.17 for the PmPmP1-up and PmPmP1-down SAMs. Regarding the structural parameters, the calculated and measured values shown better agreement for the PmPmP1- SAMs than for the PmPm- ones. In this latter case, the experimental coverage of the PmPm-up SAM was relevantly smaller than the one observed for the other SAMs. This observation was tentatively explained by a non favourable interaction between the bottom N atoms in the SAM and the metal substrate. The comparison of the simulated and measured XP spectrum shown several discrepancies, in particularly for the PmPm-SAMs, attributed to the somewhat bad quality of the films obtained for these SAMs. For the PmPmP1- systems the main discrepancy between calculated and experimental values was that the predicted electrostatic shift was much larger than the experimentally observed one. This was evident from the comparison of both the $\Delta\Phi$ values and the XP spectra. To rationalise that inconsistency, the introduction of some disorder in the system, in terms of flipped or exchange molecules, was tested. The computational analysis of such mixed SAMs indeed indicated that the experimental values are compatible with films in which defects and imperfections are present. For the PmPmP1-SAMs also several derivatives obtained introducing a polar tail substituent were presented, that according to the calculations could allow tuning the substrate work function within a range of almost 8 eV.

The results of this preliminary characterisation show that the new generation of molecules

is predicted to be particularly promising in terms of work function modification. According to the first experimental results, however, the molecules containing two bipyridine rings seem not to form good quality films, particularly in the case of the PmPm-SAMs.

4.4 Dithiocarbamate anchoring group as flexible platform for interface engineering

The characterisation of S docked SAMs is of particular interest since, as already pointed out, SAMs of thiols on the Au(111) surface are the most common metal/SAM interface. Substituting S with Se, as discussed in section 4.1, is not the only way to explore alternatively docked SAMs. Different, less usual moieties have been tested, such as for instance the dithiocarbamate (DTC) group. The peculiarity of DTC based SAMs is that they dock to the surface with both the S atoms of the DTC functional group. DTC SAMs have already been shown to form good quality films and to induce convenient work function modifications [38]. In this section two basic DTC docked SAMs are characterised by means of X-ray and ultraviolet photoelectron spectroscopy (XPS and UPS) and near edge X-ray absorption fine structure (NEXAFS) experiments and state-of-the-art density functional theory (DFT) calculations.

The results are reported in form of a manuscript ready for submission to a scientific journal. Only a reduced version of the supporting information is reported. In the extended versional also the optimised geometries in the xyz format will be included. The work was a collaboration between the groups of Florian von Wrochem, Michael Zharnikov and Egbert Zojer. Daniel Trefz and Sabine Ludwigs synthesised the molecules. Eric Sauter and Michael Zharnikov prepared the SAMs and performed UPS, XPS and NEXAFS measurements. Egbert Zojer and I contributed the simulation part. Florian von Wrochem, Michael Zharnikov and Egbert Zojer coordinated the work. The data were discussed and interpreted jointly by all the authors. A first draft of the paper was written by Michael Zharnikov. All the other authors contributed in writing the sections concerning their results and revising the draft. I performed all the calculations presented in the work, prepared figures 4, 5, 6, 7 and 8 and wrote a draft of the computational part, that was then revised and corrected by Egbert Zojer and incorporated in the manuscript by Egbert Zojer and me. I wrote the supporting information and prepared all the figures presented there. The text was revised and corrected by Egbert Zojer.

4.4.1 Manuscript

Dithiocarbamate Anchoring Group as Flexible Platform for Interface Engineering

Eric Sauter,[1,#] Giulia Nascimbeni,[2,#] Daniel Trefz,[3] Sabine Ludwigs,[3]
Egbert Zojer,[2*] Florian von Wrochem,[4*] and Michael Zharnikov[1*]

[1] *Applied Physical Chemistry, Heidelberg University, Im Neuenheimer Feld 253, 69120 Heidelberg, Germany*

[2] *Institute of Solid State Physics, NAWI Graz, Graz University of Technology, Petersgasse 16, 8010 Graz, Austria*

[3] *Chair for Structure and Properties of Polymeric Materials, Institute of Polymer Chemistry (IPOC), University of Stuttgart, Pfaffenwaldring 55, 70569 Stuttgart, Germany*

[4] *Materials Science Laboratory, Sony Deutschland GmbH, Hedelfinger Strasse 61, 70327 Stuttgart, Germany*

Abstract

Molecular organization and electronic properties of dithiocarbamate (DTC) anchored self-assembled monolayers (SAMs) linked to Au(111) substrates are studied by a combination of X-ray photoelectron spectroscopy (XPS), near-edge X-ray absorption fine structure (NEXAFS) spectroscopy, and state-of-the-art density functional theory calculations. For that, several piperidine/piperazine precursors with different architecture and substitution patterns are selected. The present data show that the DTC anchor provides a useful building block for monomolecular self-assembly on coinage metals with both sulfur atoms bonded to the substrate in a way similar to what is usually observed for the more commonly applied thiolate docking group. The combination of the DTC group with the quite flexible piperidine/piperazine cyclic linkers results in a dense molecular packing with an upright orientation of the terminal moieties. The latter comprise phenyl rings bearing various substituents, which enables tuning the interfacial dipole over a wide range. Simulations on two prototypical DTC-docked SAMs help to better understand the experimental observations and provide insight into the local origin of the SAM-induced shifts in the electrostatic energy. In particular, a comparison of measured and simulated XPS spectra reveals the significant contribution of the DTC group to the interfacial dipole.

1. Introduction

Energy level alignment and injection control at the interfaces between electrodes, organic semiconductors, and buffer layers are highly important issues in the context of modern organic electronics and photovoltaics. A popular approach in this regard is the use of self-assembled monolayers (SAMs),[1-14] which are densely packed molecular assemblies of typically rod-shaped molecules adsorbed on a substrate in a well-defined upright geometry. Generally, such molecules consist of three major building blocks, viz. a docking group that provides the anchoring to the substrate, a tail group comprising the "outer" SAM-ambient interface, and a spacer that separates the docking and tail groups and drives the self-assembly.[15,16] While all these building blocks can contribute to the joint dipole moment of the molecules constituting the film, it is mostly a dipolar tail group[2,3,5,10,17] or a polar mid-chain moiety[18-21] which is usually selected to specifically adjust the interfacial dipole. In contrast, the docking group is predominantly chosen based on the affinity to a particular substrate serving as an electrode or, in the context of organic photovoltaics, also as a buffer layer. Examples for docking groups comprise phosphonic acids for zinc oxide surfaces[10,22] (a popular interfacial layer material in organic electronics devices), phosphonic acids and triethoxy- or trichlorsilanes for indium tin oxide[9,22,23] (standard transparent electrode material for organic solar cells), and thiolates for coinage metal substrates,[7,16,17] such as gold and silver (frequently used electrode materials).

Recently, as an alternative to thiolates, the dithiocarbamate (DTC) anchor group[24-29] has been suggested as a basis for the functionalization of gold nanoparticles, for molecular electronics, and for the fabrication of dipolar SAMs to be applied in organic electronics.[30,31] In combination with piperazine and piperidine as an intermediate linker, this group provides a versatile and robust platform for the attachment of different spacer moieties and tail groups. In particular, the piperidine/piperazine linker, forming the bridge between the DTC group and the aromatic substituents, ensures the rod-like symmetry of the molecular backbone,[30,32] thus allowing a perpendicular orientation of the molecular axis relative to the substrate (a feature not available in earlier aromatic DTC derivatives)[24,27,33]. This allows the realization of a family of monolayers delivering work functions of SAM-covered Au electrodes between 4.8 eV and 3.2 eV.[30] Although the performance of DTC-docked systems in polymer junctions has been demonstrated and a first spectroscopic characterization of the films along with molecule-based calculations has been provided,[30] the precise structure and molecular orientation of DTC-based SAMs is still largely unexplored. In addition, a deeper understanding of the electronic properties of such SAMs is of fundamental interest in view of the largely unexplored potential of the used unconventional docking group. Of particular relevance in this context is the question which of

3

the contained functional blocks is actually responsible for the shift in the electronic landscape that gives rise to the comparably large work function changes.

In the present work, to gain this understanding, we applied advanced spectroscopic tools in combination with state-of-the-art quantum mechanical simulations of SAM/Au interfaces. This combination of simulations and experiments, on the one hand, provides insight into the molecular orientation and order of these films, which need to be understood to correlate the molecular properties with the electrostatic potential drop across the metal-organic interface. On the other hand, it affords an in-depth and reliable insight into the atomistic origins of potential shifts and charge rearrangements. Consequently, the primary emphasis of the following discussion was put on the two very basic systems, viz. phenyl-piperidine-DTC (PPd) and phenyl-piperazine-DTC (PPz) SAMs on Au(111) (Figure 1). These monolayers represent highly suitable model systems, which were specifically designed for the present experiments and selected for the simulations to address the distinct properties of the piperidine-DTC and piperazine-DTC docking platforms. The terminal phenyl ring of both molecules is a non-polar and well-defined structural unit supporting the formation of ordered SAMs. Convenient in the present context, it also provides a marker for the spectroscopic experiments (see below). The other DTC derivatives investigated in this study are derived from these two basic systems (parent compounds) by a simple substitution of the phenyl ring in the para position or by its fluorination. Their structures and the used abbreviations are compiled in Figure 1.
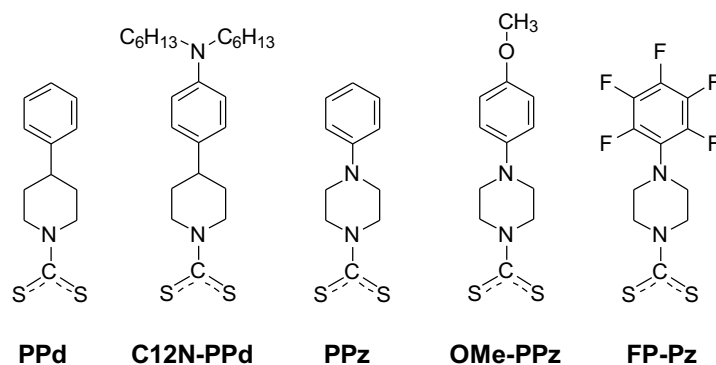
Figure 1. *Schematic structures of the DTC-based SAM constituents used in this study along with the respective abbreviations. Note that the C12N-PPd, OMe-PPz, and FP-Pz monolayers have been studied before, but in somewhat different context as compared to the present work.*[30]

2. Experimental and Theoretical Methods

2.1. SAM Preparation

The synthesis of the DTC-based SAM constituents (Figure 1) was done within an "in-situ" process involving coupling the precursor amines to CS_2. The amine precursor of C12N-PPd

4

(Figure 1) was custom-synthesized as reported in the literature.[30] All other amine precursors for the synthesis of the OMe-PPz, FP-Pz, PPd and PPz DTC derivatives (Figure 1), i.e. the 1-(4-methoxphenyl)piperazine, 1-(pentafluorophenyl)-piperazine, 4-phenylpiperidine, and 1-phenylpiperazine were obtained from Sigma Aldrich, Acros GmbH, Sigma Aldrich, and ABCR, respectively, and used as received. CS_2 (p.a.), ethanol (p.a.), and triethylamine were obtained from Sigma Aldrich and Fluka, respectively. The coupling of the precursor amines to CS_2 occurred according to the following protocol. Initially, concentrated stock solutions of CS_2 (100 mM), the amine-terminated precursors (5 mM), and triethylamine (100 mM) were prepared in ethanol. Subsequently, the CS_2 and triethylamine solutions, along with some ethanol, were added (in this sequence) to the amine precursor solution to form an equimolar 1:1:1 precursor:CS_2:triethylamine mixture (with a concentration of 1 mM each). The mixture causes the spontaneous reaction of CS_2 with the respective amine precursor yielding the desired dithiocarbamate species (1 mM), that spontaneously and irreversibly reacts with the Au(111) substrate when the latter is added to the mixture.[24,26] All steps were carried out in a glove box under nitrogen atmosphere to avoid oxidation reactions. The above DTC solutions were directly used for the SAM preparation on gold substrates. As a side note, great care has to be taken in order to avoid any contamination in the glove box, because of the significant risk that thiolate species in the vapor phase might compete with the (rather slow) chemisorption process of dithiocarbamates on Au (thus compromising SAM purity and uniformity). As substrates, atomically flat template stripped gold (TSG) was employed and prepared according to reported procedures.[34,35] The Au films exhibited a root mean square (RMS) roughness of 0.3 nm, exposing preferably (111) oriented surfaces. The organic monolayers were prepared under nitrogen by immersing the freshly stripped TSG substrates into DTC solutions for ~20 h at room temperature. After immersion, the films were copiously rinsed with ethanol, immediately blown dry with N_2 and placed in nitrogen filled glass containers for the transport to the synchrotron radiation facilities (see below). All vials and tweezers were cleaned with piranha acid and isopropyl alcohol before usage. In addition, reference SAMs of dodecanethiolate (DDT) and hexadecanethiolate (HDT) were prepared on analogous gold substrates using a standard procedure.[36]

2.2. SAM Characterization

The fabricated SAMs were characterized by synchrotron-based X-ray photoelectron spectroscopy (XPS) and angle-resolved near-edge X-ray absorption fine structure (NEXAFS) spectroscopy. XPS serves as an efficient local probe of the potential distribution within a SAM, at the same time representing a reliable benchmark for theoretical simulations.[18,19,37] NEXAFS

5

spectroscopy represents a complementary technique, which not only shows high chemical sensitivity but also has the capability of providing information on molecular orientation in adsorbate assemblies and molecular films.[38] Significantly, such information can be obtained not only for highly ordered systems, but also for samples, in which short- or medium-range order prevails. The latter is frequently the case for SAMs due to structural defects, polymorphism, and a limited size of crystalline domains. These are associated with possible imperfections of the self-assembly process and misfits between the optimal molecular lattice and the structural template provided by the substrate, as well as by the nucleation-type growth of SAMs (leading to domain boundaries).[16]

The measurements were carried out at room temperature under UHV conditions (base pressure of ~1.5×10⁻⁹ mbar). The data acquisition time at a particular sample spot was kept short to minimize possible X-ray induced damage occurring during the measurements.[39] Experiments were performed at the HE-SGM beamline of the synchrotron storage ring BESSY II (Helmholtz Zentrum Berlin, Germany) and at the D1011 beamline of the MAX IV synchrotron radiation facility (Lund, Sweden). Both are bending magnet beamlines, providing a moderate X-ray intensity, which is a prerequisite for avoiding X-ray induced damage of the comparably sensitive organic films.

The XPS spectra were acquired using either a Scienta R3000 electron energy analyzer (BESSY II) or a SCIENTA SES200 spectrometer (Max IV). The spectra acquisition was carried out in normal emission geometry with an energy resolution of either ~0.1 eV (Max IV) or ~0.3 eV, ~0.6 eV, and 0.7 eV (BESSY II) at excitation energies of 350 eV, 580 eV, and 720 eV, respectively. The binding energy (BE) scale of the XPS spectra was referenced to the Au $4f_{7/2}$ peak of the underlying substrate at a BE of 84.0 eV.[40] The obtained spectra were decomposed into individual component peaks and doublets using symmetric Voigt functions and a linear or Shirley-type background. To fit the S $2p_{3/2,1/2}$ doublets we used two peaks with the same full width at half-maximum (fwhm), employing the standard[40] spin-orbit splitting of ~1.18 eV (verified by the fit), and a branching ratio of 2 (S $2p_{3/2}$/S $2p_{1/2}$).

Based on the XPS data, the effective thickness and the packing density of the SAMs were calculated. The evaluation was performed within the standard procedures,[41,42] based on the C 1s/Au 4f and S 2p/Au 4f intensity ratios. A standard expression for the attenuation of the photoemission signal was assumed (see the Supporting Information and ref 43) and literature values for the attenuation lengths in densely packed organic films were used[44]. The spectrometer-specific coefficients were determined using reference monolayers

(dodecanethiolate and hexadecanethiolate SAMs on Au) of known thickness (14.9 Å and 18.9 Å, respectively) and packing density (4.63×10^{14} molecules/cm^2 or 21.6 Å^2/molecule)[36,45].

The acquisition of the NEXAFS spectra was carried out at the carbon K-edge in the partial electron yield (PEY) mode with a retarding voltage of −150 V. Linearly polarized synchrotron light with a polarization factor of either ~88% (Bessy II) or ~95% (Max IV) was used as the primary X-ray source; the incidence angle was varied to monitor linear dichroism effects.[38] The photon energy (PE) scale was referenced to the pronounced π* resonance of highly oriented pyrolytic graphite at 285.38 eV.[46] Raw NEXAFS spectra were normalized to the incident photon flux determined from the spectrum of a clean, freshly sputtered gold sample. Afterwards, they were reduced to the standard form by subtracting a linear pre-edge background and by normalizing to the unity edge jump.

In addition to the spectroscopic characterization, the work function of the DTC-based SAMs was measured. It was determined by measuring the secondary electron cutoff of the ultraviolet photoemission (UP) spectra following a standard approach.[47] UP spectra were obtained using a helium UV lamp as a source. The pressure of the helium plasma was adjusted such that the He I (hυ = 21.2 eV) and He II (hυ = 40.8 eV) lines were emitted at a ratio of about 4:1. The photoelectrons were collected by an energy dispersive hemispherical analyzer at a takeoff angle of 90°. The pass energy was set to 5 eV, providing an instrumental resolution of 0.15 eV. Binding energies were referenced to the Fermi level of a clean, argon ion-etched Au surface at 5.2 eV. Note that the work function measurements were performed on the freshly prepared samples, with the quality and contamination/oxidation-free character verified by laboratory XPS measurements performed simultaneously. As was found in complementary experiments, even a slight oxidation of the samples or a lower quality of the films could result in somewhat different work function values.

2.3. DFT Simulations

The theoretical simulations were performed for the two fundamental DTC structures, namely PPd and PPz, as these represent the basic motifs of the investigated class of compounds. A complication in this context is that neither the structure the molecules adopt on the surface, nor the surface unit cell (for the case of commensurate growth) are known. Considering, however, that for PPz essentially the same surface coverage as for the reference SAMs, DDT and HDT, is observed (see below), it is reasonable to assume a structure with two molecules in a (√3×3)*rect* unit cell. For the sake of consistency, we assumed the same surface unit cell for the PPd SAM, although there the surface coverage is by ca. 10% lower. The latter could, however,

7

also be caused by a coexistence of differently ordered regions as will be discussed below. The unit cells for the systems with more bulky substituents and even lower surface coverage (C12N-PPd, OMe-PPz, and FP-Pz) are virtually impossible to estimate in the absence of LEED and STM data and we, thus, refrained from modelling those SAMs. With the surface unit cell fixed, the next complication arises regarding the choice of the relative arrangement of the two molecules within the unit cell, the positions of the S atoms, and the molecular conformations (planar vs. twisted). To tackle that issue, in an attempt to sample the most important regions of the extended potential energy surface, we calculated a significant number of different structures, as described in detail in the Supporting Information. The properties of the most relevant conformations obtained in this way are discussed below.

For performing the simulations, we used the FHI-aims code[48], version 150706, employing the PBE functional[49] in combination with the Tkatchenko – Scheffler dispersion correction[50] in its parametrization for interfaces.[51] van der Waals interactions between the substrate Au atoms were turned off. The systems were simulated using periodic boundary conditions and the repeated slab approach, inserting a vacuum region of at least 20 Å in z direction and including a self-consistently calculated dipole correction[52] between the slabs. The dimensions of the ($\sqrt{3}\times3$)*rect* unit cell in the x and y directions were defined according to the calculated Au lattice constant (see the Supporting Information). The substrate surface was described using five layers of Au; the three bottom layers were held fixed in all calculations. The systems were optimized using the default FHI-aims "tight" settings and a converged Γ-centered $9 \times 5 \times 1$ k-point grid. The total energy convergence criterion for the self-consistency cycle was set to 10^{-6} eV and the optimizations were performed until the maximum residual force component per atom was below 0.01 eV/Å.

To understand the impact of chemical vs. electrostatic shifts in the XPS spectra, reduced coverage systems with nominal coverages of 1/16 and 1/36 were also considered. This dilutes dipoles to a degree that collective electrostatic effects essentially disappear.[19] Reduced coverage systems were modeled via a supercell obtained by replicating the optimized full coverage unit cell, keeping only one molecule. The geometries of the reduced coverage systems were not separately optimized to prevent the molecule from lying flat on the surface, which would result in a completely changed electronic structure dominated by Pauli pushback effects.[53] This would not serve the purpose of solely eliminating electrostatic shifts. To limit the computational cost, for the largest unit cells the metal substrate was modeled with only three Au layers, a reduced basis set, and less tight numerical settings. This was done after convergence tests to ensure that it had only a negligible impact on the obtained results (see Supporting Information).

8

The core-level binding energies were simulated within the initial state approach to avoid artefacts arising from a combination of periodic boundary conditions and explicit excitations in each unit cell.[19] The latter would, for example, occur when performing calculations based on final state approaches[54-61] in conjunction with upright standing SAMs. For obtaining the XPS spectra, we followed the procedure described by Taucher *et al.*[19]. In short, the 1s core level energies for every C atom were taken from the atom projected density of states output files. The screening of the core hole by the metal substrate was included using an electrostatic image charge model[62,63]

$$\varepsilon_{C1s,screened} = \varepsilon_{C1s} + 14.340 \frac{1}{4\varepsilon \cdot (z - z_0)} \quad , \tag{1},$$

where ε is the dielectric constant of the SAM, z is the position of the respective C atom perpendicular to the surface, and z_0 is the image plane position (both given in [Å]). The energy is obtained in eV when using the conversion factor of 14.340 (given by the product of the conversion factors between Hartree and eV, respectively, Bohr and Å). The position of the image plane was set to 0.9 Å above the average z-position of the Au atoms of the topmost layer.[64,65] For the full coverage cases, ε was set to 2.26[66], while for the reduced coverage cases it was set to 1.0. Note that this approach takes neither the finite thickness of the SAM nor screening within the dielectric into account. To model the spectra, the obtained (screened) core-level energies were convoluted with Gaussian functions with a variance of 0.19 eV for both PPz and PPd films. The contribution of every atom was weighted using an exponential attenuation function, considering the finite escape depth of the photoelectrons[44] via an attenuation length set according to a primary photon energy of 350 eV (for more details see the Supporting Information).

3. Results and Discussion

3.1. Experiments: XPS

The S 2p, C 1s, and N 1s XPS spectra of the DTC-based SAMs are presented in Figure 2. The S 2p spectra of all films exhibit a single S $2p_{3/2,1/2}$ doublet at a BE position of 161.82-161.85 eV (S $2p_{3/2}$), as previously shown for dithiocarbamates in general[24] and for the C12N-PPd, OMe-PPz, and FP-Pz monolayers in particular [30]. Significantly, the BE of this doublet is by ~0.15 eV lower than the characteristic value for thiolate species bound to noble metal surfaces (162.0 ± 0.05 eV),[39] in agreement with earlier observations.[24] This suggests a higher negative

9

partial charge on the S atoms compared to the thiolate sulfur, indeed validated by basic considerations based on DTC resonance hybrid structures (stronger donating character of the amine group coordinated to the CS_2 unit). In this sense, the lower BE of the S 2p doublet as compared to thiolate does not necessarily mean that each of the sulfur atoms in the DTC moiety is bound stronger to the substrate than in the thiolate. This is, however, the case for the entire DTC moiety, as demonstrated by thermal stability experiments in which the desorption peak of *n*-butanethiol assembled on Au(111) was observed at noticeably lower temperature (380 ± 10 K) than that of a test DTC compound (470 ± 10 K).[24] Also, the occurrence of just a single doublet at a BE of ~161.85 eV is significant, as it serves as a direct evidence for the formation of SAMs with chemically homogeneous bonding to the substrate. This contrasts positively the situation encountered usually for thiol- and thioether-based ligands with multiple attachment points, where the formation of a variety of different chemical species such as thiolates, atomic sulfur, unbound sulfur, etc. is commonly observed (based on core level shifts in their S $2p_{3/2}$ signal).[67,70] The bonding of the DTC-based SAMs to the substrate in a "thiolate-like fashion" also provides a good chemical link. This is an advantage for efficient charge transport, which is important in the context of organic and molecular electronics applications. Since the spacing between both S atoms in the DTC group (~2.96 Å) does not fit the periodicity of the Au(111) template, multiple adsorption sites can be expected. This is indeed implied by the rather high value for the fwhm of the S $2p_{3/2,1/2}$ components for the DTC-based SAMs, viz. 0.73-0.93 eV compared to dodecanthiolate monolayers measured at analogous conditions, viz. 0.54-0.59 eV.[39] Notably, also in the simulations assuming a very high degree of order with two molecules in the unit cell, inequivalent docking positions of the S atoms were found (see the Supporting Information).

Interestingly, the fwhm value for the PPz SAMs (0.73 eV) is somewhat smaller than that for its derivatives, OMe-PPz, and FP-Pz (0.84 and 0.80 eV, respectively). This suggests an even larger heterogeneity of the adsorption sites (configurations) in the latter cases. The same applies to the PPd and C12N-PPd monolayers, although here the difference (0.89 eV vs. 0.93 eV) is somewhat smaller.

The C 1s spectra of the DTC-based SAMs in Figures 2b and 2c can be decomposed into several component peaks denoted by numbers in the plot. The assignment of these peaks to specific functional groups and specific C atoms is based on electronegativity considerations,[30] the comparison to spectra of systems containing similar building blocks, and the analysis of the spectra acquired at different photon energies. The latter is particularly useful considering the stronger contribution of the buried species at higher excitation energy (580 eV vs. 350 eV). For

10

the PPz and PPd SAMs these tentative peak assignments will be refined in Section 3.4 building on the atomistic insights provided by the DFT calculations.
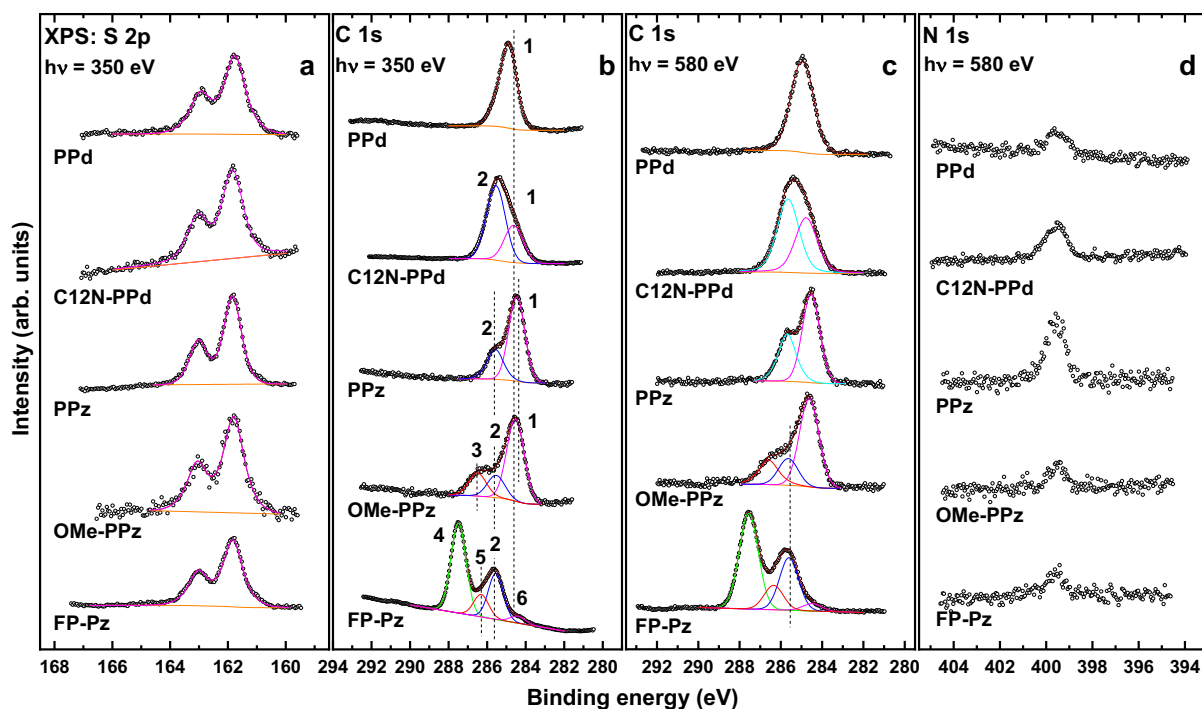
Figure 2. *S 2p (a), C 1s (b, c), and N 1s (d) XPS spectra of the DTC-based SAMs. The spectra were acquired at photon energies of 350 eV (S 2p and C 1s in panel b) and 580 eV (C 1s in panel c and N 1s). The S 2p spectra are fitted by a single S $2p_{3/2,1/2}$ doublet. The C 1s spectra, normalized to the peak height, are decomposed into individual component peaks shown in different colors and marked by numbers, separately for the PPd and PPz related films; see text for details. The vertical dashed lines are guides to the eyes.*

The C 1s spectrum of the PPd SAM exhibits only one, almost symmetric peak at ~284.9 eV (**1**) originating from a superposition of core-level excitations of the terminal phenyl ring and the piperidine moiety. A signal associated with the DTC carbon, expected at a significantly higher BE (see section 3.4), is not perceptible because of its strong attenuation. Similarly, the signal of the two C atoms in the bottom ring bonded to N, which should also appear at higher BE, is not clearly resolved and is presumably hidden in the high BE tail of the main peak. The joint contribution of the phenyl ring and piperidine can also be identified upon decomposition of the asymmetric peak observed in the C 1s spectra of the C12N-PPd SAM into two component peaks. The low BE component peak at ~284.7 eV (**1**) is then assigned to the same C atoms as the sole peak in PPd, while the high BE component at 285.4 eV (**2**) is ascribed to the terminal aliphatic chains. The intensity of this peak is comparably higher since the signal from the phenyl

11

ring and piperidine is more strongly attenuated. This is also the case for the signal stemming from the C atoms bound to the uppermost N atom.

The spectra of the PPz SAM exhibit two peaks at 285.5 eV (**2**) and 284.5 eV (**1**), according to the fits. They are assigned to the C atoms bonded to N atoms (all atoms in the piperazine ring and the lowest atom in the phenyl ring) (**2**) and to all other C atoms in the terminal phenyl ring (**1**), respectively. The origin of the splitting of the peaks in this system will become clear from the discussion in section 3.4. The above two components can also be identified in the spectra of the OMe-PPz film, where they are accompanied by an additional peak at 286.5 eV (**3**), which originates from the carbon atom in the terminal OCH_3 group. Finally, the piperazine component peak (**2**) is clearly resolved also in the spectra of the FP-Pz monolayer. The dominant component in these spectra is, however, the peak at 287.5 eV (**4**), which is related to the fluorine-bonded carbon atoms in the terminal ring. In addition, a low intensity component peak at 286.3 eV (**5**) can be identified upon spectral decomposition. This peak can be tentatively associated with the carbon atom of the upper ring, which is directly bonded to the piperazine but is also somewhat affected by the F atoms in the vicinity. Finally, there is a low BE shoulder at 284.3 eV (**6**) which cannot be assigned to any functional group of FP-Pz and, most likely, stems from contaminations.

The N 1s spectra of all DTC-based SAMs in Figure 2d exhibit a single peak at ~399.5 eV assigned to the nitrogen atoms in the piperazine and piperidine rings as well as to the nitrogen atom in the terminal dihexylamine group of the C12N-PPD film. The relative intensities of N 1s peaks correlate coarsely with the amount of the nitrogen atoms and their locations within the molecular backbone (affecting the attenuation of the respective signal). The F 1s spectrum of the FP-Pz monolayer (not shown) acquired at a photon energy of 720 eV exhibits a single peak at ~687.9 eV, assigned to the fluorine atoms in the terminal ring.

The quantitative evaluation of the XPS spectra (see section 2) results in the values for the effective thicknesses and packing densities of the DTC-based SAMs compiled in Table 1. The effective thicknesses of the monolayers are close to the sum of the respective molecular lengths and the length of the S–Au bond, suggesting an upright molecular orientation. The packing densities of the parent PPd and PPz films are very close to the value characteristic of the densely packed $(2\sqrt{3}\times\sqrt{3})R30°$ structure typical of non-substituted alkanethiolate SAMs on Au(111), viz. 4.63×10^{14} mol/cm^2.[45,36] In view of the almost double density of the sulfur atoms in the DTC case, the similarity of the packing densities is a direct indication that the packing is mostly determined by the interaction between the molecular backbones. It also implies that the docking groups in conventional thiolate SAMs, with only one S atom per molecular chain, are

comparably loosely packed. An important implication of this finding is that the presence of atomic sulfur, which is frequently observed in thiolate SAMs as a minor contamination,[39] does not necessarily indicate a poor or limited quality of the monolayers, since, apparently, the respective species can very likely coexist with the intact thiolate anchors, packed in the standard fashion, without much interference.

Table 1. *Effective thickness (Å), packing density (molecules/cm²), and relative density of the DTC-based SAMs. See text for details. The experimental errors are ±1-1.5 Å for the thickness and ±10% for the packing density. The reference packing density for a dodecanethiol SAM ($\sqrt{3} \times \sqrt{3}$ structure) is 4.63×10^{14} molecules/cm².*

Monolayer	PPd	C12N-PPd	PPz	OMe-PPz	FP-Pz
Thickness (Å)	9.9	13.3	10.8	11.9	13.1
Packing density (molecules/cm²)	4.25×10^{14}	3.5×10^{14}	4.65×10^{14}	3.4×10^{14}	2.75×10^{14}
Relative density	0.92	0.76	1.0	0.74	0.59

The packing densities of the C12N-PPd and OMe-PPz SAMs are somewhat lower and that of the FP-Pz SAM and considerably lower than those of the parent PPd and PPz monolayers (Table 1). For the FP-Pz film this can be associated with the much larger van-der-Waals radius of the fluorine atoms compared to hydrogens and the resulting larger van-der-Waals dimension of the fluorinated phenyl.[42,71] For the C12N-PPd and OMe-PPz SAMs, the lower packing densities are associated with the substituents, which, especially for C12N-PPd (two aliphatic chains per molecule), are comparably bulky. Moreover, substitution has a strong impact on intermolecular interactions, thus an effective packing in these monolayers might be affected by some degree of disorder.

3.2. Experiments: NEXAFS Spectroscopy
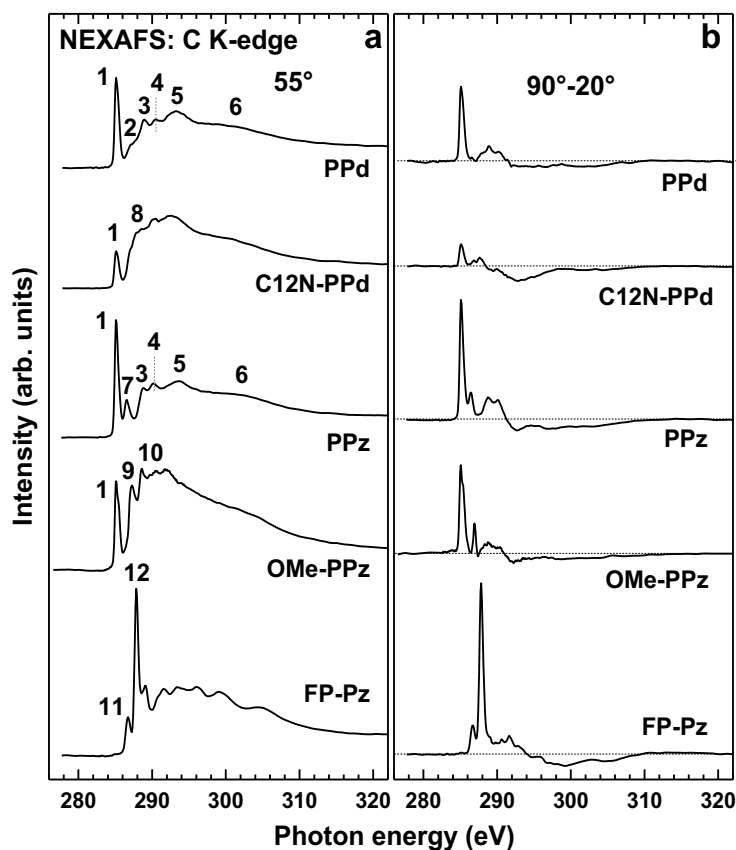
C K-edge NEXAFS spectra of the DTC-based SAMs acquired at an X-ray incident angle of 55° (magic angle) are presented in Figure 3a; the differences between the spectra collected under normal (90°) and grazing (20°) incidence are contained in Figure 3b. The 55° spectra are not affected by molecular orientation effects and are, thus, directly representative of the electronic

13

structure of the studied films.[38] In contrast, the difference spectra provide a useful tool to monitor the dependence of the magnitude of the absorption resonances on the incidence angle of the primary X-ray beam, termed as linear dichroism and delivering information on molecular orientation.[38]

The 55° spectra of the basic PPd and PPz SAMs are dominated by the characteristic absorption resonances of the terminal phenyl ring,[38,72-74] viz. the most intense π_1^* resonance at ~285.1 eV (**1**), the respective π_2^* peak at 288.8-288.9 eV (**3**), a further π^* resonance at 290.2 eV (**4**), and several σ^* resonances (**5-6**) at higher excitation energies. In addition, there are the R*/C-S* resonances[38,74] at ~287.3 eV (**2**) and the comparably strong π^* resonance at ~286.5 eV (**7**) in the case of the PPz SAM, which stems presumably from the splitting of the π_1^* feature of the phenyl ring (**1**) due to the effect of the adjacent pyperazine moiety.[38] Such a splitting also affects the π_2^* resonance (**3**) in this spectrum,[38] resulting in a stronger intensity of the 290.2 eV feature (**4**) as compared to the PPd case. The absorption structure associated with the piperidine (PPd) and piperazine (PPz) moieties could not be unequivocally identified, since the spectra of these species do not exhibit intense, discrete features in the pre-edge and at-edge regions (see refs. 75 and 76) and the related σ^* resonances overlap with those of the phenyl ring.

The 55° spectra of the C12N-PPd and OMe-PPz SAMs exhibit a significant relative weakening of the π_1^* resonance (**1**), which is associated with the substitution. This effect is especially pronounced for the C12N-PPd film, the spectrum of which shows also an additional resonance at ~287.7 eV (**8**) associated with the alkyl chains (most likely excitations into Rydberg states,[77] but there are also alternative assignments). Additionally, there is a pattern of σ^* resonances at higher photon energies. The latter resonances stem predominantly from the alkyl chains and are presumably the reason for the comparably low intensity of the π_1^* resonance, since the spectrum is normalized to the height of the absorption edge proportional to the entire number of the carbon atoms but with a stronger contribution from the alkyl chains due to the more pronounced attenuation of the signal originating from the PPd moiety. The spectrum of the OMe-PPz SAM exhibits a π^* resonance at 287.3 eV (**9**) stemming from the splitting of the π_1^* feature of the phenyl ring (**1**) due to its substitution,[38] and an additional π^* resonance at ~288.6 eV (**10**), which most likely has π_2^* (**3**) character.

Figure 3. *C K-edge NEXAFS spectra of the DTC-based SAMs acquired at an X-ray incident angle of 55° (a), along with the respective difference between the spectra collected under the normal (90°) and grazing (20°) incidence geometry (b). Individual absorption resonances are marked by numbers (see text for assignments). The horizontal dashed lines in panel b correspond to zero.*

The 55° spectrum of the FP-Pz SAM is dominated by the absorption resonances of the fluorinated phenyl ring, with the most prominent, characteristic features at ~286.65 eV (**11**) and ~287.8 eV (**12**) assigned to the $C_{1s} \rightarrow \pi^*$ transitions at the carbon atoms which are not bonded, respectively, directly bonded to fluorine atoms.[72,78] Interestingly, the position of the former feature is distinctly higher than that for pentafluorobenzene (~285.5 eV)[72] and pentafluorobenzene terminated SAMs (285.7 eV)[42], which is presumably related to the bonding of the respective carbon atom to the adjacent piperazine ring. There are several additional less intense π^*- and σ^*-like resonances, for which the positions and assignments can be found in literature.[72,78]

In addition to the the magic angle spectra analyzed above, the linear dichroism effects in the DTC-based SAMs were monitored. The 90°-20° curves for all monolayers in Figure 3b exhibit intense difference peaks at the positions of the absorption resonances. They reflect a pronounced linear dichroism suggesting high orientational order in the monolayers. In addition,

15

the signs of the observed difference peaks, viz. the positive signs for the resonances with π^*-character and the negative signs for those with σ^*-character, indicate, in view of the orientation of the respective orbitals, an upright molecular orientation in all studied SAMs.

Along with these qualitative considerations, a quantitative analysis of the entire set of the NEXAFS data acquired at different X-ray incidence angles was performed to get information about molecular orientation in the DTC SAMs. The analysis was carried out within a standard theoretical framework,[38] comparing the angular dependence of the intensities of selected absorption resonances, I, with the appropriate theoretical expression. The average angle describing the orientation of the respective molecular orbital in terms of its transition dipole moment (TDM) is used as fitting parameter[42,74] For this analysis we chose either the most prominent resonance associated with the phenyl ring (**1**) or the most prominent π^* resonance of the fluorinated phenyl ring ($C_{1s}{}^{C\text{-}F} \rightarrow \pi^*$; **12**), using these moieties as markers for the orientation determination. The average tilt angle, α, of the corresponding orbitals (with their "direction" defined perpendicular to the plane of the ring) relative to the surface normal can be derived from a standard expression for a vector-type orbital[38]

$$I(\alpha,\theta) = A\left\{P \times \tfrac{1}{3}\left[1 + \tfrac{1}{2}\cdot(3\cdot\cos^2\theta - 1)\cdot(3\cdot\cos^2\alpha - 1)\right] + (1-P)\tfrac{1}{2}\sin^2\alpha\right\}, \quad (1)$$

where A is a constant, P is the polarization degree of the x-rays, and θ is the x-ray incidence angle. The derived α values are compiled in Table 2. They can be used to calculate the average tilt angle of the molecular backbone, β, according to the relation

$$\cos(\alpha) = \sin(\beta)\cos(\gamma), \quad (2)$$

where γ is the twist angle of the molecular backbone with respect to plane spanned by the surface normal and the molecular axis; it is defined as 0, if the tilt occurs perpendicular to the plane of the ring.[79] Under the latter condition, $\beta = 90°\text{-}\alpha$, representing the minimum possible molecular inclination consistent with the NEXAFS data. The respective values are given in Table 2.

All other values of the twist angle will result in larger values of the molecular tilt angles at the given α values. Regretfully, the twist angle cannot be determined experimentally, which is a general constraint of NEXAFS experiments on aromatic SAMs. Consequently, in the given case, for the most basic PPd and PPz SAMs, we rely on theoretical simulations (section 3.4), deriving β and γ from the optimized molecular structures, calculating the respective α, and comparing them with the experimental values.

Table 2. *Average tilt angle of the π∗ orbitals of the phenyl ring and the minimal possible average molecular tilt angle for the DTC-based SAMs on gold. See text for details. The experimental error is estimated at ±3°.*

Monolayer	PPd	C12N-PPd	PPz	OMe-PPz	FP-Pz
Tilt angle of the π∗ orbitals, α	72.5°	70°	81.5°	72°	79°
Minimum molecular tilt angle, β'	17.5°	20.0°	8.5°	18.0°	11.0°

Interestingly, the inclination of the π-system expressed by α in PPz/Au is smaller than that in PPd/Au, in full agreement with the packing density values (Table 1). The substitution of the terminal phenyl ring in both PPz/Au and PPd/Au, given by the examples of C12-PPd/Au and OMe-PPz/Au, results in an increase of the inclination, which is a common behavior observed in different types of SAMs. Finally, the fluorination of the terminal phenyl ring in FP-Pz/Au does not result in a noticeable disturbance of the molecular inclination, which again appears to be a general trend for SAMs containing perfluorinated aromatic moieties.[42,80] As mentioned in section 3.2, the comparably low packing density in FP-Pz/Au (Table 1) is associated with the large van der Waals dimensions of the fluorinated ring compared to the phenyl one.

3.3. Experiments: Work Functions

The work function values of Au surfaces modified with the PPz and PPd SAMs were determined to be 3.9 eV and 3.7 eV (± 0.05), respectively; accordingly, compared to a work function of a reference Au substrate of 5.2 eV, the shifts amount to −1.3 eV and −1.5 eV. The work function values of the C12N-PPd, OMe-PPz, and FP-Pz SAMs are 3.2 eV, 3.5 eV, and 4.3 eV according to the literature.[30] They show the expected trends when compared to the work function values of the parent PPz and PPd derivatives, viz. a decrease in the work function upon substitution with the C12N and OMe groups and an increase in the work function upon perfluorination of the terminal phenyl ring.

3.4. Quantum-mechanical simulations

3.4.1. Monolayer structure

In view of the unknown structure of the adsorbate layer, we performed a (restricted) screening of the potential-energy surface of the interface to identify different polymorphs (for details see section 2.3 and the Supporting Information). The relative stabilities and selected properties of the thus-identified structures are compiled in Table 3 with the structures of the most stable conformations shown in Figure 4 and the others contained in the Supporting Information. The packing density for the simulated systems with two molecules in a ($\sqrt{3}\times3$)rect surface unit cell amounts to 4.45×10^{14} mol/cm², which is equivalent to the experimental packing density of the PPz SAM (see Table 1).

The above data reveal that in the SAMs there are different polymorphs that are reasonably close in energy. Interestingly, the lowest energy structures of the two molecules in the SAMs are fundamentally different, with the coplanar PPz structures being most stable, while for PPd a twisted conformation represents the energetic minimum. This difference is attributed to the kink in the molecular backbone induced by the sp³ hybridized top C atom in the piperidine ring. This interpretation is supported by the finding that the relative order of twisted/coplanar conformations obzained for the periodic SAMs on the surface is recovered also when calculating isolated molecules. Generally, in all cases two molecules arranged in a herringbone pattern are more stable than a cofacial arrangement, consistent with what is known for oligophenylenethiol SAMs.[81,82]

Table 3: DFT-calculated properties of various polymorphs of the PPz/Au(111) and PPd/Au(111) interfaces: ΔE_{tot} (eV) denotes total energy per molecule relative to the most stable conformation; the α's are the average tilt angles of the π-orbitals (c.f., section 3.2) of the two inequivalent molecules in the unit cell (the individual angles are reported in the SI). They have been obtained via $cos^2(\alpha) = 0.5 \cdot (cos^2(\alpha_1) + cos^2(\alpha_2))$ taking into consideration that the intensities associated with the absorption resonances are proportional to $cos^2(\alpha)$ (see Eq. 1; the $sin^2(\alpha)$ component in that equation is comparably small); BE_{C1s} refers to the energetic position of the main peak in the simulated core-level spectra (rigidly shifted by 18.95 eV, to align the simulated and measured spectra of the PPz SAM – for more details see main text); and $\Delta \Phi$ is the SAM-induced work-function change (as reference energy the theoretical work function of clean Au was used, calculated as 5.12 eV). Values for the lowest-energy structures are plotted in bold.

	arrangement	ΔE_{tot} (eV)	α / °	BE_{C1s}/eV	$\Delta \Phi$ (eV)
	herringbone, coplanar	**0**	**81.2**	**284.45**	**-1.71**
PPz	herringbone, twisted	0.135[**]	83.6	285.34	-2.60
	cofacial, coplanar	0.211	82.0	284.29	-1.57
	cofacial, twisted	0.340	89.1	285.12	-2.38
	herringbone, coplanar	0.083	81.2	285.26	-2.54
PPd	**herringbone, twisted**	**0**	**81.5**	**285.30**	**-2.58**
	cofacial, coplanar	0.275	73.0	285.03	-2.29
	cofacial, twisted	0.214	85.5	284.98	-2.29

As far as the angles of the π-planes of the terminal rings relative to the substrate surface is concerned (the values of α from section 3.2), when considering the lowest-energy structures, for the PPz SAM we see a near perfect agreement between simulations (81.2°) and experiments (81.5°). For the PPd system, the calculated value (81.5°) is larger than the experimental one (72.5°). This deviation is attributed to a non-negligible amount of disorder in the experimentally studied PPd film, which is consistent with the reduced coverage measured for the PPd SAM compared to the PPz monolayer (Table 1). Considering the twisted molecular backbone of PPd that we find in the simulations, a reduced film quality for that system appears indeed plausible.
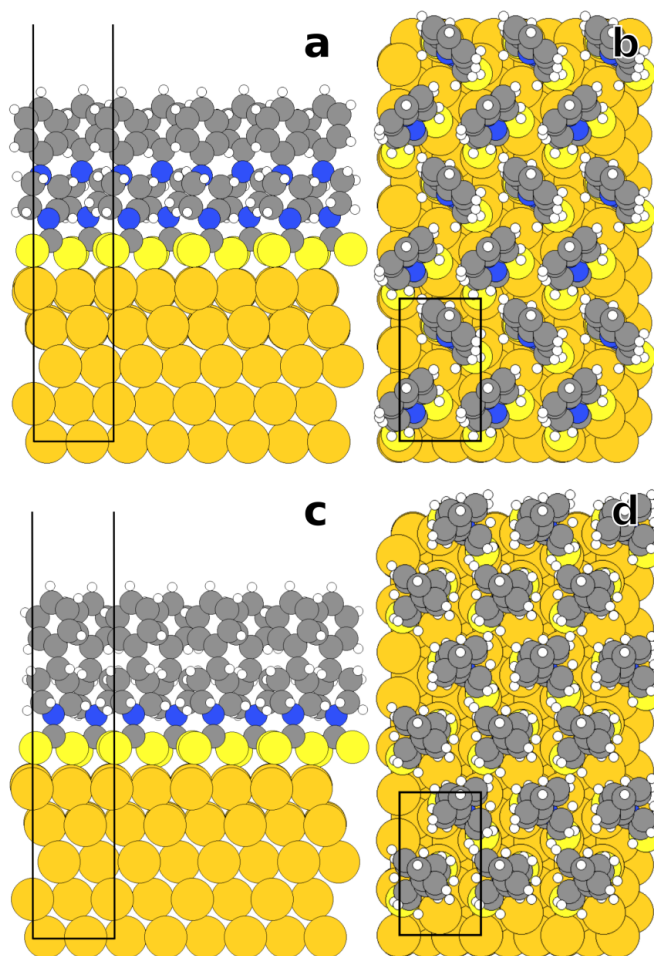
Figure 4. *Optimized structures of PPz/Au(111) and PPd/Au(111). (a) and (b): side and top view, respectively, of herringbone coplanar PPz/Au(111); (c) and (d): side and top view, respectively, of herringbone twisted PPd/Au(111). Au atoms are depicted in dark yellow, S in yellow, C in grey, H in white, and N in blue. The dashed black rectangle marks the unit cell used in the calculations.*

An advantage of the simulations is that they provide direct access to the tilt and twist angles of the individual molecules, which are compiled for the lowest-energy conformations in Table 4. These data suggest nearly upright-standing molecules in full agreement with the XPS data (see section 3.1). Notably, the tilt angles calculated for PPd are smaller than the minimum tilt angle derived from the measurements (see Table 2), which can again be attributed to some disorder in the experimentally investigated PPd films.

20

Table 4: Calculated tilt and twist angles of the two inequivalent unit molecules in the unit cells of PPz (herringbone, coplanar) and PPd (herringbone, twisted) SAMs at full coverage.

	tilt		twist	
	β_1	β_2	γ_1	γ_2
PPz	7.4	13.7	37.6	36.1
PPd	14.2	12.6	58.0	41.1

3.4.2. Calculated core-level shifts and variations in the electrostatic energy

A simulation of the C 1s XPS spectra can provide valuable information regarding SAM-induced modifications of the electrostatic potential.[18,19] In the calculations, we observe a shift of 0.85 eV between the main peaks of the core-level spectra of PPz and PPd. This agrees qualitatively with the experiments, although in absolute numbers the calculated shift is clearly larger than the value of 0.42 eV measured at 350 eV photon energy. That difference can at least partly be attributed to the lower effective coverage in the experimental PPd samples, which, on the on hand, dilutes the dipoles and, on the other hand, results in a somewhat larger tilt of the dipole direction relative to the surface normal. A quantitative estimate of the impact of both effects can be found in the Supporting Information.

As far as the shapes of the XPS spectra are concerned, they agree very well between the simulations and experiments. This can be seen in Figure 5, where it should be noted that the energy scale in the simulations has been shifted to higher BEs by 18.95 eV. This value has been chosen to make the calculated and experimental spectra of PPz/Au lie on top of each other and, for sake of consistency, has then been kept also in the PPd case. Such a shift is inevitable considering that within the initial state approach the actually calculated quantities are Kohn-Sham orbital energies.[3,83-85]
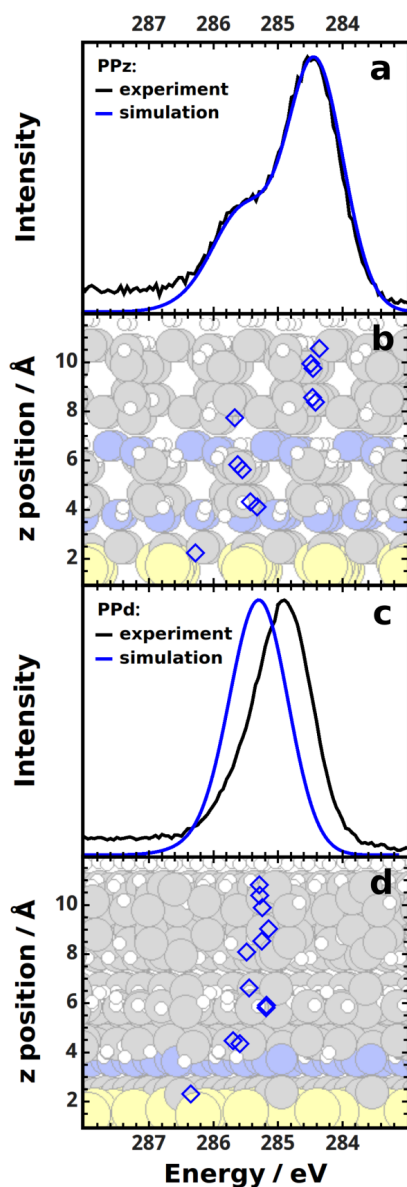
Figure 5. *Comparison between the experimental and simulated C 1s XPS spectra. (a) experimental (black) and simulated (red) C 1s spectra of PPz/Au(111); (b) calculated core level energies for each carbon atom in the PPz molecule in the respective SAM including screening by the metal; (c) experimental (black) and simulated (red) C 1s XPS spectra of PPd/Au(111); and (d) calculated core level energies for each carbon atom in the PPd molecule in the respective SAM including screening by the metal. Please note that in the panels **b** and **d** the energy values are given for only one of the two molecules in the full coverage unit cell. Since these two molecules are differently tilted, they are not symmetry equivalent and the calculated energy values are slightly different. Such differences are, however, very small, as shown in the Supporting Information. To ease the comparison between simulations and experiments, the energy scale for the simulated data has been shifted to higher BEs by 18.95 eV (aligning the measured and calculated spectra for PPz).*

For PPz/Au, the simulations fully reproduce the occurrence of a pronounced shoulder at higher binding energies (the feature denoted as "1" in the XPS spectrum of PPz/Au in Figure 2b). Conversely, for PPd/Au only a single dominant peak is observed in full agreement with the experiments. The atomically resolved core-level binding energies in Figures 5b and 5d support the original peak assignment from Section 3.1; i.e. the low BE feature in PPz/Au is associated with the carbon atoms in positions 2 – 6 of the topmost phenyl ring, while the weaker, high BE feature originates from the carbon atoms directly bonded to the nitrogen atoms in the piperazine moiety. Conversely, for PPd/Au the core-level BEs of all C atoms in the rings are between 285.3 and 285.7 eV; as a consequence of this comparably small energetic spread and due to the absence of two energetically distinct groups of carbon atoms, we obtain only a somewhat broadened single peak that dominates the spectrum.

Beyond confirming and refining the peak assignment, the simulations provide additional insight that is not apparent in the experiments due to the finite energy resolution: (i) They reveal that the core level energy of the topmost carbon in the phenyl ring is shifted by 0.2 eV compared to the neighboring carbons in PPz/Au, an effect that is not observed in PPd/Au. (ii) The aliphatic carbons in PPd/Au have essentially the same BEs as the aromatic ones in the topmost ring. (iii) Finally, the BE associated with the carbon atom bonded to the two sulfurs is shifted to higher BEs by ~ 1.0 eV (1.3 eV) in PPz/Au and by ~0.7 eV (1.0 eV) in PPd/Au compared to the C atoms in the lower ring, disregarding (including) screening effects. Due to the finite escape depth of the photoelectrons, this is at best manifested as a high BE tail in the experimental spectra.

To understand the peculiarities of the XPS spectra, it is useful to keep in mind that core-level energies are determined not only by the local chemical environments of the atoms, but also by the local electrostatic energy.[18,19,37,57,86] The latter can, for example, be changed through collective electrostatic effects via periodic arrangements of polar groups, which are common in SAMs[19] or by the Madelung energy in ionic crystals[87,88]. Conceptually, chemically and electrostatically induced shifts can be separated by reducing the density of the polar moieties in the adsorbate layer.[19] This is straightforward, at least as long as reducing the dipole density does not modify atomic charges, e.g., by changing charge transfer between substrate and adsorbate. For atoms in a SAM that are at a sufficient distance from the docking groups, this means that core-level energies will depend on the coverage only, if there are dipole layers between them and the metal substrate.[19] To analyze that, one needs to compare the core levels of densely packed films to those obtained from a calculation carried out at significantly reduced molecular coverage. In the latter case, the remaining molecules need to be fixed in the geometries they

23

adopted in the dense SAM in order to avoid a superposition of effects arising from molecular rearrangements (see section 2.3).
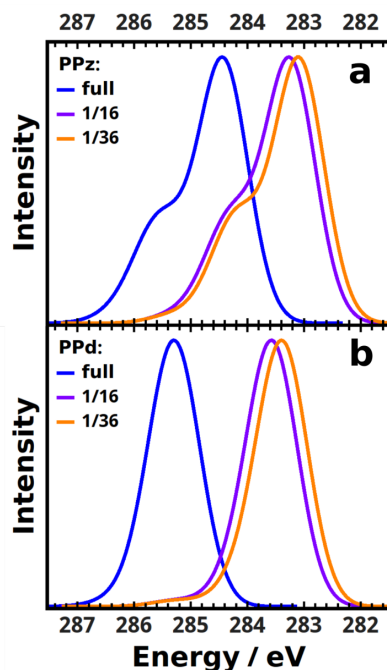
Figure 6. Comparison between the simulated XPS spectra of PPz (a) and PPd (b) on Au(111) obtained for full, 1/16 and 1/36 coverage. The legend is given in the panels.

When applying this approach to the PPd and PPz SAMs, the spectra shown in Figure 6 are obtained for full, 1/16 and 1/36 coverage. Their comparison reveals three crucial aspects: (i) The low-coverage spectra are significantly shifted with respect to the full coverage ones with the shifts of the 1/36 spectra slightly exceeding those of the 1/16 spectra; (ii) the shape of the spectra remains essentially unchanged; i.e., there is a rigid shift; and (iii) the shift for the PPd SAM (1.90 eV between full and 1/36 coverage, as measured from the positions of the maxima) clearly exceeds that for the PPz SAM (1.32 eV). As can be inferred from the description in the preceding paragraph, the first aspect suggests that significant dipoles are present in the system; the second indicates that the most significant dipoles are in the region of the immediate metal/SAM interface, i.e., closer to the metal than the carbon atoms most strongly contributing to the C 1s spectra; finally, the third aspect implies that this dipole is larger for PPd than for PPz. In addition, the comparably small shift between the 1/16 and 1/36 spectra for both PPd and PPz SAMs suggests a convergence of the calculations in terms of the low coverage limit. We note that the pronounced difference in the core level shifts observed for PPz and PPd in Fig. 6 cannot result from a different tilt angle of the DTC anchor group. According to our calculations, the plane spanned by the S-S-N atoms (with N being the nitrogen atom that

belongs to the DTC group) form an angle of 6° and 5.8° relative to the surface normal for PPz and PPd, respectively, which is a too small difference to significantly affect the interface dipole.

To consider the above trends in more detail, we analyze the atomistically resolved core-level energies shown in Figure 7 for the PPd and PPz SAMs at full and 1/36 coverage. There we report the as calculated core-level energies; i.e., not rigid shift of the spectra is applied and no screening of the core hole by the metal substrate is considered. Otherwise, "artificial" shifts due to different dielectric constants of the adsorbate layer (cf., eq 1) would obscure the more fundamental trends.
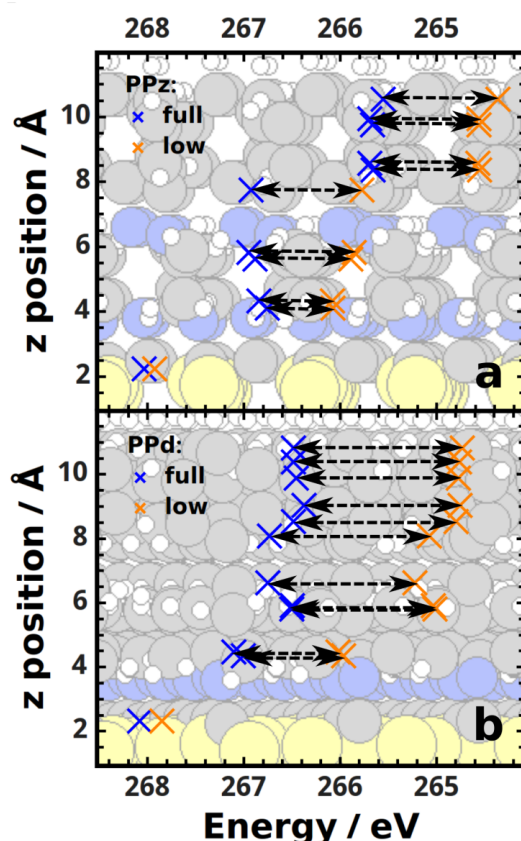
Figure 7. *Calculated, atomically resolved C 1s core-level energies for the PPz (a) and PPd (b) SAMs obtained for full (blue crosses) and low (1/36; orange crosses) coverage. The black dashed arrows serve as guides to the eye.*

We start with a discussion of the PPz case (Figure 7a): The horizontal arrows associated with the C atoms most strongly contributing to the XPS spectrum have very similar lengths (average $\Delta E_{BE} \approx 1.15$ eV, for numerical details see the Supporting Information). This supports the conclusions drawn already from the rigid shift of the spectra that significant dipoles exist that are mostly found in the vicinity of the docking region.

Interestingly, ΔE_{BE} is essentially the same also for the topmost C atom, which suggests a chemical origin for the different binding energy of that atom compared to the other phenyl carbons. As this difference is not observed in the PPd case (Figure 7b), its origin must be the N atom bonded to the C in the 1-position of the phenyl ring in PPz. Its impact can be more straightforwardly investigated using aniline as a model system. Considering the possible resonance structures of aniline indeed allows rationalizing the chemical origin of the shift, as we describe in detail in the Supporting Information.

For the carbon atoms in position 3 and 5 and in position 2 and 6 of the piperazine ring, the shift is on average reduced to ~1.05 eV and ~0.72 eV, respectively, and it almost disappears (ΔE_{BE}=0.12 eV) for the carbon atom bonded to the two sulfurs (see Figure 7a). The shift of the 1s energies of the lower nitrogen between full (378.80 eV) and 1/36 coverage (378.39 eV) amounts to 0.41 eV, which is intermediate between that for the two adjacent C atoms. This together with the vanishingly small coverage-dependent shift of the S 2p core levels energies (calculated as 0.045 eV on average) suggests that the region around those atoms is where the dipoles causing the electrostatic shifts reside. Here, it, however, has to be noted that an analysis of the coverage-dependence of the core-level shifts of atoms close to the substrate is not straightforward. The reason for that are (coverage dependent) interfacial charge rearrangements resulting from the formation of the metal to SAM bond,[89] which can easily mask the electrostatic shifts.
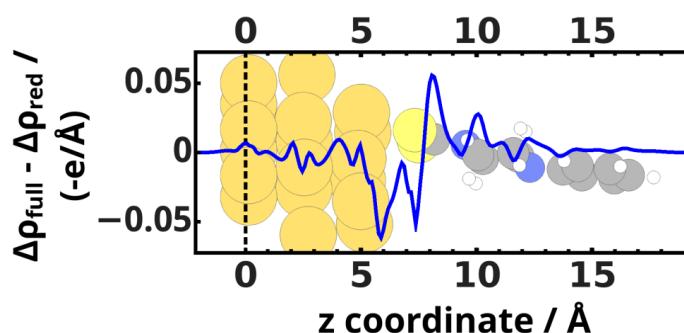
Figure 8. Difference between the z-dependent charge rearrangement per molecule integrated over the (xy)-plane within the unit cell in the full ($\Delta\rho_{full}$) coverage and in the 1/16 ($\Delta\rho_{red}$) reduced coverage cases for the PPz SAM.

To illustrate that, we analyze the (plane integrated) charge rearrangement per molecule, $\Delta\rho$, due to the bonding of PPz to the Au substrate. In particular, we focus on the difference in $\Delta\rho$ between full and 1/16 coverage, which is shown in Figure 8 (for details see the Supporting

26

Information). These data show opposing coverage dependences of the charge rearrangements at the z-positions of the S atoms and the adjacent C atom. Albeit small, such differences in charge rearrangements can results in chemical core-level shifts of several hundred meV, masking the impact of the local electrostatic potential for nuclei in the immediate vicinity of the interface. The magnitude of these coverage-dependent chemical shifts are estimated for the example of the C 1s core levels in the Supporting Information. In passing we note that in an attempt to pinpoint the exact location of the dipole, we also tested various charge partitioning schemes, but (not really unexpectedly) observed significant variations between different SAM conformations and methodological approaches rendering these attempts inconclusive.

With regards to the coverage-dependent core-level energies of PPd/Au, qualitatively similar trends as in PPz/Au are observed (see Figure 7b and the Supporting Information), the main difference being that the overall coverage-dependent shift is larger even for the bottom ring, indicative of a larger dipole in the region of the docking group.

3.4.3. Docking positions and their impact on S core-level binding energies

In this section, we would like to discuss docking positions and core-level energies of the S atoms. As indicated already in the discussion of the experimental results, we find docking positions of the four S atoms per unit cell varying between on-top and bridge including also displacements towards the hollow sites (for a plot of the S docking positions in the lowest energy structures see the Supporting Information). This results in calculated S 2p binding energies varying over ca. 0.13 eV for PPz/Au and 0.12 eV for PPd/Au, which is consistent with the comparably large fwhm of the experimental S 2p XPS spectra (see section 3.1).

3.4.4. Work-function modifications

As far as the work function modifications (see Table 3) are concerned, the value obtained for the PPz SAM somewhat overestimates the measured one (-1.7 eV vs. -1.3 eV). In fact, already in the past we have observed that calculated work function changes overestimate the measured ones, with one of the reasons being finite grain sizes and inevitable disorder in the real SAMs.[18]

As a matter of curiosity it should be mentioned that in the PPz SAMs changing the molecular conformation by rotating the phenyl ring such that it is nearly perpendicular to the piperazine unit (twisted configuration) massively increases the work function change. This can be traced back to a significant increase of the dipole moment of the molecule (for an isolated molecule it increases from 2.8 Debye for the planar configuration to 3.9 Debye for the twisted one). Even though in the experiments there is no indication for the occurrence of the twisted structure, this

result shows that inducing a twist, e.g., by chemical substitutions could be a viable strategy for boosting the molecular dipole moment of PPz derivatives and to maximize the achievable work-function modification. Note that for the PPd SAM, a change from the twisted to the planar configuration has a much weaker impact on the molecular dipoles and on the work function changes (see Table 3 and the Supporting Information), which we attribute to the absence of heteroatoms in the vicinity of the rotated bond.

When comparing the calculated SAM-induced work function decrease of PPz and PPd, PPd yields a work function that is larger by 0.87 eV. This coincides with the shifts in the simulated core-level binding energies for C 1s states in the phenyl ring (see last two columns of Table 3), a correlation that is expected based on the equivalent electrostatic origins of core-level shifts and work function changes (see above and ref 19). In the experiments, however, a distinctly smaller difference in the work functions of PPz and PPd samples is observed, i.e. on the order of only 0.2 eV. This is even smaller than the measured 0.42 eV shift in the binding energy of the main features in the XPS spectra related to the phenyl C 1s signal. The origin of this deviation between theory and experiment is not fully understood, and appears too large to be solely attributed to the lower coverage of the PPd SAMs as reported in Table 1. Here, we cannot fully exclude a certain parameter variation for the different samples employed for the different measurements within the project. Also, we cannot rule out an overestimation of the particularly large calculated dipole associated with the bonded DTC group for the PPd system.

4. Summary

In the present work we combined synchrotron-based XPS, NEXAFS spectroscopy, work function measurements and state-of-the-art DFT calculations to study molecular organization and electrostatic properties of SAMs on Au(111) formed by dithiocarbamates with rod-like symmetry, taking several representative monolayers as test systems. As the piperazine/piperidine unit constitutes the common platform of these derivatives, particular emphasis is given to the investigation of the two parent compounds, PPd and PPz. They can be substituted with different functional terminal groups, thus allowing a wide range of molecular dipoles and offering a promising avenue for work function engineering at metal-organic interfaces. From our study, it emerges that the DTC anchor group represents a useful building block for monomolecular self-assembly on coinage metal substrates. Its combination with the piperidine or piperazine moiety allows for a sufficient flexibility, enabling the self-assembly of more rigid terminal groups (such as the phenyl rings in the case of PPd, PPz, and FP-Pz). It also allows the substitution with additional groups such as secondary amines, alkoxy groups, cyano groups, and many more (e.g. for C12N-PPd and OMe-PPz). Importantly, both sulfur atoms in

the DTC anchor group bind to the substrate in a bidentate fashion, a very advantageous feature distinguishing the DTC moiety from other thiol-based dipodal and tripodal docking groups, that frequently show a heterogeneous chemistry for each individual sulfur atom (with coexisting thiolate, atomic sulfur, unbound sulfur, and disulfide configurations). Notwithstanding its bulkier bonding configuration, the DTC anchor, in combination with the piperidine or piperazine linkers, allows a dense molecular packing (see Table 1), with almost the same density as for monodentate docking groups such as thiolates in alkanethiolate and arylthiolate SAMs on Au(111). Such a dense molecular packing is characterized by small molecular inclinations, as evidenced both by NEXAFS experiments and theoretical simulations (see Tables 2 and 3). This inclination is only slightly altered upon substitution of the PPd and PPz backbones with dipolar tail groups, or by partial fluorination of these moieties, a very favorable property in view of interface-dipole engineering, e.g. for the efficient alignment of transport levels in organic semiconductors.

As an overall trend, we find an excellent agreement between the results from spectroscopic experiments and theoretical simulations in terms of molecular organization of PPd and PPz films. This not only refers to the molecular orientation but, for example, also to the heterogeneity of sulfur absorption sites in DTC anchor groups. In addition, the XPS spectra of the films could be reproduced by theory, in spite of a certain deviation between calculated and measured work function values. The most important conclusion with regards to the electrostatic properties of PPd and PPz SAMs concerns the location of the electrostatic dipole layer within these films, found to be in a region immediately adjacent to the metal/SAM interface. Interestingly, there is no significant potential step in the region of the additional nitrogen atom in PPz, at least as long as in PPz a coplanar molecular geometry prevails. The additional nitrogen atoms, however, induce a minor chemical shift affecting the carbon atom in the terminal phenyl ring in the PPz SAM.

The most relevant difference found between the PPd and PPz platforms is a more upright orientation of the molecular backbone associated with a higher coverage for PPz, making especially this platform highly promising in view of further substitution of the terminal phenyl ring by polar groups, thereby providing access to a broad variety of interface dipoles.

■ **Associated Content**

Supporting Information. Details on the starting geometries and optimization procedure; tilt and twist angles of the two symmetry-inequivalent molecules in all considered conformations; further information on the employed computational methodology; estimate of the impact of disorder and reduced coverage in PPd SAMs on the shifts in electrostatic energy at the interface;

29

additional information on calculated core-level binding energies of PPd and PPz SAMs; evolution of C1s binding energy of an isolated C atom as a function of adding/removing (fractional)electrons and discussion of its impact on core-level shifts in the immediate vicinity of the interface; details of the calculated interfacial charge rearrangements; listings of the geometries of the most stable polymorphs. This information is available free of charge *via* the Internet at http://pubs.acs.org.

■ Author Information

Corresponding Authors

*E-mail: egbert.zojer@tugraz.at (E.Z.).
*E-mail: Florian.vonwrochem@eu.sony.com (F. vW.).
*E-mail: Michael.Zharnikov@urz.uni-heidelberg.de (M.Z.).

ORCID

Florian von Wrochem: 0000-0003-2298-9270

Michael Zharnikov: 0000-0002-3708-7571

Egbert Zojer: 0000-0002-6502-1721

Notes

[#] E.S. and G.N. contributed equally to the present paper.

The authors declare no competing financial interest.

■ References

(1) Campbell, I. H.; Rubin, S.; Zawodzinski, T. A.; Kress, J. D.; Martin, R. L.; Smith, D. L.; Barashkov, N. N.; Ferraris, J. P. Controlling Schottky Energy Barriers in Organic Electronic Devices using Self-Assembled Monolayers. *Phys. Rev. B* **1996**, *54*, 14321–14324.

(2) de Boer, B.; Hadipour, A.; Mandoc, M. M.; van Woudenbergh, T.; Blom, P. W. M. Tuning of Metal Work Functions with Self-Assembled Monolayers. *Adv. Mater.* **2005**, *17*, 621–625.

(3) Heimel, G.; Romaner, L.; Brédas, J. L.; Zojer, E. Interface Energetics and Level Alignment at Covalent Metal-Molecule Junctions: p-conjugated thiols on gold, *Phys. Rev. Lett.* **2006**, *96*, 196806.

(4) Hamadani, B. H.; Corley, D. A.; Ciszek, J. W.; Tour, J. M.; Natelson, D. Controlling Charge Injection in Organic Field-Effect Transistors Using Self-Assembled Monolayers. *Nano Lett.* **2006**, *6*, 1303-1306.

(5) Cheng, X.; Noh, Y.-Y.; Wang, J.; Tello, M.; Frisch, J.; Blum, R.-P.; Vollmer, A.; Rabe, J. P.; Koch, N.; Sirringhaus, H. Controlling Electron and Hole Charge Injection in Ambipolar Organic Field-Effect Transistors by Self-Assembled Monolayers. *Adv. Funct. Mater.* **2009**, *19*, 2407–2415.

(6) DiBenedetto, S. A.; Facchetti, A.; Ratner, M. A.; Marks, T. J. Molecular Self-Assembled Monolayers and Multilayers for Organic and Unconventional Inorganic Thin-Film Transistor Applications. *Adv. Mater.* **2009**, *21*, 1407–1433

(7) Boudinet, D.; Benwadih, M.; Qi, Y.; Altazin, S.; Verilhac, J.-M.; Kroger, M.; Serbutoviez, C.; Gwoziecki, R.; Coppard, R.; Le Blevennec, G.; et al. Modification of Gold Source and Drain Electrodes by Self-Assembled Monolayer in Staggered N- and P-Channel Organic Thin Film Transistors. *Org. Electron.* **2010**, *11*, 227–237.

(8) Halik, M.; Hirsch, A. The Potential of Molecular Self-Assembled Monolayers in Organic Electronic Devices. *Adv. Mater.* **2011**, *23*, 2689–2695.

(9) Chiu, J. M.; Tai, Y. Improving the Efficiency of ZnO Based organic Solar Cell by Self-Assembled Monolayer Assisted Modulation on the Properties of ZnO Acceptor Layer, *ACS Appl. Mater. Interfaces* **2013**, *5*, 6946-6950.

(10) Lange, I.; Reiter, S.; Pätzel, M.; Zykov, A.; Nefedov, A.; Hildebrandt, J.; Hecht, S.; Kowarik, S.; Wöll, C.; Heimel, G.; et al. Tuning the Work Function of Polar Zinc Oxide Surfaces Using Modified Phosphonic Acid Self-Assembled Monolayers. *Adv. Funct. Mater.* **2014**, *24*, 7014–7024.

(11) Song, C. K.; Luck, K. A.; Zhou, N.; Zeng, Li; Heitzer, H. M.; Manley, E. F.; Goldman, S.; Chen, L. X.; Ratner, M. A.; Bedzyk, M. J.; et al. "Supersaturated" Self-

Assembled Charge-Selective Interfacial Layers for Organic Solar Cells. *J. Am. Chem. Soc.* **2014**, *136*, 17762−17773.

(12) Kim, J.; Rim, Y. S.; Liu, Y.; Serino, A. C.; Thomas, J. C.; Chen, H.; Yang, Y.; Weiss, P. S. Interface Control in Organic Electronics Using Mixed Monolayers of Carboranethiol Isomers. *Nano Lett.* **2014**, *14*, 2946−2951.

(13) Piersimoni, F.; Schlesinger, R.; Benduhn, J.; Spoltore, D.; Reiter, S.; Lange, I.; Koch, N.; Vandewal, K.; Neher, D. Charge Transfer Absorption and Emission at ZnO/Organic Interfaces. *J. Phys. Chem. Lett.* **2015**, *6*, 500−504.

(14) Casalini, S.; Bortolotti, C. A.; Leonardi, F.; Biscarini, F. Self-Assembled Monolayers in Organic Electronics. *Chem. Soc. Rev.* **2017**, *46*, 40-71.

(15) Ulman, A. Formation and Structure of Self-Assembled Monolayers. *Chem. Rev.* **1996**, *96*, 1533-1554.

(16) Love, J. C.; Estroff, L. A.; Kriebel, J. K.; Nuzzo, R. G.; Whitesides, G. M. Self-Assembled Monolayers of Thiolates on Metals as a Form of Nanotechnology. *Chem. Rev.* **2005**, *105*, 1103-1169.

(17) Schmidt, C.; Witt, A.; Witte, G. Tailoring the Cu(100) Work Function by Substituted Benzenethiolate Self-Assembled Monolayers. *J. Phys. Chem. A* **2011**, *115*, 7234–7241.

(18) Abu-Husein, T.; Schuster, S.; Egger, D. A.; Kind, M.; Santowski, T.; Wiesner, A.; Chiechi, R.; Zojer, E.; Terfort, A.; Zharnikov, M. The Effects of Embedded Dipoles in Aromatic Self-Assembled Monolayers. *Adv. Funct. Mater.* **2015**, *25*, 3943–3957.

(19) Taucher, T. C.; Hehn, I.; Hofmann, O. T.; Zharnikov, M.; Zojer, E. Understanding Chemical versus Electrostatic Shifts in X-Ray Photoelectron Spectra of Organic Self-Assembled Monolayers. *J. Phys. Chem. C* **2016**, *120*, 3428–3437.

(20) Cabarcos, O. M.; Schuster, S.; Hehn, I.; Zhang, P. P.; Maitani, M. M.; Sullivan, N.; Giguère, J.-B.; Morin, J.-F.; Weiss, P. S.; Zojer, E.; Zharnikov, M.; Allara, D. L. Effects of Embedded Dipole Layers on Electrostatic Properties of Alkanethiolate Self-Assembled Monolayers. *J. Phys. Chem. C* **2017**, *121*, 15815–15830.

(21) Sauter, E.; Gilbert, C.-O.; Boismenu-Lavoie, J.; Morin, J.-F.; Zharnikov, M. Mixed Aliphatic Self-Assembled Monolayers with Embedded Polar Group. *J. Phys. Chem. C* **2017**.

(22) Paniagua, S. A.; Giordano, A. J.; Smith, O. N. L.; Barlow, S.; Li, H.; Armstrong, N. R.; Pemberton, J. E.; Brédas, J.-L.; Ginger, D.; Marder, S. R. Phosphonic Acids for Interfacial Engineering of Transparent Conductive Oxides. *Chem. Rev.* **2016**, *116*, 7117−7158.

(23) Knesting, K. M.; Hotchkiss, P. J.; MacLeod, B. A.; Marder, S. R.; Ginger, D. S. Spatially Modulating Interfacial Properties of Transparent Conductive Oxides: Patterning Work Function with Phosphonic Acid Self-Assembled Monolayers. *Adv. Mater.* **2012**, *24*, 642–646.

(24) von Wrochem, F.; Gao, D.; Scholz, F.; Nothofer, H. G.; Nelles, G.; Wessels, J. M. Efficient Electronic Coupling and Improved Stability With Dithiocarbamate-Based Molecular Junctions. *Nat. Nanotech.* **2010**, *5*, 618-624.

(25) Wessels, J. M.; Nothofer, H. G.; Ford, W. E.; von Wrochem, F.; Scholz, F.; Vossmeyer, T.; Schroedter, A.; Weller, H.; Yasuda, A. Optical and Electrical Properties of Three-Dimensional Interlinked Gold Nanoparticle Assemblies. *J. Am. Chem. Soc.* **2004**, *126*, 3349-3356.

(26) Zhao, Y.; Pérez-Segarra, W.; Shi, Q.; Wei, A. Dithiocarbamate Assembly on Gold. *J. Am. Chem. Soc.* **2005**, *127*, 7328-7329.

(27) Gao, D.; Scholz, F.; Nothofer, H.-G.; Ford, W. E.; Scherf, U.; Wessels, J. M.; Yasuda, A. von Wrochem, F. Fabrication of Asymmetric Molecular Junctions by the Oriented Assembly of Dithiocarbamate Rectifiers. *J. Am. Chem. Soc.* **2011**, *133*, 5921–5930.

(28) Reeler, N. E. A.; Lerstrup, K. A.; Somerville, W.; Speder, J.; Petersen, S. V.; Laursen, Bo W.; Arenz, M.; Qiu, X.; Vosch, T.; Nørgaard. K. Gold Nanoparticles Assembled with Dithiocarbamate-Anchored Molecular Wires. *Sci. Rep.* **2015**, *5*, 15273.

(29) Simonsen, J. B.; Reeler, N. E. A.; Fossum, A.; Lerstrup, K. A.; Laursen, Bo W.; Nørgaard, K. Quantifying and Sorting of Gold Nanoparticle Dimers from Complex Reaction Mixtures Using Flow Cytometry. *Nano Res.* **2016**, *9*, 3093–3098.

(30) Ford, W. E.; Gao, D.; Knorr, N.; Wirtz, R.; Scholz, F.; Karipidou, Z.; Ogasawara, K.; Rosselli, S.; Rodin, V.; Nelles, G.; et al. Organic Dipole Layers for Ultralow Work Function Electrodes. *ACS Nano* **2014**, *8*, 9173–9180.

(31) Meyer, D.; Schäfer, T.; Schulz, P.; Jung, S.; Rittich, J.; Mokros, D.; Segger, I.; Maercks, F.; Effertz, C.; Mazzarello, R.; Wuttig, M. Dithiocarbamate Self-Assembled Monolayers as Efficient Surface Modifiers for Low Work Function Noble Metals. *Langmuir,* **2016**, *32*, 8812–8817.

(32) Zhao, Y.; Newton, J. N.; Liu, J.; Wei, A. Dithiocarbamate-Coated SERS Substrates: Sensitivity Gain by Partial Surface Passivation. *Langmuir* **2009**, *25*, 13833–13839.

(33) Ford, W. E.; Gao, D.; Scholz, F.; Nelles, G.; von Wrochem, F. Conductance Modulation in Tetraaniline Monolayers by HCl-Doping and by Field-Enhanced Dissociation of H2O, *ACS Nano* **2013**, *7*, 1943–1951.

(34) Naumann, R.; Schiller, S. M.; Giess, F.; Grohe, B.; Hartman, K. B.; Karcher, I.; Koper, I.; Lubben, J.; Vasilev, K.; Knoll, W. *Langmuir* 2003, *19*, 5435-5443.

(35) Nakamaru, S.; Scholz, F.; Ford, W.E.; Goto, Y.; von Wrochem, F. Photoswitchable Sn-Cyt *c* solid-state devices. *Adv. Mater.* **2017**, *29*, 1605924.

(36) Chesneau, F.; Zhao, J.; Shen, C.; Buck, M.; Zharnikov, M. Adsorption of Long-Chain Alkanethiols on Au(111) - A Look from the Substrate by High Resolution X-Ray Photoelectron Spectroscopy. *J. Phys. Chem. C* **2010**, *114*, 7112–7119.

(37) Hehn, I.; Schuster, S.; Wächter, T.; Abu-Husein, T.; Terfort, A.; Zharnikov, M.; Zojer, E. Employing X-ray Photoelectron Spectroscopy for Determining Layer Homogeneity in Mixed Polar Self-Assembled Monolayers. *J. Phys. Chem. Lett.* **2016**, *7*, 2994−3000.

(38) Stöhr, J. *NEXAFS spectroscopy*; Springer-Verlag: Berlin, 1992.

(39) Zharnikov, M. High-Resolution X-Ray Photoelectron Spectroscopy in Studies of Self-Assembled Organic Monolayer. *J. Electron Spectr. Relat. Phenom.* **2010**, *178-179*, 380-393.

(40) Moulder, J. F.; Stickle, W. E.; Sobol, P. E.; Bomben, K. D. *Handbook of X-ray Photoelectron Spectroscopy*, Chastian, J., Ed.; Perkin-Elmer Corp.: Eden Prairie, MN, **1992**.

(41) Thome, J.; Himmelhaus, M.; Zharnikov, M.; Grunze, M. Increased Lateral Density in Alkanethiolate Films on Gold by Mercury Adsorption. *Langmuir* **1998**, *14*, 7435–7449.

(42) Chesneau, F.; Schüpbach, B.; Szelągowska-Kunstman, K.; Ballav, N.; Cyganik, P.; Terfort, A.; Zharnikov, M. Self-Assembled Monolayers of Perfluoroterphenyl-Substituted Alkanethiols: Specific Characteristics and Odd-Even Effects. *Phys. Chem. Chem. Phys.* **2010**, *12*, 12123-12127.

(43) Ratner, M.; Castner, D. Electron Spectroscopy for Chemical Analysis, in Surface Analysis - The principal techniques; Vickerman, J. Ed.; Wiley: Chichester, 1997.

(44) Lamont, C. L. A.; Wilkes, J. Attenuation Length of Electrons in Self-Assembled Monolayers of *n*-Alkanethiols on Gold. *Langmuir* **1999**, *15*, 2037-2042.

(45) Schreiber, F. Structure and Growth of Self-Assembling Monolayers. *Prog. Surf. Sci.* **2000**, *65*, 151-256.

(46) Batson, P. E. Carbon-1s Near-Edge-Absorption Fine-Structure in Graphite. *Phys. Rev. B* **1993**, *48*, 2608-2610.

(47) Ahn, H.; Zharnikov, M.; Whitten, J. E. Abnormal Pinning of the Fermi and Vacuum Levels in Monomolecular Self-Assembled Films. *Chem. Phys. Lett.* **2006**, *428*, 283-287.

(48) Blum, V.; Gehrke, R.; Hanke, F.; Havu, P.; Havu, V.; Ren, X.; Reuter, K.; Scheffler, M. *Ab initio* molecular simulations with numeric atom-centered orbitals. *Comput. Phys. Commun.* **2009**, *180*, 2175 – 2196.

(49) Perdew, J. P.; Burke, K.; Ernzerhof, M. Generalized gradient approximation made simple. *Phys. Rev. Lett.* **1996**, *629*, 453 – 462.

(50) Tkatchenko, A.; Scheffler, M. Accurate molecular van der Waals interactions from Ground-State electron density and free-atom reference data. *Phys. Rev. Lett.* **2009**, *102*, 073005.

(51) Ruiz, V. G.; Liu, W.; Zojer, E.; Scheffler, M.; Tkatchenko, A. Density-functional theory with screened van der Walls interactions for the modeling of hybrid inorganic-organic systems. *Phys. Rev. Lett.* **2012**, *108*, 146103

(52) Freysoldt, C.; Eggert, P.; Rinke, P.; Schindlmayr, A.; Scheffler, M. Screening in two dimensions: GW calculations for surfaces and thin films using the repeated-slab approach. *Phys. Rev. B: Condens. Matter Mater. Phys.* **2008**, *77*, 214517

(53) Verwüster, E.; Hofmann, O. T.; Egger, D. A.; Zojer, E. Electronic Properties of Biphenylthiolates on Au(111): The Impact of Coverage Revisited. *J. Phys. Chem. C* **2015**, *119*, 7817-7825.

(54) Pehlke, E. ; Scheffler, M. Evidence for Site-Sensitive Screening of Core Holes at the Si and Ge (001) Surface. *Phzs. Rev. Lett.* **1993**, *71*, 2338 – 2341.

(55) Lizzit, S.; Baraldi, S.; Groso, A., Reuter, K.; Ganduglia-Pirovano, M. V.; Stampfl, C.; Scheffler, M.; Stichler, M.; Keller, C.; Wurth, W.; et al. Surface Core-Level Shifts of Clean and Oxygen-Covered Ru(0001). *Phys. Rev. B* **2001**, *63*.

(56) Olovsson, W.; Göransson, C.; Marten, T.; Abrokosov, I. A. Core-Level Shifts in Complex Metallic Systems from First Principle. *Phys. Status Solidi B* **2006**, *243*, 2447-2464.

(57) Cabellos, J. L.; Mowbray, D. J.; Goiri, E.; El-Sayed, A.; Floreano, L.; de Oteyza, D. G.; Rogero, C.; Ortega, J. E.; Rubio, A. Understanding Charge Transfer in Donor-Acceptor/Metal Systems: A Combined Theoretical and Experimental Study. *J. Phys. Chem. C* **2012**, *116*, 17991-18001.

(58) García-Gil, S.; García, A.; Ordejón, P. Calculation of Core Level Shifts within DFT Using Pseudopotentials and Localized Basis Sets. *Eur. Phys. J. B* **2012***, 85.*

(59) Baerends, E. J.; Gritsenko, O. V.; van Meer, R. The Kohn-Sham Gap, the Fundamental Gap and the Optical Gap: The physical Meaning of Occupied and Virtual Kohn-Sham Orbital Energies. *Phys Chem. Chem. Phys.* **2013**, *16*, 16408.

(60) Pueyo Bellafont, N.; Illas, F.; Bagus, P. S. Validation of Koopmans' Theorem for Density Functional Theory Binding Energies. *Phys. Chem. Chem. Phys.* **2015**, *17*, 4015-4019.

(61) Pueyo Bellafont, N.; Bagus, P. S.; Illas, F. Prediction of Core Level Binding Energies in Density Functional Theory: Rigorous Definition of Initial and Final State Contributions and Implications on the Physical Meaning of Kohn-Sham Energies. *J. Chem Phys.* **2015**, *142*, 214102.

(62) Jackson, J. D. *Classical electrodynamics*. 3rd ed.; Wiley: New York, **1999**.

(63) Neaton, J.; Hybertsen, M.; Louie, S. Renormalization of molecular electronics levels at metal-molecules interfaces. *Phys. Rev. Lett.* **2006**, *97*, 216405.

(64) Li Y.; Lu, D.; Galli, G. Calculation of quasi-particle energies of aromatic self-assembled monolayers on Au(111). *J. Chem. Theory Comput.* **2009**, *5*, 881 – 886.

35

(65) Egger, D. A.; Liu, Z.-F.; Neaton, J. B.; Kronik, L. Reliable energy level alignement at physisorbed molecule-metal interfaces from density functional theory. *Nano Lett.* **2015**, *15*, 2448 – 2455.

(66) Cabarcos, O. M.; Shaporenko, A.; Weidner, T.; Uppili, S.; Dake, L. S.; Zharnikov, M.; Allara, D. L. Physical and electronic structure effects of embedded dipoles in self assembled monolayers: characterization of mid-chain ester functionalized alkanethioles on Au(111). *J. Phys. Chem. C* **2008**, *112*, 10842 – 10854.

(67) Park, J.-S.; Vo, A. N.; Barriet, D.; Shon, Y. S.; Lee, T. R. Systematic Control of the Packing Density of Self-Assembled Monolayers Using Bidentate and Tridentate Chelating Alkanethiols. *Langmuir* **2005**, *21*, 2902–2911.

(68) Weidner, T.; Ballav, N.; Siemeling, U.; Troegel, D.; Walter, T.; Tacke, R.; Castner, D. G.; Zharnikov, M. Tripodal binding units for self-assembled monolayers on gold: A comparison of thiol and thioether headgroups. *J. Phys. Chem. C* **2009**, *113*, 19609–19617.

(69) Sander, F.; Peterle, T.; Ballav, N.; von Wrochem, F.; Zharnikov, M.; Mayor, M. Loops vs. Stems: Benzylic Sulfide Oligomeres Forming Carpet Type Monolayers. *J. Phys. Chem. C* **2010**, *114,* 4118–4125.

(70) Lindner, M.; Valášek, M.; Homberg, J.; Edelmann, K.; Gerhard, L.; Wulfhekel, W.; Fuhr, O.; Wächter, T.; Zharnikov, M.; Kolivoška, V.; et al. Importance of the Anchor Group Position (Para vs. Meta) in Tetraphenylmethane Tripods: Synthesis and Self-Assembly Features. *Chem. Eur. J.* **2016**, *22*, 13218–13235.

(71) Ford, W. E.; Abraham, F.; Scholz, F.; Nelles, G.; Sandford, G.; von Wrochem, F. Spectroscopic Characterization of Fluorinated Benzylphosphonic Acid Monolayers on AlO$_x$/Al Surfaces. *J. Phys. Chem. C* **2017**, *121*, 1690–1703.

(72) Hitchcock, A. P.; Fisher, P.; Gedanken, A.; Robin M. B. Antibonding σ* Valence MOs in the Inner-Shell and Outer-Shell Spectra of the Fluorobenzenes. *J. Phys. Chem.* **1987** *91*, 531-540.

(73) Yokoyama, T.; Seki, K.; Morisada, I.; Edamatsu, K.; Ohta, T. X-Ray Absorption Spectra of Poly-p-Phenylenes and Polyacenes: Localization of π* Orbitals. *Phys. Scr.* **1990**, *41*, 189-192.

(74) Frey, S.; Stadler, V.; Heister, K.; Eck, W.; Zharnikov, M.; Grunze, M.; Zeysing, B.; Terfort, A. Structure of Thioaromatic Self-Assembled Monolayers on Gold and Silver. *Langmuir* **2001**, *17*, 2408-2415.

(75) Plashkevych, O.; Snis, A.; Yang, L.; Ågren, H.; Matar, S. F. Near-Edge X-ray Absorption Spectra of Carbon-Nitride Molecules and Solids. *Phys. Scripta* **2001**, *63*, 70-86.

(76) Zubavichus, Y.; Zharnikov, M.; Shaporenko, A.; Grunze, M. NEXAFS study of glycine and glycine-based oligopeptides. *J. Electron Spectrosc. Relat. Phenom.* **2004**, *134*, 25-33.

(77) Bagus, P. S.; Weiss, K.; Schertel, A.; Wöll, Ch.; Braun, W.; Hellwig, H.; Jung, C. Identefication of Transitions into Rydberg States in the X-ray Absorption Spectra of Condensed Long-Chain Alkanes. *Chem. Phys. Lett.* **1996**, *248*, 129.

(78) Plashkevych, O.; Yang, L.; Vahtras, O.; Agren, H.; Pettersson L. G. M. Substituted Benzenes as Building Blocks in Near-Edge X-ray Absorption Spectra. *Chem. Phys.* **1997**, *222*, 125-137.

(79) Ballav, N.; Schüpbach, B.; Dethloff, O.; Feulner, P.; Terfort, A.; Zharnikov, M. Direct Probing Molecular Twist and Tilt in Aromatic Self-Assembled Monolayers. *J. Am. Chem. Soc.* **2007**, *129*, 15416-15417.

(80) Zhang, Z.; Wächter, T.; Kind, M.; Schuster, S.; Bats, J. W.; Nefedov, A.; Zharnikov, M.; Terfort, A. Self-Assembled Monolayers of Perfluoroanthracenylaminoalkane Thiolates on Gold as Potential Electron Injection Layers. *ACS Appl. Mater. Interfaces* **2016**, *8*, 7308–7319.

(81) Azzam, W.; Fuxen, C.; Birkner, A.; Rong, H.-T.; Buck, M.; Wöll, C. Coexistence of Different Structural Phases in Thioaromatic Monolayers on Au(111). *Langmuir* **2003**, *19,* 4958-4968.

(82) Bashir, A.; Sauter, E.; Rohwerder, M.; Zharnikov, M.; Azzam, W. Side Group Induced Polymorphism in Self-Assembled Monolayers: 3,5-Bis(trifluoromethyl) benzenethiolate Films on Au(111). *ChemPhysChem* **2017**, *18*, 702 –714.

(83) Vackář, J.; Hyt'ha, M.; Šimůnek, A. All-Electron Pseudopotentials. *Phys. Rev. B : Condens. Matter Mater. Phys.* **1998**, *58*, 12712—12720.

(84) Methfessel, M.; Fiorentini, V.; Oppo, S. Connection between Charge Transef and Alloying Core.Level Shifts Based on Density-Functional Calculations. *Phys. Rev. B : Condens. Matter Mater. Phys.* **2000**, *61*, 5229—5236.

(85) Morikawa, Y. ; Hayashi, T. ; Liew, C. C. ; Nozoye, H. First-Principles Theoretical Study of Alkylthiolate Asdoprtion on Au(111). *Surf. Sci.* **2002**, *507*, 46—50.

(86) El-Sayed, A.; Borghetti, P.; Goiri, E.; Rogero, C.; Floreano, L.; Lovat, G.; Mowbray, D. J.; Cabellos, J. L.; Wakayama, Y.; Rubio, A.; Ortega, J. E.; de Oteyza, D. G. Understanding Energy-Level Alignment in Donor – Acceptor/Metal Interfaces from Core-Level Shifts, *ACS Nano*, **2013**, *7*, 6914-6920.

(87) Bagus, P. S. ; Pacchioni, G. ; Sousa, C. ; Minerva, T. ; Parmigiani, F. Chemical Shifts of the Core-Level Binding Energies for the Alkaline-Earth Oxides. *Chem. Phys. Lett.* **1992**, *196*, 641 – 646.

(88) Bagus, P. S. ; Ilton, E. S. ; Nelin, C. J. The Interpretation of XPS Spectra : Insights into Materials Properites. *Surf. Sci. Rep.* **2013**, *68*, 273 –304.

(89) Heimel, G.; Romaner, L.; Brédas, J.-L.; Zojer, E. Organic/Metal Interfaces in Self-Assembled Monolayers of Conjugated Thiols: A First-Principles Benchmark Study. *Surf. Sci.* **2006**, *600*, 4548–4562.

TOC Graphic
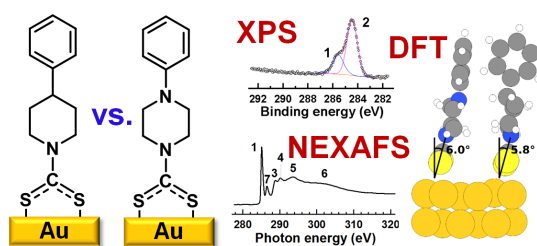
4.4.2 Supporting information

Computational details

Considered structures - Starting geometries and optimisation procedure. The starting geometry for PPz was chosen as follows. First, the isolated molecule was optimised in gas phase. With the distance between the two S atoms in the optimised structure comparable to the one between two high symmetry docking sites on the Au(111) surface, several trial geometries were set up, with the docking groups in *fcc*-hollow, *hcp*-hollow and ontop positions, respectively. For all docking positions both a cofacial and a herringbone arrangement were tested. A preliminary geometry optimisation was performed using the FHI-aims light default basis set. The most stable cofacial and herringbone arrangements were then further optimised using the tight default basis set. On these two geometries, the impact of twisting the phenyl rings by 90° was tested, too, to check the role of intra-molecular interactions. The final, optimised geometries of the four polymorphs are shown in figure 4.27. The overall most stable arrangement is herringbone coplanar (see table 2 in the main manuscript).
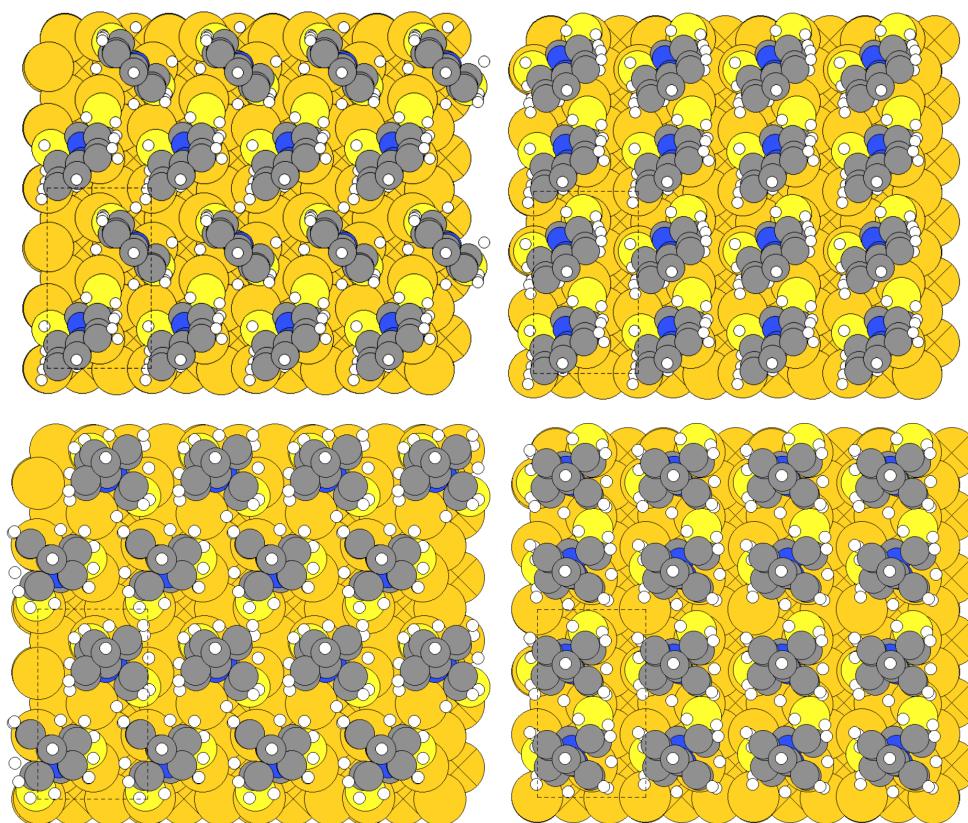
Figure 4.27: Herringbone coplanar (top left panel), cofacial coplanar (top right panel), herringbone twisted (bottom left panel) and cofacial twisted (bottom right panel) optimised PPz geometries. The unit cell is marked by the dashed black line. Au atoms are depicted in dark yellow, S atoms in light yellow, C atoms in grey, N atoms in blue and H atoms in white.

Both in the herringbone and cofacial arrangements, the four S atoms in the unit cell occupy essentially the same docking positions: one docks in ontop position, one in bridge position and the remaining two dock in ontop positions shifted towards hollow/bridge sites (see figure 4.28) in agreement with the experimentally observed inequivalent S docking positions (see main manuscript).

Figure 4.28: S positions in the herringbone (left) and cofacial (right) optimised geometries. The unit cell is marked by the dashed black line. Au atoms are depicted in dark yellow, S atoms in light yellow.

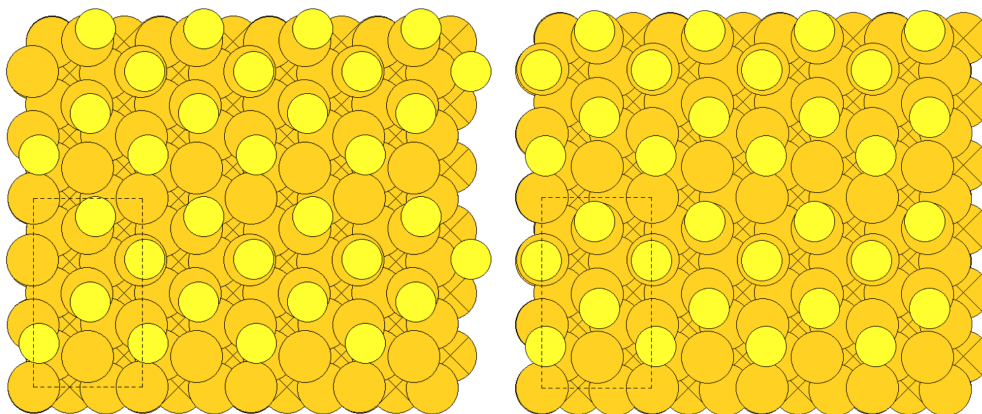The above strategy to identify the most suitable arrangement and conformation performs a restricted sampling of the potential energy surface. There could in principle be (many) other ways for the molecules to dock to the surface and possibly larger unit cells containing a larger number of symmetry-inequivalent molecules. An extensive exploration of the full potential energy surface is beyond the purpose of the present work. Nevertheless, it is worthwhile to note that all the initial starting geometries (both cofacial and herringbone arranged) ended up with the S atoms occupying essentially the same sites. Moreover, it is interesting to take a look at the work function change $\Delta\Phi$ for the different polymorphs (table 4.14, where also the total energies are reported): within the same arrangement (cofacial or herringbone) the values are similar (with the exception of the least stable polymorph). A larger difference can be noted comparing cofacial and herringbone polymorphs, while between coplanar and twisted SAMs the difference is much more relevant (see table 1 in the main manuscript).

Table 4.14: Energy per unit cell and work function change ($\Delta\Phi$) of different coplanar PPz polymorphs, named after the arrangement (Hb for herringbone and Cf for cofacial) and the initial position of the docking atoms. The given values are slightly different from the ones reported in the main text due to the light basis set used for the preliminary optimisations. Only the most stable polymorphs for every arrangement (Hb hcp and Cf hcp) were subsequently optimised using the tight basis set.

Polymorph	Energy per unit cell / eV	$\Delta\Phi$
Hb hcp	$-16\,142\,284.468$	-1.69
Hb fcc	$-16\,142\,284.366$	-1.64
Hb ontop	$-16\,142\,284.426$	-1.70
Cf hcp	$-16\,142\,284.023$	-1.51
Cf fcc	$-16\,142\,283.971$	-1.54
Cf ontop	$-16\,142\,283.420$	-1.63

For PPd, we first performed several tests on isolated, gas phase molecule, optimising the geometries of different conformers. This was done to take in account that the piperidine ring can assume different conformations (chair, boat, twist, half chair) and that the H atom and the phenyl ring in position 4 can orient in different ways with respect to the lowest part of the molecule. Since these conformers are separated by energy barriers that are very unlikely

overcome during the optimisation, this approach was adopted to sample the potential energy surface, although to a limited extent. The most stable structure obtained this way was used to set up the unit cell. Considering that both the PPz and PPd molecules have the same bottom part, it is reasonable to assume that they will also have the same docking sites. Moreover, in the PPz case the impact of different starting S atoms arrangements turned out to have a negligible impact and all tested arrangements resulted in the same S atom positions. Based on this reasoning, the docking arrangement of the PPz optimised geometry was then used as starting point for building the PPd SAM: the metal part and the bottom part of the molecules were kept and the uppermost part was replaced, using the most stable conformer. The structures were subsequently optimised using the FHI-aims tight default basis set and are shown in figure 4.29. Both, the herringbone and the cofacial arrangement and both the coplanar and the twisted conformation were tested, similar to what has been done for PPz. Again, as shown in the main text, the herringbone arrangement is more favourable, but contrary to PPz, in the most stable geometry the molecules assume a twisted conformation.
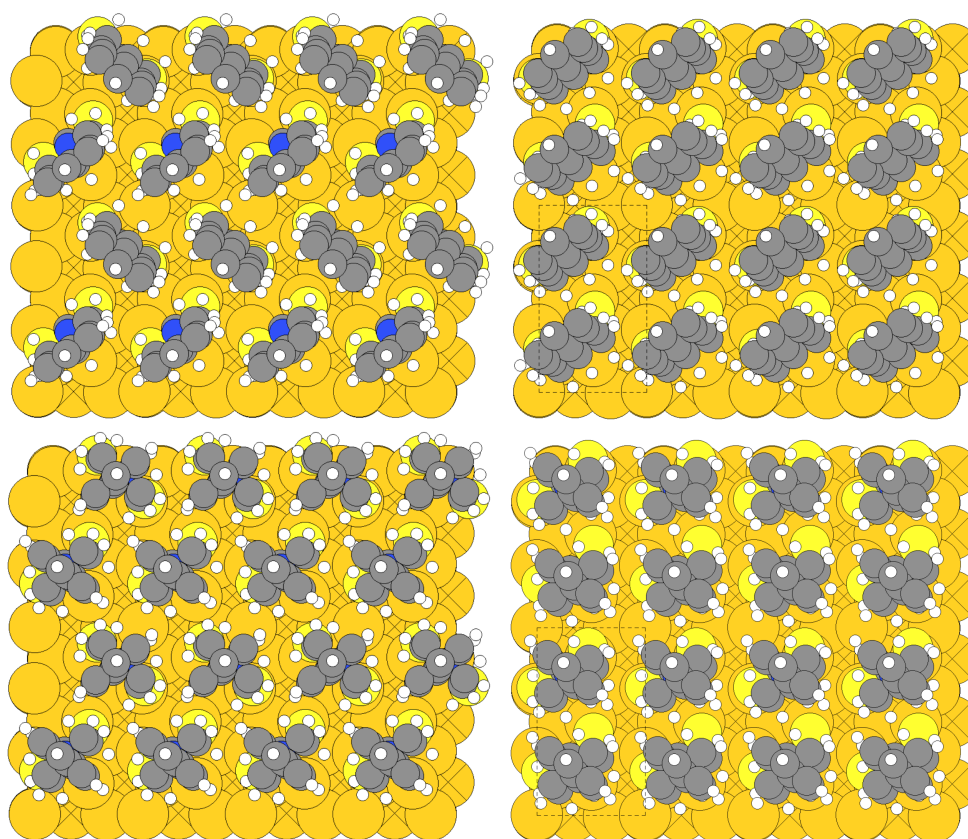
Figure 4.29: Herringbone coplanar (top left panel), cofacial coplanar (top right panel), herringbone twisted (bottom left panel) and cofacial twisted (bottom right panel) optimised PPd geometries. The unit cell is marked by the dashed black line. Au atoms are depicted in dark yellow, S atoms in light yellow, C atoms in grey, N atoms in blue and H atoms in white.

With the C atom in position 4 in the piperidine ring sp^3 hybridised, in the PPd herringbone SAM there could in principle be four different ways for the molecules to arrange with respect to the neighbours. This is due to the different orientations of the phenyl ring and the H atom bonded to that C atom. To see how this would possibly impact the observables, an optimisation using a light basis set was performed. The optimised structures are shown in figures 4.30 and 4.31, where also the names assigned to them are given.

Figure 4.30: Four different PPd herringbone twisted conformers. Top left: tw1 (most stable conformer), top right: tw2, bottom left: tw3, bottom right tw4.
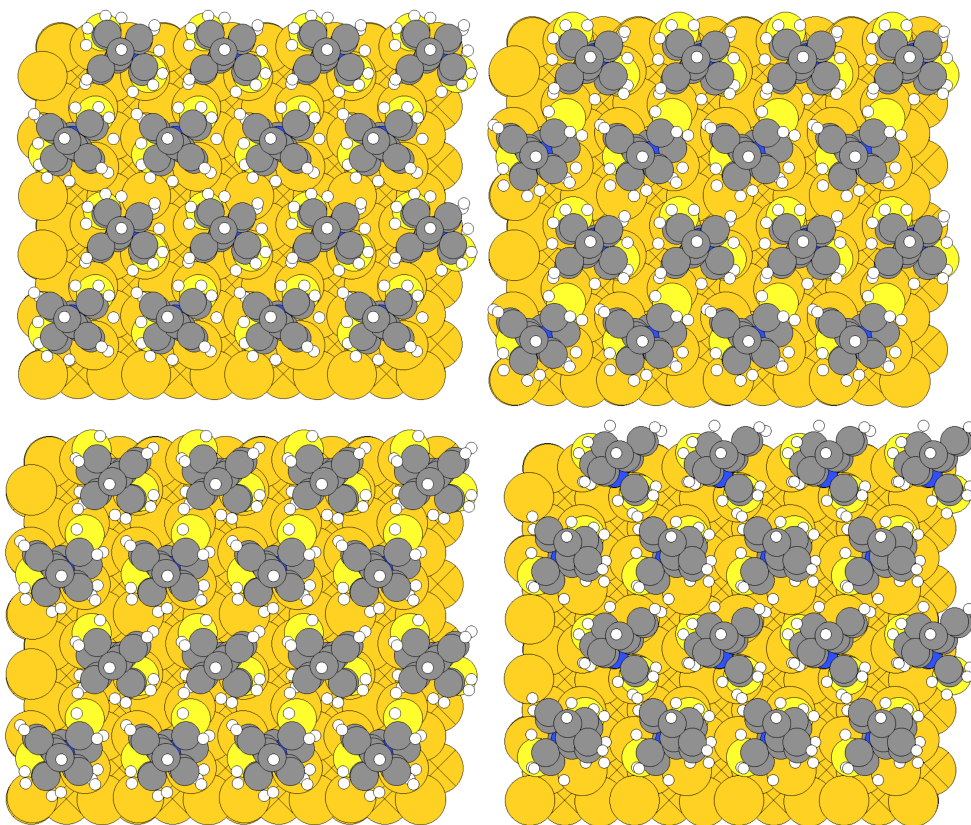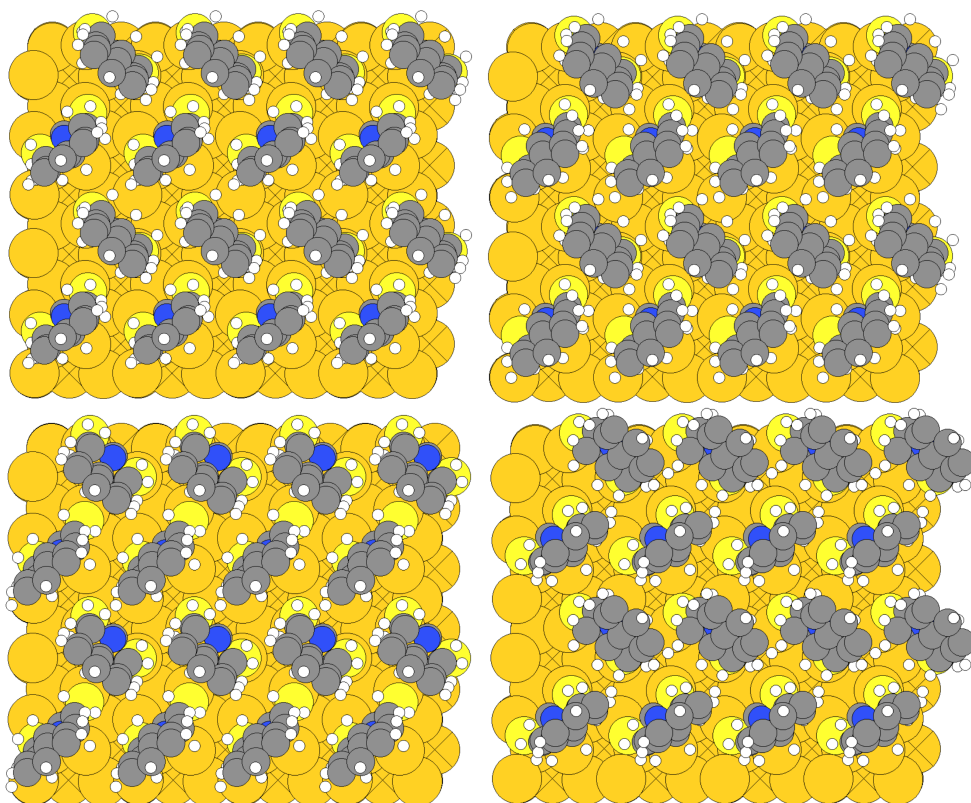

Figure 4.31: Four different PPd herringbone coplanar conformers. Top left: cf1 (most stable conformer), top right: cf2, bottom left: cf3, bottom right cf4.

The energy and work function change values are reported in table 4.15. A certain variability in the work function change can be noticed, with on average larger values for the twisted polymorphs. However, no clear trend can be identified. The conformers named 1cp and 1tw are the most stable among the coplanar and the twisted ones, respectively, and were used for the optimisation with the tight basis set.

Table 4.15: Energy per unit cell and work function change ($\Delta\Phi$) of the different herringbone twisted and coplanar PPd conformers. The structures are named according to figures 4.30 and 4.31. The given values are slightly different from the ones reported in the main text due to the light basis set used for the preliminary optimisations. Only the most stable twisted and coplanar conformers (1tw and 1cp) were subsequently optimised using the tight basis set.

Polymorph	Energy per unit cell / eV	$\Delta\Phi$
1tw	$-16\,141\,410.807$	-2.59
2tw	$-16\,141\,410.705$	-2.51
3tw	$-16\,141\,410.460$	-2.46
4tw	$-16\,141\,410.621$	-2.56
1cp	$-16\,141\,410.697$	-2.53
2cp	$-16\,141\,410.528$	-2.35
3cp	$-16\,141\,410.668$	-2.54
4cp	$-16\,141\,410.280$	-2.45

Tilt angles of the π^* orbitals of the phenyl ring and molecular tilt and twist angles of the main conformers. The calculated tilt angles of the π^* orbitals of the phenyl ring (α) and the molecular tilt and twist angles (β and γ, respectively) for the main conformers of the PPz and PPd SAMs are reported in table 4.16. The values of the two inequivalent molecules in the unit cell are given. Additionally, the average value of α is reported calculated as defined in the caption of table 3 in the main manuscript. Since the phenyl C atoms are not all perfectly in a plane, the choice of the atoms used to define the plane of the ring could slightly change the obtained value. The differences were, however, found to be negligible and for sake of consistency for every polymorph the plane of the phenyl ring was defined by taking the atoms in position 1 and 4 together with the next atom with the lowest z coordinate.

Table 4.16: calculated tilt angles of the π^* orbitals of the phenyl ring and molecular tilt and twist angles of the main PPz and PPd conformers. The subscripts 1 and 2 refer to the two inequivalent molecules in the unit cell. Additionally, for α the average value according to the equation given in the caption of table 3 in the main manuscript is given.

			α / °			β / °		γ / °	
			α_1 / °	α_2 / °	α_{av} / °	β_1 / °	β_2 / °	γ_1 / °	γ_2 / °
PPz	herringbone	coplanar	84.1	79.0	81.2	7.4	13.7	37.6	36.1
		twisted	89.5	81.0	83.6	0.7	10.6	44.3	31.4
	cofacial	coplanar	82.5	81.6	82.0	11.0	9.8	47.0	30.6
		twisted	89.3	88.9	89.1	4.9	4.2	81.9	74.4
PPd	herringbone	coplanar	89.6	77.5	81.2	6.2	12.9	86.5	14.2
		twisted	82.5	80.6	81.5	14.2	12.6	58.0	41.1
	cofacial	coplanar	72.8	73.3	73.0	17.8	16.8	13.9	6.0
		twisted	86.1	85.0	85.5	10.9	12.1	68.8	65.2

Details of the employed computational methods. The preliminary geometry optimisations mentioned in the previous section were performed using the default FHI-aims light basis set for all the elements and setting the following self consistency cycle criteria: sc_accuracy_rho 1e-5, sc_accuracy_etot 1e-6, sc_accuracy_forces 1e-4, sc_accuracy_eev 1e-3. The more accurate geometry optimisations were performed using the default FHI-aims tight basis set for all the elements and adding the self consistency cycle accuracy criterion sc_accuracy_potjump 1e-4. Regarding the reduced coverage unit cells, 1/16 and 1/36 coverage were considered. Since calculating them using the previously described settings would have been computationally particularly expensive, as already mentioned in the main text the metal bulk was modelled with 3 layers of Au instead of 5 and the following reduced settings for basis set and self-consistency criteria were applied: The tags sc_accuracy_rho and sc_accuracy_etot were set to 1e-3 and 1e-4, respectively. The sum of eigenvalues (sc_accuracy_eev) and the vacuum level potential shift (sc_accuracy_potjump) were not used as convergence criteria. For the C, H, N and S atoms the default tight basis set was used. For the Au atoms the default tight basis set was modified as follows: the l_hartree tag was set to 4, the onset radius of the cutoff potential to 3.9 and the radial width of the cutoff potential to 1.8, one more division line was commented, the outer grid was consequently set to 302 and the h basis function of the first tier was commented. These settings were chosen as a consequence of the convergence test explained below.

The calculations on the periodic systems and on the isolated gas phase molecules were performed defining the occupation of the Kohn-Sham eigenstates using a Gaussian broadening function and setting the with to 0.1 and 0.01 eV, respectively. The core level energies were obtained from the atom projected density of states output files (2001 data points for a range of 20 eV with the value for the Gaussian broadening set to 0.1 eV). The energy (first column of the output file) corresponding to the maximum value of the total dos (second column of the output file) was taken as the value of the core level binding energy. The energy ranges were chosen after calculating the core level energies of a single isolated atom.

The aforementioned convergence tests were performed to guarantee that the use of reduced and less expensive computational settings still gives reliable and converged results. Convergence is reached when the results obtained using more accurate settings differ by less than a certain convergence criterion, set according to the purpose of the calculation. The value of the work function change and of the relative core level energies were taken as convergence criteria. Regarding the basis set, for the investigated cases the results obtained using the FHI-aims default tight settings were compared to the ones obtained increasing the accuracy of the settings: for every element the onset radius and the radial width of the cutoff potential were increased to 4.1 and 2.1 Å, respectively, the radius of the outermost shell of the basic grid was increased to 7.1 Å, the radial multiplier was set to 3, the outer_grid tag was set to 590, the corresponding division line of the angular_grids tag was uncommented and a further basis function was added, specifically the first basis function of the second tier for Au, the first of the third tier for H, C and N and the third of the second tier for S. Regarding the k-points, the $5 \times 9 \times 1$ k-point grid was compared to a $15 \times 27 \times 1$ grid. The variations in the work-function modification were always below 0.025 eV and the relative core level energy differences always below 0.010 eV, values widely acceptable for the present purposes.

The Au bulk was modelled using the theoretically optimised lattice constant value. To obtain that, single point calculations were performed using different lattice constants, the total energy was plotted as a function of the lattice constant and the curve was fitted with a quadratic function. The value of the lattice constant corresponding to the minimum of the curve was taken as the optimised one. The value of the lattice constant was changed by 0.0025 Å each step. A conventional unit cell with 4 Au atoms was used. A $12 \times 12 \times 12$

and a $24 \times 24 \times 24$ k-point grids were adopted, with the obtained values being in agreement up to the third decimal digit. The obtained value for the lattice constant was 4.158 Å, corresponding to a nearest neighbour distance of 2.940 Å. The same settings adopted to get the optimised lattice constant were employed to describe the Au atoms in any calculation used to get the reported results.

Calculation of the work function change. The work function change has been calculated as the difference between the work function of the SAM/Au(111) systems and the work function of a clean Au(111) slab. The same settings were used for the optimisation and in both cases the three bottom Au layers have been kept fixed during all the calculations while the topmost two have been relaxed.

Details of the XP spectra simulations. The damping factor for weighting the contribution of every atom was introduced using the following exponential attenuation function:

$$w_i(d) = w_0 e^{\frac{-d}{\lambda}}. \tag{4.4}$$

w_0 is a scaling constant that does not change the shape of the spectrum. $w_i(d)$ is the individual weight of the i-th atom, that depends on the vertical distance d between the atom and the topmost C atom in the SAM and on a damping factor λ. According to Lamont and Wilkes[121], λ is defined as $\lambda = 0.3 E_{kin}^{\beta}$, where E_{kin} is the kinetic energy of the escaping electron and β is an empirical attenuation factor. E_{kin} is given by the difference between the energy of the incident photon (350 eV in this case) and the calculated binding energy of the C 1s electron. The value of β was set to 0.405, after tuning it in such a way that the calculated relative intensities of the peaks matched the experimental ones.

Further information on the calculated core-level binding energies.

To estimate the impact of reduced coverage and ensuing disorder in the PPd SAMs on the SAM-induced shift in electrostatic energy, ΔE, one can start from the ideal situation considered in the simulations and then estimate the impact of reduced coverage, Θ, and increased molecular tilt, β, observed in the experiments via:

$$\Delta E^* = \Delta E \frac{cos(\beta_{calc})\Theta_{calc}}{cos(\beta_{exp})\Theta_{exp}}. \tag{4.5}$$

Inserting the values from Tables 1, 2, and 3 of the main manuscript (for the latter taking the average of the two molecules in the unit cell) and setting Θ_{calc} to 1, one obtains $\Delta E^* = \Delta E \times 0.90$.

Based on the calculated shift in electrostatic energy, which corresponds to the work function change ($\Delta\Phi_{PPd,calc} = 2.54$ eV) this yields $\Delta E^* = 2.29$ eV (i.e., a disorder-induced reduction by 0.25 eV). Note that the above considerations only provide a rough estimate, as they neglect the coverage dependence of depolarisation effects, for the experimental tilt angle only the lower boundary can considered, and also a possible tilt angle dependence of the interfacial charge transfer is neglected.

Inequivalent molecules in the full coverage unit cell. As already explained in the main text, in the full coverage unit cell used in the simulations there are two molecules. Since they are not symmetry equivalent and have slightly different tilt angles, there are some small differences also in the core level energies. In figure 4.32 a (PPz) and b (PPd) the non screened energies of the two molecules in the full coverage unit cell of the most stable polymorph are reported. The energies are given without any shift and screening effects are

not included either, as we are seeking for "conceptual" differences between the core level binding energies of the C atoms, which would just be obscured by a distance dependent screening. In the simulation of the full coverage XP spectrum the average values were taken in account. Since for the reduced coverage case only one molecule was kept in the unit cell, the comparison was always made taking as reference the molecule of the full coverage case used to set up the low coverage unit cell.
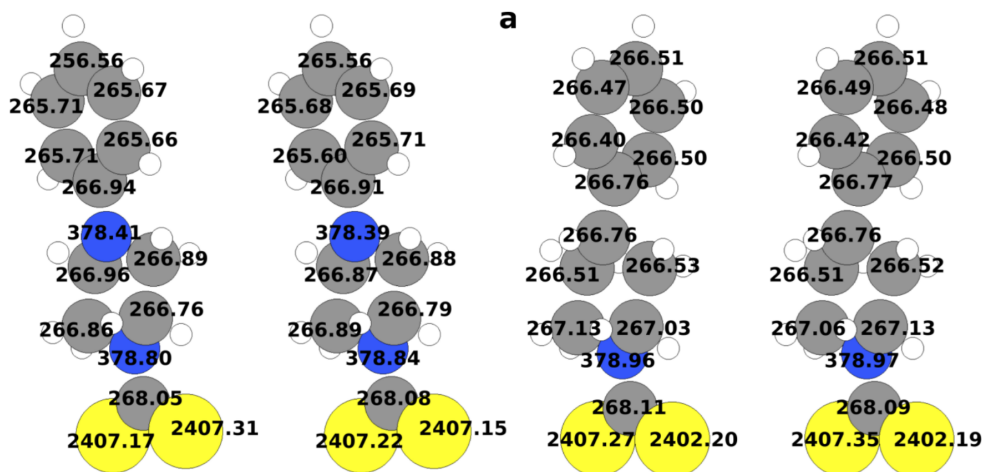

Figure 4.32: C1s core level energies without screening effects of the PPz (a) and PPd (b) molecules in the full coverage unit cell. Carbon atoms are depicted in grey, H in white, N in blue and S in light yellow.

PPz binding energies. As reported in the main text, the 1s binding energy of the topmost C atoms is shifted relative to its neighbours both at full and at reduced coverage. To understand that shift, the C1s core level binding energies were calculated for the isolated PPz molecule, this way excluding any non chemical effects. From the energy values, reported in figure 4.33, one can see that the shift of about 0.2 eV between the topmost C atom and its neighbours is still present.
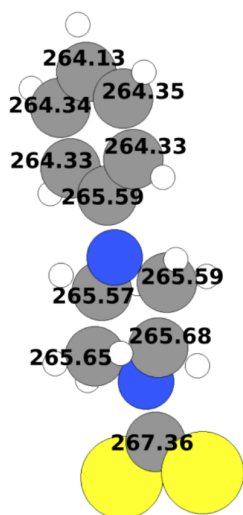

Figure 4.33: C1s core level energies of an isolated PPz molecule. Carbon atoms are depicted in grey, H in white, N in blue and S in light yellow.

The chemical origin of this shift can be better understood considering the aniline molecule as model system (figure 4.34). In this case the difference between the carbon in position 4

and the carbons in positions 3 and 5 is larger and a shift is also present between these 2 latter carbons and the ones in position 2 and 6, whereas in the PPz molecule this is not the case. Looking at the resonance forms of aniline (figure 4.35), a negative charge is sitting on the ortho and para positions, consistent with a smaller absolute values of the core level energies of these atoms with respect to the other ones.
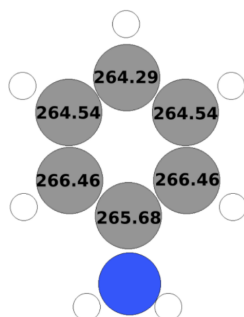

Figure 4.34: Calculated C 1s core level energies of aniline. Carbon atoms are depicted in grey, H in white and N in blue.
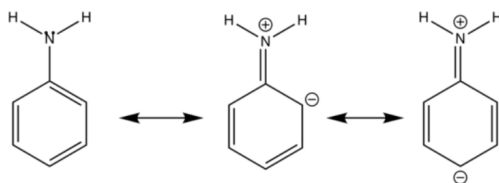

Figure 4.35: Resonance forms of aniline.

The difference between the para and the meta positions is larger than the one between the meta and the ortho ones: the ortho carbons bonded to the C1 feel the negative charge to a lower extent, because of the inductive effect due to the N atom. Comparing the aniline to the ph-piperazine-DTC, in the latter case the shifts are smaller (actually there is almost no difference between the meta carbons and the ortho ones). This can be understood considering that for ph-piperazine-DTC the nitrogen atom belongs to a piperazine ring instead of being bonded to two H atoms. Therefore, the negative charge that can delocalise is significantly smaller than in the aniline case.

Coverage dependent shifts. In figures 4.36 a (PPz) and b (PPd) the C 1s, N 1s and S 1s core level energy differences between full and 1/36 coverage cases are given. It can be seen that the differences are larger for the atoms that are further away from the metal surface, meaning that the atoms closer to the surface to some extent feel the dipole also in the reduced coverage cases and that the effects of such a dipole rapidly decays moving away from it. The energy of the S atoms and of the C directly bonded to them show a very weak coverage dependence. In the PPd case the shift is larger, which is consistent with this system inducing a stronger interface dipole. This can be concluded also comparing the calculated work function changes: -1.71 eV for PPz and -2.58 for PPd.
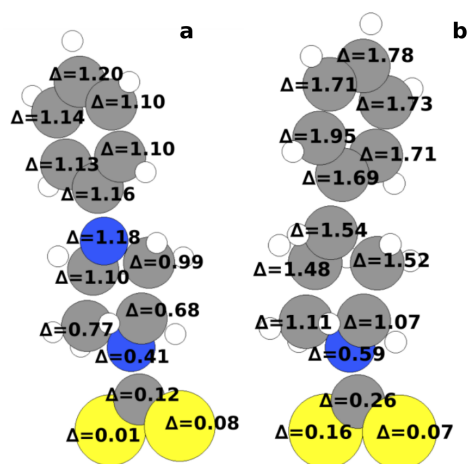
Figure 4.36: C1s, N1s and S1s core level energy differences between full and 1/36 coverage for PPz (a) and PPd (b). C atoms are depicted in grey, H in white, N in blue and S in light yellow.

C1s core level energies. In figure 4.37 the C1s binding energy of an isolated C atom is plotted as a function of charging the atom. Charges between -e and e are considered and the energy values are referenced to the binding energy of the neutral atom. It can be noticed that even small changes in the charge cause large shifts in the binding energy. Moreover, the more positive the charge, the larger the magnitude of the shifts. The obtained evolution is not strictly linear. As a consequence, the calculated slopes vary between 0.09 eV and 0.17 eV for the change in binding energy per 0.01×e change in atomic charge.
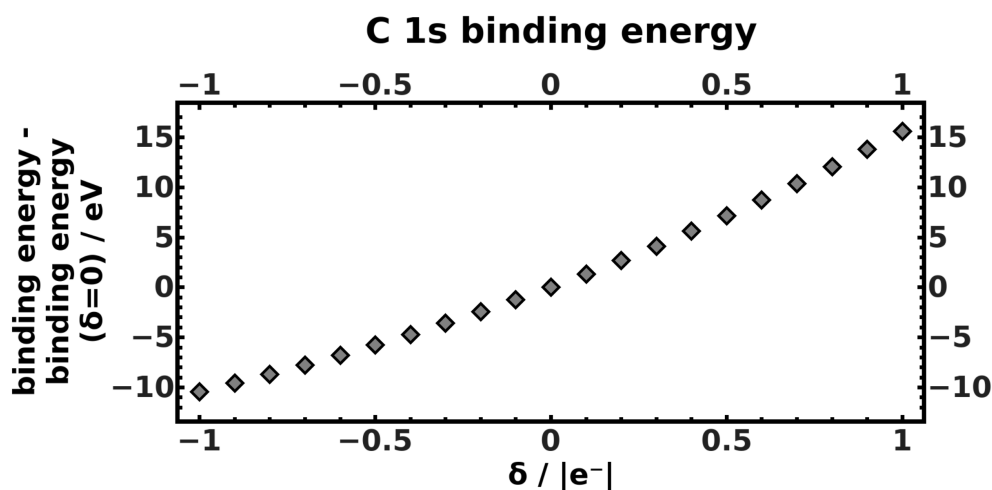
Figure 4.37: Evolution of the C1s core level energies depending on the charge δ sitting on the C atom. The energies are given aligned to the 1s core level energy of the neutral C atom.

The simple model of charging a spherically symmetric atom cannot be quantitatively transferred to the much more complex charge rearrangement pattern at the DTC/Au(111) interface, but it shows that changes in the atomic charge of a few hundredths of the elementary charge (as observed in figure 8 of the main manuscript) can result in BE shifts of several hundred meV.

Details of the calculated interfacial charge rearrangements

Upon formation of the bond between a SAM and a metal surface, rearrangements of the charge density $\Delta\rho$ occur. Such rearrangements are modelled via the following equation:

$$\Delta\rho = \frac{1}{n}[\rho_{SAM/Au} - (\rho_{Au} + \rho_{SAMH} - \rho_H)], \tag{4.6}$$

where n is the number of molecules in the unit cell and $\Delta\rho$ is calculated using the charge densities associated with the combined SAM/metal system, $\rho_{SAM/Au}$, the isolated metal slab, ρ_{Au}, the isolated SAM with the S atoms saturated with H atoms, ρ_{SAMH}, and the isolated H atoms, ρ_H. To get the charge densities of the subsystems, the geometries they later adopt in the optimised combined structure were maintained. In the SAMH case, only the position of the H atoms was relaxed. The optimised H positions were then used to calculate ρ_H. To get a plot similar to Figure 8 in the main paper, the quantity $\Delta\rho$ was integrated over the x,y plane within the unit cell. $\Delta\rho$ for the full and reduce coverage case of the PPz SAM are plotted in figure 4.38.
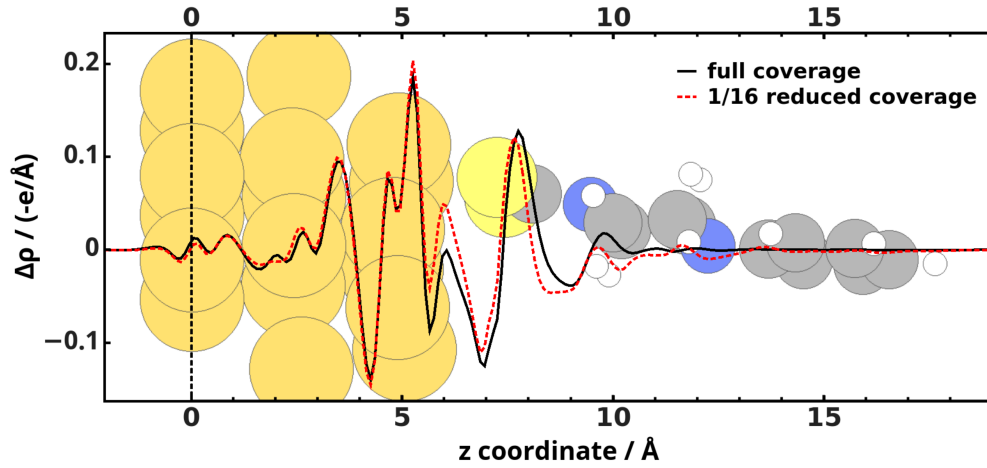

Figure 4.38: x,y plane integrated $\Delta\rho$ per molecule for the full (black solid line) and 1/16 reduced (red dashed line) coverage case of the PPz SAM.

4.5 1,8,13-substituted triptycene-based molecular tripods: versatile scaffold for vertical surface adsorption

The dithiocarbamate (DTC) based SAMs investigated in section 4.4 have been shown to dock with both the S atoms of the DTC functionality, with only a slightly inhomogeneity in the docking sites. The observation is interesting in the spirit of growing SAMs of molecules bearing multiple docking groups. The purpose would be to better control the orientation of the molecules. To this aim, triptycene based SAMs, with three S atoms as docking groups groups were grown on the Au(111) surface. Two basic systems are considered in this work.

The results are presented in form of a manuscript that has been submitted to the *Journal of American Chemical Society* and is currently under revision. Only a reduced version of the supporting information is reported. The complete supporting information contains additional data of the synthesis of the molecules, NMR, IR and high resolution mass spectra, single crystal X-ray structural analysis and optimised geometries in the xyz format. The work was a collaboration between the groups of Takanori Fukushima, Michael Zharnikov and Egbert Zojer. Fumitaka Ishiwari, Hiromu Tago, Yoshiaki Shoji, Shintaro Fujii, Manabu Kiguchi and Takanori Fukushima synthesised the molecules and registered the STM pictures. Egbert Zojer and I contributed the simulation part. Eric Sauter and Michael Zharnikov prepared the SAMs and performed X-ray photoelectron spectroscopy (XPS) and near edge X-ray absorption fine structure (NEXAFS) measurements. Takanori Fukushima, Michael Zharnikov and Egbert Zojer coordinated the work. The data were discussed and interpreted jointly by all the authors. A first draft of the paper was written by Fumitaka Ishiwari. All the other authors contributed in writing the sections concerning their results and revising the draft. I performed all the calculations presented in the work, prepared figures 5 and 6 and wrote a draft of the computational part, that was then revised and corrected by Egbert Zojer and incorporated in the manuscript by Egbert Zojer and me. I wrote the computational section contained in the supporting information and prepared all the figures presented there. The text was revised and corrected by Egbert Zojer.

4.5.1 Submitted manuscript

Triptycene Tripods for the Formation of Highly Uniform and Densely Packed Self-Assembled Monolayers with Controlled Molecular Orientation

Fumitaka Ishiwari,[†,‡] Giulia Nascimbeni,[#,‡] Eric Sauter,[§,‡] Hiromu Tago,[†] Yoshiaki Shoji,[†] Shintaro Fujii,[||] Manabu Kiguchi,[||] Tomofumi Tada,[⊥] Michael Zharnikov,[*,§] Egbert Zojer,[*,#] and Takanori Fukushima[*,†]

[†]Laboratory for Chemistry and Life Science, Institute of Innovative Research, Tokyo Institute of Technology, 4259 Nagatsuta, Midori-ku, Yokohama 226-8503, Japan.

[#]Institute of Solid State Physics, NAWI Graz, Graz University of Technology, Petersgasse 16, 8010 Graz, Austria.

[§]Applied Physical Chemistry, Heidelberg University, Im Neuenheimer Feld 253, 69120 Heidelberg, Germany.

[||]Department of Chemistry, Graduate School of Science and Engineering, Tokyo Institute of Technology, Meguro, Tokyo 152-8551, Japan.

[⊥]Materials Research Center for Element Strategy, Tokyo Institute of Technology, 4259 Nagatsuta, Midori-ku, Yokohama 226-8503, Japan.

Supporting Information Placeholder

ABSTRACT: When employing self-assembled monolayer (SAM) for tuning surface- and interface-properties, organic molecules that enable strong binding to the substrate, large-area structural uniformity, precise alignment of functional groups, and control of their density are highly desirable. To achieve these goals, tripod systems bearing multiple bonding sites have been developed as an alternative to conventional monodentate systems. Bonding of all three sites has, however, hardly been achieved, with the consequence that structural uniformity and orientational order in tripodal SAMs are usually quite poor. To overcome that problem, we designed 1,8,13-trimercaptomethyltriptycene (**T1**) and 1,8,13-trimercaptotriptycene (**T2**) as potential tripodal SAM precursors and investigated their adsorption behavior on Au(111) combining several advanced experimental techniques and state-of-the-art theoretical simulations. Both SAMs adopt dense, nested hexagonal structures but differ in their adsorption configurations and structural uniformity. While the **T2**-based SAM exhibits a low degree of order and noticeable deviation from the desired tripodal anchoring, all three anchoring groups of **T1** are equally bonded to the surface as thiolates, resulting in an almost upright orientation of the benzene rings and large-area structural uniformity. These superior properties are attributed to the effect of conformationally flexible methylene linkers at the anchoring groups, absent in the case of **T2**. Both SAMs display interesting electronic properties and, bearing in mind that the triptycene framework can be functionalized by tail groups in various positions and with high degree of alignment, especially **T1** appears as an ideal docking platform for complex and highly functional molecular films.

INTRODUCTION

Self-assembled monolayers (SAMs) enable tailoring the wettability, adhesiveness, and work functions of solid substrates as well as organic/inorganic hybrid interfaces. As surfaces and interfaces typically determine the performance of devices especially at the nanoscale, the application of SAMs is of particular technological importance. Besides conventional monodentate SAMs with a single anchor group, several types of molecular platforms with multiple anchoring sites have recently been developed. This aims at more effectively controlling the orientation, spatial and lateral arrangement, and density of the molecules bonded to solid surfaces. Moreover, multiple anchoring groups help achieving a robust anchoring configuration.[1] Of particular interest in this context are molecular tripods that usually consist of rigid tetrahedral cores bearing three anchors, such as thiol groups for binding to Au(111).[2–22] Examples for such systems include triarylmethane-based molecular tripods featuring an sp³-hybridized carbon[4–8] or

silicon[9–13] core (**A** and **B** in Figure 1a). Also a methylene thiol-appended adamantane-based tripod (**C** in Figure 1a)[14–17] has been reported to form a hierarchical chiral network structure on Au(111).[15] Recently, Mayor *et al.*[4] investigated the impact of the configuration of anchor groups on the surface adsorption behavior, by comparing triarylmethane-based molecular tripods with *meta*- and *para*-type substitution patterns (**D**_*meta*_ and **D**_*para*_ in Figure 1a). They showed that the former can form covalently bonded monolayers on Au(111), while the latter only grow in multilayers.[4] This result underlines that careful molecular design of tripods is crucial for developing an optimal molecular platform for the controlled assembly on solid surfaces. Such a system should yield an adsorption state with all anchor groups equally bonded to the surface. Ideally, that would also result in a fully vertical molecular orientation. However, the most existing molecular tripods adopt unfavorable conformations, where the anchor groups orient away from the surface due to free bond rotation of the sulfur-containing functionalities (as indicated by curved red arrows in Figure 1a). This leads

to significant deviations from the desired tripodal configuration.

Herein, to overcome this problem and to develop an "ideal platform", we propose novel molecular tripods based on a highly rigid triptycene framework (Figure 1b). We have recently shown that 1,8,13-trisubstituted triptycenes exhibit superb self-assembling abilities to form well-defined, dense two-dimensional (2D) hexagonal structures through a nested packing of the aromatic blades.[23–28] Consequently, the trisubstituted triptycenes should offer a starting point for the development of ideal SAMs featuring well controlled molecular density and orientation. Notably, due to the tridentate configuration, the present systems differ distinctly from previously reported monodentate triptycene-based monolayers with a single thiol or selenol group attached in the bridgehead position.[29,30] There, the triptycene moieties are prone to adopting a substantially tilted configuration.

In the present study, we synthesized two types of molecular tripods (Figure 1b) bearing anchoring thiol groups attached to the 1,8,13-positions of the triptycene framework either directly (**T2**) or via a methylene linker (**T1**). The latter exhibits a certain flexibility in terms of the configuration of the sulfur-containing groups. Importantly, the three thiol groups in both systems are arranged in a way that they cannot individually rotate away from the surface. Furthermore, the interatomic distances between the sulfur atoms in **T1** and **T2** can be such that they quite closely fit the lattice structure of Au(111).[31]
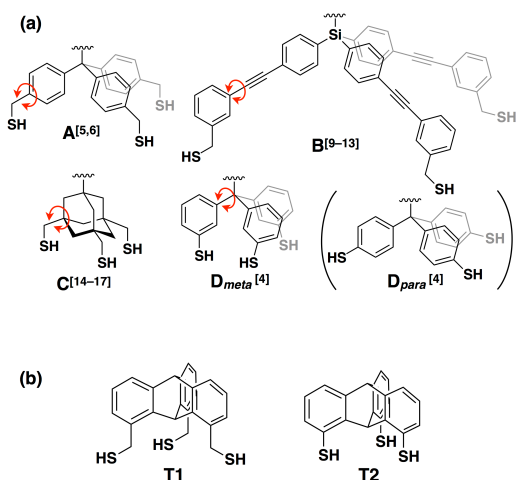
Figure 1. (a) Schematic structures of selected examples of reported molecular tripods (**A**–**D**). (b) Chemical structures of 1,8,13-substituted triptycene-based molecular tripods (**T1** and **T2**). In **A**–**D**, free rotation of the single bonds highlighted by the curved red arrows might result in anchoring groups pointing away from the substrate. Such an unfavorable configuration cannot occur in **T1** and **T2**.

A general advantage of triptycenes as anchoring platforms is that they can be substituted with functional units in various ways taking advantage of the four vacant sites per molecule, i.e., the bridgehead,[25] 4, 5, and 16-positions.[24] To lay the foundations for the further development of triptycene-anchored SAMs, in the present study we focus on the self-assembly behavior of the fundamental triptycene-based tripods **T1** and **T2** on Au(111). For that, we use a variety of complementary experimental tools, including scanning tunneling microscopy (STM), X-ray photoelectron spectroscopy (XPS), near-edge X-ray absorption fine structure (NEXAFS) spectroscopy, and Kelvin probe (KP). The experimental findings are

rationalized through dispersion-corrected density functional theory (DFT) simulations. We demonstrate that the triptycene-based tripods, especially **T1**, can adopt an adsorption configuration with (nearly) all thiol groups equivalently bonded to the substrate. Moreover, the **T1** molecules in the monolayers display an almost upright molecular orientation, an exceptionally high degree of order, and interesting electronic properties.

RESULTS AND DISCUSSION

Synthesis of T1 and T2. The synthesis of **T1** is illustrated in Scheme 1. The reaction of 1,8,13-trihydroxytriptycene (**3**) with triflic anhydride (Tf$_2$O) in the presence of pyridine gave tristriflate **4**,[24] which was converted into **5** by a Kumada-Tamao coupling reaction[32,33] using methylmagnesium chloride and Ni(dppp)Cl$_2$ (dppp = 1,3-bis(diphenylphosphino)propane). Compound **5** was reacted with N-bromosuccinimide (NBS) in the presence of azobisisobutyronitrile (AIBN),[33] affording **6**. Treatment of **6** with potassium thioacetate (AcSK)[5,6] gave **7**, whose acetyl groups were hydrolyzed with HBr, which was generated in situ from acetyl bromide (AcBr) and MeOH,[34] to afford 1,8,13-trimercaptomethyltriptycene **T1**.

1,8,13-Trimercaptotriptycene **T2** was synthesized from **3** according to Scheme 2. The hydroxyl groups of **3** were acylated with N,N-dimethylthiocarbamoyl chloride in the presence of NaH[35] to give **8**. Upon heating of **8** at 260 °C in diphenyl ether, the Newman-Kwart rearrangement[35] occurred to afford **9**. The carbamoyl groups of **9** were hydrolyzed with KOH in a mixture of MeOH and THF, resulting in **T2**. Compounds **T1** and **T2** were unambiguously characterized by ^{1}H and ^{13}C NMR spectroscopy, by FT-IR spectroscopy, and by high-resolution APCI-TOF mass spectrometry (Figures S18–S22 and Figures S30–S33 for **T1** and **T2**, respectively, see the Supporting Information). Successful preparation of single crystals of **T1** suitable for X-ray analysis allowed us to further determine the molecular structure of **T1** (Figure S1, see the Supporting Information).

Scheme 1. Synthesis of T1^a
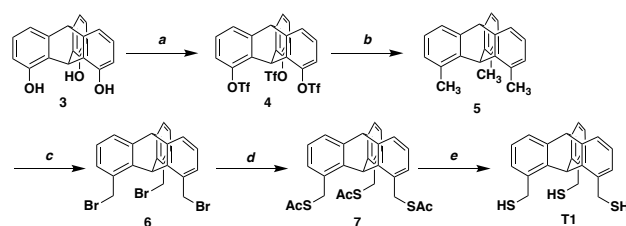
^{a}Reagents and conditions: (a) Tf$_2$O, pyridine, 1,2-dichloroethane, 0~60 °C, 97%; (b) MeMgCl, Ni(dppp)Cl$_2$, THF, 80 °C, 80%; (c) NBS, AIBN, benzene, 50 °C, 59%; (d) AcSK, THF, 25 °C, 79%; (e) AcBr, MeOH, THF, –78~25 °C, 88%.

Scheme 2. Synthesis of T2^a
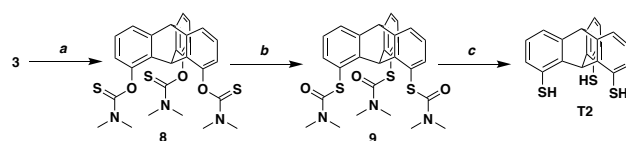
^{a}Reagents and conditions: (a) NaH, N,N-dimethylthiocarbamoyl chloride, DMF, 0~70 °C, 83%; (b) Ph$_2$O, 260 °C, 84%; (c) KOH, MeOH, THF, 80 °C, 88%.

Preparation of SAMs of T1 and T2 on Au(111). Standard thermally evaporated Au(111) substrates were used. SAMs of **T1** (**T1**/Au) and **T2** (**T2**/Au) were fabricated by simply immersing Au(111) substrates into a THF solution of **T1** and **T2** for 24 h at 25 °C. Then, the samples were washed with THF, dried under ambient conditions, and annealed at 120 °C. Further details are provided in the Experimental Section. As a reference sample for the spectroscopic analysis, we also prepared benzylthiol (**B1**) SAMs on Au(111) using a standard procedure.[36]

STM Imaging of T1/Au and T2/Au SAMs. Large-area (50 nm × 50 nm) STM images of **T1**/Au (Figure 2a) and **T2**/Au (Figure 2c) both show smooth and homogeneous terraces with steps of *ca.* 2.5 Å, which is consistent with the well-known interlayer spacing at Au terraces on the surface of Au(111). This observation suggests that **T1** and **T2** cover the Au(111) surface uniformly. Close-up views (10 nm × 10 nm) of **T1**/Au (Figure 2b) and **T2**/Au (Figure 2d), which focus on a terrace, are very similar to one another and display hexagonally aligned bright spots at *ca.* 5 Å separation, indicating that both **T1** and **T2** self-assemble on Au(111) to form highly ordered domains. We assume that the bright spots stem from the phenyl rings of the triptycene units (as their most conductive parts directly linked to the substrate via the anchor groups). Thus, the **T1** and **T2** molecules on Au(111) likely assemble into a 2D nested hexagonal structure (Figure 2e), which is consistent with the packing of 1,8,13-trialkoxytriptycenes observed in X-ray diffraction experiments.[23–28] Consequently, also the centers of the phenyl groups align hexagonally with a separation of *ca.* 5 Å. From that a packing density of the thiolate groups of 4.6 x 10^14 thiolates/cm² can be calculated (Table 1).
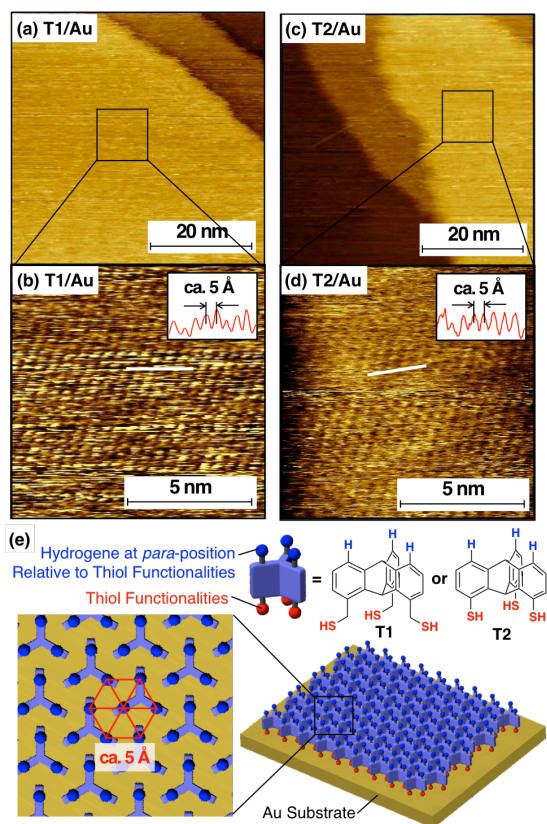
Figure 2. STM images of (a,b) **T1**/Au and (c,d) **T2**/Au acquired at 25 °C, and (e) schematic illustration of the proposed molecular arrangement of **T1** and **T2** on Au(111).

XPS and NEXAFS Analysis of T1/Au and T2/Au SAMs. By means of XPS and NEXAFS spectroscopy, we further characterized **T1**/Au and **T2**/Au SAMs in terms of the sulfur-Au bonding state, packing density, orientation, and configuration of the triptycene molecules. Figure 3 shows representative S 2p (Figure 3a–c) and C 1s (Figure 3d–f) XP spectra of **T1**/Au and **T2**/Au, along with those of **B1**/Au as a reference. The S 2p spectrum of **T1**/Au (Figure 3a) is very similar to that of **B1**/Au (Figure 3c): It is dominated by a characteristic S 2p doublet of thiolate bound to Au (Figure 3a, doublet 1) at ~162.0 eV (S 2p_{3/2}), with an only small (~10%) admixture of an additional feature at 161.0 eV (S 2p_{3/2}).[37] This suggests that almost all "legs" of the triptycene molecules in **T1**/Au are bound to the Au substrate as thiolates. This is an exceptionally good result for tripod-type molecules, which usually exhibit multiple bonding geometries with a significant portion of unbound and weakly bound anchoring groups.[4,38,39] The small feature at 161.0 eV (Figure 3a, doublet 2) is frequently observed in high-resolution XP spectra of thiolate-based SAMs[37] and is also present in the reference **B1**/Au SAM (Figure 3c). It can be attributed either to an anchoring configuration differing from a thiolate or, more likely, to atomic sulfur bound to the substrate, as discussed in detail in ref. 37. Note that a small amount of atomically bound sulfur should not disturb the molecular packing, as the thiolate groups are quite loosely packed on the surface (see below).

The S 2p spectrum of **T2**/Au is also dominated by a characteristic S 2p doublet of thiolate bound to Au (Figure 3b, doublet 1). However, this spectrum contains noticeable contributions associated with physisorbed/unbound thiols (Figure 3b, doublet 3; ~163.4 for S 2p_{3/2}) and oxidized thiol groups (Figure 3b, doublet 4; ~167.5 for S 2p_{3/2}). These usually provide only a weak bonding to the substrate. For the spectrum presented in Figure 3b, the portions of these species were estimated to be ~15% and ~20%, respectively. Thus, compared to **T1**/Au, **T2**/Au exhibits a more heterogeneous bonding structure with some of the "legs" being only weakly bound, not bound, or oxidized.
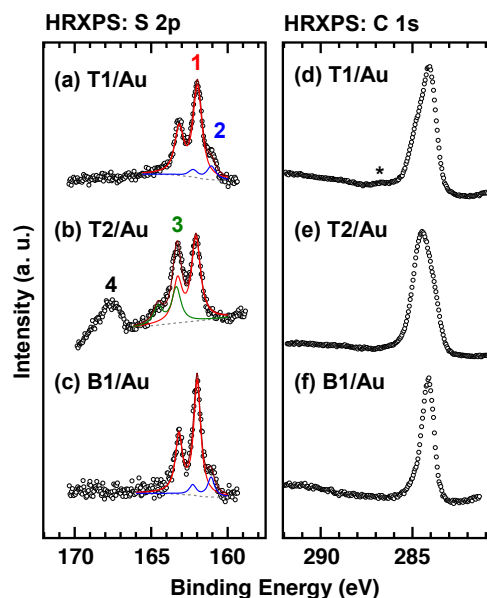
Figure 3. (a–c) S 2p and (d–f) C 1s XP spectra of **T1**/Au (a,d), **T2**/Au (b,e), and **B1**/Au (c,f) SAMs. Individual doublets in the S 2p spectra are color-coded and marked by numbers (see text for details); background is shown by gray dashed line.

Table 1. Observed and calculated effective thickness, packing density of the thiolate groups, average tilt angle of the π plane (α), average molecular tilt angle (β), work-function changes (ΔΦ), and position of the calculated XPS peaks (binding energy) of T1/Au, T2/Au, and B1/Au.

System	Effective thickness (Å)	Packing density / 10^{14} (thiolate/cm²)			Average tilt angle of π plane α (°)[a]		Average molecular tilt angle β (°)[a]		Work-function change $\Delta\Phi$ (eV)[b]		Binding energy (eV)	
		STM	XPS	Calcd.[c]	NEXAFS	Calcd.	NEXAFS	Calcd.	Kelvin Probe	Calcd.	XPS	Calcd.
T1/Au	9	4.6	4.6	4.5	81	86.8	7.5	3.4	−0.80	−1.33	284.5	284.47
T2/Au	10.5	4.6	4.1	4.5	67	85.1	36	6.7	−0.75	−1.73	284.1	284.11
B1/Au	7	–	3.7	4.5	80	77.4	10	14.0	–	–	284.1	284.00

[a]The tilt angle refers to the orientation of the phenyl rings with respect to the substrate normal. See text for details. The experimental errors are ±1–1.5 Å for the thickness, ±10% for the packing density, and ±3° for the average tilt angle. [b]In the simulations, work-function changes are reported relative to a calculated work function of a relaxed Au surface of 5.13 eV. [c]The slightly smaller value of the simulated packing density is a consequence of using the calculated Au lattice constants for reasons discussed in the Methods section.

The C 1s XP spectra of **T1**/Au (Figure 3d), **T2**/Au (Figure 3e), and **B1**/Au (Figure 3f) exhibit only one peak at 284.1 eV, 284.5 eV, and 284.1 eV, respectively. No contributions related to contaminations or oxidized species are observed, except for the spectrum of **T1**/Au, in which a very weak signal (asterisk) at ~286.5 eV probably due to CO[40] is perceptible. While the peak in the spectrum of **B1**/Au is symmetric, the C 1s peaks for **T1**/Au and **T2**/Au display some asymmetry, with a higher intensity at the low binding-energy side for **T1**/Au and the opposite situation for **T2**/Au.

A quantitative analysis of the XP spectra (for details see Methods section) provides information on the effective thickness of the SAMs and the packing density of the thiolate groups. The results are listed in Table 1. The packing density of the thiolate groups determined by the XPS analysis of **T1**/Au (4.6×10^{14} thiolate/cm²)[41] agrees perfectly with the estimate from the STM imaging. It corresponds to the ideal value of *ca.* one S atom per $\sqrt{3} \times \sqrt{3}$ surface unit cell and is also found for high-quality alkanethiolate SAMs on Au(111).[1] This testifies to the ideal surface coverage in the **T1**/Au system. For **T2**/Au, the average coverage derived from the XPS data (4.1×10^{14} thiolate/cm²) is somewhat smaller. The area-averaging character of the XPS measurements, in combination with the higher local coverage observed for **T2**/Au in the STM images, suggest the coexistence of densely packed and more defective (*i.e.*, less densely packed) areas in **T2**/Au. Notably, all determined packing densities for the triptycene-based SAMs are distinctly higher than that of the reference **B1** system (3.7×10^{14} thiolate/cm²), underlining their superior quality. Consistently, the effective thickness of **T1**/Au is slightly higher than that of the reference **B1**/Au SAM (Table 1). The even higher effective thickness of **T2**/Au, despite the lower density of thiolate groups, is attributed to the presence of some physisorbed molecules.

NEXAFS spectroscopy experiments provided further insight into the structural quality of the SAMs and the molecular orientation. Representative data in Figure 4 comprise spectra acquired at the so-called magic angle of X-ray incidence (55°). They are independent of the molecular orientation and, thus, exclusively display the electronic structure of the SAMs.[42] Additionally, the differences between the spectra acquired under normal (90°) and grazing (20°) incidence are shown. They provide information on the molecular orientation.[42]

The 55° spectra of **T1**/Au (Figure 4a) and **T2**/Au (Figure 4e) are similar to one another and also do not significantly deviate from the spectrum of **B1**/Au (Figure 4c) and from reported spectra of oligophenyl SAMs in general.[43] They are dominated by the intense

π₁* resonance of phenyl rings (Figure 4a, peak 1) which, however, appears at a slightly higher photon energy (~285.3 eV) than for benzene (~285.0 eV)[44] or oligophenyl SAMs (285.0–285.1 eV)[43] or even for triptycene SAMs with monodentate bonding configuration (~285 eV).[30] We attribute that shift to a destabilization of the lowest unoccupied orbital in the triptycenes due to minor distortions of the phenyl rings by the central bridge but, obviously, the tridentate bonding configuration is of importance as well. Additional low intensity resonances of oligophenyl SAMs, such as the R*/C-S* resonance at ~287.3 eV and the π₁* resonance at 288.8–288.9 eV (Figure 4c, peak 2) are also resolved in spectra.[43] They are marginally smeared out for **T1**/Au and **T2**/Au, presumably due to their overlap with the features stemming from the sp³ carbons at the bridgehead positions. In addition, the spectra exhibited a variety of σ*-like resonances (Figure 4a, peaks 3 and 4) at higher excitation energies.
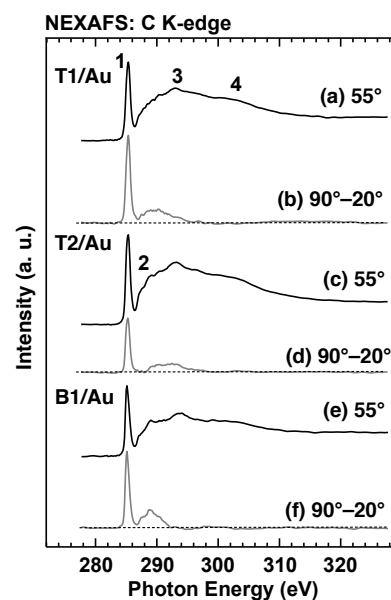
Figure 4. C K-edge NEXAFS data for the **T1**/Au (a,b), **T2**/Au (c,d), and **B1**/Au SAMs (e,f). They comprise the spectra acquired at an X-ray incidence angle of 55° (a,c,e) and the difference between the spectra acquired at X-ray incidence angles of 90° and 20° (b,d,f). Characteristic absorption resonances are marked by numbers (see text for details). Horizontal dashed lines in the difference spectra correspond to zero.

The 90°–20° NEXAFS spectra of **T1**/Au and **T2**/Au exhibit pronounced linear dichroism (Figure 4b,d) with the effect being particularly strong for the π_1^* resonances of the phenyl rings (Figure 4a, peak 1). In view of the specific orientation of the respective orbitals (perpendicular to the ring plane), a positive sign of the π_1^* difference peaks suggests upright molecular orientation of the phenyl rings relative to the substrate. This geometry corresponds to a predominantly downward orientation of the anchoring groups, allowing efficient anchoring of the triptycene tripods to the substrate, in full agreement with the conclusions from the XPS data.

A quantitative analysis of the NEXAFS data was performed within the commonly applied theoretical framework,[42] relying on the most prominent π_1^* resonance. To that aim, we correlated the dependence of its intensity on the incidence angle of the X-ray beams (θ) with a theoretical expression for a vector-like orbital,[42] using the average tilt angle of the π_1^* orbitals (α)[45] as the sole fitting parameter. The resulting values of α are 81°, 67°, and 80° for the **T1**/Au, **T2**/Au and **B1**/Au, respectively (Table 1). Due to the three-fold symmetry of **T1** and **T2**, the average value of the molecular tilt angle (β) can be directly obtained from the dependence of the intensity of the π_1^* resonance on $\cos^2\theta$.[30] The resulting values of β are shown in Table 1, along with the value for the **B1**/Au SAM. The latter can, however, only be considered as a lower limit of the average tilt angle in that system due to the lower molecular symmetry, which results in a dependence of the calculated value of β on the molecular twist (here set to 0° yielding the minimum value of β for a given α).[46]

The average value of β for **T1**/Au is quite small (~7.5°), suggesting that the benzene blades of **T1** are almost perpendicular to the substrate, which agrees well with the identical adsorption mode of all three anchoring groups (Table 1). The deviation from the fully parallel orientation could be explained by a possible corrugation of the specific anchoring sites of the three thiolate groups. This is, however, not supported by the simulations (see below). Therefore, we rather attribute it to a (small) number of defects, *e.g.*, at domain boundaries or step edges and to the grain structure of the substrate within the macroscopically large area probed by NEXAFS spectroscopy.

For **T2**/Au, the average value of β is noticeably higher (Table 1), reflecting the lower quality of this monolayer compared to **T1**/Au. This does not necessarily mean that **T2**/Au SAM contains no highly ordered areas of well-aligned molecules (see, *e.g.*, STM experiments). These domains, however, must then coexist with areas of inhomogeneously bound and probably even physisorbed molecules with a strongly inclined or even stochastic orientation. This notion is consistent with the interpretation of the S 2p XP spectra and the derived coverages discussed above.

Computational Studies on the Structures of T1/Au and T2/Au. To gain atomistic insight into the properties of the **T1**/Au(111) and **T2**/Au(111) SAMs, we performed dispersion-corrected density-functional theory (DFT) calculations on periodic, infinitely extended interfaces. To be consistent with the experimental situation, we here generated densely packed SAMs by choosing a 3×3 Au surface unit cell containing one molecule. This results in a hexagonal arrangement of triptycene molecules (Figure 5a,b) with a packing density of 4.45×10^{14} thiolate/cm^2 consistent with the experimental values.[47] The length of the resulting surface unit-cell vectors is 8.82 Å,[48] which is somewhat larger than the unit-cell vector in the bulk assemblies of tripodal triptycenes, such as

1,8,13-tridecyloxytriptycene (8.1 Å).[23–28] This difference arises from the fact that the dimensions of the surface unit cell are determined by the periodicity of the Au substrate, while the periodicity in the bulk reflects the optimum intrinsic distance for a hexagonal assembly of triptycene molecules. Consequently, one can expect some strain in the adsorbate layer, which might be one of the reasons for the structural imperfections found particularly for **T2** (without flexible methyl linkers).
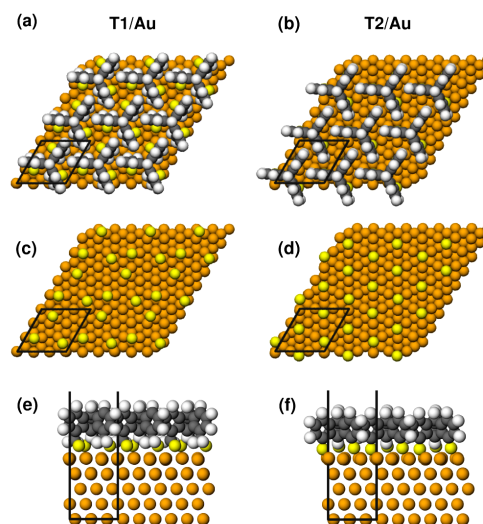
Figure 5. DFT-optimized structures of **T1**/Au (a and e; top and side views, respectively) and **T2**/Au (b and f; top and side views, respectively) on a 5-layer Au(111) slab. Anchoring positions of the thiolate groups of **T1** (c) and **T2** (d). Only the S atoms and the Au slab are shown. The black rectangles represent the unit cell of the interfaces.

A screening of possible anchoring sites for the densely packed monolayers yields S atoms located on the bridge sites shifted towards fcc hollow positions in the case of **T1**/Au and S atoms at fcc-hollow sites in **T2**/Au (Figure 5a,b). This is consistent with the computational results for isolated adsorbed molecules on Au(111).[31] The difference in anchoring sites is clearly visible in Figure 5c,d, where only the S atoms on the Au(111) surface are shown. The site in **T1**/Au corresponds to the ideal anchoring position typically found when simulating thiolate-bonded SAMs on Au(111) using a methodology similar to the present one.[49,50] The occurrence of a supposedly less ideal anchoring site in **T2**/Au is attributed to the structural rigidity of **T2**. It enforces an unusual arrangement of the S–C bonds nearly perpendicular to the Au surface, with the actual values varying between 0.7° and 3.4°. The unusual thiolate bonding geometry results in some distortions of the molecular structure of **T2** upon adsorption, with the distance between neighboring S atoms increasing by 0.2 Å compared to an isolated molecule. For **T2**/Au also the heights of the three docking groups vary quite significantly (between 0.61 Å and 1.03 Å relative to the topmost Au layer), while they are essentially the same (1.16 Å) for all S atoms in **T1**/Au (see Figure 5e and f). Consistent with the less ideal bonding configuration of **T2**/Au, the binding energy per molecule (representative of breaking the bond between the substrate and the adsorbate) is significantly smaller than for **T1**/Au (5.43 eV vs. 7.16 eV). A similar trend is observed for the adsorption energy characteristic of bond formation (1.62 eV vs. 2.67 eV).

Simulated structural parameters for the absorbed molecules are summarized in Table 1. The tilt angle of the π_1^* orbitals (α) and the molecular tilt angles (β) for **T1**/Au are 86.8° and 3.4°, respec-

tively, which is in good agreement with the NEXAFS results (α = 81° and β = 7.5°). Conversely, the simulated values for well-ordered **T2**/Au (α = 85.1° and β = 6.7°) differ significantly from the NEXAFS values (α = 67° and β = 36°). As indicated already earlier, we attribute that to the coexistence of ordered and disordered domains in **T2**/Au, with essentially upright-standing molecules (β = 7.5°) in the ordered regions separated by severely disordered structures in between (see discussion of S 2p XP spectra).

Electronic Properties of the Interface. Functionalization of metal surfaces with SAMs is useful for tailoring the electronic properties of metal substrates.[51–55] Here, the triptycene-based SAM systems have a particularly high potential as surface modifier, because: (i) They form dense and ordered monolayers with, in the case of **T1**, essentially upright-standing molecules. (ii) They can be efficiently chemically modified with various (polar) functional groups at the SAM-ambient interface at the 4,5,16-[24] and bridge-head position.[25] To establish the basis for such application, we here discuss experimental and theoretical investigations of the electronic properties of the "parent" interfaces **T1**/Au and **T2**/Au.

Kelvin-probe experiments on **T1**/Au and **T2**/Au yield work functions (Φ) of 4.40 eV and 4.45 eV, respectively. With a Φ value of a bare, freshly sputtered Au(111) substrate of 5.20 eV,[56] this results in work-function modifications ($\Delta\Phi$) of –0.80 eV (for **T1**) and –0.75 eV (for **T2**). These values are comparable to those obtained for biphenylthiolate monolayers on Au(111) (Φ = 4.35–4.42 eV).[57]

As Kelvin probe is an area-averaging technique, the similarity in the final work-function of **T1**/Au and **T2**/Au might seem surprising considering the much higher degree of disorder in the **T2**/Au films. Disorder ought to result in much less ideally aligned dipoles and, consequently, a distinctly reduced work-function modification. As this is not observed, we conclude that for an ideally arranged **T2**/Au interface, much larger work-function changes than for **T1**/Au should be observed.

To test this hypothesis, we resorted to the simulations, which represent the situation of two perfectly ordered monolayers: The calculated work-function modification for **T1**/Au ($\Delta\Phi$ = –1.33 eV) somewhat overestimates the experimental value. This is in line with what we typically observe for polar SAMs[55] and can partly be attributed to the residual disorder in the experiments caused by step edges and grain boundaries. Additionally, the calculated molecular dipoles and bond dipoles are influenced by the employed computational methodology (see the Supporting Information). In line with the value for **T1**/Au, we calculate a work-function change of –1.38 eV for the biphenylthiolate SAM. In sharp contrast to those two cases, for a perfectly ordered **T2**/Au interface a much larger value of $\Delta\Phi$ = –1.73 eV is obtained, as expected based on the arguments in the previous paragraph.

What remains to be explained is why the intrinsic work-function change for a **T2**/Au interface is by *ca.* 0.4 eV larger than for **T1**/Au. To clarify that, we performed the following test: We modeled benzylthiolate (**B1**) and benzenethiolate (**B2**) SAMs, which differ only in the presence of a methyl linker between the phenyl and the thiolate in the former system. A full geometry optimization for both systems results in structures with the S atoms in bridge position shifted towards fcc-hollow sites (*i.e.*, consistent with the situation for **T1**/Au). This yields a slightly larger work-function change of –1.44 eV for **B2**/Au compared to –1.33 eV for **B1**/Au. When

the S atom of the **B2** molecule is fixed at the fcc-hollow position (*i.e.*, the favorable position for **T2**), the $\Delta\Phi$ value for **B2**/Au increased to –1.52 eV. When additionally fixing the position of the C atom bonded to the thiolate to the position it assumes in **T2**/Au, $\Delta\Phi$ rises further to –1.65 eV. This shows that the difference in $\Delta\Phi$ between **T2**/Au and **T1**/Au arises from the different hybridization states of the C atom bonded to the thiolate (sp² *vs.* sp³ hybridized) and, even more importantly, from differences in the C-S-Au bonding geometries.

A more local view of the electrostatics of the SAMs can be gained from an in-depth analysis of the XPS data.[58,59] The calculated C 1s XP spectra of **T1**/Au and **T2**/Au at a photon energy of 350 eV are reported in Figure 6. The energies scale is shifted by 18.88 eV in both systems[57,58] to align the experimental and calculated maxima for **T1**/Au. Fully consistent with the experiments, the positions of the peak maxima in the calculations differ by 0.4 eV between **T1**/Au (284.1 eV) and **T2**/Au (284.5 eV). The magnitude of that difference is close to the shift in $\Delta\Phi$ between the simulated **T1**/Au and **T2**/Au interfaces. As shifts in the electrostatic energy directly impact core-level binding energies,[58] this further supports the notion that for perfectly ordered SAMs the interfacial dipoles are larger in the **T2**/Au case. The reason why the electrostatic shift is resolved in the XPS experiments in spite of the disordered regions is that binding energies are impacted by the local electrostatic potential at the position of the excited atom such that variations of the electrostatic potential do not average out.[59] Figure 6 also shows the energetic positions of the C 1s core levels of the individual C atoms in the SAMs, which allows a direct comparison between **T1**/Au and **T2**/Au on an atom by atom level. Obviously, beyond the global shift between the spectra, the differences in binding energies between **T1**/Au and **T2**/Au are small for electrons from equivalent C atoms, except for CB and C1 carbons (see insets in Figure 6). This confirms the earlier conclusion that differences in electrostatic energies and work functions in the two SAMs originate from the immediate anchoring region.
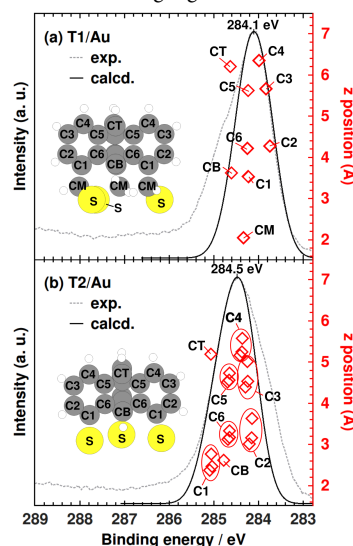
Figure 6. Simulated C 1s XP spectra of **T1**/Au (a) and **T2**/Au (b) for a primary photon energy of 350 eV. The contributions of the different groups of chemically equivalent C atoms are also shown, where the vertical position represents their *z* coordinates with respect to the image plane position (0.9 Å above the average *z* position of the topmost Au layer).

CONCLUSIONS

Combining experimental and computational studies, we have demonstrated that triptycene-based molecular tripods (**T1** and **T2**) with thiol-containing functionalities at the 1,8,13-poistions self-assemble into dense, uniform, and ordered monolayers on a metal surface with an upright orientation of the benzene planes. The key of the molecular design of **T1** and **T2** is that the three thiol groups are attached to a rigid triptycene framework in a way that they can efficiently bond to a surface, irrespective of possible conformational states. Moreover, 1,8,13-substituted triptycenes have a strong tendency to adopt nested 2D hexagonal structures, which promotes the self-assembly process.

The synthesis of **T1** and **T2** is achieved by sequential organic transformations from 1,8,13-trihydroxytriptycene in good overall yields. STM imaging of **T1** and **T2** assembled on Au(111) suggest the formation of uniform self-assembled monolayers (SAM) with an ordered 2D hexagonal arrangement of the triptycenes. Based on our XPS data, we conclude that (nearly) all of the S atoms of **T1** bind to Au(111). This results in an upright orientation of the molecules, as confirmed by NEXAFS measurements and quantum-mechanical simulations with a measured (calculated) tilt angle of 7.5° (3.4°). Conversely, the SAM of **T2** may contain significant amounts of unbound or weakly bound thiol groups, which causes partial oxidation of the thiol functionality. The large average tilt angle of 36° of **T2** on Au(111) determined by NEXAFS spectroscopy in combination with the STM, XPS, and modeling results, suggests the coexistence of well-ordered domains with essentially upright standing molecules and highly disordered regions. The lower structural quality of the **T2**/Au interface can be traced back to a less favorable bonding arrangement in the immediate interface region, which also results in lower binding energies. Interestingly, despite the significantly different degrees of order in the **T1** and **T2** SAMs, the changes in area-averaged work-function caused by the SAMs are essentially the same for both interfaces (*ca.* –0.8 eV). Based on the simulations and the XPS experiments, this can be rationalized by a significantly larger change in the well-ordered regions of **T2**/Au caused mostly be the different bonding geometry, which is eventually diminished by smaller values for the disordered parts of the film.

The results presented in this study establish a new type of tripodal SAM, whose architecture is distinctly different from conventional monolayers of molecular tripods. The advantages of the triptycene system, particularly **T1**, are the reliable tripodal adsorption configuration, the efficient large-area uniform 2D self-assembly, and an almost ideal upright orientation of the benzene rings, projected to the attached functional groups. Importantly, the triptycene tripods can be readily decorated using the bridgehead[25] or the 4,5,16-positions.[24] As either one or three functional groups per tripod can then be substituted, their density and separation can readily be varied. Thus, the presented systems can serve as stable and conformationally rigid anchors, *e.g.*, for polar entities modifying sample work functions, for recognition functionalities in combination with biomolecules, or for receptor groups in sensing applications. This makes them highly promising building blocks for applications in organic and molecular circuits, biomedical devices, optical and chemical sensors, solid catalyst, and many more.

EXPERIMENTAL SECTION

Materials. Unless otherwise stated, all commercial reagents were used as received. Benzylthiol (**B1**) and hexadecanethiol (HDT) were purchased from Sigma-Aldrich. Compound **3** was prepared according to previously reported procedures[23] and unambiguously characterized by nuclear magnetic resonance (NMR) spectroscopy and atmospheric pressure chemical ionization time-of-flight (APCI-TOF) mass spectrometry.

General. NMR spectroscopy measurements were carried out on a Bruker AVANCE-500 spectrometer (500 MHz for ^{1}H and 125 MHz for ^{13}C) or AVANCE-400 spectrometer (400 MHz for ^{1}H and 100 MHz for ^{13}C). Chemical shifts (δ) are expressed relative to the resonances of the residual non-deuterated solvents for ^{1}H [CDCl$_3$: ^{1}H(δ) = 7.26 ppm, acetone-d_6: ^{1}H(δ) = 2.05 ppm] and ^{13}C [CDCl$_3$: ^{13}C(δ) = 77.16 ppm, acetone-d_6: ^{13}C(δ) = 29.8 and 206.3 ppm]. Absolute values of the coupling constants are given in Hertz (Hz), regardless of their sign. Multiplicities are abbreviated as singlet (s), doublet (d), triplet (t), multiplet (m), and broad (br) (See the Supporting Information). Infrared (IR) spectra were recorded at 25 °C on a JASCO FT/IR-6600ST Fourier-transform infrared spectrometer. High-resolution mass spectrometry measurements were carried out on a Bruker micrOTOF II mass spectrometer equipped with an atmospheric pressure chemical ionization (APCI) probe or an electrospray ionization (ESI) probe.

STM Measurements. STM tips were mechanically cut from a tungsten wire (diameter 0.25 mm; Nilaco). Au(111) substrates, obtained by thermal evaporation of Au onto a freshly cleaved mica substrate, were flame-annealed and quenched in ethanol prior to use. Samples for STM imaging were prepared by immersing an Au(111) substrate into a THF solution (2.0 μmol/L) of **T1** or **T2** for 24 h, and the resultant substrate was washed with THF, dried in air, and then thermally annealed (120 °C, 1 h) under reduced pressure. Constant current-mode STM imaging was carried out on a Nanoscope III STM system (Digital Instruments). All STM measurements were performed at 25 °C in air. The STM scanner was calibrated with an Au(111) substrate prior to the experiments. The observed STM contrast (apparent height) difference of 2.5 Å was consistent with the well-known interlayer separation at Au terraces on Au(111).

Preparation of SAMs for the Spectroscopy and Kelvin Probe Measurements: The SAMs for these experiments were prepared on commercial Au substrates (Georg Albert PVD, Silz, Germany). These substrates were prepared by thermal evaporation of 30 nm of Au (99.99% purity) onto a polished single-crystal silicon (100) wafer (Silicon Sense) that had been precoated with a 5 nm titanium adhesion layer. The resulting Au films are polycrystalline, having a grain size of 20–50 nm and predominantly exhibiting a (111) orientation. The SAMs were prepared by immersion of a fresh substrate in a THF solution (2 μM–1 mM) of **T1** or **T2** for 24 h at 25 °C. After immersion, the film was washed with THF and dried by blowing argon. Finally, some of the samples were annealed at 100 °C for 1 h either under inert gas atmosphere or under ultra-high vacuum (UHV) conditions. In addition, several reference SAMs, *i.e.*, those of **B1** and HDT on Au(111), were prepared using standard procedures.[36] HDT/Au was used as a reference system for the XPS and work-function measurements (see below). **B1**, can be regarded as a partial structure of **T1**, making it a suitable monothiol reference. Due to the presence of the methylene linker between the benzene ring and thiol group, a sufficiently good quali-

ty of this monolayer can be expected, similar to the analogous nitrile-substituted system.[60] At the same time, we refrained from studying benzenethiol as the monothiol reference to **T2**, as it has been shown to form SAMs of only limited quality when employing the standard immersion procedure.[43,61]

XPS and NEXAFS Spectroscopy Measurements: The XPS, NEXAFS spectroscopy, and work function measurements were performed under UHV conditions (1.5×10^{-9} mbar) at 25 °C.

Laboratory XPS measurements were carried out with a MAX200 (Leybold-Heraeus) spectrometer equipped with an Mg Kα X-ray source (200 W) and a hemispherical analyzer. The spectra were corrected for the spectrometer transmission and the binding energy (BE) scale was referenced to the Au $4f_{7/2}$ peak at 84.0 eV.[40] Since the quality of the laboratory spectra in terms of statistics and energy resolution were inferior to the synchrotron data, they were mostly used to verify the film thickness and packing density.

Synchrotron-based XPS measurements were carried out at the bending magnet HE-SGM beamline of the synchrotron storage ring BESSY II in Berlin, Germany. This beamline provides a moderate X-ray intensity helping to avoid X-ray damage during the spectra acquisition. The spectra were collected with a Scienta R3000 electron energy analyzer in normal emission geometry. The photon energy (PE) was set to either 350 eV or 580 eV, depending on the BE range. The BE scale was referenced to the Au $4f_{7/2}$ peak at 84.0 eV.[40] The energy resolution was ~0.3 eV at a PE of 350 eV and ~0.5 eV at 580 eV.

The XPS data were used to calculate the effective thickness and packing density of the SAMs, relying on the C 1s/Au 4f and S 2p/Au 4f intensity ratios using standard procedures.[62,63] For the thickness evaluation, a standard expression for the attenuation of the photoemission signal was assumed[64] together with literature values for the attenuation lengths.[65] The spectrometer-specific coefficients were determined with the help of the reference HDT SAM with a known thickness (18.9 ±0.1 Å) and packing density (4.63×10^{14} molecules/cm^2; $\sqrt{3} \times \sqrt{3}$ structure).[36]

NEXAFS spectroscopy measurements were performed at the same beamline. The spectra were collected at the C K-edge in the partial electron yield mode with a retarding voltage of –150 V. The polarization factor of the X-rays was estimated as ~88%; the energy resolution was ~0.30 eV. The incidence angle of the light was varied from 90° (normal incidence geometry; ***E***-vector in surface plane) to 20° (grazing incidence geometry; ***E***-vector near surface normal) in steps of 10°–20°, which is a standard approach enabling the determination of the molecular orientation from NEXAFS data.[42] Raw spectra were normalized to the incident photon flux by division through a spectrum of a clean, freshly sputtered gold sample. The PE scale was referenced to the pronounced π* resonance of highly oriented pyrolytic graphite at 285.38 eV.[66]

Kelvin Probe Measurements. Work function measurements were carried out using a UHV Kelvin Probe 2001 system (KP technology Ltd., UK). The pressure in the UHV chamber was ~10^{-9} mbar. As reference, we used HDT/Au with the work function value set to 4.30 eV according to literature.[67] The latter value was additionally verified by referencing it to the work function of freshly sputtered gold set to 5.20 eV.[68] The accuracy of the WF values is ca. ±0.05 eV.

Computational Methodology. The calculations were performed using the FHI-aims code[69] and employing the PBE func-

tional[70] in combination with the surface parametrization[71] of the Tkatchenko–Scheffler dispersion correction.[72] The latter were turned off between the bulk Au atoms. Periodic boundary conditions and the repeated slab approach including a vacuum region of at least 20 Å in the z direction were employed to represent the interface. To compensate for the electrostatic asymmetry of the slab, a self-consistently calculated dipole layer was inserted in the vacuum.[73] To sample the reciprocal space a non-orthogonal 6×6×1 Γ-centered k-point grid was used. The dimensions of the unit cells in the x and y directions were defined according to the calculated Au nearest neighbor distance (2.940 Å), to avoid spurious surface relaxations. The metal was modeled using 5 layers of Au, with the bottom 3 layers fixed at their bulk positions during the optimization. The presented results were obtained using the default FHI-aims "tight" basis set and setting the total energy criterion for the self-consistency cycle to 10^{-6} eV. The optimizations were performed until the maximum residual force component per atom was below 0.01 eV/Å. For the initial screening of different docking sites, less accurate settings were adopted, using the default FHI-aims "light" basis set and stopping the optimization when the maximum residual force component per atom was below 0.05 eV/Å.

Binding energies, E_{bind}, are defined such that they reflect the energy needed to break the bond between the molecule and the substrate and to remove the molecules from the SAM:

$$E_{bind} = E_{Trip/Au} - E_{Au} - E_{Trip} \qquad (1)$$

Here, $E_{Trip/Au}$ is the energy per unit cell of the SAM adsorbed to the surface, E_{Au} is the energy of the optimized pristine Au slab and E_{Trip} is the energy of the optimized gas phase molecular radical. Conversely, adsorption energies, E_{ads}, reflect the energetics of forming the monolayers and at the same time replacing the molecular S-H bonds by bonds to the Au surface. They are, thus, defined as:

$$E_{ads} = E_{Trip/Au} - E_{Au} - E_{Trip-H} + 3/2\, E_{H2} \qquad (2)$$

E_{Trip-H} in this equation represents the energy of the optimized gas phase triptycene molecule in which all S atoms are saturated with hydrogens and E_{H2} is the energy of an isolated H_2 molecule.

The XP spectra were simulated within the initial state approach to avoid artifacts arising from a combination of periodic boundary conditions and explicit excitations in each unit cell.[58] For obtaining the spectra, the 1s core level energies for every C atom were taken from the atom projected density of states output files. Subsequently, they were shifted considering the screening of the core hole by the metal substrate via an electrostatic image charge model[74,75] assuming a dielectric constant of the SAM of 3.9.[76] To model the spectra, the individual resonances were broadened using Gaussian functions with a variance of 0.15 eV and an intensity scaled using an exponential attenuation function to account for the finite escape depth of the photoelectrons. Additionally, the energy scales for both interfaces were rigidly shifted by the same energy to align the calculated and measured positions of the C 1s peaks for **T1**/Au. This is inevitable, considering that when employing the initial state approach, Kohn-Sham orbital energies are calculated. For more details see references [57] and [58].

In the simulations of the benzylthiolate (**B1**) and benzenethiolate (**B2**) SAMs, two molecules per $(3 \times \sqrt{3})rect$ unit cell in a herringbone arrangement were considered. For that cell, we chose an orthogonal 9×5×1 Γ-centered k-point grid. When placing the molecules at specific adsorption sites, only the positions of the S atoms were fixed. All the other were relaxed. When also fixing the

molecular tilt, this was achieved by only fixing the coordinates of the C atom directly bonded to S.

ASSOCIATED CONTENT

Supporting Information

The following files are available free of charge.
The details of synthesis, NMR, IR, high-resolution MS spectra, single crystal X-ray structural analysis, and computational details (PDF)
Crystallographic data for **T1** (CIF)

AUTHOR INFORMATION

Corresponding Authors

*michael.zharnikov@urz.uni-heidelberg.de (M.Z.)
*egbert.zojer@tugraz.at (E.Z.)
*fukushima@res.titech.ac.jp (T.F.)

Author Contribution

‡F.I., G.N., and E.S. contributed equally.

Notes

The authors declare no competing financial interest.

REFERENCES

(1) Love, J. C.; Estroff, L. A.; Kriebel, J. K.; Nuzzo, R. G.; Whitesides, G. M. Self-Assembled Monolayers of Thiolates on Metals as a Form of Nanotechnology. *Chem. Rev.* **2005**, *105*, 1103–1169.

(2) Valášek, M.; Lindner, M.; Mayor, M. Rigid Multipodal Platforms for Metal Surfaces. *Beilstein J. Nanotechnol.* **2016**, *7*, 374–405.

(3) Valášek, M.; Mayor, M. Spatial and Lateral Control of Functionality by Rigid Molecular Platforms. *Chem. Eur. J.* **2017**, *23*, 13538–13548.

(4) Lindner, M.; Valášek, M.; Homberg, J.; Edelmann, K.; Gerhard, L.; Wulfhekel, W.; Fuhr, O.; Wächter, T.; Zharnikov, M.; Kolivoška, V.; Pospíšil, L.; Mészáros, G.; Hromadová, M.; Mayor, M. Importance of the Anchor Group Position (Para versus Meta) in Tetraphenylmethane Tripods: Synthesis and Self-Assembly Features. *Chem. Eur. J.* **2016**, *22*, 13218–13235.

(5) Hirayama, D.; Takimiya, K.; Aso, Y.; Otsubo, T.; Hasobe, T.; Yamada, H.; Imahori, H.; Fukuzumi, S.; Sakata Y. Large Photocurrent Generation of Gold Electrodes Modified with [60]Fullerene-Linked Oligothiophenes Bearing a Tripodal Rigid Anchor. *J. Am. Chem. Soc.* **2002**, *124*, 532–533.

(6) Zhu, S.-E; Kuang, Y.-M.; Geng, F.; Zhu, J.-Z.; Wang, C.-Z.; Yu, Y.-J.; Luo, Y.; Xiao, Y. Liu, K.-Q.; Meng, Q.-S.; Zhang, L.; Jiang, S.; Zhang, Y.; Wang, G.-W.; Dong, Z.-C.; Hou, J. G. Self-Decoupled Porphyrin with a Tripodal Anchor for Molecular-Scale Electroluminescence. *J. Am. Chem. Soc.* **2013**, *135*, 15794–15800.

(7) Nikitin, K.; Lestini, E.; Lazzari, M.; Altobello, S.; Fitzmaurice, D. A Tripodal [2]Rotaxane on the Surface of Gold. *Langmuir* **2007**, *23*, 12147–12153.

(8) Sakamato, R.; Ohirabaru, Y.; Matsuoka, R.; Maeda, H.; Katagiri, S.; Nishihara, H. Orthogonal Bis(terpyridine)–Fe(II) Metal Complex Oligomer Wires on a Tripodal Scaffold: Rapid Electron Transport. *Chem. Commun.* **2013**, *49*, 7108–7110.

(9) Chen, K.-Y.; Ivashenko, O.; Carroll, G. T.; Robertus, J.; Kistemaker, J. C. M.; London, G.; Browne, W. R.; Rudolf, P.; Feringa, B. L. Control of Surface Wettability Using Tripodal Light-Activated Molecular Motors. *J. Am. Chem. Soc.* **2013**, *136*, 3219–3224.

(10) Jian, H.; Tour, J. M. En Route to Surface-Bound Electric Field-Driven Molecular Motors. *J. Org. Chem.* **2003**, *68*, 5091–5103.

(11) Shirai, Y.; Cheng, L.; Cheng, B.; Tour, J. M. Characterization of Self-Assembled Monolayers of Fullerene Derivatives on Gold Surfaces: Implications for Device Evaluations. *J. Am. Chem. Soc.* **2006**, *128*, 13479–13486.

(12) Ramachandra, S.; Schuermann, K. C.; Edafe, F.; Belser, P.; Nijhuis, C. A.; Reus, W. F.; Whitesides, G. M.; De Cola, L. Luminescent Ruthenium Tripod Complexes: Properties in Solution and on Conductive Surfaces. *Inorg. Chem.* **2011**, *50*, 1581–1591.

(13) Chen, K.-Y.; Ivashenko, O.; Carroll, G. T.; Robertus, J.; Kistemaker, J. C. M.; London, G.; Browne, W. R.; Rudolf, P.; Feringa, B. L. Control of Surface Wettability Using Tripodal Light-Activated Molecular Motors. *J. Am. Chem. Soc.* **2014**, *136*, 3219–3224.

(14) Kitagawa, T.; Idomoto, Y.; Matsubara, H.; Hobara, D.; Kakiuchi, T.; Okazaki, T.; Komatsu, K. Rigid Molecular Tripod with an Adamantane Framework and Thiol Legs. Synthesis and Observation of an Ordered Monolayer on Au(111). *J. Org. Chem.* **2006**, *71*, 1362–1369.

(15) Katano, S.; Kim, Y.; Matsubara, H.; Kitagawa, T.; Kawai, M. Hierarchical Chiral Framework Based on a Rigid Adamantane Tripod on Au(111). *J. Am. Chem. Soc.* **2007**, *129*, 2511–2515.

(16) Kitagawa, T.; Matsubara, H.; Komatsu, K.; Hirai, K.; Okazaki, T.; Hase, T. Ideal Redox Behavior of the High-Density Self-Assembled Monolayer of a Molecular Tripod on a Au(111) Surface with a Terminal Ferrocene Group. *Langmuir* **2013**, *29*, 4275–4282.

(17) Kitagawa, T.; Matsubara, H.; Okazaki, T.; Komatsu, K. Electrochemistry of the Self-Assembled Monolayers of Dyads Consisting of Tripod-Shaped Trithiol and Bithiophene on Gold. *Molecules* **2014**, *19*, 15298–15313.

(18) Wagner, S.; Leyssner, F.; Kördel, C.; Zarwell, S.; Schmidt, R.; Weinelt, M.; Rück-Braun, K.; Wolf, M.; Tegeder, P. Reversible Photoisomerization of an Azobenzene-Functionalized Self-Assembled Monolayer Probed by Sum-Frequency Generation Vibrational Spectroscopy. *Phys. Chem. Chem. Phys.* **2009**, *11*, 6242–6248.

(19) Takamatsu, D.; Fukui, K.; Aroua, S.; Yamakoshi, Y. Photoswitching Tripodal Single Molecular Tip for Noncontact AFM Measurements: Synthesis, Immobilization, and Reversible Configurational Change on Gold Surface. *Org. Biomol. Chem.* **2010**, *8*, 3655–3808.

(20) Valášek, M.; Edelmann, K.; Gerhard, L.; Fuhr, O.; Lukas, M.; Mayor, M. Synthesis of Molecular Tripods Based on a Rigid 9,9'-Spirobifluorene Scaffold. *J. Org. Chem.* **2014**, *79*, 7342–7357.

(21) Šebera, J.; Kolivoška, V.; Valášek, M.; Gasior, J.; Sokolová, R.; Mészáros, G.; Hong, W.; Mayor, M.; Hromadová, M. Tuning Charge Transport Properties of Asymmetric Molecular Junctions. *J. Phys. Chem. C* **2017**, *121*, 12885–12894.

(22) Gerhard, L.; Edelmann, K.; Homberg, J.; Valášek, M.; Bahoosh, S. G.; Lukas, M.; Pauly, F.; Mayor, M.; Wulfhekel, W. An Electrically Actuated Molecular Toggle Switch. *Nat. Commun.* **2017**, *8*, 14672.

(23) Seiki, N.; Shoji, Y.; Kajitani, T.; Ishiwari, F.; Kosaka, A.; Hikima, T.; Takata, M.; Someya, T.; Fukushima, T. Rational Synthesis of Organic Thin Films with Exceptional Long-range Structural Integrity. *Science* **2015**, *348*, 1122–1126.

(24) Shioya, H.; Shoji, Y.; Seiki, N.; Nakano, M.; Fukushima, T.; Iwasa, Y. Raising the Metal–Insulator Transition Temperature of VO₂ Thin Films by Surface Adsorption of Organic Polar Molecules. *Appl. Phys. Express* **2015**, *8*, 121101.

(25) Leung, F. K.-C.; Ishiwari, F.; Kajitani, T.; Shoji, Y.; Hikima, T.; Takata, M.; Saeki, A.; Seki, S.; Yamada, Y. M. A.; Fukushima, T. Supramolecular Scaffold for Tailoring the Two-Dimensional Assembly of Functional Molecular Units into Organic Thin Films. *J. Am. Chem. Soc.* **2016**, *138*, 11727–11733.

(26) Yokota, T.; Kajitani, T.; Shidachi, R.; Tokuhara, T.; Kaltenbrunner, M.; Shoji, Y.; Ishiwari, F.; Sekitani, T.; Fukushima, T.; Someya, T. A Few-Layer Molecular Film on Polymer Substrates to Enhance the Performance of Organic Devices. *Nat. Nanotech.* **2018**, *13*, 139–144.

(27) Ishiwari, F.; Shoji, Y.; Fukushima, T. Supramolecular Scaffolds Enabling the Controlled Assembly of Functional Molecular Units. *Chem. Sci.* **2018**, *9*, 2028–2041.

(28) Ishiwari, F.; Okabe, G.; Ogiwara, H.; Kajitani, T.; Tokita, M.; Takata, M.; Fukushima, T. Terminal Functionalization with a Triptycene Motif that Dramatically Changes the Structural and Physical Properties of an Amorphous Polymer. *J. Am. Chem. Soc.* **2018**, *140*, 13497–13502.

(29) Liu, J.; Wachter, T.; Irmler, A.; Weidler, P. G.; Gliemann, H.; Pauly, F.; Mugnaini, V.; Zharnikov, M.; Woll, C. Electric Transport Properties of Surface-Anchored Metal-Organic Frameworks and the Effect of Ferrocene Loading. *ACS Appl. Mater. Interfaces* **2015**, *7*, 9824–9830.

(30) Liu, J.; Kind, M.; Schüpbach, B.; Käfer, D.; Winkler, S.; Zhang, W.; Terfort, A.; Wöll, C. Triptycene-Terminated Thiolate and Selenolate Monolayers on Au(111). *Beilstein J. Nanotechnol.* **2017**, *8*, 892–905.

(31) Tada, T.; Ishiwari, F.; Shoji, Y.; Fukushima, T. First-Principles Study of the Adsorption Behavior of Triptycene Molecular Tripods on Au(111): Site-Selectivity and Unambiguous Molecular Orientation. Submitted for publication.

(32) Tamao, K.; Sumitani, K.; Kiso, Y.; Zembayashi, M.; Fujioka, A.; Kodama, S.; Nakajima, I.; Minato, A.; Kumada, M. Nickel-Phosphine Complex-Catalyzed Grignard Coupling. I. Cross-Coupling of Alkyl, Aryl, and Alkenyl Grignard Reagents with Aryl and Alkenyl Halides: General Scope and Limitations. *Bull. Chem. Soc. Jpn.* **1976**, *49*, 1958–1969.

(33) Ooi, T.; Kameda, M.; Maruoka K. Design of *N*-Spiro *C₂*-Symmetric Chiral Quaternary Ammonium Bromides as Novel Chiral Phase-Transfer Catalysts: Synthesis and Application to Practical Asymmetric Synthesis of *α*-Amino Acids. *J. Am. Chem. Soc.* **2003**, *125*, 5139–5151.

(34) Kawauchi, T.; Oguchi, Y.; Nagai, K.; Iyoda, T. Conical Gradient Junctions of Dendritic Viologen Arrays on Electrodes. *Sci. Rep.* **2015**, *5*, 11122.

(35) Lloyd-Jones, G. C.; Moseley, J. D.; Renny, J. S. Mechanism and Application of the Newman-Kwart O–>S Rearrangement of *O*-Aryl Thiocarbamates. *Synthesis* **2008**, *5*, 661–689.

(36) Schreiber, F. Structure and growth of self-assembling monolayers. *Prog. Surf. Sci.* **2000**, *65*, 151–256.

(37) Zharnikov, M. High-Resolution X-Ray Photoelectron Spectroscopy in Studies of Self-Assembled Organic Monolayers. *J. Electron Spectr. Relat. Phenom.* **2010**, *178–179*, 380–393.

(38) Park, J.-S.; Vo, A. N.; Barriet, D.; Shon, Y. S.; Lee, T. R. Systematic Control of the Packing Density of Self-Assembled Monolayers Using Bidentate and Tridentate Chelating Alkanethiols. *Langmuir* **2005**, *21*, 2902–2911.

(39) Weidner, T.; Ballav, N.; Siemeling, U.; Troegel, D.; Walter, T.; Tacke, R.; Castner, D. G.; Zharnikov, M. Tripodal Binding Units for Self-Assembled Monolayers on Gold: A Comparison of Thiol and Thioether Headgroups. *J. Phys. Chem. C* **2009**, *113*, 19609–19617.

(40) Moulder, J. F.; Stickle, W. E.; Sobol, P. E.; Bomben, K. D. Handbook of X-ray Photoelectron Spectroscopy, Chastian, J., Ed.; Perkin-Elmer Corp.: Eden Prairie, MN, **1992**.

(41) The molecular packing densities in the Trip1S/Au and TripS/Au represent 1/3 of the values in Table 1, *i.e.*, 1.53 x 10¹⁴ and 1.37 x 10¹⁴ molecules/cm², respectively.

(42) Stöhr, J. *NEXAFS Spectroscopy*; Springer-Verlag: Berlin, **1992**.

(43) Frey, S.; Stadler, V.; Heister, K.; Eck, W.; Zharnikov, M.; Grunze, M.; Zeysing, B.; Terfort, A. Structure of Thioaromatic Self-Assembled Monolayers on Gold and Silver. *Langmuir* **2001**, *17*, 2408–2415.

(44) Horsley, J.; Stöhr, J.; Hitchcock, A. P.; Newbury, D. C.; Johnson, A. L.; Sette, F. Resonances in the K Shell Excitation Spectra of Benzene and Pyridine: Gas Phase, Solid, and Chemisorbed States. *J. Chem. Phys.* **1985**, *83*, 6099–6107.

(45) The definitions of *α* and *β* of **T1** and **T2** are identical to those in ref. 30.

(46) Ballav, N.; Schüpbach, B.; Dethloff, O.; Feulner, P.; Terfort, A.; Zharnikov, M. Direct Probing Molecular Twist and Tilt in Aromatic Self-Assembled Monolayers. *J. Am. Chem. Soc.* **2007**, *129*, 15416–15417.

(47) The slightly smaller value arises from using the calculated lattice constant of Au rather than the experimental one.

(48) The lattice constant is calculated to be 8.65 Å when employing the experimental bulk lattice constant of Au at room temperature instead of the calculated one.

(49) Felice, R. D.; Selloni, A.; Molinari, E. DFT Study of Cysteine Adsorption on Au(111). *J. Phys. Chem. B* **2003**, *107*, 1151–1156.

(50) Gottschalk, J.; Hammer, B. A Density Functional Theory Study of the Adsorption of Sulfur, Mercapto, and Methylthiolate on Au(111). *J. Chem. Phys.* **2002**, *116*, 784–790.

(51) Campbell, I. H.; Rubin, S.; Zawodzinski, T. A.; Kress, J. D.; Martin, R. L.; Smith, D. L.; Barashkov, N. N.; Ferraris, J. P. Controlling Schottky Energy Barriers in Organic Electronic Devices Using Self-Assembled Monolayers. *Phys. Rev. B* **1996**, *54*, 14321–14324.

(52) Heimel, G.; Romaner, L.; Zojer, E.; Bredas, J.-L. The Interface Energetics of Self-Assembled Monolayers on Metals. *Acc. Chem. Res.* **2008**, *41*, 721–729.

(53) Alloway, D. M.; Hofmann, M.; Smith, D. L.; Gruhn, N. E.; Graham, A. L.; Colorado, R.; Wysocki, V. H.; Lee, T. R.; Lee, P. A.; Armstrong, N. R. Interface Dipoles Arising from Self-Assembled Monolayers on Gold: UV-Photoemission Studies of Alkanethiols and Partially Fluorinated Alkanethiols. *J. Phys. Chem. B* **2003**, *107*, 11690–11699.

(54) de Boer, B.; Hadipour, A.; Mandoc, M. M.; van Woudenbergh, T.; Blom, P. W. M. Tuning of Metal Work Functions with Self-Assembled Monolayers. *Adv. Mater.* **2005**, *17*, 621–625.

(55) Abu-Husein, T.; Schuster, S.; Egger, D. A.; Kind, M.; Santowski, T.; Wiesner, A.; Chiechi, R.; Zojer, E.; Terfort, A.; Zharnikov, M. The Effects of Embedded Dipoles in Aromatic Self-Assembled Monolayers, *Adv. Funct. Mater.* **2015**, *25*, 3943–3957.

(56) Derry, G. N.; Kern, M. E.; Worth, E. H. Recommended Values of Clean Metal Surface Work Functions. *J. Vac. Sci. Technol. A* **2015**, *33*, 060801.

(57) M. Gärtner, M.; Sauter, E.; Nascimbeni, G.; Petritz, A.; Wiesner, A.; Kind, M.; Abu-Husein, T.; Bolte, M.; Stadlober, B.; Zojer, E.; Terfort, A.; Zhanikov, M. Tailor-Made Self-Assembled Monolayers with Embedded Dipole Moments for Interface Engineering in Organic Electronics. *J. Phys. Chem. C* **2018**, *122*, 28757–28774.

(58) Taucher, T. C.; Hehn, I.; Hofmann, O. T.; Zharnikov, M.; Zojer, E. Understanding Chemical versus Electrostatic Shifts in X-Ray Photoelectron Spectra of Organic Self-Assembled Monolayers. *J. Phys. Chem. C* **2016**, *120*, 3428–3437.

(59) Hehn, I.; Schuster, S.; Wächter, T.; Abu-Husein, T.; Terfort, A.; Zharnikov, M.; Zojer, E. Employing X-ray Photoelectron Spectroscopy for

1
2
3
4
5
6
7
8
9
10
11
12
13
14
15
16
17
18
19
20
21
22
23
24
25
26
27
28
29
30
31
32
33
34
35
36
37
38
39
40
41
42
43
44
45
46
47
48
49
50
51
52
53
54
55
56
57
58
59
60

Determining Layer Homogeneity in Mixed Polar Self-Assembled Monolayers. *J. Phys. Chem. Lett.* **2016**, *7*, 2994–3000.

(60) Hamoudi, H.; Neppl, S.; Kao, P.; Schüpbach, B.; Feulner, P.; Terfort, A.; Allara, D.; Zharnikov, M. Orbital-Dependent Charge Transfer Dynamics in Conjugated Self-Assembled Monolayers. *Phys. Rev. Lett.* **2011**, *107*, 027801.

(61) Shaporenko, A.; Terfort, A.; Grunze, M.; Zharnikov, M. A Detailed Analysis of the Photoemission Spectra of Basic Thioaromatic Monolayers on Noble Metal Substrates. *J. Electron Spectrosc. Relat. Phenom.* **2006**, *151*, 45–51.

(62) Thome, J.; Himmelhaus, M.; Zharnikov, M.; Grunze, M. Increased Lateral Density in Alkanethiolate Films on Gold by Mercury Adsorption. *Langmuir* **1998**, *14*, 7435–7449.

(63) Chesneau, F.; Schüpbach, B.; Szelągowska-Kunstman, K.; Ballav, N.; Cyganik, P.; Terfort, A.; Zharnikov, M. Self-Assembled Monolayers of Perfluoroterphenyl-Substituted Alkanethiols: Specific Characteristics and Odd–Even Effects. *Phys. Chem. Chem. Phys.* **2010**, *12*, 12123–12127.

(64) Ratner, M.; Castner, D. Electron Spectroscopy for Chemical Analysis, in *Surface Analysis–The Principal Techniques*; Vickerman, J. Ed.; Wiley: Chichester, 1997.

(65) Lamont, C. L. A.; Wilkes, J. Attenuation Length of Electrons in Self-Assembled Monolayers of *n*-Alkanethiols on Gold. *Langmuir* **1999**, *15*, 2037–2042.

(66) Batson, P. E. Carbon 1s Near-Edge-Absorption Fine Structure in Graphite. *Phys. Rev. B* **1993**, *48*, 2608–2610.

(67) Cabarcos, O. M.; Schuster, S.; Hehn, I.; Zhang, P. P.; Maitani, M. M.; Sullivan, N.; Giguère, J.-B.; Morin, J.-F.; Weiss, P. S.; Zojer, E.; et al. Effects of Embedded Dipole Layers on Electrostatic Properties of Alkanethiolate Self-Assembled Monolayers. *J. Phys. Chem. C* **2017**, *121*, 15815–15830.

(68) Ford, W. E.; Gao, D.; Knorr, N.; Wirtz, R.; Scholz, F.; Karipidou, Z.; Ogasawara, K.; Rosselli, S.; Rodin, V.; Nelles, G.; von Wrochem, F. Organic Dipole Layers for Ultralow Work Function Electrodes. *ACS Nano* **2014**, *8*, 9173–9180.

(69) Blum, V.; Gehrke, R.; Hanke, F.; Havu, P.; Havu, V.; Ren, X.; Reuter, K.; Scheffler, M. *Ab Initio* Molecular Simulations with Numeric Atom-Centered Orbitals. *Comput. Phys. Commun.* **2009**, *180*, 2175 – 2196.

(70) Perdew, J. P.; Burke, K.; Ernzerhof, M. Generalized Gradient Approximation Made Simple. *Phys. Rev. Lett.* **1996**, *629*, 453–462.

(71) Ruiz, V. G.; Liu, W.; Zojer, E.; Scheffler, M.; Tkatchenko, A. Density-Functional Theory with Screened van der Walls Interactions for the Modeling of Hybrid Inorganic-Organic Systems. *Phys. Rev. Lett.* **2012**, *108*, 146103

(72) Tkatchenko, A.; Scheffler, M. Accurate molecular van der Waals interactions from Ground-State Electron Density and Free-Atom Reference Data. *Phys. Rev. Lett.* **2009**, *102*, 073005.

(73) Freysoldt, C.; Eggert, P.; Rinke, P.; Schindlmayr, A.; Scheffler, M. Screening in Two Dimensions: GW Calculations for Surfaces and Thin Films using the Repeated-Slab Approach. *Phys. Rev. B: Condens. Matter Mater. Phys.* **2008**, *77*, 214517.

(74) Jackson, J. D. Classical electrodynamics. 3rd ed.; Wiley: New York, **1999**.

(75) Neaton, J.; Hybertsen, M.; Louie, S. Renormalization of Molecular Electronics Levels at Metal-Molecules Interfaces. *Phys. Rev. Lett.* **2006**, *97*, 216405.

(76) Levstik, A.; Filipič, C.; Levstik, I. Dielectric properties of Biphenyl. *J. Phys.: Condens. Matter* **1990**, *2*, 3031–3033.

1
2
3
4
5
6
7
8
9
10
11
12
13
14
15
16
17
18
19
20
21
22
23
24
25
26
27
28
29
30
31
32
33
34
35
36
37
38
39
40
41
42
43
44
45
46
47
48
49
50
51
52
53
54
55
56
57
58
59
60

Insert Table of Contents artwork here

1,8,13-Substituted-Triptycene Tripods

HS HS SH
T1

SH SH SH
T2

✔ *Reliable Tripodal Adsorption Configuration*
✔ *Upright Molecular Orientation*
✔ *Dense 2D Hexagonal Packing*
✔ *High Uniformity at the large Scale*

T1 or T2

SAM Formation on Au(111)

Au Substrate

12

150
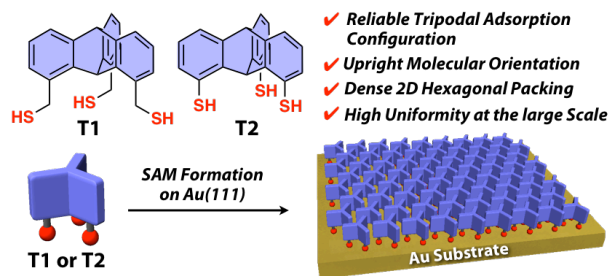
4.5.2 Supporting information

Computational details

Starting geometries and optimisation procedure. The optimised geometries of both the T1/Au and T2/Au SAMs were found using the following procedure. First the molecules were optimised in gas phase and subsequently four high symmetry docking sites for the S atoms on the Au(111) surface were tested (i.e., optimisations were started with the S atoms put at these positions in the initial geometries). These include the ontop, bridge, *fcc*-hollow and *hcp*-hollow positions. For this preliminary screening of the docking positions, the default FHI-aims light basis set was used for all the elements and the following self consistency cycle accuracy parameters were adopted: sc_accuracy_rho = 1×10^{-5} e$^-$, sc_accuracy_etot = 1×10^{-5} eV, sc_accuracy_forces = 1×10^{-4} eV/Å and sc_accuracy_eev = 1×10^{-3} eV. The optimisations were stopped when the maximum residual force component per atom was below 0.05 eV/Å. The most stable among the test geometries were then further optimised using the default FHI-aims tight settings, setting the sc_accuracy_etot and sc_accuracy_potjump tags to 1×10^{-6} eV and 1×10^{-4} eV, respectively, and stopping the optimisations when the maximum residual force component per atom was below 0.01 eV/Å.

Work function change. The calculated work function change is given with respect to the work function of a clean Au slab consisting of 5 Au layers, of which the 3 bottom ones are kept fixed and the 2 top ones are relaxed using the same self-consistency settings adopted to optimise the SAM/Au(111) system.

Dependence of the calculated $\Delta\Phi$ on the methodology. As mentioned in the main manuscript, the calculated $\Delta\Phi$ overestimates the measured one. A possible reason for that discrepancy is the adopted methodology. Because of its good compromise between accuracy of the results and computational time, the generalised gradient approximation (GGA) functional PBE[27] has been used to obtain all the simulation results presented in this work. However, it has to be kept in mind that the applied methodology can have a non-negligible impact on the obtained results. In particular, in table 4.17 we show the impact of the methodology on the values of $\Delta\Phi$ and its components ΔE_{vac} (representing the work function change of a hypothetical free standing monolayer) and the bond dipole (representing the potential energy step originating from the interfacial charge rearrangements; for more details see, for instance, reference 123). We compare values calculated using the GGA functional PBE and the hybrid functional HSE06[82].

Table 4.17: Calculated $\Delta\Phi$ and its components ΔE_{vac} and Bond Dipole for the T1/Au and T2/Au SAMs using a GGA (PBE) and a hybrid (HSE06) functional. Light and tight refer to the default light and tight FHI-aims basis sets.

		$\Delta\Phi$ / eV	ΔE_{vac} / eV	Bond dipole / eV
T1/Au	PBE light	−1.35	−0.02	−1.33
	PBE tight	−1.33	−0.06	−1.26
	HSE06 light	−1.11	−0.03	−1.08
T2/Au	PBE light	−1.74	−0.61	−1.13
	PBE tight	−1.73	−0.65	−1.08
	HSE06 light	−1.60	−0.68	−0.92

This comparison shows that for both SAMs the HSE06 calculated $\Delta\Phi$ values are some-

what smaller, mostly due to the smaller value of the calculated bond dipole. The difference between T1/Au and T2/Au is similar, albeit somewhat larger in the HSE06 case.

4.6 COO bonded triptycene based self-assembled monolayers on the Ag(111) surface: preliminary computational characterisation

The essentially upright standing orientation and the convenient property of bearing four sites available for chemical functionalisation make the tripticene based SAMs, in particular T1, interesting building blocks to modify the properties of the Au(111) surface. The transferability of such advantageous features also to triptycene based SAMs docked on a different substrate with a different docking group was investigated, too. An intermediate of the synthesis of the T1 and T2 molecules bearing three COOH groups was deposited onto the Ag(111) surface. The preliminary characterisation of that interface, schematically shown in figure 4.39, is reported in this section.

The molecules have been synthesised in the group of Professor Takanori Fukushima at the Tokio Institute of Technology and deposited on the metal surface by the group of Professor Manfred Buck at St Andrews University. The used substrate is Au(111), on which two layers of Ag with the same orientation were grown.

Experimental STM pictures acquired in the group of Professor Buck were available and used as starting point for the simulations and to compare the results. Valuable input for the discussion of the latter came from the groups of Professor Buck and Fukushima and from Professor Michael Zharnikov from the Heidelberg University.

The experimental STM picture is shown in figure 4.40. Interestingly, two phases could be identified, whereas for the systems investigated in section 4.5 only one phase was observed. The two phases are referred to as hexagonal and porous. The latter is by far the most abundant, representing the 95%.
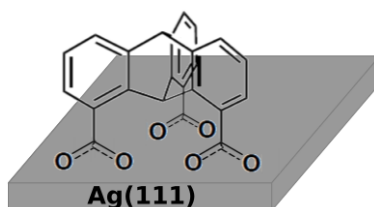

Figure 4.39: Schematic of the COO bonded triptycene based molecules on the Ag(111) surface investigated in this section.
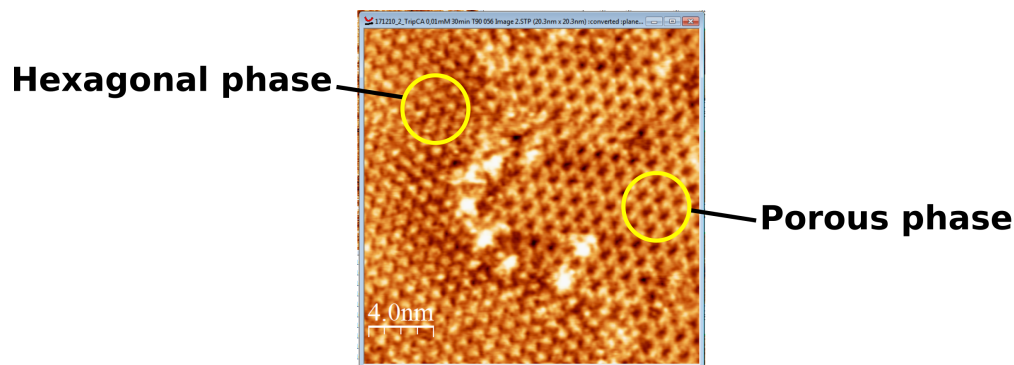

Figure 4.40: Experimental constant current STM picture with the indication of the two identified phases.

4.6.1 Computational methods

The calculations were performed with the code FHI-aims[26] using the PBE functional[27] and the surface version[28] of the Tkatchenko-Scheffler[29] corrections for the van der Waals interactions. Periodic boundary conditions and the so called repeated slab approach were used. For these preliminary calculations, to keep the computational cost low, the metal substrate was modelled using 2 layers of Ag on top of 1 layer of Au and all the atoms were described using the default FHI-aims light settings. The total energy criterion for the self-consistency cycle was set to 10^{-5} eV and geometry optimisations were performed until the maximum residual force component per atom was below 0.05 eVÅ. The dimensions of the unit cells in the x and y directions are given in units of the theoretically calculated Au lattice constant (primitive lattice constant of 4.158 Å, corresponding to a nearest neighbour distance of 2.940 Å), used also for the 2 topmost Ag layers. The dimension in the z direction was set in such a way that a vacuum region of at least 20 Å was included between the slabs, to spatially decouple the consecutive replicas. To electrostatically decouple them a self-consistently calculated dipole correction was inserted in the z direction. The dimensions of the unit cell and the bottom Au layer were kept fixed in in the calculations, i.e. only the atomic positions of the molecule and the 2 topmost Ag layers were optimised.

STM pictures were simulated within the Tersoff-Hamann approximation[124] following the procedure described in detail in reference 77. The FHI-aims stm cube files were postprocessed using a routine written by Dr. Oliver T. Hofmann, from the Institute of Solid State Physics of the Graz University of Technology, in order to obtain the (blurred) constant height and constant current STM pictures. To obtain the blurred pictures an active tip radius of 1.0 $Å^2$ was used. The sample bias is specified in the corresponding section for each simulated image.

The HOMO shown in figure 4.44 was calculated using the software Gaussian 09, Revision D.03[104] at the b3lyp/6-31g(d,p) level of theory.

4.6.2 Hexagonal phase

In the hexagonal phase the molecules assume the same arrangement observed for the S bonded triptycenes investigated in the previous section. The initial geometry was therefore set up placing the gas phase optimised triptycene based molecule into a (3×3) surface unit cell. The optimised geometry is shown in figure 4.41. All the three anchoring groups occupy the same docking position: the O atoms pointing towards the outer part of the molecule occupy ontop positions, while the ones pointing towards the centre of the tripodal backbone occupy bridge sites. The bottom C atoms occupy *hcp*-hollow positions. Analogously to what observed for the S based SAMs of the previous section, the molecules have an almost perfectly upright standing orientation, with a calculated tilt angle of 1.95°. The upright standing orientation and the homogeneous bonding configuration suggest the suitability of the triptycene backbone as building block for surface modifications also when combined with different docking groups and different substrates.

4.6.3 Porous phase

An enlarged picture of the porous phase is shown in figure 4.42. Identifying the molecular arrangement for this phase was not straightforward: the bright centres bearing six "arms" could not be univocally associated with any arrangement of the tripodal molecules.

Among the initially proposed arrangements, shown in figure 4.42, 1, 1b and 2 were excluded: the latter is not compatible with the observed sixfold symmetry, while 1 and 1b are chiral and from the experimental picture no chirality can be appreciated. The simulation
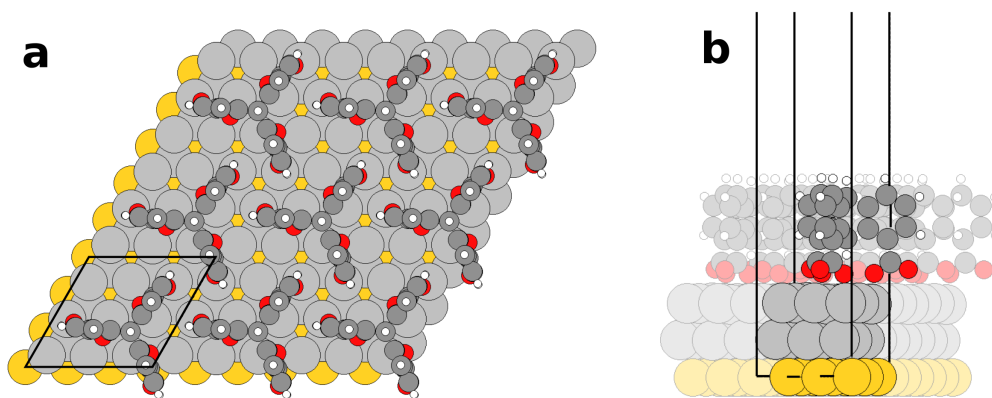
Figure 4.41: Top (a) and side (b) view of the optimised TripCOO/Ag(111)/Au(111) geometry in the hexagonal phase. Au atoms are depicted in dark yellow, Ag atoms in light grey, O atoms in red, C atoms in dark grey and H atoms in white. The black lines enclose the unit cell.
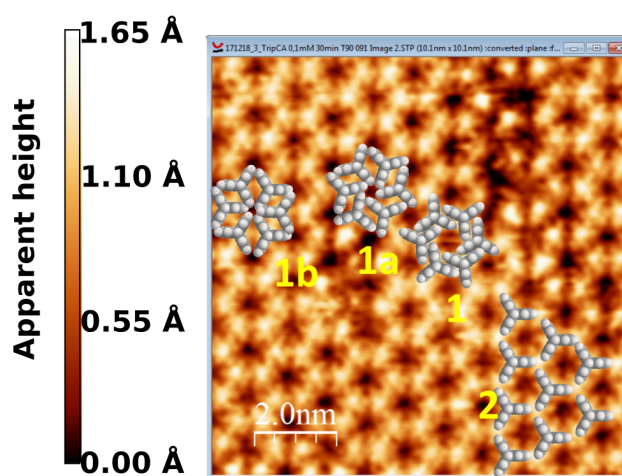

Figure 4.42: Experimental constant current STM picture of the porous phase. 1, 1a, 1b and 2 indicate four different proposed arrangement of the molecules. A colour coded legend for the apparent height is also shown.

unit cell was then set up according to arrangement 1b, with 2 molecules in a (4×4) surface unit cell. The optimised structure is shown in figure 4.43.

Also in this case the molecules are essentially upright standing, with an average calculated tilt angle of 2.14°. The anchoring configuration is the same observed and described for the hexagonal phase. This allows making the same considerations exposed above regarding the potential of the triptycene based SAMs for surface modifications.

The honeycomb pattern seen in experiments can be easily identified also in the optimised geometry, with the distance between the corners of the hexagons being compatible with the distance between the experimentally observed bright spots. Interestingly, the optimised structure fits very well arrangement 1 of figure 4.42, that due to its chirality was excluded. Moreover, the bright spots seen in experiments apparently stem form the centre of the molecules, but this does not seem to be consistent with the localisation of the HOMO of the isolated gas phase TripCOOH molecule, shown in figure 4.44.

An alternative non chiral arrangement was suggested by Professor Fumitaka Ishiwari, from the group of Professor Fukushima, and is shown in figure 4.45. However, also using the proposed structure as starting geometry, in the course of the optimisation the molecules assume again the chiral arrangement previously found.

The impact of changing the conformation of the docking atoms was tested, too, to in-
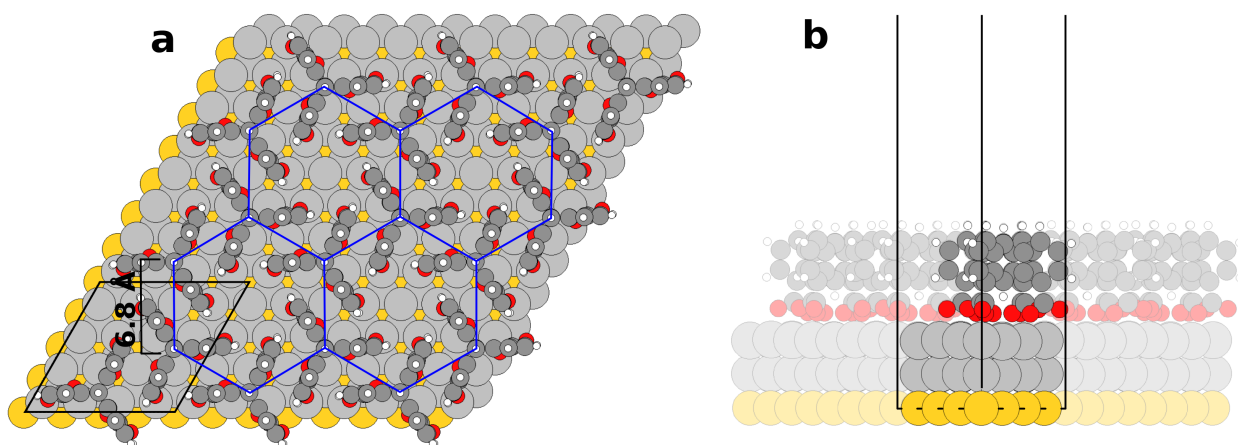
Figure 4.43: Top (a) and side (b) view of the optimised TripCOO/Ag(111)/Au(111) geometry in the porous phase. Au atoms are depicted in dark yellow, Ag atoms in light grey, O atoms in red, C atoms in dark grey and H atoms in white. The unit cells are enclosed by the black lines. The blue hexagons are a guide to the eye to more easily identify the honeycomb pattern. The length of the side of the hexagons is also indicated.
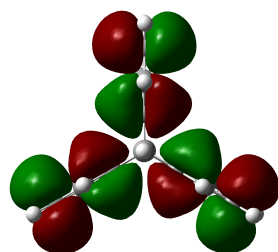
Figure 4.44: Highest Occupied Molecular Orbital of the isolated gas phase TripCOOH molecule.

vestigate if this could influence the arrangement assumed by the molecules. In figure 4.46, panel a, a starting non chiral geometry with a particular pattern of the docking O atoms is shown. The optimisation leads however again to a chiral arrangement, as can be seen in panel b of figure 4.46. What it is interesting to emphasise is that just by slightly rotating one of the two molecules, a final geometry with the opposite chirality is obtained, shown in panel c of figure 4.46. This indicates that in principle the molecules could go from one chiral arrangement to the other one by means of a collective rotation without colliding.
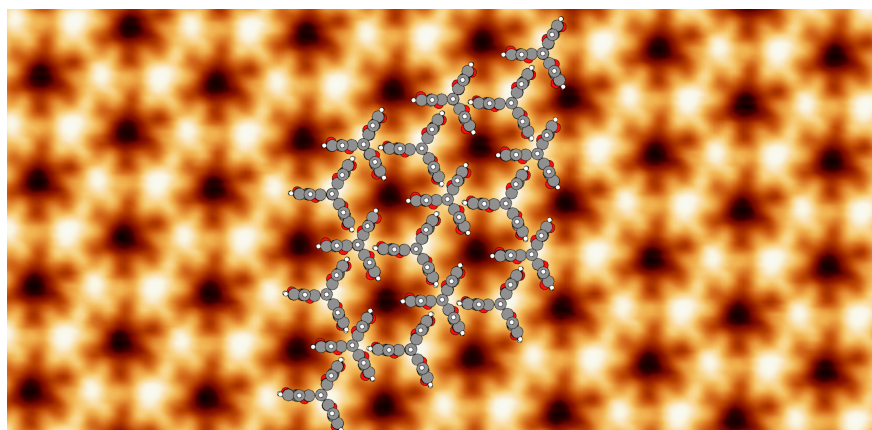
Figure 4.45: Non chiral arrangement suggested by Professor Ishiwari.
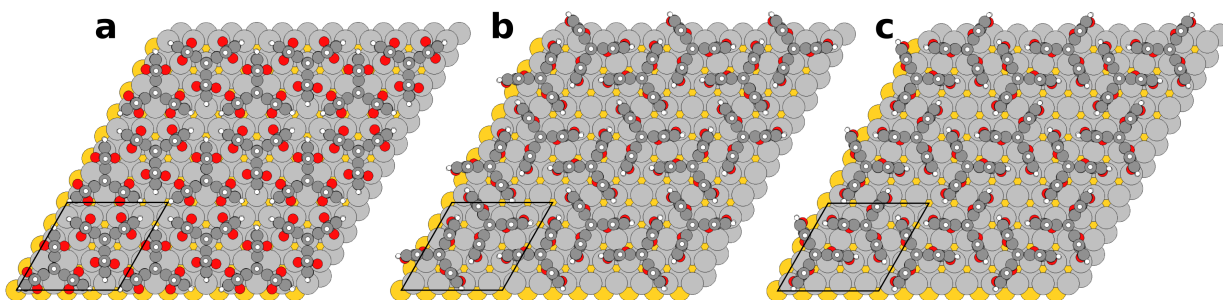
Figure 4.46: Panel a: starting geometry to test the impact of the docking atoms configuration. Panel b and c: optimised arrangements with opposite chirality.

Surface reconstruction

The next step was to consider whether and how the presence of adatoms could prevent the molecules from arranging in the structure of figure 4.43, that in the calculations is definitely the most stable one on the clean unreconstructed Ag(111) surface. Several surface reconstruction motifs were tested, with up to 6 Ag adatoms/unit cell. The adatoms were placed in positions where they could possibly hinder the tendency of the molecules to arrange like in figure 4.43. In all cases the optimised structure was very far from the proposed non chiral arrangement. Starting and optimised reconstructed interfaces are shown in figure 4.47.

The presence of Ag adatoms on the surface is not unlikely, however the optimised geometries of figure 4.47 obviously indicate that in none of the considered cases they prevent the molecules from assuming a chiral arrangement, in which every arm of the triptycene backbone tends to arrange cofacial and herringbone, respectively, with two arms of a neighbouring molecule and herringbone with one arm of another neighbouring molecule (see figure 4.43). This intermolecular interaction seems to be the strongest driving force for the most favourable arrangement.

Simulated STM pictures

To analyse in more detail the apparent inconsistency between calculated and experimental results, STM pictures of the optimised chiral arrangement were simulated. Since in the experimental setup the tip was positively biased, the occupied molecular states were used for the simulation. To see where the highest occupied state of the SAM is energetically localised, the density of states (DOS) projected onto the molecules was plotted (see figure 4.48). The local DOS (LDOS) in a 0.1 eV interval centred at the energy of the highest occupied state is shown in figure 4.49: the localisation is not different from the case of an isolated molecule, shown in figure 4.44, in particular there is no localisation at all at the centre of the molecule.

The simulated constant height STM pictures at different heights are depicted in figure 4.50. Indeed, consistent with the LDOS plot, in the pictures the centre of the molecule is not bright.

Constant height STM pictures were then simulated accounting for all the states between the Fermi energy and the energy just below the highest molecular occupied state (in figure 4.48 the red arrow indicates that energy and the green double arrow shows the considered interval). The corresponding STM pictures are shown in figure 4.51.

Interestingly, using this energy interval the centre of the molecule looks bright, in agreement with the experimental pictures. What is also worthwhile mentioning is that the simulated pictures at 1.8 Å above the SAM hardly show any chirality (panel b in figures 4.50 and 4.51). For better comparing the simulated and experimental pictures, the resolution of
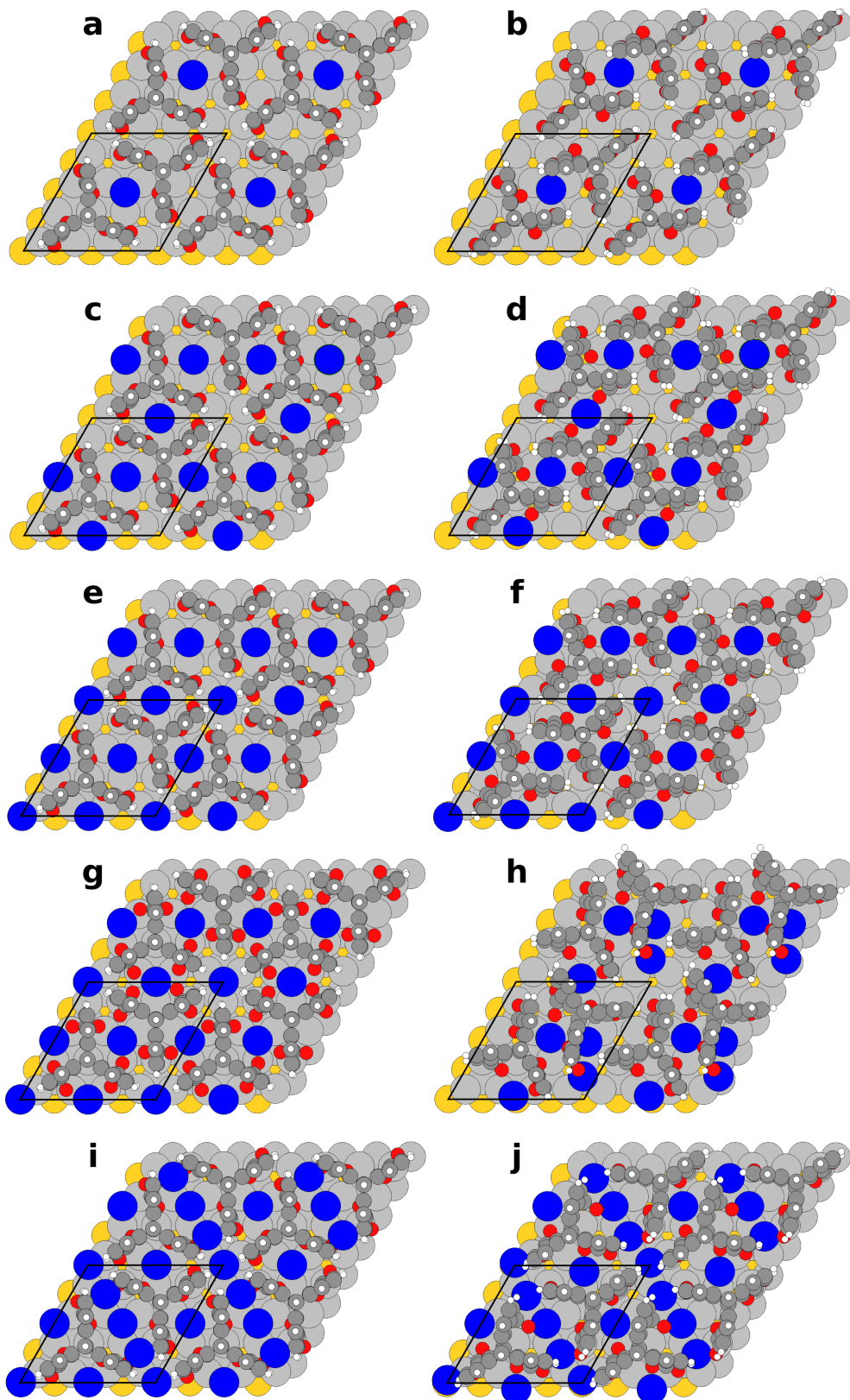
Figure 4.47: Reconstruction motifs tested to investigate the impact of adatoms. Left panels: starting geometries, right panels: optimised geometries. Au atoms are depicted in dark yellow, Ag atoms in light grey, Ag adatoms in blue, O atoms in red, C atoms in dark grey and H atoms in white. The unit cells are enclosed by the black lines.
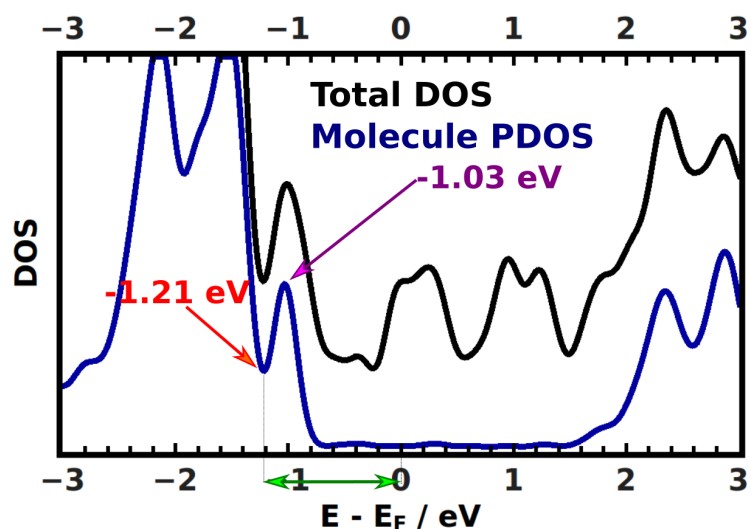
Figure 4.48: Total DOS (black line) and DOS projected on the molecule (blue line) of the structure of figure 4.43. The purple arrow indicates the peak of the PDOS corresponding to the highest occupied molecular state, the red arrow indicates the energy just below that peak and the green double arrow shows the interval enclosed between that energy and the Fermi energy.
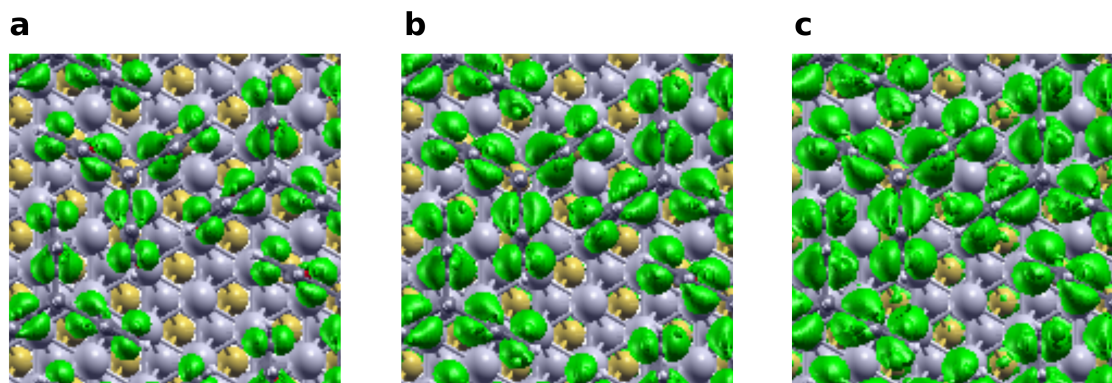
Figure 4.49: Localisation of the highest occupied molecular state (plotted in green) at different isovalues: 0.1 (panel a), 0.05 (panel b) and 0.03 (panel c) $e^-/\text{Å}^3$. This confirms that the fact that no localisation at the centre of the molecules is observed is not an artefact of the chosen isovalue. Au atoms are depicted in dark yellow, Ag atoms in light grey, O atoms in red, C atoms in dark grey and H atoms in white.
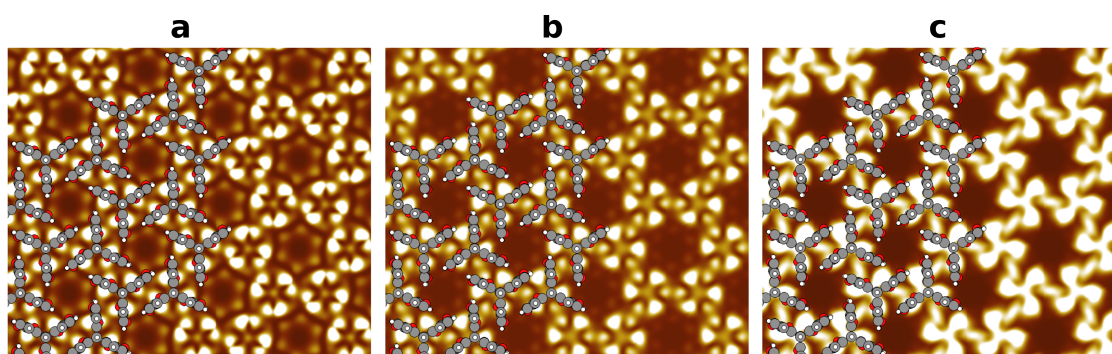
Figure 4.50: Simulated constant height STM pictures obtained using the states in a 0.1 eV energy window centred at the energetic position of the highest occupied molecular state (-1.03 eV, indicated by the purple arrow in figure 4.48). The energy range is the same used to plot the LDOS of figure 4.49. The images are plotted at 0.5 (a), 1.8 (b) and 2.2 (c) Å above the position of the centre of the highest atom. The optimised arrangement of figure 4.43 is superimposed to the simulated STM pictures.

Figure 4.51: Simulated constant height STM pictures obtained using all the states between the energy just below the molecular highest occupied state (red arrow in figure 4.48) and the Fermi energy (interval indicated by the green double arrow in figure 4.48) at 0.5 (a), 1.8 (b) and 2.2 (c) Å above the position of the centre of the highest atom. The optimised arrangement of figure 4.43 is superimposed to the simulated STM pictures.

the simulated one was artificially lowered by blurring it using a tip with an active area of 1 Å^2 (for further details see the computational details section and the references therein). In figure 4.52 the blurred simulated constant height STM picture at 2.2 Å above the molecules is compared to the experimental constant current STM picture.

The agreement is excellent, particularly because the simulated picture fully reproduces the bright centre and the six arms. Three of the latter correspond to the three phenyl rings of the tripodal backbone. The other three, that seem to connect the centre of every molecule with the closest three ones, are attributed to the superposition of the orbitals localised on the phenyl rings cofacially arranged. Blurring the simulated picture strongly reduces the perceived chirality, that can however still be identified in the simulated picture, while, as already discussed, in the experimental one this is not the case.

A constant current STM picture was simulated, too, and compared to the experimental one in figure 4.53. Also in this case the chirality of the arrangement is somewhat less evident. Since this was already observed for the constant height STM picture at 1.8 Å above the SAM, this rises the question whether under certain conditions a chiral arrangement could appear non chiral in imaging experiments. In order to clarify this issue, the next step will be to perform further experiments, varying the measurement parameters, to investigate how the images change.
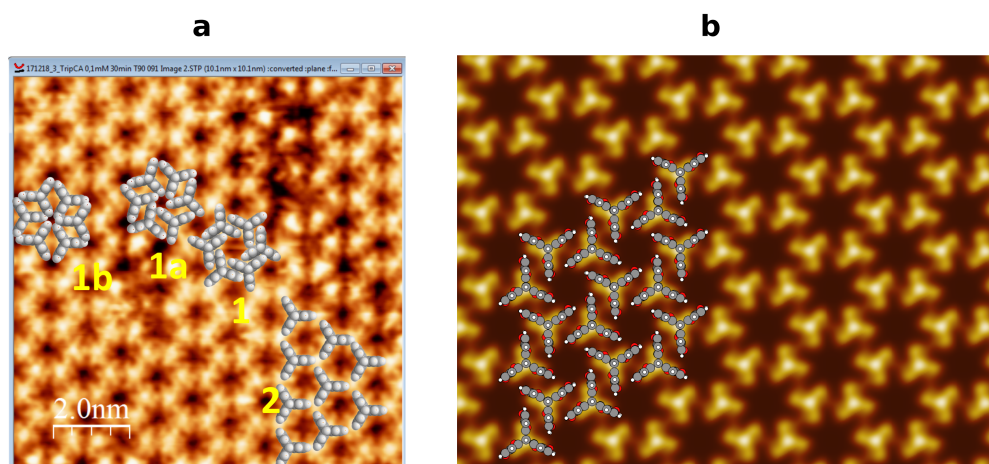
Figure 4.52: Comparison between the experimental constant current STM picture (a) and the simulated constant height one at 2.2 Å above the position of the centre of the highest atom (b). The optimised arrangement of figure 4.43 is superimposed to the simulated STM picture.
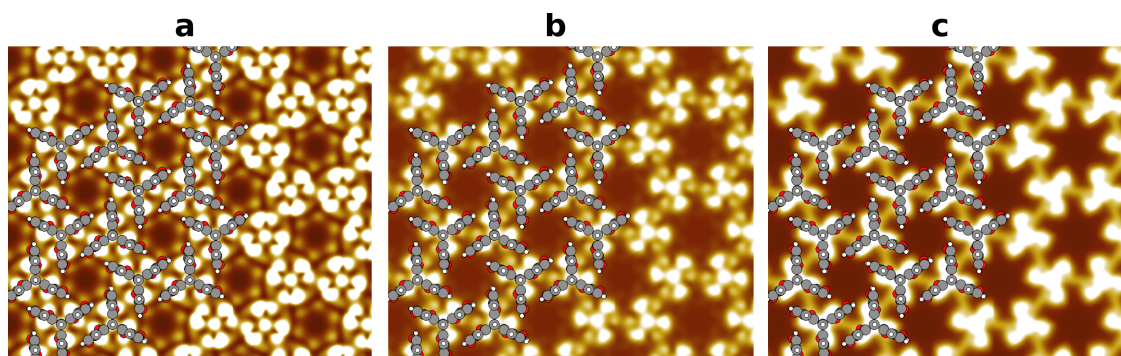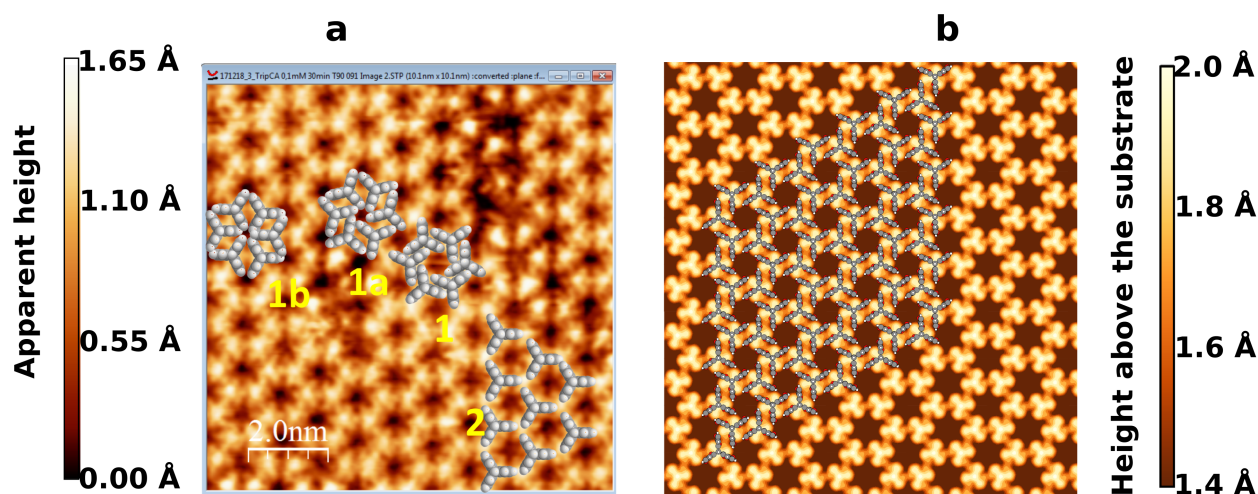
Figure 4.53: Comparison between the experimental (a) and the simulated (b) constant current STM pictures. The optimised arrangement of figure 4.43 is superimposed to the simulated STM picture.

A further scenario could be the collective rotation of the molecules on the surface, that would allow them to alternatively assume both chiral arrangements, leading therefore to averaged STM pictures in which the chirality would not be detectable any longer. In figure 4.54 the constant height STM picture at 2.2 Å above the SAM obtained averaging the STM pictures of the two chiral structures of figure 4.46 is shown.

In this regard, measuring STM at low temperature, at which the molecules are frozen on the surface, could help excluding or confirming such hypothesis. A collective rotation cannot be excluded, since the molecules could in principle rotate without colliding, as observed above. To achieve a more detailed insight into how this could happen, the research of a possible transitions state could help understanding which energetic barriers would come into play.
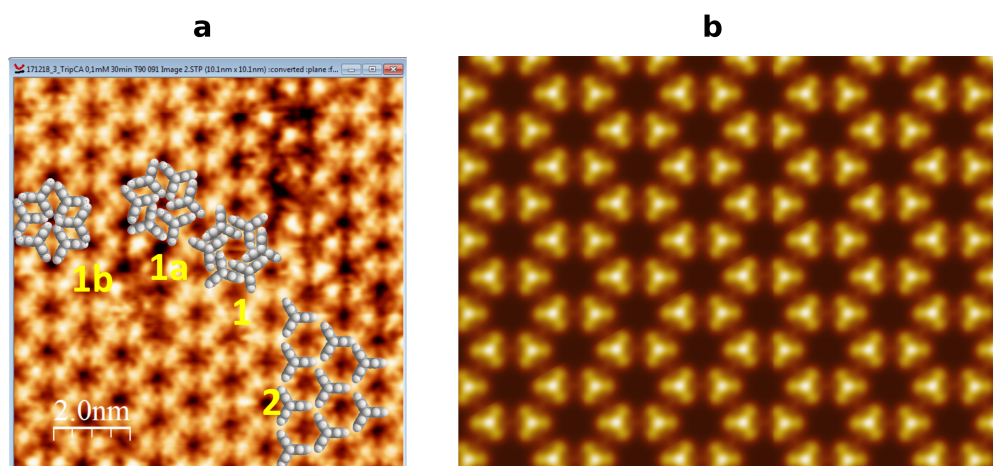
Figure 4.54: Comparison between the experimental constant current STM picture (a) and the simulated constant height one at 2.2 Å above the position of the centre of the highest atom (b) obtained averaging the STM structures simulated for the two chiral structures of figure 4.46.

4.6.4   Conclusions

In this section the preliminary characterisation of triptycene based COO bonded SAMs on the Ag(111) surface has been presented. The main purpose was to find a suitable structure

to model the properties of this peculiar system. This was not straightforward: the main issue was that in the calculated optimised geometry the molecules assume a chiral arrangement, not observed however in the experimentally measured STM pictures. Even more puzzling is that in the simulated STM pictures, both at constant current and constant height, the chirality is much less evident than looking at the geometries. An explanation for this peculiar observation could be that under certain conditions (for instance resolution or voltage of the tip) even on chiral arrangements non chiral pictures can be measured. To test this hypothesis further experiments are needed.

A different, equally interesting situation would be the occurrence of a simultaneous collective rotation of all the molecules, to go from one chiral arrangement to the one with the opposite chirality. This intriguing hypothesis could be checked both from an experimental and a computational point of view, performing STM measurements at low temperatures and calculating the energetic barriers for such collective motions.

4.7 Understanding the interplay of chemical and electrostatic shifts in XPS: the prototypical case of K/Au(111)

As already repeatedly pointed out, metal/SAM interfaces such as the ones investigated in this work are conceived to be integrated in organic electronic devices. An example of how this can be successfully done, by means of the second generation molecules described in section 4.2, is given in reference 1. For this purpose, a detailed knowledge of the atomistic structure and of the level alignment at such interfaces is of fundamental importance. Among the available experimental surface characterisation techniques, XPS plays a fundamental role[18]. It allows obtaining information about, for instance, the chemical identity of the adsorbed species or their density. Moreover, as already mentioned, it has also been shown that XPS signals are affected by collective electrostatic effects[19]. In this regard, some puzzling observations were reported for species close to the metal (see for instance section 4.4 of this work and reference 125), so that the impact of electrostatics on the core level binding energies is not clear yet. In this section we try to clarify this issue by means of a model K/Au(111) interface. The results are organised in the form of the draft of a manuscript. I wrote the text and prepared the figures.

4.7.1 Draft of the manuscript

Abstract

Depositing self-assembled monolayers of organic molecules on metal surfaces allows tuning the substrate work function thanks to collective electrostatic effects. The latter have been demonstrated to affect also X-ray photoelectron spectra (XPS), that could therefore be exploited to probe electrostatic shifts. However, for species close to the metal surface the situation becomes more entangled, due to adsorption induced charge rearrangements that could give rise to chemical shifts masking the electrostatic effects. In this work density functional theory (DFT) simulations are used to investigate the interplay between chemical and electrostatic shifts in such cases. By means of a model K/Au(111) interface we rationalise the impact of the different effects, showing how their competition affects the measured binding energies. On one side, this allows a detailed understanding of the XPS spectra of such interfaces. On the other side, our results contribute to clarifying the energy level alignment at metal/organic interfaces.

Introduction

The deposition of self-assembled monolayers of organic molecules is a widely exploited technique to modify and tune many surface properties, like, for instance, wettability[4,5], corrosion[6,7] and adhesion[8,9]. In particular, in the field of organic electronics SAMs are commonly used to change the work function of metal electrodes[126,127]. The modification is based on so called collective electrostatic effects[23–25], that occur whenever a 2D periodic arrangement of dipolar units is present. The superposition of the fields of the dipoles induces an abrupt shift in the electrostatic potential energy between the two sides of the dipole sheet.

Recently, it has been shown that such collective electrostatic effects also modify the binding energies of a SAM, impacting X-ray photoelectron spectra (XPS)[19]. XPS is a convenient and widely used surface science characterisation method, due to the accurate information it allows to achieve and to the availability of the experimental equipment in many laboratories[18]. The technique is sensible to the chemical environment of the species

and is commonly employed to obtain information about the chemical identity and packing density of the molecules in the SAM, the thickness of the film and the possible presence of disorder. Being aware that XPS signals are also affected by electrostatics is not only of crucial importance for the correct interpretation of the spectra, but also allows analysing the distribution of the dipolar units within the SAM, as discussed in reference 19. Moreover, knowing how electrostatic effects affect XPS offers a convenient way to probe the SAM induced electrostatic shifts. In reference 39, for instance, it is shown how the shifts in the C1s XPS signal of mixed SAMs of different mixing ratios fully correlate with the shift of the SAM induced work function change of the substrate.

An exception to this behaviour is reported in reference 125. Upon K evaporation on a C12 SAM on the Au(111) surface, the C1s signal shifts following the change in work function due to the K deposition, while for the S and the K signals this is apparently not the case. The S signal stays constant, while the shift of the K core level energies has no evident correlation with the pbe work function change. This observation was rationalised assuming different energy level pinning schemes for the docking group (Fermi level pinning) and the molecular backbone (vacuum level pinning). This tentative explanation presents however some unclear points. For instance, it is not clear which pinning scheme the K atoms should undergo. Moreover, the density functional theory (DFT) results reported in reference 19 and in section 4.4 of this thesis seem not to confirm such a model. According to the atomically resolved raw (not screened) calculated C1s binding energies for the full and reduced coverage SAMs, where reducing the coverage has the purpose of diluting the dipole density and turning collective electrostatic effects off, also the C atoms bonded to the docking groups do not show any shift. Additionally, interpreting these observations on the basis of electrostatics, the shift in the electrostatic potential energy should occur only above the bottom C atom. This would in turn unrealistically imply that there would be no dipoles between the surface and the docking group and between the docking group and the bottom C atom of the backbone.

These observations led to the hypothesis that for species close to the metal surface additional chemical effects play a role, that could mask the electrostatic ones. In the present work, we perform DFT calculations on a conceptual K/Au(111) interface at full and reduced K coverage, to indeed demonstrate that the core level binding energies of atoms close to the metal surface are governed by a subtle interplay between electrostatic and chemical effects. The former are analysed by comparing the full and the reduced K coverages, since, as already mentioned, diluting the dipole density lowers the impact of collective electrostatic effects. Chemical effects are investigated by considering the different partial charges sitting on the K atoms at different coverages and by comparing the K atoms adsorbed on the surface with free standing sheets of K atoms and isolated K atoms. Our results show that such non trivial superposition of chemical and electrostatic effects cannot be disregarded for the correct interpretation of XPS signals of metal/organic interfaces.

Computational methodology

The calculations were performed using the codes FHI-aims[26] and VASP[99–102], employing the PBE functional[27] and applying periodic boundary conditions combined with the repeated slab approach. Van der Waals interactions were accounted for within the Tkatchenko-Scheffler scheme[29] in its parametrisation for interfaces[28]. The FHI-aims code was used for the geometry optimisation and to get all the work function change and K1s binding energy values reported in this work. The VASP code was used for single point calculations on the FHI-aims geometries to generate the charge density files CHGCAR necessary to calculate partial charges within the Bader partitioning scheme[95] (see below). The full coverage unit cell was obtained placing one K atom in a $(\sqrt{3} \times \sqrt{3})$ Au surface unit cell. The K atom was

placed in *fcc*-hollow position and the structure was optimised. The dimensions of the unit cell in the x and y directions were set according to the theoretically calculated Au lattice constant of 4.158 Å, corresponding to a nearest neighbour distance of 2.940 Å. The dimension in the z direction was determined such that a vacuum region of at least 20 Å was included between two consecutive replicas of the slab. To decouple the slabs also electrostatically a self-consistently calculated dipole correction was inserted between them[115]. The metal substrate was modelled using 5 layers of Au atoms, with the 3 bottom ones kept fixed during the relaxation. All the atoms were described using the default FHI-aims tight settings and a Γ centred $8 \times 8 \times 1$ k-point grid was used. The total energy criterion for the self-consistency cycle was set to 10^{-6} eV and the optimisation was stopped when the maximum residual force component per atom was below 0.01 eV/Å. After the optimisation the two bottom Au layers were removed and a single point with the total energy criterion set to 10^{-4} eV was performed. This was done in order to keep the calculations cheap in view of the larger unit cell needed for the reduced coverage calculations. The comparison of work function changes and K1s binding energies shown that despite reducing the accuracy of the settings the results were converged for the purposes of the present analysis. For the reduced coverage calculations a $(3\sqrt{3} \times 3\sqrt{3})$ unit cell was used, obtained replicating the full coverage one three times in the x and y directions and removing all the K atoms but one. No geometry optimisation was performed for the reduced coverage unit cell. A smaller Γ centred $2 \times 2 \times 1$ k-point grid was accordingly used. The VASP calculations were performed using projector augmented wave potentials[128] (Au 04Oct2007 and K_pv 17Jan2003) with a cutoff energy of 350 eV for the plane wave basis set and Monkhorst-Pack[129] $8 \times 8 \times 1$ and $2 \times 2 \times 1$ k-point grids for the full and the reduced coverage, respectively. The aedens module was included, which allows obtaining also the core charge density from the PAW calculations. To perform the charge partitioning, the version 1.0 of the Bader Charge Analysis code[130–133] and the chgsum.pl script developed in the Henkelman group at the University of Texas at Austin were used, following the instructions available on the group webpage[134]. Binding energies are calculated within the initial state approach, to avoid the artefacts arising from combining periodic boundary conditions and the final state approach[19]. The work function changes are given relative to the upper work function of a clean Au(111) slab consisting of 5 Au layers, of which the two topmost ones were relaxed using the same computational settings used for the K/Au(111) interface. As done for the K covered surface, the two bottom Au layers were then removed. The upper work function obtained performing a single point calculation with the settings described above was taken as reference. For calculating isolated K atoms and free-standing K atom sheets spin polarised calculations were performed.

Investigated systems

The considered systems are depicted in figure 4.55. In the full coverage and reduced coverage cases one K atom is placed in a $(\sqrt{3} \times \sqrt{3})$, respectively $(3\sqrt{3} \times 3\sqrt{3})$, surface unit cell. The reduced coverage corresponds thus to 1/9 of the full coverage.

The docking position was kept fixed at both coverages (see computational methodology section). It has to be mentioned that according to the literature[135,136] the arrangement of the K atoms on the Au(111) surface depends on the K coverage. Moreover, as pointed out in the computational analysis performed in reference 136, a realistic description cannot disregard surface reconstructions. In particular, for the full coverage case the most favourable adsorption position is calculated to be a substitutional site. For the lowest coverage considered in the study, corresponding to 1/3 of the full coverage, the most favourable docking positions are instead the hollow sites. For reasons that will become clear with the help of the next two schematics, using different docking positions at different coverages would not
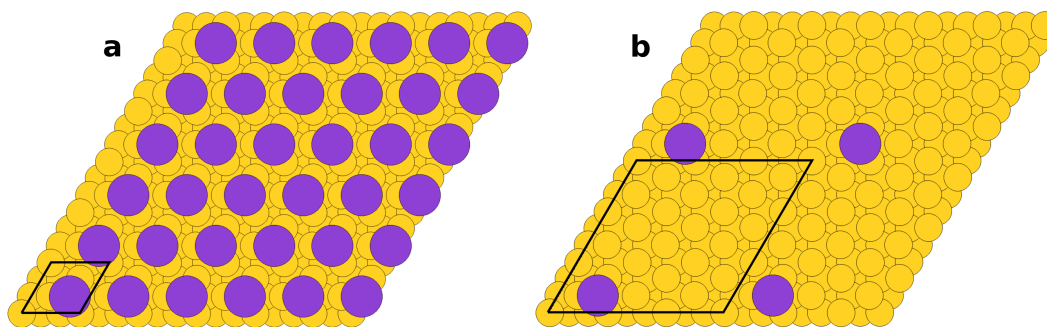
Figure 4.55: Top view of the K/Au(111) interfaces investigated in this work. Panel a: full coverage. Panel b: 1/9 reduced coverage. K atoms are depicted in purple, Au atoms in yellow. The black lines enclose the unit cells.

be suitable for the purposes of the present study. However, the particular docking position is not really relevant for the analysis we want to conduct. The K/Au(111) interface treated in this investigation is meant as a *Gedankenexperiment*. At the light of this fact it has to be pointed out that a comparison of the calculated results presented in this work and the experimental ones reported, for instance, in reference 125 would not be sensible.

This specific system was chosen as simple model that allows separating chemical and electrostatic shifts at different coverages. Figures 4.56 and 4.57 help understanding how this is done.

In figure 4.56 the energy level alignment for a generic metal/SAM interface is sketched. In panel a the surface and the SAM are not yet in contact an the vacuum level VL is the same throughout the whole system. The metal work function is the difference between the VL and the metal Fermi level E_F (for sake of simplicity the effect of the tailing out of the surface of the electron cloud is not explicitly accounted for). The highest occupied molecular orbital (HOMO) and the lowest unoccupied molecular orbital (LUMO) of the SAM are also shown.

In panel b the metal/SAM interface is formed. Upon adsorption of the SAM molecules, due to the Pauli pushback effect and to the charge rearrangements upon formation of the bond between the metal substrate and the docking groups, a step in the potential occurs at the metal/SAM interface. Such step is commonly called bond dipole and, in most cases, has a negative sign, lowering the vacuum level, as shown in the sketch. The lowering of the vacuum level results not only in the reduction of the work function, but also in the lowering, with respect to E_F, of all the molecular states above the dipoles. This holds both for the valence states and for the core levels. It is important to point out that, for a dipole layer spatially localised between the metal surface and the adsorbate, the states of the latter get shifted with respect to E_F, while with respect to the vacuum level the position of the adsorbate states is unchanged. If the molecules forming the SAM contain a dipole, a further potential step occurs, as shown in panel c, again shifting the vacuum level and all the molecular states above the step.

The relevant energy levels for the system considered in this work are sketched in figure 4.57. The lower vacuum level, LVL, depicted on the left is the vacuum level of a clean Au(111) surface. The distance between the LVL and the metal Fermi energy, E_F, is the lower work function Φ, that corresponds to the Φ of the clean Au(111) surface. The upper vacuum level, UVL, depicted on the right, is the vacuum level of the K covered surface. The distance between the UVL and the E_F, is the upper Φ. Due to K deposition, the lower and the upper Φ are different, as a result of the energetic shift between LVL and UVL. The shift amounts to the work function change $\Delta\Phi$. Since $\Delta\Phi$ has a purely electrostatic origin, it can be used as a measure of the electrostatic shifts.
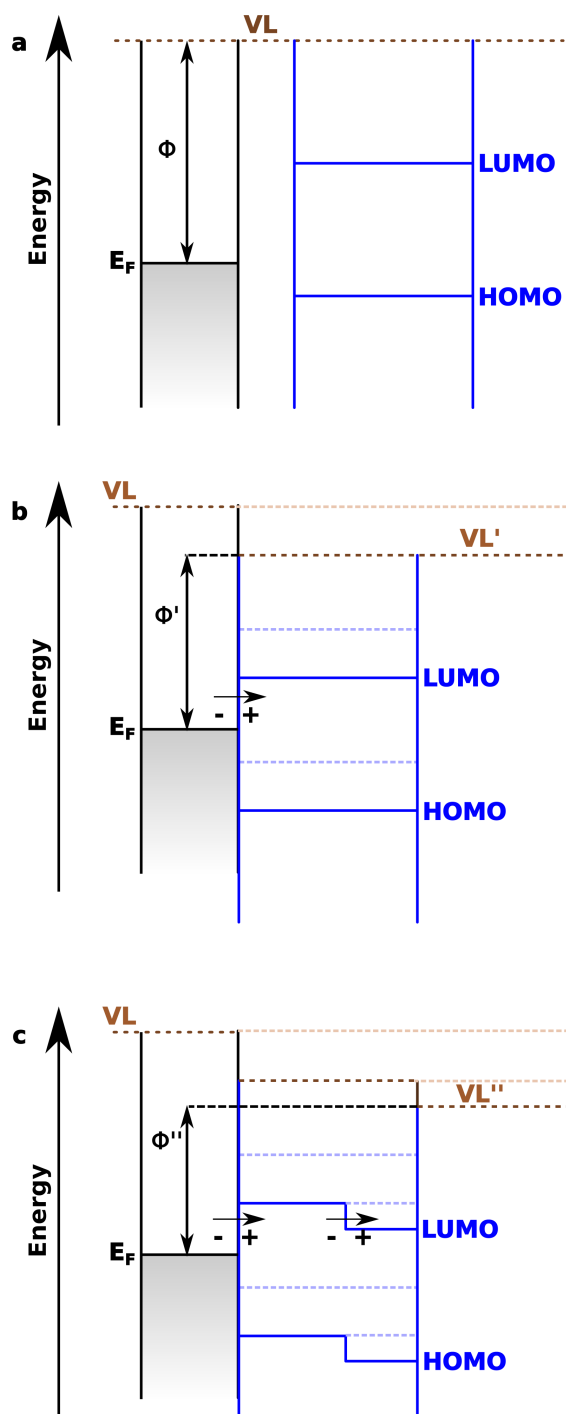
Figure 4.56: Energy level alignment of a generic metal/organic interface. The Fermi energy E_F, the vacuum level VL, the work function of the metal Φ and the frontier states of the organic material HOMO (highest occupied molecular orbital) and LUMO (lowest unoccupied molecular orbital) are shown. Panel a: the metal surface and the organic layer are not yet in contact. The VL is the same at both sides of the system and Φ is the distance between VL and E_F. Panel b: the metal surface and the organic layer are put in contact. At the interface a potential step (bond dipole, BD) occurs due to Pauli pushback and adsorption induced charge rearrangements (the resulting dipole is indicated by the black arrow). The step lowers all the states lying above the dipole. The vacuum levels at the two sides of the system are now shifted. The new work function, Φ', is the distance between the new vacuum level VL$'$ and the E_F. Panel c: evolution of the energy levels for the hypothetic scenario of the organic layer containing an embedded dipole, indicated by the orange arrow. The dipole induces a further shift in the energy levels above it. The new work function Φ'' is the distance between the new vacuum level VL$''$ and E_F.
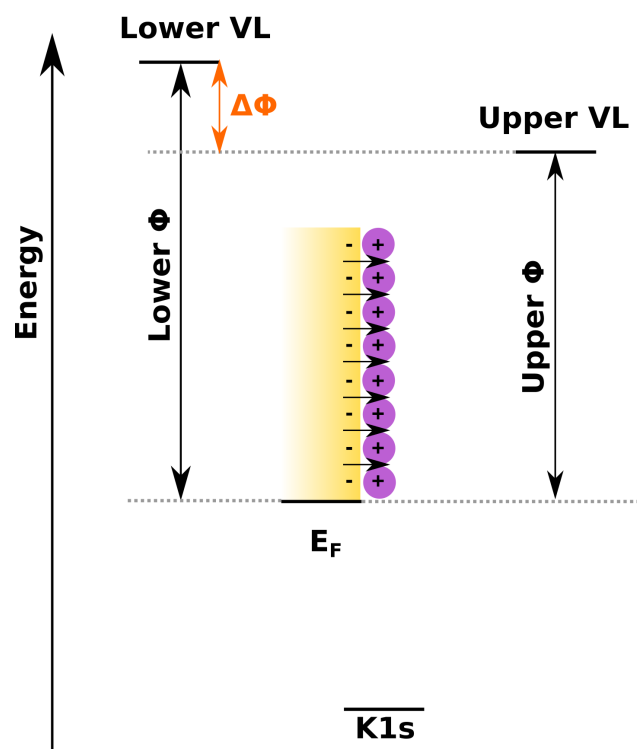
Figure 4.57: Relevant energy levels for the systems investigated in this work. The K/Au(111) is sketched in the middle. The lower vacuum level (lower VL) depicted on the left is the VL of the clean metal surface. With respect to the lower VL the work function of the clean surface is determined (lower Φ), as the distance between the lower VL and the Fermi energy of the metal E_F. The upper vacuum level is depicted on the right. It is shifted with respect to the lower VL due to the collective electrostatic effects caused by the deposition of the K atoms. The work function of the K covered surface (upper Φ) is determined as the difference between the upper VL and E_F. The shift between upper and lower Φ is $\Delta\Phi$, shown by the orange double arrow. Referencing the K1s core level binding energies to the upper VL allows accounting for chemical shifts only, since the dipoles responsible for the shift of the upper VL (depicted by the black arrows at the interface) are localised below the plane of the K atoms. Referencing the K1s core level binding energies to the E_F, as done in XPS experiments, both chemical and electrostatic effects are instead included.

The K1s core level energies, also indicated in the schematic, can be referenced either to the UVL or the E_F. E_F referenced binding energies are the quantities measured in an XPS experiment when dealing with conductive samples[137]. The E_F alignment framework is commonly applied also for SAM covered metals, since, being the films thin enough, their insulating nature can be disregarded[125]. Calculations allow instead obtaining both E_F and UVL referenced energies. This can be conveniently exploited for our analysis, under the assumption that the potential step at the interface occurs *below* the K atoms, while in reality it could extent somewhat further beyond the K plane. As consequence of this assumption, the K atoms are localised above the potential step and their binding energies are shifted with respect to the metal E_F but not with respect to the UVL, as discussed above. When comparing different coverages, referring the K1s energies to the UVL allows thus probing the chemical shifts. Comparing the full and reduced coverage K/Au(111) interfaces analysed in this work it is therefore possible to identify (i) chemical shifts of the K1s binding energies, by referring them to the UVL, (ii) energy shifts due to collective electrostatic effects, by comparing the different $\Delta\Phi$ at different coverages, and (iii) the impact of the superposition of (i) and (ii) on the K1s binding energies, by referring them to E_F. The condition for this to hold is that the K atoms have the same docking site and lie in the same plane, at both coverages. On one side, different docking positions would change the interaction between the adsorbed atoms and the substrate, thus impacting the chemical shifts. On the other side, the different electrostatic shifts between full and reduced coverage can be ascribed to the reduced K atoms density only if the latter have the same distance from the surface in both cases. For this reasons, it is crucial that the K atoms have the same the docking position at both coverages, as anticipated above. Performing such analysis on a system such as the C12 SAM considered in the experiments reported in reference 125 would also not be suitable. First, it would not be possible to calculate the chemical shift from the UVL aligned binding energies, since the UVL position could shift due to the presence of dipole layers above the investigated species. Second, also calculating the electrostatic shifts by taking the difference in the work function changes at the two coverages would not be correct for atoms at the very interface. This is because these latter are affected only by the potential step in the immediate vicinity of the surface, while the work function change includes also the contributions stemming from potential steps occurring above the considered atoms.

Results and discussion

$\Delta\Phi$ and K1s binding energies aligned to E_F at full and reduced coverage. We start our analysis by focusing on how the calculated $\Delta\Phi$ and K1s core level energy referenced to the E_F vary by modifying the K coverage. The data are reported in table 4.18.

The adsorption of the K atoms decreases the work function of the metal substrate, with the work function change $\Delta\Phi$ having therefore a negative sign. Reducing the density of K atoms the magnitude of $\Delta\Phi$ decreases from 3.22 to 1.09 eV. The electrostatic shift between full and 1/9 coverage amounts thus to 2.13 eV. Based on the diagram shown in figure 4.56, the electrostatic shift should equally affect the K1s core level binding energies, that would be expected to shift by 2.13 to lower values upon reducing the K coverage. As show in table 4.18 this is however not the case: the K1s energies are smaller in the reduced coverage case, but only by 0.17 eV, a small fraction of the overall electrostatic shift obtained from the difference in $\Delta\Phi$. Although surprising at a first glance, the result is qualitatively consistent with the experimental data reported in reference 125: in spite of the relevant $\Delta\Phi$ shifts upon K deposition, only a smaller shift is detected for the position of the K2p XPS signal.

Table 4.18: Calculated work function change $\Delta\Phi$ and E_F referenced K1s core level binding energies K1s$_{EF}$ for the K/Au(111) interface at full and 1/9 reduced coverage. Δ is the difference between the reduced and the full coverage case.

	$\Delta\Phi$ / eV	K1s$_{EF}$ / eV
Full coverage	-3.22	-3533.73
1/9 reduced coverage	-1.09	-3533.56
Δ (1/9 - full)	2.13	0.17

K1s binding energies referenced to the UVL at full and reduced coverage. In order to gain insight into the factors affecting the K binding energies at different coverages, the K1s binding energies referenced to the UVL were calculated. As discussed above, this allows identifying the chemical contribution to the energy shift. The values are reported in table 4.19.

The calculated K1s energies referenced to the UVL shift to larger values going from full to 1/9 coverage, with the magnitude of the shift amounting to about 2.1 eV. The chemical shift has essentially the same magnitude of the electrostatic one. The sign of the shifts is however opposite, resulting in an almost quantitative compensation of the two effects. This is the reason for the K1s energies referenced to E_F hardly showing any change when considering different K coverages, both in simulations and in experiments. Indeed, the small shift of the K1s energies referenced to E_F is about the sum of the electrostatic shift, calculated as difference of the $\Delta\Phi$ values at different coverages, and the chemical shift, defined as difference of the K1s energies referenced to the UVL. The small discrepancy is a consequence of the reduced computational settings needed to reduce the computational cost for the reduced coverage system.

Table 4.19: Calculated K1s core level binding energies referenced to the UVL K1s$_{UVL}$ for the K/Au(111) interface at full and 1/9 reduced coverage. Δ is the difference between the reduced and the full coverage case.

	K1s$_{UVL}$ / eV
Full coverage	-3535.58
1/9 reduced coverage	-3537.65
Δ (1/9 - full)	-2.07

Chemical effects - isolated K atom vs monolayer. To understand the origin of the relevant chemical shift between the full and the 1/9 coverage, first of all the differences in terms of binding energies between a hypothetic free standing monolayer (i.e. without the underlying substrate) of K atoms at different coverages were considered. In table 4.20 the K1s binding energies of a K atom in a free standing monolayer at full and 1/9 coverage are reported. As reference, the K1s energy of an isolated K atoms is also given.

According to the calculated values, there is almost no difference between the three considered case. The K atoms of the 1/9 reduced coverage monolayer have essentially the same 1s energy of an isolated K atom. Going from the reduced coverage situation to the full free standing monolayer, the energies shift by about 0.05 eV to smaller values. In the light of such negligible shifts, it becomes clear that the density of the K atoms cannot be responsible for the chemical shift of about 2 eV calculated above.

Table 4.20: Calculated VL aligned K1s core level binding energies K1s$_{VL}$ for an isolated K atom and hypothetic free-standing monolayers of K atoms at full and reduced coverages. The subscript VL is adopted since when dealing with symmetric slabs LVL=UVL.

	K1s$_{VL}$ / eV
Isolated K	−3537.29
Full coverage	−3537.21
1/9 reduced coverage	−3537.26

Chemical effects - charge transfer processes. The next step to clarify the chemical shift of the K1s energies was to focus on the interaction of the K atoms with the metal substrate at the different coverages. In the adopted model, the height of the K atom above the metal surface and its docking position are kept fixed in both coverages. Therefore, the only plausible difference between full and 1/9 coverage has to lie in different charge transfer processes between the metal surface and the adsorbed K atoms. To check the hypothesis, the partial charges sitting on the K atoms at full and reduced coverage were calculated within the Bader partitioning scheme[95]. The results are reported in table 4.21. In both cases the K atoms are positively charged, in the full coverage case by 0.59 |e$^-$| and in the 1/9 coverage case by 0.85 |e$^-$|. This confirms that indeed there are consistent differences in the charge carried by the K atoms at different coverages. From a qualitative point of view, a more positive partial charge leads to larger core level energies. In the 1/9 coverage situation the K atoms carry a more positive charge than in the full coverage case, shifting the K binding energies to larger values. Remembering that the electrostatic effects would shift the energy levels to *smaller* values at reduced coverage, as reported in table 4.18, the impact of the different partial charges sitting on the K atoms at different densities seems really to be the explanation for the observed compensation. For a more quantitative evaluation, the 1s core level binding energy of isolated K atoms charged by the partial charges they assume on the Au surface at the different coverages were calculated. The results are given in table 4.21.

Table 4.21: Calculated Bader partial charges δ_K on the K atoms at full and reduced coverages and K1s binding energies K1s(δ) calculated for an isolated K atom charged by the partial charge sitting on the K atoms on the Au(111) surface at the corresponding coverage. Δ is the difference between the reduced and the full coverage case.

	δ_K / |e$^-$|	K1s(δ) / eV
Full coverage	0.59	−3541.06
1/9 reduced coverage	0.85	−3542.81
Δ	0.26	−1.75

As expected, more positively charged K atoms have larger 1s core level energies. The binding energy difference between the two cases amounts to about 1.75 eV. Summed to the 0.05 eV calculated as chemical shift for the reduced and full coverage free-standing monolayer of K atoms described above, the shift almost fully matches the about 2 eV of chemical shift calculated in table 4.19. This fully confirms the proposed hypothesis of charge transfer processes impacting the core level energies of the K atoms. In the specifically considered case the chemical effects almost quantitatively compensate and mask core level energy shifts of electrostatic nature. The discussion can consistently be transferred to the cases mentioned in the introduction. For instance, considering the interfaces investigated in section 4.4 of this thesis, comparing full and reduced coverage calculations essentially no shift in the binding

energies of the S docking atoms and of the C atoms directly bonded to the S ones was observed. In the light of the results reported in this work, it is reasonable to assume that this is due to different charge transfer processes between the metal surface and the SAM at different coverages. For the docking groups the chemical shifts due to the charge transfer process again almost fully compensate the electrostatic shifts due to the reduced dipole density. For the C atoms bonded to the docking groups the compensation of the electrostatic shifts can be very likely attributed to the chemical effect of being bonded to an atom bearing a different partial charge.

Also the experimental observations made during the K deposition on the C12 SAM on the Au(111) surface[125] can be analogously rationalised, although in that case the situation might be even more involved. First, the deposited K atoms are supposed to be placed more or less in the same plane as the S docking atoms, therefore the electrostatic shift induced by the K atoms affect the docking moieties only to a minor extent. Moreover, the presence of the K atom modifies the chemical environment of the S ones, modifying thus also their core level energies. Last, the K atoms on the surface could very likely have an impact on the charge distribution between the metal substrate and the docking group. As discussed above, this can be responsible of quantitatively relevant chemical shifts. Regarding the K atoms, the reason why the shifts in K2p binding energies are not correlated with the change in work function is the compensation of electrostatic and chemical shifts, as demonstrated in this work. At this stage the question arises, if the almost full compensation of chemical and electrostatic shifts found for the specific interface considered in this work is a coincidence or has general validity. Under different circumstances, like for instance different coverages or presence of other species, one of the two effects might prevail, as it seems indeed to be the case for the experimental K binding energies measured in reference 125.

Understanding the interplay of chemical and electrostatic shifts is not only important for the correct interpretation of XP spectra, but is also essential to clarify the energy level alignment at such metal/SAM interfaces. As mentioned in the introduction, in reference 125 a different aligning scheme for the docking atoms and for the backbone is proposed, to elucidate the evolution of the binding energies of the different species. Our calculations instead demonstrate that the explanation is to be found in competing electrostatic and chemical effects.

Chemical effects - K1s energies at different K heights. After having presented a model to rationalise the calculated and measured core level binding energies shifts for atoms close to the metal surface, we last discuss the comparison between the K1s energies referenced to the UVL of the full coverage K/Au(111) interface and the K1s energies of the full coverage free standing monolayer of K atoms. According to the values reported in tables 4.18 and 4.20, upon adsorption on the metal substrate the K1s energies get by 1.65 eV smaller. Considering that on the adsorbed K atoms a positive partial charge of 0.59 was calculated, the shift of the K1s energies to smaller values seems somewhat counterintuitive. To better understand this finding, the K atoms were progressively moved further from the metal surface and at each distance the UVL aligned K1s energies were calculated. How the latter depend on the distance is plotted in figure 4.58.

Two distinct regions can be identified in the plotted data. For distances larger than about 2 Å from the equilibrium position, the K1s energies are essentially constant and tend to the K1s value of the free standing monolayer of K atoms. For distances smaller than 2 Å, the energies become smaller in absolute value and reach the value of the equilibrium position. Clearly, the shift to smaller values of the K1s energies is a consequence of the chemical interaction of the K atoms with the surface, that becomes significant at about 2 Å above the equilibrium position. The decrease of 1.65 eV is actually the superposition of
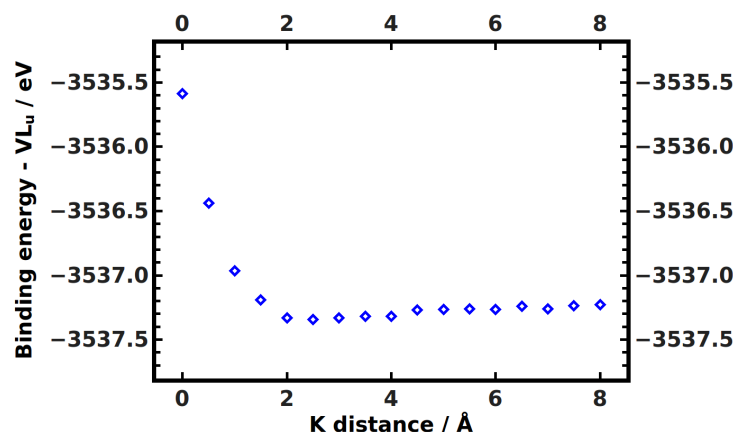
Figure 4.58: K1s core level binding energies referenced to the UVL plotted as a function of the distance of the K atom from the metal surface in the full coverage situation. 0 corresponds to the equilibrium position.

two chemical effects. On one side the positive charge on the K atoms should cause the shift of the core level energies to larger values. On the other side, the interaction with the metal substrate is responsible for a shift in the opposite direction whose magnitude is then by 1.65 eV larger than the chemical shift due to the K positive partial charge.

Conclusion

In this work DFT simulations have been applied to the investigation of the impact of chemical and electrostatic shifts on the core level binding energies of atoms adsorbed on metal surfaces. By means of a model K/Au(111) interface at different K coverages it was possible to separate the impact of chemical and electrostatic effects onto the K core level energies. The outcome of the calculations demonstrates that both effects relevantly affect the binding energies of atoms close to the metal surface. However, since the electrostatic and the chemical shift have opposite signs, the two effects compete and, for the specific case considered in this work, compensate. This allowed showing how the interplay of chemistry and electrostatics can lead to non trivial effects on the core level energies of atoms adsorbed on metal surfaces. The result was conceptually transferred to rationalise the observations made for more complex systems. Moreover, the investigation carried out in this work confirmed the advantage of using simulations to support the correct analysis of experimental data.

TOC
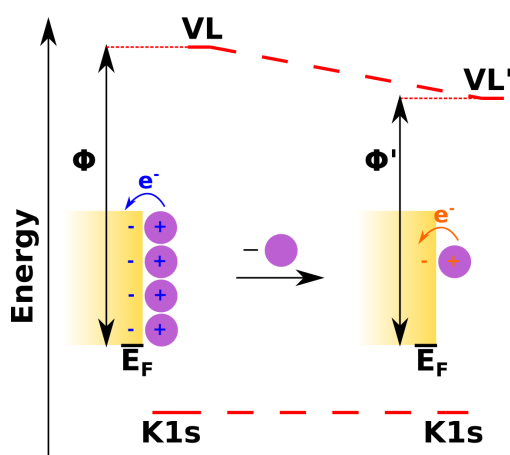
4.8 Electrostatically designed metal-organic frameworks for organic electronics applications

Throughout this whole work the possibility of modifying the work function of metal substrates via the deposition of polar self-assembled monolayers (SAMs) has been extensively discussed. As already explained, such a modification is due to so called collective electrostatic effects, that occur every time a two-dimensional periodic arrangement of dipolar units is present: the superposition of the fields of the dipoles causes an abrupt step in the electrostatic potential energy between the two sides of the dipole sheet.

The presence of many studies regarding the impact of such electrostatic effects for metal/SAM interfaces provides a detailed insight into their nature, suggesting effective ways to introduce polar units in the SAMs. They can for instance be embedded in the molecular backbone, as discussed in section 4.2. This allows obtaining the desired work function modification without modifying the chemistry of the upper part of the SAM, therefore without impacting the growth of the materials subsequently deposited on the SAM modified substrate. This is of fundamental importance for example when dealing with organic (opto)-electronic devices, where the atomistic arrangement at metal/organic semiconductor (OSC) interfaces influences properties such as the growth of the OSC and the carrier injection/extraction processes, thus crucially determining the performance of the device. In other cases, the dipolar moieties can be more conveniently attached as tail groups, for example to achieve large work function modifications beyond pinning effects, as explained in reference 122 and in section 4.3.

While for such metal/SAM interfaces collective electrostatic effects are very widely exploited, as the aforementioned examples testify, for other materials they are still largely unexplored. In this sense, recently a novel design strategy, referred to as electrostatic design, has been developed and applied to various systems, from graphene[138] to 2D materials[139] to covalent organic frameworks (COFs)[140]. The approach exploits collective electrostatic effects[23–25] to advantageously manipulate the electrostatic potential of the considered materials.

In this section, this original strategy is exploited to design metal-organic frameworks (MOFs) with innovative electronic properties. As already mentioned in the introduction, MOFs are a class of porous extended hybrid organic/inorganic materials consisting of metal containing nodes, referred to as secondary building units (SBUs), linked by organic ligands[40]. Thanks to the possibility to vary both the SBUs and the organic linkers in order to modify the dimension of the pores or to introduce suitable chemical functionalities, MOFs are highly versatile materials, commonly applied for gas storage, separation and sensing[42,43].

Here we propose a way to further widen the application of these materials: employing density functional theory (DFT) simulations, combined with periodic boundary conditions and the repeated slab approach, we design and characterise SURMOFs (*surface grown, crystalline metal-organic framework multilayers*[49]), whose properties are determined by the above described collective electrostatic effects via the introduction of a suitably chosen dipolar apical linker. The idea was conceived by Professor Christof Wöll from the Karlsruhe Institute of Technology, who also provided a starting structure for the investigated system (see following sections).

The stability of the system, the evolution of the HOMO-LUMO gap and the work function change upon introducing more layers of polar linkers are examined. Two fundamental effects are observed. First, the band gap between the HOMO and the LUMO, that are localised on opposite ends of the system, drops, tending to vanish for a certain number of layers of dipolar linkers. Second, the work function change between the two sides of the film increases

and then saturates. Both the drop of the band gap and the work function change increase before the saturation depend linearly on the number of polar units. The presence of the polar layers leads to a gradient in the electrostatic potential between the two sides of the system, that could be conveniently applied in organic electronic devices such as, for instance, organic solar cells.

The computational characterisation carried out in this work represents the starting point for the experimental synthesis of the new materials, ideally by means of the aforementioned LPE technique.

4.8.1   Investigated system

The model system we chose for our simulations consists of di-zinc SBUs connected in the x,y plane by terephthalic units and in the z direction by 3,5-difluoro-4,4'-bypiridine molecules, as shown in figure 4.59.

The structure depicted contains one layer of polar apical linkers and is, therefore, referred to as 1 layer system. The upper and lowermost pyridine rings are inserted in order to electronically saturate the upper and lowermost Zn atoms. The dimensions of the unit cell in the x and y directions are optimised (see below), while in the z direction the dimension is chosen in order to include a vacuum region of at least 20 Å between two consecutive slabs.

Analogously, systems with increasing number of polar layers were set up, alternating the in plane and the polar apical components and coordinating the two end Zn atoms with pyridine units. It was possible to add up to 7 layers of polar linkers, since for larger systems serious self-consistency cycle convergence problems were encountered.

Details of the starting geometry

The starting structure was derived from the bulk structure of a symmetric MOF (depicted in 4.60), provided by the group of professor Wöll and consisting of di zinc complexes connected in plane by terephthalic acid units and between the planes by 4,4'-bypiridine linkers.

First, both the atomic positions and the unit cell parameters of the bulk structure were optimised. While the starting unit cell was monoclinic, the full geometry optimisation shown that a unit cell with mutually orthogonal edges (tetragonal) was energetically more favourable. All the subsequent calculations were performed keeping the angles between the unit cell edges fixed. The H atoms in position 3 and 5 in the bipyridine system were then replaced with F and the resulting structure was relaxed optimising both atomic positions and unit cell dimensions. From the optimised bulk structure the slab with 1 layer of polar elements was set up, saturating the terminal Zn atoms with 2 pyridine rings. The unit cell dimensions in the x and y directions were set to the values obtained for the bulk while in the z direction a vacuum region of 20 Å was inserted between two consecutive slabs to prevent their spatial interaction. To decouple the slabs also electrostatically a self consistently calculated dipole correction was included in all the calculations. Atomic positions and unit cell edges in the x and y directions were optimised. Since the latter were found not to change upon optimisation, in all subsequent calculations they were constrained. The slabs with larger numbers of polar layers were obtained extending the optimised structures and reoptimising the atomic positions (as illustrative example the geometry with 2 polar layers is shown in figure 4.61).

Up to the 3 layers system full geometry optimisations of all atomic positions were performed. Since no significant differences in the properties of the slabs before and after geometry optimisation were observed, for the systems with a larger number of polar layers only single point calculations were performed. To set up the geometry for the p-i-n junction (see corresponding section) the non polar component with two layers of symmetric apical linkers
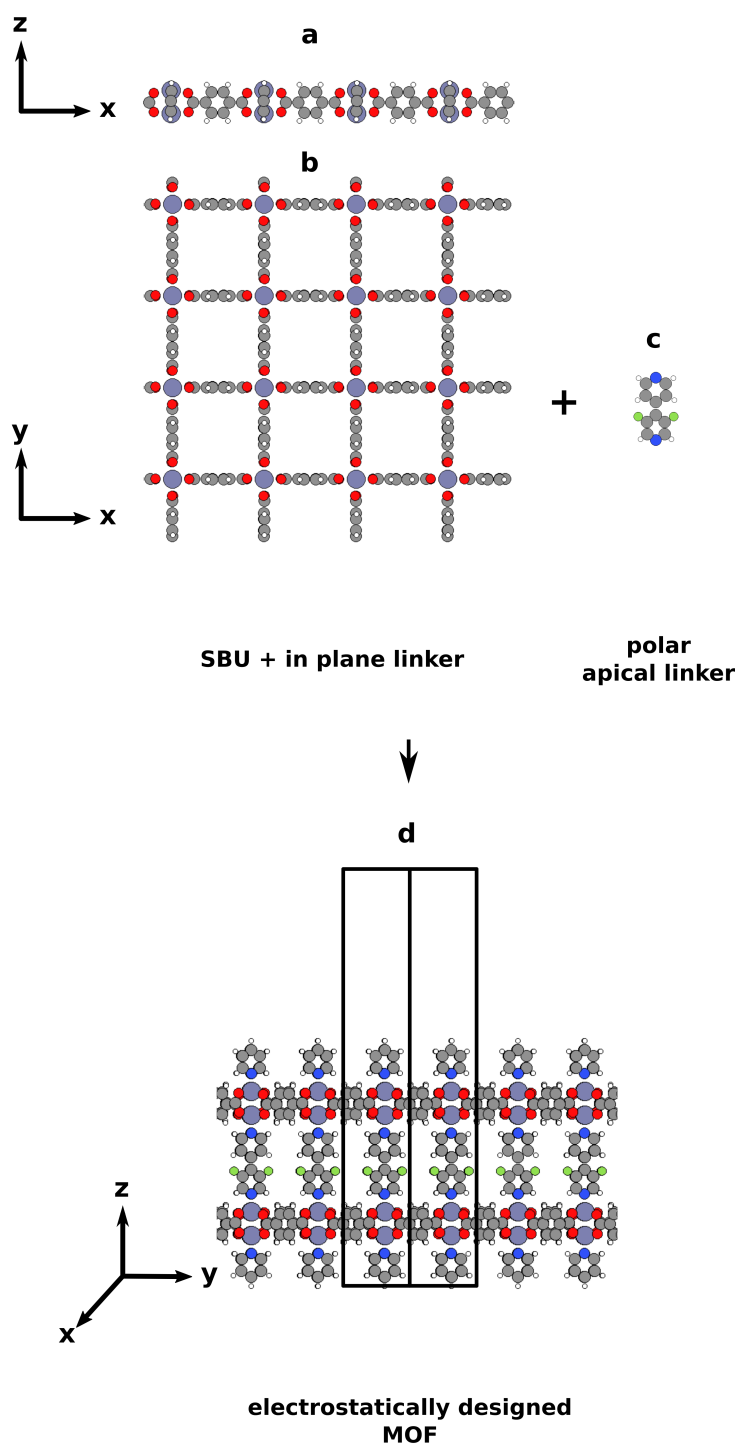
Figure 4.59: Structure of the MOF investigated in this work. a and b show two different views of the Zn containing secondary building units (SBU) connected by the in plane linkers. c shows the dipolar apical linker. d shows the final combined system, whose topmost and bottom Zn atoms have been electronically saturated with pyridine units (see text for further details). C atoms are depicted in grey, H in white, N in blue, O in red, F in green and Zn in light blue. The black line encloses the unit cell used in the calculations. The x and y dimensions are optimised, while in the z direction a vacuum region of at least 20 Å is included (further computational details in the corresponding section).

was separately optimised, relaxing the atomic positions and keeping the unit cell parameters fixed. Combining the individual subsystems the 8 layers structure was built. On the final system only a single point calculation was performed.
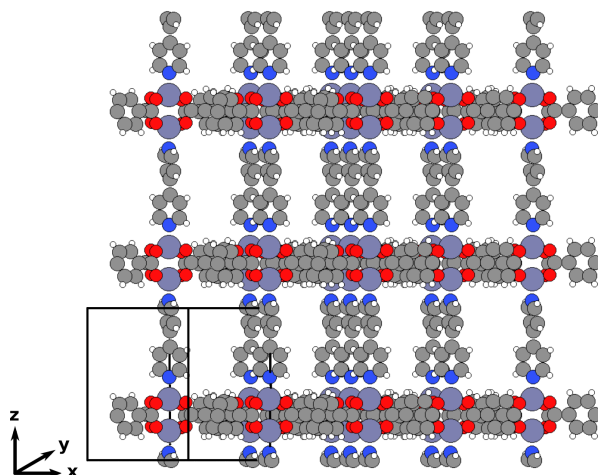
Figure 4.60: Bulk structure of the starting symmetric MOF. C atoms are depicted in grey, H in white, N in blue, O in red and Zn in light blue. The unit cell is enclosed by the black line.
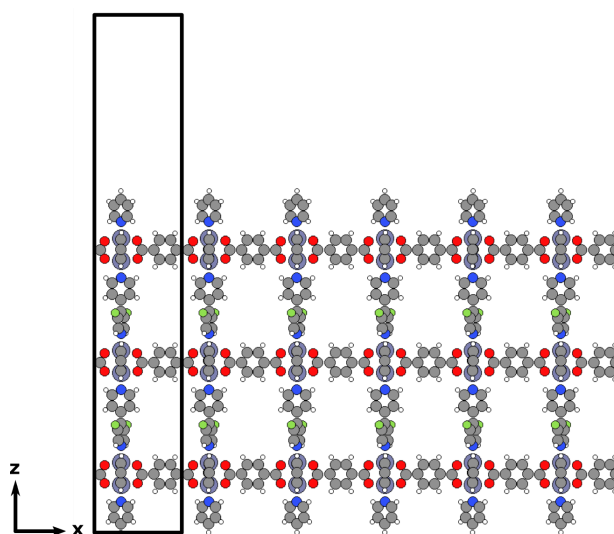
Figure 4.61: SURMOF investigated in this work containing two polar layers. C atoms are depicted in grey, H in white, N in blue, O in red and Zn in light blue. The unit cell is enclosed by the black line.

4.8.2 Computational methods

All the calculations have been performed using the FHI-aims code[26] applying periodic boundary conditions and the repeated slab approach. Bulk calculations and slab ones have been performed using $6 \times 6 \times 4$ and $4 \times 4 \times 1$ k-points grids, respectively. The grid sizes have been fixed after convergence tests that shown there were no relevant differences in the results obtained using a larger number of k-points. For PBE[27] calculations the FHI-aims default light settings, tier 2, have been used for every atom. Convergence criteria for the self-consistency cycle based on the charge density, on the total energy and on the forces have been set to the default values. The geometry optimisations have been performed using the

trust radius method enhanced version of the Broyden-Fletcher-Goldfarb-Shanno optimisation algorithm[26], with a tolerance threshold of 10^{-2} eV·Å^{-1}. To determine the occupation of the Kohn-Sham eigenstates a Gaussian broadening function with a width of 0.01 eV (default value) has been used. For the system with 7 layers of polar linkers the value had to be increased to 0.02 for the self-consistency cycle to converge. Using 0.01 or 0.02 was observed not to cause any difference for the other systems. As the studied system contains Zn atoms, to account for the relativistic effects the atomic ZORA approximation has been used[141]. DOS and PDOS plots have been obtained using a Gaussian broadening function with the same width used to determine the occupation of the Kohn-Sham eigenstates. The DOS projected onto a particular region has been obtained summing up the DOS projected on each atom belonging to that region. In all the calculations the band gap (Kohn-Sham gap) has been obtained as the energy difference between the lowest unoccupied and the highest occupied states. Even if the Kohn-Sham gap corresponds neither to the fundamental nor to the excitation gap, its value can be considered as a guideline to link the system properties with the real gap. Work function differences have been obtained from the difference between the work function value for the upper slab surface and the value for the lower one. The plots of the localisation of the frontier states and of the electrostatic potential energy in the x,z plane have been obtained using XCRYSDEN[142].

4.8.3 Band gap and work function change evolution

In table 4.22 the band gap (Kohn-Sham gap, see previous section) of all the calculated structures, i.e. from 1 up to 7 layers of polar linkers, is reported. From the 1st up to the 6th layer, increasing the size of the system the band gap decreases linearly: starting from a value of 1.60 eV for the 1st layer, it decreases by about 0.26 eV at each step. The linear evolution of the gap with the number of layers n shows that the system is not an extended conjugated one, for which the gap would have been proportional to $\frac{1}{n}$. Instead, the linear behaviour is due to the addition of further dipole units, that shift the energies of the frontier orbitals localised at opposite terminal layers by the same amount at each step, as it will be discussed in the following section. At the 7th layer the gap tends to vanish: it still drops, but not linearly anymore, decreasing only by 0.19 eV and reaching the value of 0.08 eV. The band gap closure is the reason for the aforementioned convergence problems. Note that considering the fundamental underestimation of the band gap by the employed PBE[27] functional (see computational details), and GGA functionals in general, we expect the true band-closure to happen only for thicker systems.

Table 4.22: Band gap and work function change for up to seven layers of polar linkers. Band gap diff.: difference between the band gap of the corresponding system and the band gap of the system with one fewer polar layer. $\Delta\Phi$: work function change. $\Delta\Phi$ diff: difference between $\Delta\Phi$ of the corresponding system and $\Delta\Phi$ of the system with one fewer polar layer.

N. of polar layers	Band gap / eV	Band gap diff. / eV	$\Delta\Phi$ / eV	$\Delta\Phi$ diff. / eV
1	1.60		0.28	
2	1.33	-0.27	0.54	0.26
3	1.07	-0.26	0.80	0.26
4	0.80	-0.27	1.07	0.27
5	0.53	-0.27	1.34	0.26
6	0.27	-0.26	1.62	0.26
7	0.08	-0.19	1.79	0.17

The work function change $\Delta\Phi$, defined as the difference between the vacuum potentials on the two sides of the hypothetical free-standing MOF, displays a similar behaviour: starting from +0.28 eV for the 1st layer, the value increases by about 0.26 eV for each additional layer, up to the 6th layer. At the 7th layer, with a smaller increase of 0.17 eV, $\Delta\Phi$ approaches the value of 1.79 eV. The band gap and work function change evolutions are shown in figures 4.62 and 4.63.
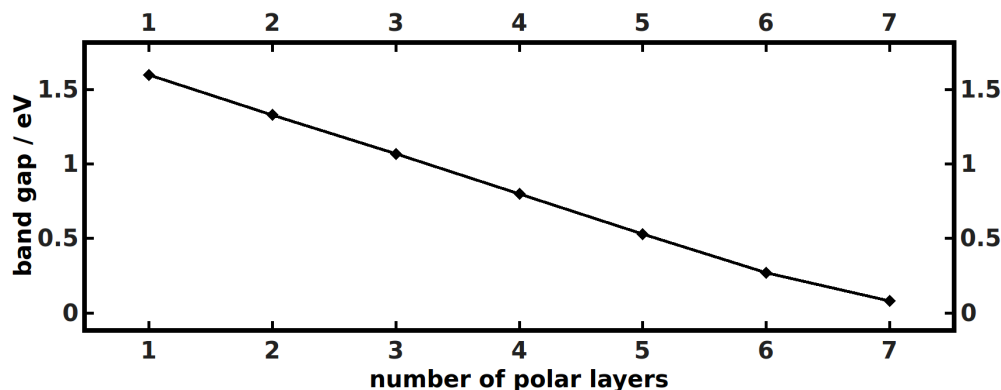
Figure 4.62: Evolution of the calculated band gap increasing the number of layers of polar apical linkers.
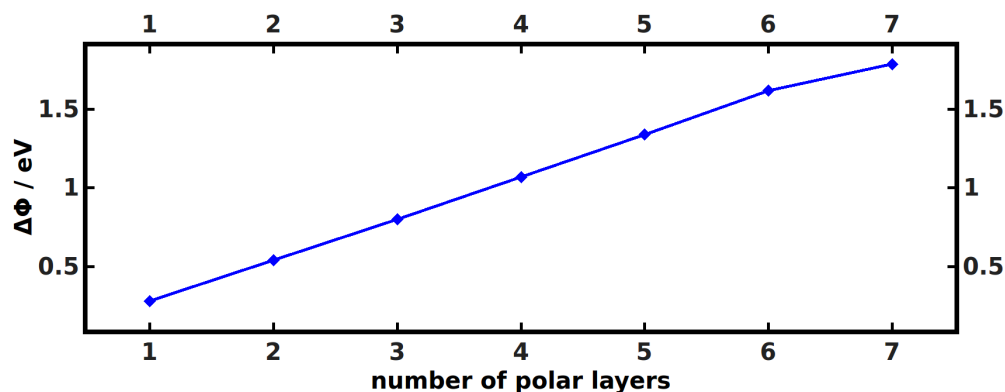
Figure 4.63: Evolution of the calculated work function change $\Delta\Phi$ increasing the number of layers of polar apical linkers.

To understand the evolution of the electronic structure of the system upon the introduction of the polar layers, it is useful to have a look at the density of states (DOS) projected onto different molecular regions. In figure 4.64 the global DOS and the DOS projected onto the regions where the frontier orbitals are localised are shown for the system with seven layers, to emphasise the band gap closure and the localisation of the frontier orbitals on the opposite ends of the system. As shown in the picture, the highest occupied molecular orbital (HOMO) is localised on the uppermost SBU-in plane ligand complex, whereas the lowest unoccupied molecular orbital (LUMO) is localised on the lowermost difluorobipyridine unit.

The overall effect of the polar units on the electronic structure of the system is shown in figures 4.65 and 4.66. In figure 4.65 the DOS projected (PDOS) on the SBU-in plane ligand complexes of the 7 layers structure is depicted: at each complex the PDOS shifts rigidly up in energy, due to the collective electrostatic interaction of the dipolar units placed in between. This progressive shift is what leads to the band gap closure. Looking at the complexes, for each of them the "local" gap between the highest occupied PDOS peaks and the lowest unoccupied ones has the same size. The particular local and global band gap evolutions
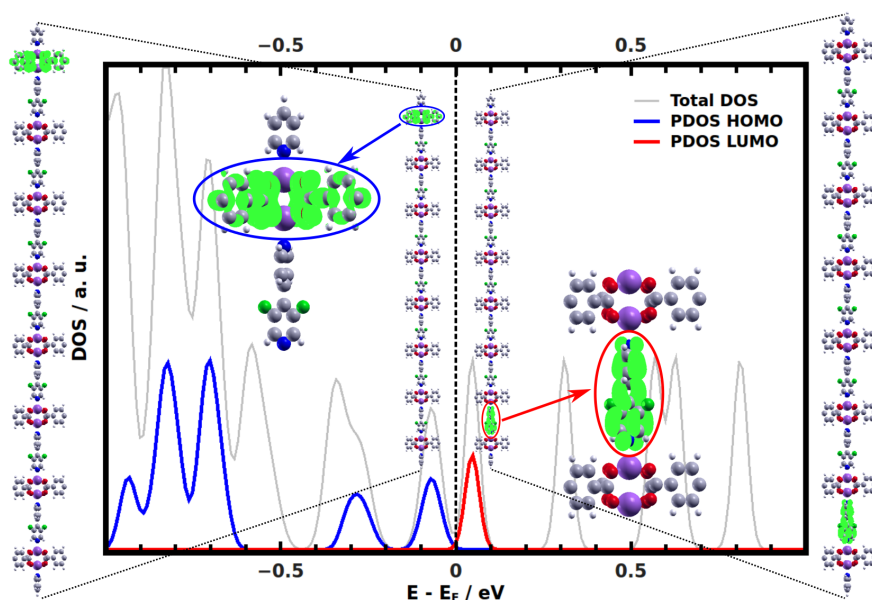
Figure 4.64: Total density of states (Total DOS, grey line), DOS projected onto the molecular region where the HOMO is localised (PDOS HOMO, blue line) and DOS projected onto the molecular region where the LUMO is localised (PDOS LUMO, red line). All the energies are aligned to the Fermi energy (dashed black vertical line). The charge densities associated with the HOMO and the LUMO are depicted and enlarged to improve the visibility.

are another consequence of the collective electrostatic effects induced by the dipolar linkers. A similar behaviour is observed for the DOS projected onto the difluorobipyridine units, plotted in figure 4.66: also in this case, by the addition of more layers, the local gap keeps the same size, whereas, as already pointed out, the global one decreases and tends to vanish, similar to what has been observed for a SAM made up of pyrimidines on the Au(111) surface investigated in reference 143.
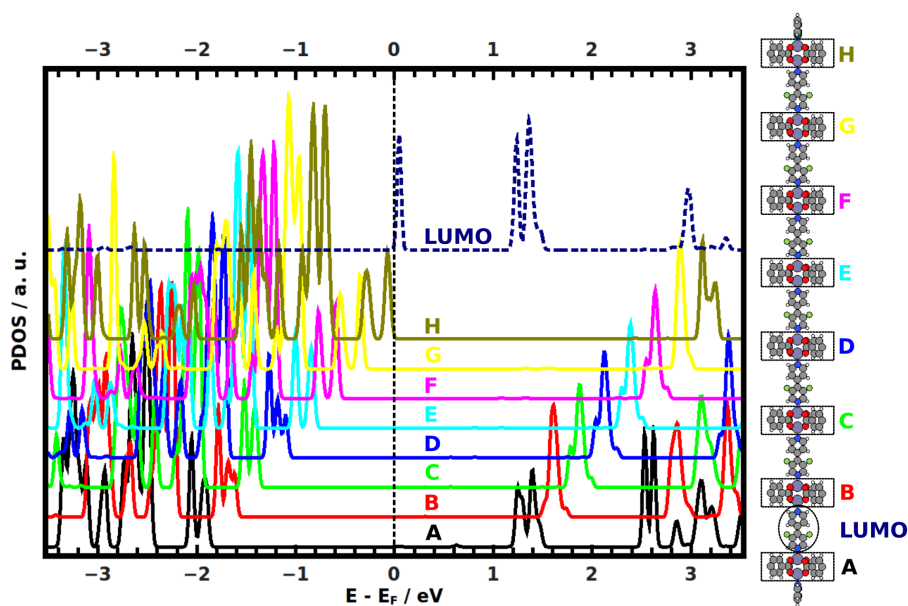
Figure 4.65: Density of states projected onto the metal-in plane ligand complexes (uppercase letters) and onto the molecular region where the LUMO is localised (LUMO, uppermost dashed plot). On the left the 7 layers system is depicted, to indicate the different molecular regions which the plots refer to. The energies are aligned to the Fermi Energy, highlighted in the picture with the vertical dashed line. The PDOS values have been offset to improve the readability.

180
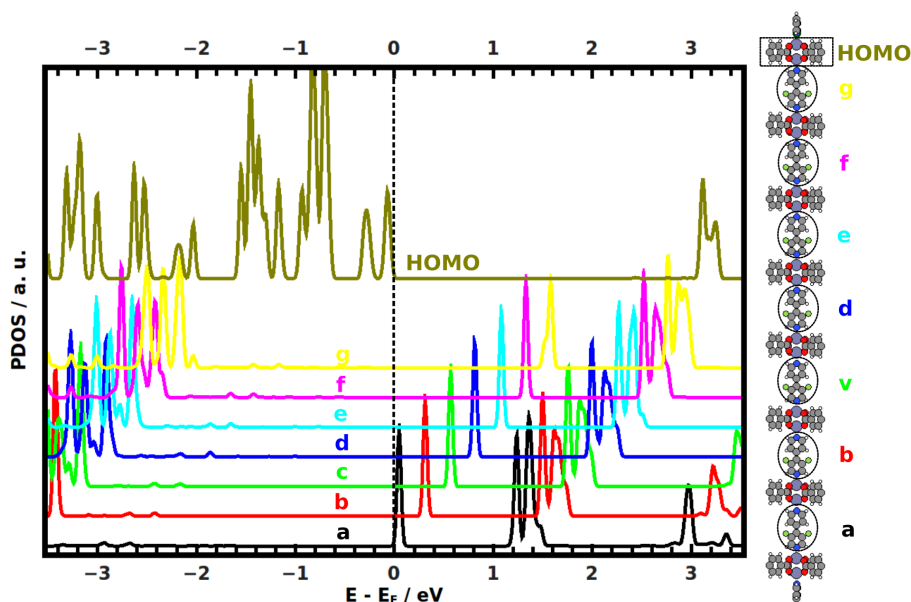
Figure 4.66: Density of states projected onto the difluorobipyridine units (lowercase letters) and onto the molecular region where the HOMO is localised (HOMO, uppermost dashed plot). On the left the 7 layers system is depicted, to indicate the different molecular regions which the plots refer to. The energies are aligned to the Fermi Energy, highlighted in the picture with the vertical dashed line. The PDOS values have been offset to improve the readability.

4.8.4 Electrostatic potential energy

A further result of the presence of the dipoles intimately interconnected with the above-discussed observations is the presence of an electrostatic potential energy gradient between the opposite ends of the system. This effect is shown in figure 4.67, where the electrostatic potential energy of an electron in the x,z plane is depicted, and figure 4.68, where the x,y plane averaged electrostatic potential energy along the z direction is plotted. Both pictures show the increase of the electrostatic potential energy going from the left to the right end of the molecule: it can be clearly concluded that the difference between the right and the left vacuum levels depends on the number of layers of the system.

| ■ -2.1 eV | ■ -1.2 eV | ☐ -0.3 eV | ■ +0.6 eV | ■ -1.5 eV |
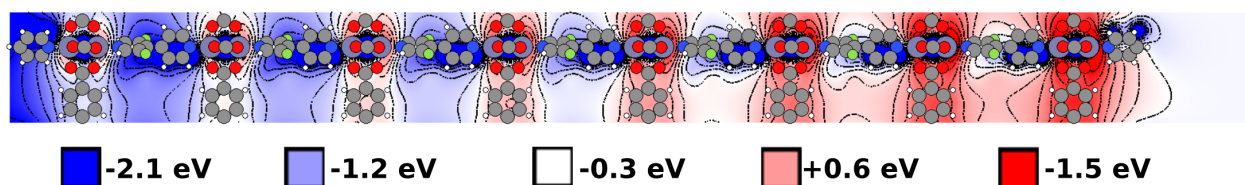
Figure 4.67: Electrostatic potential energy of an electron in the x,z plane. An energy interval of 5.6 eV is considered and isolines are drawn every 0.3 eV. Note that the plane is chosen such that it contains the O atoms of the terephthalic in plane linker.

The electrostatic potential energy gradient can also be be visualised in terms of change in the core level binding energies (see, for instance reference 19). The latter can often be comparably easily obtained from XPS and could be used as an experimental tool for mapping such electrostatic shifts, at least as long as the screening effects from the substrate on which the SURMOF is grown do not blur the results. Indeed, compared to UPS, the advantage of using core level energies would be to deal with strongly localised initial states. By way of example, the Zn 2s core level binding energies have been calculated. The results are reported in table 4.23. Please note that the calculated Kohn-Sham energies would have to be shifted
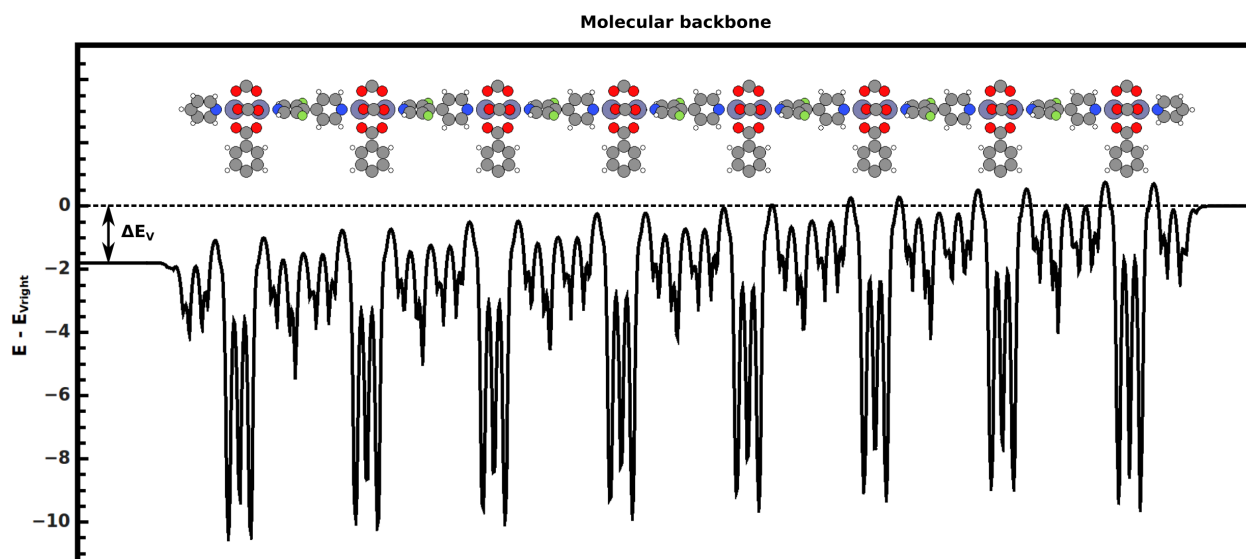
Figure 4.68: Plane averaged electrostatic potential energy of an electron along the z axis. The energy is aligned to the right vacuum level. The energy difference ΔE_V between the two ends is shown by the arrow.

Table 4.23: Zn 2s core level binding energies. Capital letters in the first column refer to the different dimetallic units (see figure 4.65). The energies are aligned to the Fermi energy. As in every unit the energies of the two Zn atoms is very close, with differences smaller than 0.035 eV, the averaged value of each unit has been reported.

Dimetallic unit	Zn 1s binding energy / eV
A	−1156.10
B	−1155.85
C	−1155.60
D	−1155.34
E	−1155.07
F	−1154.82
G	−1154.58
H	−1154.29

to be aligned to the experimental values. The calculated relative shifts are however typically reliable[19,113]. Between every dimetallic unit a shift of about 0.25 eV is predicted, that is in good agreement with the electrostatic potential energy gradient plotted in the previous pictures and the work function change evolution reported above.

4.8.5 Bond energies between Zn and N

As mentioned in the introduction, the envisioned method for the eventual experimental synthesis is the LPE technique, due to the generally good quality of the SURMOFs grown using this method. It would then be convenient if the Zn–N bond energy depended on the different orientation of the dipole, as illustrated in figure 4.69. Indeed, if there were a relevant difference in binding energies, one particular dipole orientation would noticeably be more favourable. A further relevant aspect to be considered is the interaction of the individual dipoles with the (anti)parallel ones within the layers and with those in adjacent layers lying above and below the considered one. If the parallel orientation within the layer turned

182

Figure 4.69: Monomeric units consisting of a dimetallic Zn complex and a 3,5-difluoro-4,4'-bipyridine unit. The different orientations of the dipolar units are shown by the arrows, "up" in panel a and "down" in panel b. "Up" and "down" refer to the orientation of the dipole moment associated with the substituted pyridine ring (the direction is determined considering the dipole pointing from the negative side towards the positive one). C atoms are depicted in grey, H in white, O in red, N in blue, Zn in light blue and F in green.

out to be unfavourable due to repulsive interactions, it could be difficult to grow a layer of asymmetric bipyridine units with dipoles oriented in the same direction. On the other hand, if the interaction of one dipole unit with the above and below ones were favourable due to attractive effects, this would make it easier to grow further layers of linkers with dipoles pointing in the same direction.
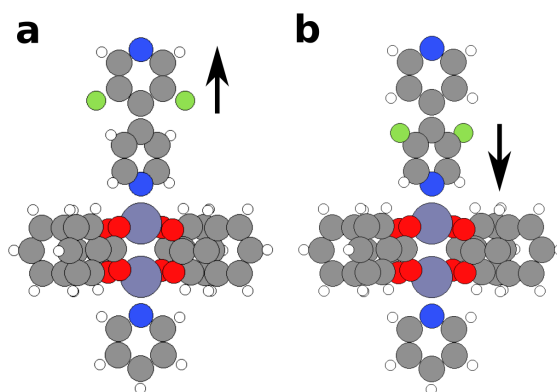
Monomeric unit - 1 dipole unit

First, to check the bond energy between the di-zinc complex and the bipyridine linker, the monomeric units depicted in 4.69 have been considered. The bond energy has been calculated as follows:

$$E_{bond} = -E_{monomer} + E_{linker} + E_{complex}, \qquad (4.7)$$

where $E_{monomer}$ is the energy of the combined system consisting of the di-zinc complex and the difluorobipyridine unit, E_{linker} is the energy of the optimised 3,5-difluorobipyridine unit and $E_{complex}$ is the energy of the optimised dimetallic complex. The difference between the bond energies is about 70 meV, with the system named "up" being slightly more stable.

Monolayer of dipole units

To check whether the interactions between neighbouring dipole units play a role, slab calculations have been performed on the three systems depicted in figure 4.70. In the "up" and "down" configurations, the dipole units are parallel, instead in the "checkerboard" system the orientation of the dipoles is alternate. Considering the results obtained in the previous section, a small difference was expected comparing the "up" and "down" structure, whereas the "checkerboard" structure was supposed to be the most stable one, due to the favourable attractive interaction between the antiparallel dipole units. The Zn–N bond energies are compared in table 4.24: contrary to the expectation, the "checkerboard" structure is not the most stable one. Indeed, the bond energy of this structure has exactly the average value between the ones calculated for the "up" and "down" configurations. This result is to be attributed to the distance between the dipoles in the plane, about 11 Å. To verify that assumption, we compared the quantum-mechanical results to the expectations from a simple classical model: the interaction energy U between two parallel dipoles is given by

$$U = \frac{\frac{1}{4\pi\epsilon_0}\mu^2}{r^3}, \tag{4.8}$$

where μ is the dipole moment in SI units and r is the distance between the dipoles in SI units. In our case, with $\mu = 0.76\,\mathrm{D} = 2.54 * 10^{-30}\,\mathrm{C \cdot m}$ and $r = 11 * 10^{10}$ m, we get $U = 0.361$ meV, which means that the interaction between the dipoles is very weak. Considering then an infinite periodic 2-D array of dipoles with moment μ in a quadratic arrangement, the mutual potential energy per dipole U' can be evaluated according to reference 144 as follows: $U' = 4.5168 * U$, which in our case gives $U' = 1.63$ meV. While the order of magnitude of the effect is the same obtained in the simulations (about 70 meV), the observation that the net effect in the simulations is larger is most likely a consequence of the larger dipole moments due to an asymmetry in the Zn-N bond dipoles. Overall, as a consequence of the large inter-dipole distance, already for the comparably short linkers considered in the present systems, the electrostatic repulsion/attraction is too weak to affect the formation of the dipolar layers.
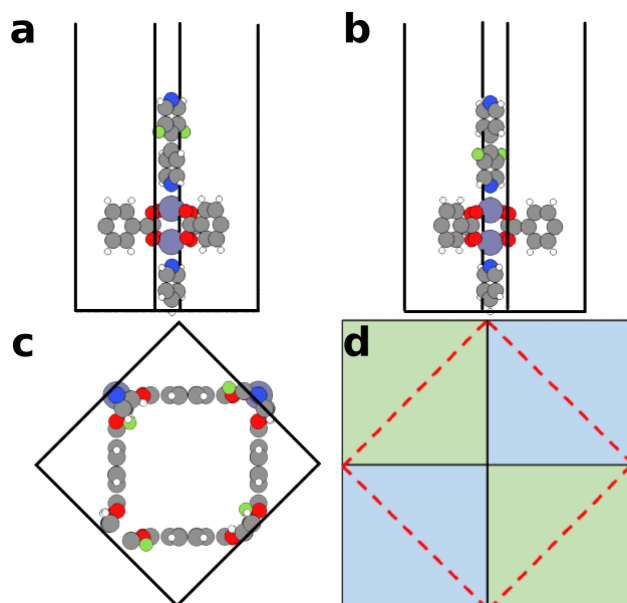
Figure 4.70: Systems used for slab type calculations to investigate the interactions between adjacent dipole units. In panels a and b the "up" and "down" systems are depicted, respectively. In panel c a top view of the unit cell used for the "checkerboard" system is shown. Such a unit cell contains two molecules and is set up as sketched in panel d, where green and blue colours mean the checkerboard arrangement of the dipoles and the red dashed line defines the unit cell. C atoms are depicted in grey, H in white, O in red, N in blue, Zn in light blue and F in green. The black lines enclose the unit cells.

Table 4.24: Comparison between the Zn–N bond energies of the "up", "down" and "checkerboard" slab systems.

	Zn–N bond energy / meV	Difference / meV
up	1108	
down	1048	-60
chequerboard	1082	

Monomeric unit - 2 dipole units

The interactions of the dipole units with the ones above and below have been investigated, too, considering the structures depicted in figure 4.71. The bond energies have been compared to check, whether the structure with the dipoles pointing in the same direction is energetically more favourable than the one with the dipoles pointing in opposite directions. The comparison of the results is reported in table 4.25: the difference between the 2 structure turns out to be again comparably small, and has essentially the same absolute value we found before, when we compared the monomeric units with one dipole. This leads us to conclude that the dipole units within a layer do not experience any significant repulsive or attractive interaction due to the dipoles of the above and below layers. This can be explained considering the comparably large distances between the dipoles.

For a periodic structure the effect is expected to be even weaker. The reason is that for a rectangular, infinite and periodic two-dimensional array of dipoles the maximum decay length of the electric field l turns out to be $l = max(\frac{a}{2\pi}, \frac{b}{2\pi})$, where a and b are the dimensions of the unit cell[24]. In our case $a = b \approx 11$ Å and then $l_{max} = 1.75$ Å, whereas the distance between the two dipoles separated by the zinc complex is about 14Å.
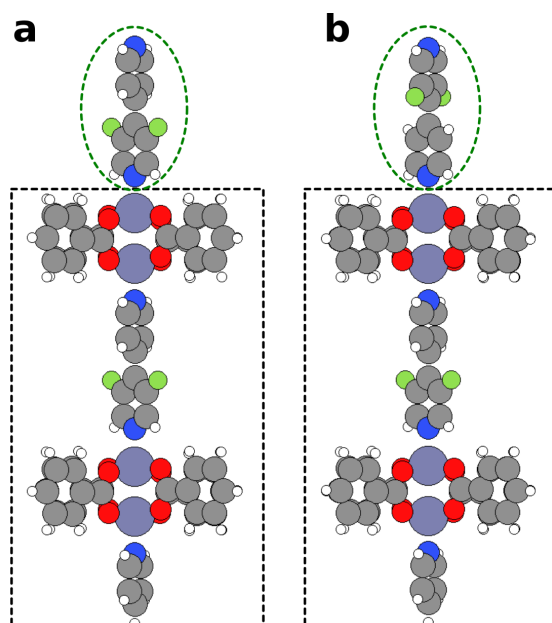
Figure 4.71: Monomeric systems with 2 dipole units. a: dipole units pointing in the same direction. b: dipole units pointing in the opposite direction. C atoms are depicted in grey, H in white, O in red, N in blue, Zn in light blue and F in green. The dashed rectangles and ovals enclose the fragments used to evaluate the Zn-N bond energy.

Table 4.25: Comparison between the Zn–N bond energies for a system consisting of two dipole units pointing in the same and in the opposite direction. The fragments considered to evaluate the bond energies are enclosed by a dashed rectangle and a dashed oval in figure 4.71.

	Zn–N bond energy / meV	Difference / meV
same direction	1022	
opposite direction	1090	68

4.8.6 Alternative linkers

Having seen that using the difluorobipyridine units the difference between the bond energies of the "up" and "down" configurations is potentially too small to induce a noticeable asymmetry in the system, some different linkers have been considered, namely 4-s-triazinil-pyridine, 3,5-dimetil-4-s-triazinil-pyridine, 3,5-dinitro-4,4'-bipyridine and 3,5-dicyano-4,4'-bipyridine. These systems, depicted in figure 4.72, have been chosen based on the effects that the strength of the dipoles and the π- or σ-acceptor character of the ring substituents could have on the bond energies. The calculated dipoles and Zn-N bond energies for the "up" and "down" configurations are reported in tables 4.26 and 4.27, respectively. As the tables show, even for these alternative linkers the differences are small, although the dipoles of the systems are quite different.
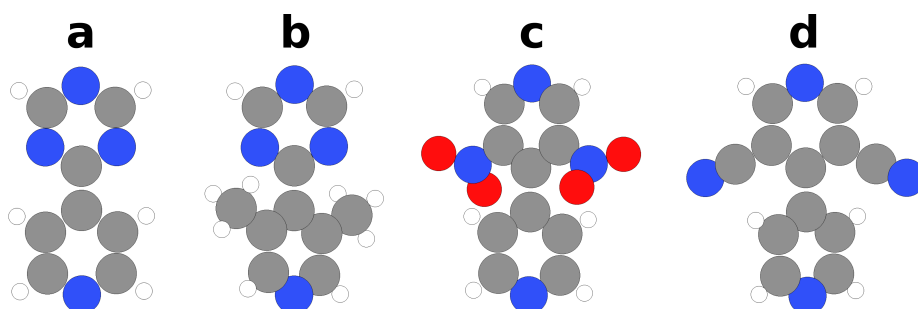
Figure 4.72: Alternative linkers tested for the induced electrostatic asymmetry. C atoms are depicted in grey, H in white, O in red and N in blue. a: 4-s-triazinilpyridine; b: 3,5-dimetil-4-s-triazinilpyridine, c: 3,5-dinitro-4,4'-bipyridine; d: 3,5-dicyano-4,4'-bipyridine.

Table 4.26: Absolute dipole moments of the investigated dipolar linkers. The values are reported for the isolated units and for the "up" and "down" configurations.

		Dipole moment / Debye
3,5-difluoro-4,4'-bipyridine	Isolated	0.76
	Up	1.40
	Down	3.60
4-s-triazinilpyridine	Isolated	1.30
	Up	0.66
	Down	4.40
3,5-dimetil-4-s-triazinilpyridine	Isolated	2.00
	Up	0.16
	Down	5.00
3,5-dinitro-4,4'-bipyridine	Isolated	1.90
	Up	0.49
	Down	6.00
3,5-dicyano-4,4'-bipyridine	Isolated	2.20
	Up	0.33
	Down	6.20

Table 4.27: Comparison between the Zn–N bond energies of the "up" and "down" configurations of the investigated linkers.

		Bond energy / meV	Difference / meV
4-s-triazinilpyridine	Up	1058	
	Down	946	−112
3,5-dimetil-4-s-triazinilpyridine	Up	942	
	Down	945	12
3,5-dinitro-4,4'-bipyridine	Up	1029	
	Down	943	−85
3,5-dicyano-4,4'-bipyridine	Up	1021	
	Down	948	−73

For this reason we considered a 2,6 substitute asymmetric linker, 2,6-difluoro-4,4'- bipyridine, depicted in figure 4.73, to possibly exploit sterical effects. The results for this system are reported in tables 4.28 and 4.29: in this case the difference in the bond energies turns out to be much more significant ($\approx$0.5 eV). As the individual bond energies reveal, the increased asymmetry is a consequence of the reduced bond energy of the "up" configuration. Considering the bond length between Zn and N in the "up" system, the distance is 2.19 Å, which is in the range of the usual Zn-N bond length (see for example references 145,146).

Using the 2,6 substituted linker, we set up a periodic system with one polar layer, analogously to what we did using the 3,5-difluorobipyridine unit. Band gap and work function change are reported in table 4.30, where the results obtained for the original linker are included for the sake of comparison.
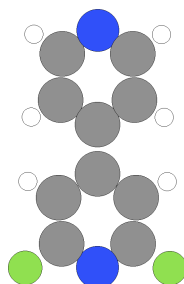
Figure 4.73: 2,6-difluoro-4,4'-bipyridine linker tested to exploit sterical effects. C atoms are depicted in grey, H in white, N in blue and F in green.

Table 4.28: Absolute dipole moments of the 2,6-difluoro-4,4'-bipyridine linker. The values are reported for the isolated units and for the "up" and "down" configurations.

		Dipole moment / Debye
2,6-difluoro-4,4'-bipyridine	Isolated	1.90
	Up	0.61
	Down	4.30

Table 4.29: Comparison between the Zn-N bond energies of the "up" and "down" configurations for the 2,6-difluoro-4,4'-bipyridine linker.

	Zn–N bond energy / meV	Difference / meV
up	590	
down	1057	-467

Looking at the values, we can see that for this new system the band gap decreases by about 0.21 eV with respect to the previously considered one, while for the work function change we observe essentially the same absolute values. The different sign is due to the fact that the dipoles of the two systems point in opposite directions. As the dipole moments of the two isolated linkers are noticeably different (see tables 4.26 and 4.28), one might have not expected identical absolute values for the work function changes. That this is not the case is attributed to different bonding-induced rearrangements of the electronic charge at the interface between the metal and the linker.

Table 4.30: Comparison between the band gap and the work function change $\Delta\Phi$ of the first layer for the two different difluorobipyridine linkers.

	Band gap / eV	$\Delta\Phi$ / eV
3,5-difluoro-4,4'-bipyridine	1.60	0.28
2,6-difluoro-4,4'-bipyridine	1.39	−0.28

We performed a slab calculation also on a 2 layers system, to be able to do some predictions for thicker structures. In table 4.31 the results of the second layer are reported and compared with the ones obtained for the 1st layer.

The difference in the band gap predicted for the addition of a further polar layer is somewhat larger than the difference obtained using the other difluorobipyridine linker. As already mentioned, the band gap for this new system is smaller and therefore, it can be predicted that using the new dipolar linker a smaller number of layers could be added before the gap closes. On the other hand, the change in the work function per layer is almost the same obtained using the previously considered linker.

Finally, it should be noted that both the band gap and the work function change could in principle be tuned using other halogen atoms, like Br or Cl, instead of F.

Table 4.31: Comparison between the results of the first and the second layer of the system set up using the 2,6-difluoro-4,4'-bipyridine linker. Band gap diff.: difference between the band gaps of the second and the first layer. $\Delta\Phi$: work function change. $\Delta\Phi$ diff: difference between $\Delta\Phi$ of the second and the first layer.

N. of polar layers	Band gap / eV	Band gap diff. / eV	$\Delta\Phi$ / eV	$\Delta\Phi$ diff. / eV
1	1.39		0.28	
2	1.07	−0.32	0.61	0.33

4.8.7 Electrostatically designed SURMOF based p-i-n junctions

The peculiar electrostatic potential energy evolution shown in figures 4.67 and 4.68 immediately suggests a possible practical application for such electrostatic designed materials. The energy profile resembles the one typically observed in conventional inorganic p-i-n junctions, consisting of an intrinsic semiconductor sandwiched between a p- and an n- doped region and commonly exploited in electronic devices like photodetectors and solar cells. A model structure that illustrates how such SURMOF based organic p-i-n junction could be built is illustrated in figure 4.74. Four layers of polar apical linkers are sandwiched between four non polar ones, with the resulting calculated plane averaged electrostatic potential energy shown in figure 4.75.
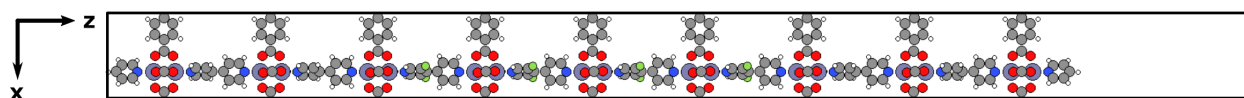
Figure 4.74: Prototypical MOF base p-i-n junction. C atoms are depicted in grey, H in white, N in blue, O in red, F in green and Zn in light blue. The unit cell is enclosed by the black line.
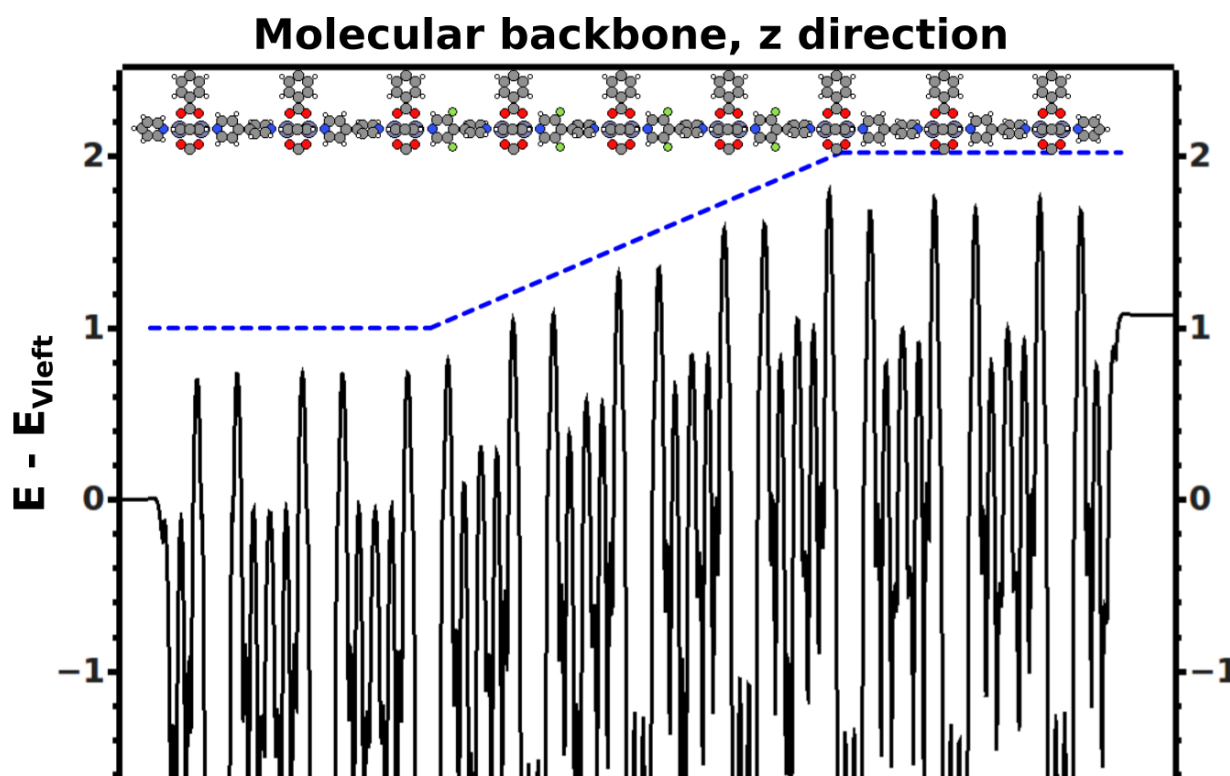
Figure 4.75: Electrostatic potential energy of an electron along the z direction aligned to the energy at the left side (E_{Vleft}) of the slab (black solid curve) and its schematic evolution (blue dashed curve). The structure of the system is also shown, C atoms are depicted in grey, H in white, N in blue, O in red, F in green and Zn in light blue.

The results are in line with what is expected on the basis of electrostatics. Within the first two layers the energy remains constant, along the four central polar layers it increases and in the two last non polar layers it stays again constant. The shift between the two first and last layers is equal to 1.07 eV, consistent with the work function change reported in table 4.22 for the 4 layers system. This is a nice example of a possible advantageous application of the SURMOFs presented in this work. Moreover, it is possible to modify the energy profile

using alternative linkers with different polarities or changing the non polar linkers in the x,y plane, and therefore the density of polar units, to tune the induced step, the width of the central region and the slope of the potential energy. As can be appreciated from figure 4.75, the shift occurs in the region in which the polar units are localised, therefore by introducing more or fewer units it is possible to continuously tune the width of that region. Alternatively, employing a linker with a stronger (weaker) dipole moment it is possible to induce a larger (smaller) energy shift and, thus, a steeper (less steep) energy profile.

The herein proposed application could become even more attractive when combined with the so called conductive MOFs[58], recently become of interest even as active channels in field-effect transistors[147]. Alternatively, guest molecules with conducting properties could be introduced in the SURMOF pores, as described in references 60,61.

4.8.8 Conclusions

In this work electrostatically designed SURMOFs were characterised in terms of their electronic properties using DFT simulations combined with periodic boundary conditions and the repeated slab approach. The design principle was based on the introduction of polar apical linkers to manipulate the electrostatic potential energy within the SURMOF in an advantageous way. The evolution of the work function change and the band gap upon increasing the number of polar layers n was investigated, showing that both properties linearly depend on n. The band gap linearly decreases, with the band gap closure determining the maximum achievable film thickness, while the work function change increases. The total DOS and the DOS projected onto different regions of the investigated systems shown a peculiar evolution: the size of the "local" gaps associated with each metal complex and each apical linker does not change while the global gap decreases and vanishes. A related effect is the formation of a gradient in the electrostatic potential between the two ends of the system, whose profile can be advantageously exploited for organic electronic applications, as shown with the prototypical example of a SURMOF based p-i-n junction. A further note of merit of such novel materials is their high degree of tunability: for instance, by changing the polar linker, therefore acting on orientation and magnitude of the dipolar units, or the in plane linkers, varying then the dipole density, it is possible to modify the potential step, its extension and its slope.

4.8.9 Appendix: HSE06 calculations

As GGA functionals severely underestimate band gaps, to get somewhat improved values some systems have been calculated using the hybrid functional HSE06 (full Heyd-Scuseria-Ernzerhof exchange correlation functional[77,148]), bearing however in mind that also these gaps are typically significantly smaller than actual values of fundamental gaps. The calculations were performed using omega=0.11 bohr^{-1}, light settings and tier 1 with the further addition of the first 2 radial functions of the tier 2, as using full tier 2 would have made the calculations too computationally expensive. The use of fewer basis functions is justified by convergence tests, that shown that there were no relevant differences between the results obtained with the full and the reduced tier 2. Due to the high computational costs, only single point calculations on the PBE optimised structures of 1, 2 and 3 layers systems were performed. Knowing the band gap values for these three structures, it has been possible to predict the number of layers at which the band gap will close. The HSE06 results, reported in table 4.32, show that the band gap values are considerably larger than those calculated at PBE level, as expected.

Assuming a linear evolution of the values, the band gap can be predicted to close after

Table 4.32: HSE06 results for systems up to three layers. Band gap diff.: difference between the band gap of the corresponding layer and the band gap of the previous one. $\Delta\Phi$: work function change. $\Delta\Phi$ diff: difference between $\Delta\Phi$ of the corresponding layer and $\Delta\Phi$ of the previous one.

N. of polar layers	Band gap / eV	Band gap diff. / eV	$\Delta\Phi$ / eV	$\Delta\Phi$ diff. / eV
1	3.21		0.34	
2	2.88	−0.33	0.66	0.32
3	2.56	−0.33	0.99	0.33

12 layers, as shown in figure 4.76. Therefore a significantly bigger system size seems to be achievable. Assuming a linear behaviour for the work function change, it is easily possible to estimate the value it would assume at the band gap closure. As shown in figure 4.77, this value amounts to about 4.2 eV.

The slight difference in the slopes of the PBE and HSE06 calculated curves for the work function change and the band gap (see previous pictures) is due to the differences of these two functionals in evaluating dipoles. A further comparison between the HSE06 and PBE results is done in figure 4.78, where the total DOS and the DOS projected onto the molecular regions where the HOMO and the LUMO are localised are plotted. Comparing the curves, the difference in the calculated band gap becomes very obvious. What is also interesting to mention are some changes especially in the shapes of the occupied DOSs between PBE and HSE06 calculations. This is a priori not that surprising considering that the infamous self-interaction error of (semi)local DFT (which is at least mitigated by hybrid functionals) affects differently localised orbitals to a different degree. This being said, the trends in the band-gap as well as calculated work function changes obtained with are reliably, considering that they primarily originated from charge densities and the resulting electrostatic potentials, which is expected to be properly described also at the GGA level.
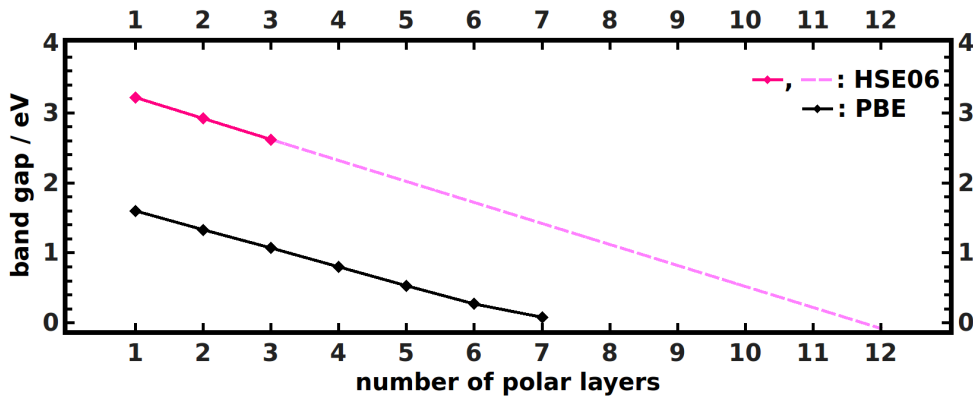
Figure 4.76: Comparison between the PBE and the HSE06 calculated band gap. The dashed line is the extrapolated resulted assuming a linear evolution.
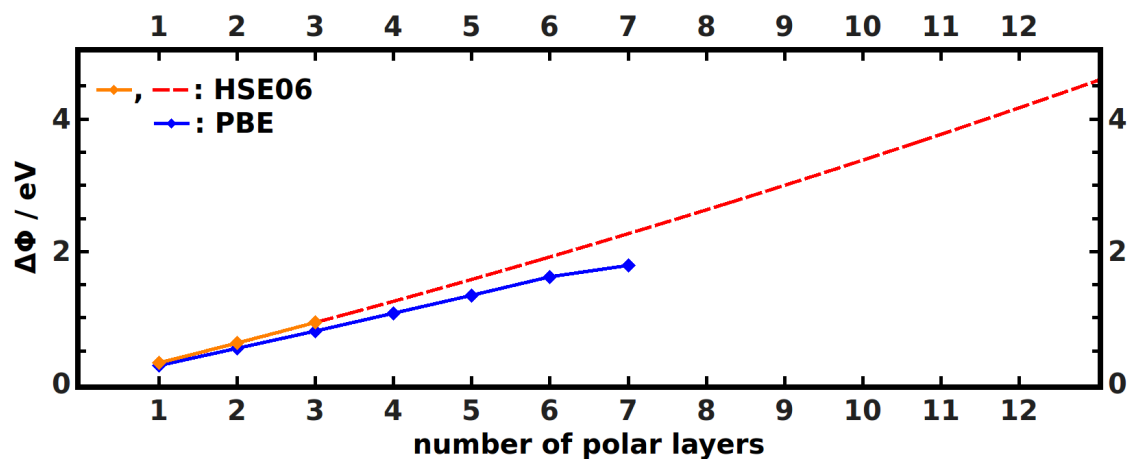
Figure 4.77: Comparison between the PBE and the HSE06 calculated work function changes. The dashed line is the extrapolation resulted assuming a linear evolution. Dashed grey lines are a guide to guess the $\Delta\Phi$ considering 12 as the maximum achievable number of layers. Assuming an evolution similar to the one simulated with PBE functional, a value close to 4.2 eV can be guessed as the final one.
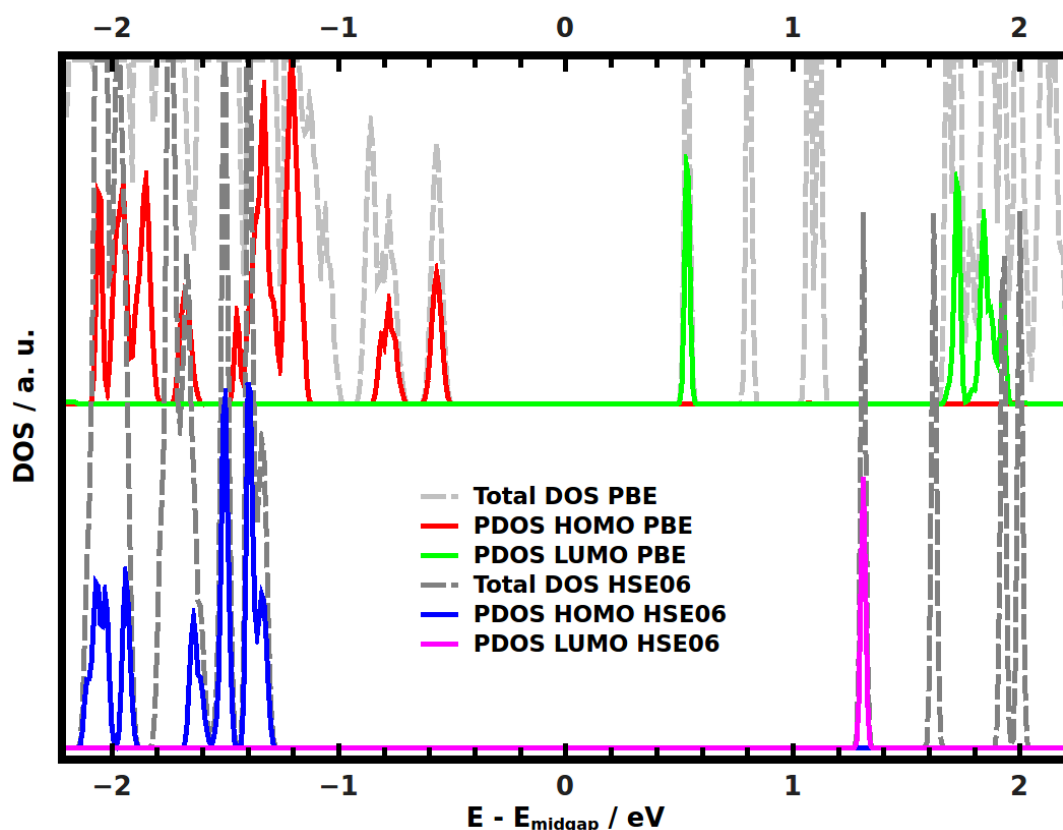
Figure 4.78: Comparison between HSE06 and PBE calculated density of states for the three layers system. Total DOS: density of states of the global system. PDOS HOMO: density of states projected onto the molecular region where the HOMO is localised. PDOS LUMO: density of states projected onto the molecular region where the LUMO is localised. The picture shows that from HSE06 calculations a much larger band gap is obtained.

5　Summary

In this thesis atomistic density functional theory (DFT) simulations have been applied to study structural and electronic properties of technologically relevant hybrid inorganic/organic materials. Metal/self-assembled monolayer (SAM) interfaces and metal-organic frameworks (MOFs) have been investigated, confirming the potential of simulations for characterising and designing materials. In many cases, the modelling results have been combined with experimental observations to gain a full understanding of the structure-to-property relations crucial for any application of such systems.

Metal/SAM interfaces are widely exploited in organic electronic devices to modify the properties of the metal electrodes. The most investigated systems are thiol based SAMs on the Au(111) surface, although in recent years several advantages of Se-based SAMs, such as better structural quality, have been reported[30–35]. Since for any practical purpose of such systems the detailed knowledge of the atomistic structure at the interface is of crucial importance, comparing different docking groups and their impact on the SAM properties is of fundamental interest. In this regard, the investigations performed in this work allowed clarifying the thermal stability of CN substituted S and Se docked naphthalene based SAMs on the Au(111) surface. The main point was the analysis of the relative strength of the bonds between the metal surface and the docking groups and between the docking groups and the molecular backbone.

From a computational point of view, such a comparison turned out to be more challenging than expected. The first problem was related the choice of the unit cell: two SAM molecules arranged in a herringbone fashion did not fit the $(3 \times \sqrt{3})$ unit cell suggested according to the experimental STM pictures. A larger $(4 \times \sqrt{3})$ unit cell was, therefore, initially adopted. A further non-negligible concern was that the calculated bonding energies were so close that particularly tight computational settings were needed in order to achieve the required level of accuracy. The main issue was, however, the disagreement between the simulated and measured order of the bonding strengths. According to the experimental data, for both SAMs the strongest bond was between metal and docking group, with the overall bond order being Au–Se > Au–S > S–C > Se–C. From the calculated data a different scenario was instead obtained: the bonds between docking groups and molecular backbone were stronger than the bonds between substrate and docking group. The calculated bond order was S–C > Se–C ⩾ Au–Se ⩾ Au–S.

To understand the reason for this discrepancy, the impact of surface reconstructions was investigated. Several reconstruction motifs were tested with one and two Au adatoms per unit cell. Interestingly, the introduction of the Au adatoms allowed fitting the molecules in the experimentally suggested $(3 \times \sqrt{3})$ unit cell. Moreover, for the reconstructed case with two Au adatoms per unit cell, the measured bond order could be observed also in the simulations. This confirms the advantage of combining experimental and simulated results to obtain a more complete understanding of the examined systems: the modelling results were crucial to identify the role played by surface reconstructions. Regarding the bon order, the Se–C bond is the weakest one and makes the Se docked SAM therefore thermally less stable, even if the Au–Se bond is stronger than the Au–S one. This demonstrates that

the relative stability of SAMs cannot be defined solely based on the strength of the bonds between substrate and docking group.

As already mentioned, systems like the CN substituted SAMs treated above are often integrated into devices. The main application is the modification of the work function of the electrodes. For this purpose, not only the structural but also the electronic properties of the metal/SAM interface are of fundamental importance. A considerable part of the work carried out in this thesis demonstrates the valuable contribution that simulations can provide for the electronic and structural characterisation of such interfaces. Several mono-, di- and tridentate thiol based SAMs on the Au(111) surface were investigated.

The monothiol based SAMs were designed following the embedded dipole approach[36,37]: dipolar pyrimidine units were inserted in the molecular backbone of aromatic SAMs. This allows inducing the desired work function modification without changing the chemistry of the upper part of the molecules. This is important when integrating the interfaces in devices, as discussed in reference 1. Molecules with both one (second generation molecules) and two (third generation molecules) embedded pyrimidine rings were considered. The second generation SAMs were conceptually derived from biphenylthiol (BPT) by substituting the topmost or the bottom phenyl ring with a pyrimidine unit with the N atoms pointing towards, respectively, away from, the substrate.

The SAMs were shown to induce the expected opposite work function modifications. The experimental and the simulated data were in qualitatively excellent agreement and shown the possibility to tune the work function change within a range of about 1 eV. As recently discussed in literature[19,39], the same collective electrostatic effects responsible for the work function modifications have a relevant impact also on the X-ray photoelectron spectra (XPS) of the adsorbate. Also for the second generation molecules the effect of electrostatics on XPS was analysed. The atomic resolution provided by the simulations allowed clarifying the experimentally observed peak shapes and positions. The overall excellent agreement between simulated and measured properties shown that the behaviour of the molecules on the surface follows what is expected on the basis of the simulations, confirming the high effectiveness of the investigated SAMs. A further validation of the second generation SAMs capabilities was given via the realisation of p- and n- type organic thin film transistors containing SAM modified Au electrodes and pentacene or C60 as active layers[1]. Employing the second generation SAMs it was possible to relevantly reduce the contact resistance and the growth of the active materials was essentially not influenced by the orientation of the pyrimidine unit.

Regarding the third generation molecules, both molecules containing two aromatic rings directly bonded to the S docking atom (PmPm-up/down SAMs) and longer molecules containing three aromatic with a -CH_2- spacer between the molecular backbone and the docking atom (PmPmP1-SAMs) were investigated. Calculated work function changes, structural parameters and C1s XP spectra were compared to experimental results.

Analysing the molecules without -CH_2- spacer, several discrepancies were observed comparing calculated and experimental data. The calculated work function changes strongly overestimated the measured ones. The structural parameters of the optimised geometries shown relevant deviations from the parameters extracted from the experimental measurements. Important discrepancies were observed also comparing the simulated and measured XP spectra, for both the position and the shape of the peaks. The disagreement was more striking for the PmPm-up SAM, for which the experimental packing density was also somewhat lower than for the other investigated systems. The discrepancies between experimental and simulated results were attributed to the somewhat bad quality of the films formed by the PmPm molecules.

For the PmPmP1-SAMs, the structural parameters obtained from the simulated geome-

tries and from the experimental data agreed quite well. However, also in this case the calculated work function changes severely overestimated the measured ones. Also comparing simulated and experimental XPS, a certain disagreement in the position and the shape of the peaks was observed. Interestingly, the situation improved performing the calculations on SAMs containing a fraction of flipped or exchanged molecules, pointing towards the presence of defects or imperfections in the experimentally analysed films.

Calculations were performed also on derivatives of the PmPmP1 SAMs, obtained by introducing polar tail groups. The results predicted that the substituted SAMs would allow changing the work function of the substrates beyond pinning effects. According to the calculations, the work function of a Au(111) surface could be tuned over a range of almost 8 eV. However, it should be kept in mind that calculations performed with the methodology described in this work usually overestimate work function changes by about 30%. Moreover, as discussed above, the bipyrimidine containing SAMs seemed not to form good quality films. The actual potential in terms of work function modification of the substituted PmPmP1 SAMs is, therefore, expected to be smaller.

Contrary to what was observed for the second generation molecules, the third generation SAMs apparently do not behave as it would have been expected on the basis of the simulations.

Thiol base SAMs on the Au(111) surface such as the second and third generation SAMs considered in this work are the most common metal/SAM interfaces. Substituting S with Se, as was done in the naphthalene based SAMs described above, is not the only strategy to find alternativly docked SAMs with possibly superior properties. Other less common moieties have also been tested, such as the dithiocarbamate (DTC) group. The peculiarity of DTC based SAMs is the bonding to the metal substrate via two S atoms. Being known that DTC SAMs can form robust and stable films and induce interesting work function modifications[38], two basic phenyl-piperidine-DTC (PPd) and phenyl-piperazine-DTC (PPz) SAMs were characterised in this work, to correlate their structure to the observed substrate property modifications.

The simulations were combined with XPS, NEXAFS and UPS experiments, with the results agreeing overall very satisfactorily. The SAMs bonded to the surface with both the two S atoms of the DTC functionality, with only a slight inhomogeneity in the S docking positions that somehow deviated from the ideal S docking site. This was ascribed to the spacing between the S atoms not being commensurate with the Au(111) lattice. In both SAMs the molecules arranged very densely, with the same packing density usually observed for monothiols. This was a notable result, since it implies that the density of S atoms on the surface is twice the density commonly observed. Moreover, this did not seem to disturb the ordered arrangement of the molecules. Both simulations and experiments presented a scenario in which both SAMs form ordered films, with only the PPd SAM showing a somewhat lower packing density, very likely due to the bulkier conformation assumed by the PPd molecules. According to the calculated most stable geometries, both SAMs assumed a herringbone arrangement, differing, however, in the conformation of the uppermost phenyl ring. In the PPd molecules the phenyl ring was twisted by 90° with respect to the bottom piperidine ring, while in the PPz case the phenyl and the piperazine ring assumed an essentially coplanar conformation.

Regarding the electronic properties, the measurements reported similar values of $\Delta\Phi$, with a difference of only 0.2 eV, for the two SAMs. The simulations however depicted a different scenario. The calculated $\Delta\Phi$ of the PPz SAM overestimated by about 30% the experimental value, being therefore in line with what usually observed when comparing measured and PBE calculated $\Delta\Phi$. In the PPd case the simulations predicted a value by about 0.9 eV larger than for the PPd SAM. Additionally, while for the XPS of the PPz

SAM the agreement between theory and experiments was excellent and both the shape of the spectrum and the peak positions were fully reproduced in the simulations, in the PPd case the shape of the spectrum was comparable, but the simulated peak was found to lie at 0.4 eV larger binding energy. An explanation for such discrepancies in the PPd cases could not be found only in the lower packing density of the SAM. The disagreement was tentatively ascribed to a certain sample-to-sample variation within the different samples used to perform the measurements. This hypothesis could be supported by the observation that in the simulations the shift between the main PPz peak and the PPd one was 0.9 eV, thus perfectly correlated with the difference in $\Delta\Phi$. This is consistent with the fact that both shifts are due to the same electrostatic effects. In the experiments, on the other hand, the shift between the XPS peaks was about 0.5 eV, while the shift in $\Delta\Phi$ was smaller and amounted to only 0.2 eV.

The DTC moiety contains several heteroatoms and is, therefore, more complex than other common docking groups. Moreover, the two considered basic systems differ for the presence of a piperazine ring in one case and a piperidine one in the other case. Simulations were therefore exploited to understand where the dipole(s) responsible for the work function modifications sit in the SAM. The same approach as the one described in reference 19 was used, calculating reduced coverage systems to exclude collective electrostatic effects arising from the periodic arrangement of the molecules. The reduced coverages of 1/16 and 1/36 were considered. Going from the full to the reduced coverage only a rigid shift of the spectrum to lower binding energies was observed. The shape of the spectra remained essentially unchanged, indicating that the potential step occurs at the very metal/SAM interface. A final interesting and puzzling observation was made when considering the atom resolved binding energies at different coverages: for the docking atoms and the bottom C atoms essentially no shift was observed. Based on electrostatics, this should mean that all the dipoles in the SAM sit above the bottom C atom. This hypothesis however did not seem very likely and an alternative explanation was proposed, based on different charge rearrangements taking place at different coverages. These could compensate the electrostatic shifts for atoms very close to the substrate.

Overall, the investigation confirmed the potential of DTC SAMs as building blocks for effective surface modifications. Additionally, thanks to the level of insight provided by the simulations, it was shown that the moiety inducing the work function change is the DTC functionality itself.

The essentially homogeneous docking configuration of the DTC moiety is a promising result when thinking of SAMs bearing multiple docking atoms, to better control the orientation of the molecules within the SAM. Developing that further was the idea behind the triptycene based SAMs investigated in this work. Triptycene based molecules are already known for showing promising self-assembling ability and forming dense well defined two-dimensional hexagonal structures[149–154]. Thanks to the rigid backbone, the triptycene based SAMs were expected to dock to the surface with all three S atoms, assuming thus an essentially upright standing orientation. Two basic systems were considered, referred to as T1 and T2. The two SAMs differ for the presence of a methylene linker between the S atoms and the triptycene backbone in T1, while in T2 the docking groups are directly bonded to the triptycene unit.

STM and XPS experiments shown that the density of the S atoms on the surface was comparable to the case of common monothiol SAMs, with the T2 SAM showing a somewhat lower value. STM images also shown that the molecules arrange in a hexagonal pattern. Based on these observations, in the simulations a (3×3) surface unit cell was used. The optimisation yielded an almost perfectly upright standing SAM for the T1 case, with a tilt angle of about 3°, that correlated well with the 7.5° extrapolated from the experiments. The optimised T2 SAM, on the other hand, turned out to somewhat deviate from the upright

standing orientation, with a calculated tilt angle of almost 7°. A much more important deviation was instead observed in experiments, that yielded a tilt angle of almost 40°. Such relevant discrepancy could not be explained only by the lower packing density of the T2 SAM. Together with the S2p XPS showing the massive presence of unbound/physisorbed S and oxidised thiol groups, it rather indicated a more serious issue involving the docking configuration. Indeed, also in the simulations a certain inhomogeneity in the docking positions of the T2 SAM was observed: the S atoms were found to occupy *fcc*-hollow position, deviating from the most favourable S docking sites on the Au(111) surface, shifted towards bridge. Moreover, the three docking groups shown different heights above the surface, consistent with the tilted orientation. In the T1 SAM, instead, all docking groups had the same height and docked at the optimum *fcc*-hollow shifted towards bridge position. These differences were ascribed to the presence of a methylene spacer between the triptycene backbone and the docking atoms in the T1 SAM. The spacer provides a certain flexibility, that helps reducing the strain deriving from the distance between the docking groups not being commensurate with the Au(111) lattice constant and from the Au–S–C bond angle.

Regarding the electronic properties, Kelvin probe (KP) measurements reported similar $\Delta\Phi$ values for the two SAMs, comparable with the $\Delta\Phi$ induced by a reference BPT SAM. The calculated value for T1, despite overestimating the measured one, was very close to what calculated for BPT, agreeing thus qualitatively with the experimental observations. $\Delta\Phi$ of the T2 SAM was instead calculated to be by 0.4 eV larger than in the T1 and BPT cases. The discrepancy was clarified considering that actually the high calculated $\Delta\Phi$ describes a nearly "perfect" film, while the experimental value reflected a disordered SAM, with a lower packing density and much larger tilt angles. The difference in the simulated $\Delta\Phi$ of the two SAMs could be rationalised thanks to the simulations and was ascribed to the different hybridisation of the C atoms bonded to the docking groups and to the different Au–S–C bonding geometries. Despite the notable discrepancy between simulated and experimental structural properties and induced $\Delta\Phi$ of the T2 SAM, surprisingly the simulated XP spectrum excellently agreed with the experimental one for both systems. The experimental shift of 0.4 eV between the T1 and T2 peaks was fully reproduced in the simulations, with the T2 peak lying at larger energies, as it was expected considering the larger $\Delta\Phi$ calculated for the T2 SAM. Somewhat puzzling was the observation that in the T2 case, despite the discrepancy between calculated and measured $\Delta\Phi$, simulated and measured XPS totally agree. This was explained considering the large area averaging of KP measurements and the more local character of XPS experiments. Very likely, the T2 SAM forms pretty inhomogeneous films, in which more or less ordered domains coexist with disordered ones. A further observation consistent with the worse T2 film quality could be made on the basis of the atom resolved C1s core level energies: while in the T1 case the chemically equivalent C atoms of the backbone had the same binding energy, in the T2 case the binding energies were more spread. Overall, the study demonstrated the capability of triptycene based molecules of docking to the Au(111) surface with all the three S atoms, with the T1 molecules forming particularly good quality films. This property, combined with the convenient feature of such SAMs of having four sites available for attaching various tail groups, makes especially the T1 SAM a highly promising candidate for the formation of SAMs of controlled density and orientation.

The transferability of such advantageous properties was tested also for triptycene based SAMs bonded to a different surface by means of a different docking group. The investigated systems was an intermediate of the synthesis of the T1 and T2 SAMs discussed above. The molecule bears three COOH groups and was deposited onto the Ag(111) surface. Also in this case ordered SAMs docked with all the three docking groups were observed. While for the S docked T1 and T2 SAMs only the hexagonal phase was observed, the COO docked SAMs on the Ag(111) surface shown both a hexagonal and a porous phase. In both phases

the molecules formed ordered films. The calculated tilt angles are about 2° and all the COO groups occupy the same docking sites. When discussing the porous phase an interesting discussion arose. The most stable arrangement found in the simulations was chiral, while no chirality could be observed in the experimental STM pictures. Several different non chiral arrangements were tested as starting geometries, but in all cases the optimisation led to the chiral one. The impact of surface reconstructions was tested, too. However, not even the presence of Ag adatoms on the surface could prevent the molecules from assuming a chiral arrangement. Testing the different starting geometries, it was observed that for the molecules it would be in principle possible to go from one chiral arrangement to the one with the opposite chirality by means of a collective rotation without colliding. This led to the hypothesis that the structure observed in the experimentally registered STM images could be an average of two arrangements with the opposite chirality. An interesting outcome was also provided by the STM images simulated for the chiral arrangement. In the images the chirality was much less evident and in some cases it could hardly be appreciated. It was then suggested that under certain conditions the chirality of the arrangement could be hidden in STM images. To test the two hypothesis further analysis is needed, from both an experimental and a theoretical point of view.

Coming back to the more deeply investigated interfaces between thiols and the Au(111) surface, the examples discussed in this work show that the combination of simulations and experimental techniques is an effective tool for the full characterisation of material properties. An important point was the comparison of simulated and experimental XP spectra. XPS is a convenient tool to monitor the properties of metal/SAM interfaces[18] and to probe electrostatic shifts within the SAM[19]. In this context, when discussing the DTC SAMs described above an interesting and surprising observation was made. The binding energies of the S atoms and of the C atoms bonded to them hardly shown any shift when reducing the SAM coverage. The system treated in section 4.7 had the purpose of helping to understand why this was the case. The investigated system was a simple K/Au(111) interface at full and reduced coverage. Changing the K density modified the work function change by more than 2 eV, but only a minor shift was observed for the K1s core level binding energies. The proposed explanation was that there could be effects of chemical nature playing a role that compensates the electrostatic shift and masks it. To the test the hypothesis, the upper vacuum level aligned K binding energies were calculated for the two different coverages. This allows accounting purely for chemical shifts, as long as the K atoms have the same docking position and the same height at both coverages. Indeed, it could be shown that a chemical shift of almost 2 eV affects the K core level energies when changing the K density on the surface. As presumed, the chemical effect shifted the energies in the opposite direction than the electrostatic shift. The origin of the chemical shift was demonstrated to be the different charge transfer processes taking place between the substrate and the K atoms at different coverages. On the contrary, comparing the core level energies of a sheet of K atoms without any underlying substrate at the two considered coverages and of an isolated K atom, no difference could be observed. This means that what is responsible for the chemical shift is in this case only the different amount of charge sitting on the K atoms. This outcome allowed rationalising both what observed for the DTC SAMs and some experimental measurements reported in reference 125. Moreover, understanding the interplay of different effects for the atoms close to the interface was useful to clarify the energy level alignment at metal/organic interfaces.

The analysis of the numerous interfaces investigated in this work allowed showing the fundamental role played by collective electrostatic effects for such systems. As already pointed out, this is not only important for understanding material properties but can also be advantageously exploited to design materials with the desired characteristics, as illustrated by

means of the (substituted) embedded dipole SAMs described before. With these considerations in mind it is then natural to think about intentionally exploiting such effects also for other materials. Metal-organic frameworks (MOFs) were the ideal candidates, due to their high versatility. The systems of interest treated in this work are a particular class of MOFs known as SURMOFs, standing for *surface grown, crystalline metal-organic framework multilayers*. The proposed strategy was to insert polar apical linkers in the structure, to manipulate the electrostatic potential energy within the system. The metal nodes of the considered SURMOF were based on metal complexes containing two Zn atoms connected in the x,y plane by terephthalic units. In the z direction polar 3,5-difluoro-4,4'-bipyridine units were introduced. First of all, the maximum number of layers of polar linkers that could be grown was determined. With the difluorobipridine linker mentioned above, a maximum number of seven polar layers was predicted. The limitation was due to the band gap closure: by adding more polar layers the band gap decreased linearly for the first six layers and vanished at the seventh one. Another effect due to the addition of the polar layers was the change in work function between the two sides of the slab. Adding more polar layers, the work function change increased linearly for the first six layers and saturated at the seventh layer. The density of states projected onto the in-plane units shown that at each unit the states shifted up in energy. The same evolution was observed for the density of states projected onto the polar linkers. The shift caused the global band gap closure, while the size of the "local" gaps did not change. The HOMO and the LUMO were predicted to be localised on the topmost in-plane ligand and on the lowermost apical linker, respectively. The visualisation of the electrostatic potential energy within the system allowed appreciating the gradient that builds up as a consequence of the collective electrostatic effects.

Growing a SURMOF with polar linkers with dipoles pointing all in the same direction could be challenging from a practical point of view. It would therefore be beneficial if the bond energy between the Zn atoms of the metal node and the N atoms of the apical linker depended on the orientation of the dipole unit. The calculations shown that for the difluorobipyridine linker no asymmetry in the bond energies could be appreciated depending on the dipole orientation. Moreover, also the interaction with the neighbouring dipole units and the ones in the above and below layer was predicted not to disturb the parallel arrangement of the dipoles. Different apical linkers based on a 4,4'-bipyrimidine moiety bearing different dipolar substituents were tested. A non negligible asymmetry in the Zn-N bond energy was observed for a 2,6-difluoro-4,4'-bipyrimidine linker.

The experimental realisation of such SURMOFs containing polar elements would allow to obtain versatile materials whose electrostatic potential could be conveniently manipulated. An example was presented, in which the resulting electrostatic potential energy evolution mimics the energy profile of a p-i-n junction.

In summary, the work carried out in this thesis confirms the essential role played by simulations for designing materials and understanding their properties. The performed calculations supported the analysis of experimental data, being in many cases crucial for the correct interpretation. Moreover, it was shown how simulations can be exploited for conceiving new materials with novel properties. A critical comparison of experimental and calculated data was also discussed, emphasising that the aim of simulations is not obtaining perfect agreement with the measured data but gaining fundamental insight to rationalise material properties.

Bibliography

[1] A. Petritz, M. Krammer, E. Sauter, M. Gärtner, G. Nascimbeni, B. Schrode, A. Fian, H. Gold, A. Cojocaru, E. Karner-Petritz, R. Resel, A. Terfort, E. Zojer, M. Zharnikov, K. Zojer, and B. Stadlober. Embedded dipole self-assembled monolayers for contact resistance tuning in p-type and n-type organic thin film transistors and flexible electronic circuits. *Adv. Funct. Mater.*, 28(45):1804462.

[2] S. Zhang. Fabrication of novel biomaterials through molecular self-assembly. *Nat. Biotechnol.*, 21:1171–1178, 2003.

[3] A. Ulman. Formation and structure of self-assembled monolayers. *Chem. Rev.*, 96(4):1533–1554, 1996.

[4] G. M. Whitesides and P. E. Laibinis. Wet chemical approaches to the characterization of organic surfaces: self-assembled monolayers, wetting, and the physical-organic chemistry of the solid-liquid interface. *Langmuir*, 6:87–96, 1990.

[5] M. C. Etter and T. W. Panunto. 1,3-bis(m-nitrophenyl)urea: an exceptionally good complexing agent for proton acceptors. *J. Am. Chem. Soc.*, 110(17):5896–5897, 1988.

[6] P. E. Laibinis and G. M. Whitesides. Self-assembled monolayers of n-alkanethiolates on copper are barrier films that protect the metal against oxidation by air. *J. Am. Chem. Soc.*, 114(23):9022–9028, 1992.

[7] Y. Yamamoto, H. Nishihara, and K. Aramaki. Self-assembled layers of alkanethiols on copper for protection against corrosion. *J. Electrochem. Soc.*, 140(2):436–443, 1993.

[8] D. L. Allara, A. F. Hebard, R. G. Nuzzo, and D. R. Falcone. Self-assembled monolayers of n-alkanethiolates on copper are barrier films that protect the metal against oxidation by air. *J. Vac. Sci. Technol. A*, 1, 1983.

[9] F. A. Armstrong, H. A. O. Hill, and N. J. Walton. Direct electrochemistry of redox proteins. *Acc. Chem. Res.*, 21(11):407–413, 1988.

[10] M. Halik, H. Klauk, U. Zschieschang, G. Schmid, C. Dehm, M. Schütz, S. Maisch, F. Effenberger, M. Brunnbauer, and F. Stellacci. Low-voltage organic transistors with an amorphous molecular gate dielectric. *Nature*, 431:963–966, 2004.

[11] H. Klauk, U. Zschieschang, J. Pflaum, and M. Halik. Ultralow-power organic complementary circuits. *Nature*, 445:745–748, 2007.

[12] I. Kymissis, C. D. Dimitrakopoulos, and S. Purushothaman. High-performance bottom electrode organic thin-film transistors. *IEEE Trans. on Electron Devices*, 48(6):1060–1064, 2001.

[13] I. H. Campbell, S. Rubin, T. A. Zawodzinski, J. D. Kress, R. L. Martin, D. L. Smith, N. N. Barashkov, and J. P. Ferraris. Controlling schottky energy barriers in organic electronic devices using self-assembled monolayers. *Phys. Rev. B*, 54(20):14321–14324, 1996.

[14] I. H. Campbell, J. D. Kress, R. L. Martin, D. L. Smith, N. N. Barashkov, and J. P. Ferraris. Controlling charge injection in organic electronic devices using self-assembled monolayers. *Appl. Phys. Lett.*, 71(24):3528–3530, 1997.

[15] S. Casalini, C. A. Bortolotti, F. Leonardi, and F. Biscarini. Self-assembled monolayers in organic electronics. *Chem. Soc. Rev.*, 46:40–71, 2017.

[16] F. Schreiber. Structure and growth of self-assembling monolayers. *Progr. Surf. Sci.*, 65:151–256, 2000.

[17] H. Lüth. *Solid Surfaces, Interfaces and Thin Films*. Springer, 2010.

[18] M. Zharnikov. High-resolution x-ray photoelectron spectroscopy in studies of self-assembled organic monolayers. *J. Electron Spectros. Relat. Phenomena*, 178-179:380–393, 2010.

[19] T. C. Taucher, I. Hehn, O. T. Hofmann, M. Zharnikov, and E. Zojer. Understanding chemical versus electrostatic shifts in x-ray photoelectron spectra of organic self-assembled monolayers. *J . Phys. Chem. C*, 120(6):3428–3437, 2016.

[20] *https:\\www.ifg.kit.edu\downloads\NEXAFS_final.pdf*.

[21] E. Zojer and O. T. Hofmann. *Organic semiconductors: fundamentals and applications*. Institute of Solid State Physics, Graz University of Technology, Summer semester 2016.

[22] H. Ishii, K. Sugiyama E. Ito, and K. Seki. Energy level alignment and interfacial electronic structures at organic/metal and organic/organic interfaces. *Adv. Mater.*, 11(8):605–625, 1999.

[23] G. Heimel, F. Rissner, and E. Zojer. Modeling the electronic properties of π-coniugated self-assembled monoayers. *Adv. Mater.*, 22:2494–2513, 2010.

[24] A. Natan, L. Kronik, H. Haick, and R. T. Tung. Electrostatic properties of ideal and non-ideal polar organic monolayers: Implications for electronic devices. *Adv. Mater.*, 19:4103–4117, 2007.

[25] O. L. A. Monti. Understanding interfacial electronic structure and charge transfer: An electrostatic perspective. *J. Phys. Chem. Lett.*, 3:2342–2551, 2012.

[26] Volker B., Ralf Gehrke, F. Hanke, P. Havu, V. Havu, X. Ren, K. Reuter, and M. Scheffler. *Ab initio* molecular simulations with numeric atom-centered orbitals. *Comput. Phys. Commun.*, 180:2175–2196, 2009.

[27] J. P. Perdew, K. Burke, and M. Ernzerhof. Generalized gradient approximation made simple. *Phys. Rev. Lett.*, 77:3865–3868, 1996.

[28] V. G. Ruiz, W.i Liu, E. Zojer, M. Scheffler, and A. Tkatchenko. Density-functional theory with screened van der waals interactions for the modeling of hybrid inorganic-organic systems. *Phys. Rev. Lett.*, 108:146103, 2012.

[29] A. Tkatchenko and M. Scheffler. Accurate molecular van der waals interactions from ground-state electron density and free-atom reference data. *Phys. Rev. Lett.*, 102:073005, 2009.

[30] L. V. Romashov and V. P. Ananikov. Self-assembled selenium monolayers: From nanotechnology to materials science and adaptive catalysis. *Chem. - Eur. J.*, 319:17640–17660, 2013.

[31] A. Shaporenko, P. Cyganik, M. Buck, A. Ulman, and M. Zharnikov. Self-assembled monolayers of semifluorinated alkaneselenolates on noble metal substrates. *Langmuir*, 21:8204–8213, 2005.

[32] D. Käfer, A. Bashir, and G. Witte. Interplay of anchoring and ordering in aromatic self-assembled monolayers. *J. Phys. Chem. C*, 111:10546–10551, 2007.

[33] A. Bashir, D. Käfer, J. Müller, C. Wöll, A. Terfort, and G. Witte. Selenium as a key element for highly ordered aromatic self- assembled monolayers. *Angew. Chem., Int. Ed.*, 47:5250–5253, 2008.

[34] P. Cyganik, K. Szelagowska-Kunstman, A. Terfort, and M. Zharnikov. Odd-even effect in molecular packing of biphenyl-substituted alkaneselenol self-assembled monolayers on Au(111): Scanning tunneling microscopy study. *J. Phys. Chem. C*, 112:15466–15473, 2008.

[35] M. Dendzik, A. Terfort, and P. Cyganik. Odd-even effects in the polymorphism of self-assembled monolayers of biphenyl-substituted alkaneselenolates on Au(111). *J. Phys. Chem. C*, 116:19535–19542, 2012.

[36] A. Kovalchuk, T. Abu-Husein, D. Fracasso, D. A. Egger, E. Zojer, M. Zharnikov, A. Terfort, and R. C. Chiechi. Transition voltages respond to synthetic reorientation of embedded dipoles in self-assembled monolayers. *Chem. Sci.*, 7:781–787, 2016.

[37] O. M. Cabarcos, S. Schuster, I. Hehn, P. P. Zhang, M. M. Maitani, N. Sullivan, J.-B. Gigure, J-F. Morin, P. S. Weiss, E. Zojer, M. Zharnikov, and D. L. Allara. Effects of embedded dipole layers on electrostatic properties of alkanethiolate self-assembled monolayers. *J. Phys. Chem. C*, 121(29):15815–15830, 2017.

[38] W. E. Ford, D. Gao, N. Knorr, R. Wirtz, F. Scholz, Z. Karipidou, K. Ogasawara, S. Rosselli, V. Rodin, G. Nelles, and F. von Wrochem. Organic dipole layers for ultralow work function electrodes. *ACS Nano*, 8(9):9173–9180, 2014.

[39] E. Sauter, C.-O. Gilbert, J.-F. Morin, A. Terfort, and M. Zharnikov. Mixed monomolecular films with embedded dipolar groups on Ag(111). *The Journal of Physical Chemistry C*, 122:19514–19523, 2018.

[40] H. Furukawa, K. E. Cordova, M. O'Keeffe, and O. M. Yaghi. The chemistry and applications of metal-organic frameworks. 341(6149), 2013.

[41] J. Jiang, Y. Zhao, and O. M. Yaghi. Covalent chemistry beyond molecules. *J. Am. Chem. Soc.*, 138(10):3255–3265, 2016.

[42] S. Yuan, L. Feng, K. Wang, J. Pang, M. Bosch, C. Lollar, Y. Sun, J. Qin, X. Yang, P. Zhang, Q. Wang, L. Zou, Y. Zhang, L. Zhang, Y. Fang, J. Li, and H.-C. Zhou. Stable metal–organic frameworks: Design, synthesis, and applications. *Adv. Mater.*, 30:1704303, 2018.

[43] J.-L. Zhuang, A. Terfort, and C. Wöll. Formation of oriented and patterned films of metal–organic frameworks by liquid phase epitaxy: A review. *Coord. Chem. Rev.*, 307(2):391–424.

[44] V. Stavila, A. A. Talin, and M. D. Allendorf. Mof-based electronic and opto-electronic devices. *Chem. Soc. Rev.*, 43:5994–6010, 2014.

[45] M. D. Allendorf, A. Schwartzberg, V. Stavila, and A. A. Talin. A roadmap to implementing metal–organic frameworks in electronic devices: Challenges and critical directions. *Chem. Eur. J.*, 17:11372–11388, 2011.

[46] J. Liu, W. Zhou, J. Liu, I. Howarda, G. Kilibarda, D. Coupry S. Schlabach, M. Addicoat, S. Yoneda, Y. Tsutsui, T. Sakurai, S. Seki andZ. Wang, P. Lindemann, E. Redel, T. Heine, and C. Wöll. Photoinduced charge-carrier generation in epitaxial mof thin films: High efficiency as a result of an indirect electronic band gap? *Angew. Chem. Int. Ed.*, 54:7441–7445, 2015.

[47] C. G. Silva, A. Corma, and H. Garcìa. Metal–organic frameworks as semiconductors. *J. Mater. Chem.*, 20:3141–3156, 2010.

[48] D. Zacher, O. Shekhah, C. Wöll, and R. A. Fischer. Thin films of metal–organic frameworks. *Chem. Soc. Rev.*, 38:1418–1429, 2009.

[49] O. Shekhah, J. Liu, R. A. Fischer, and C. Wöll. Mof thin films: existing and future applications. *Chem. Soc. Rev.*, 40:1081–1106, 2011.

[50] D. L. Allara and R. G. Nuzzo. Spontaneously organized molecular assemblies. 2. quantitative infrared spectroscopic determination of equilibrium structures of solution-adsorbed n-alkanoic acids on an oxidized aluminum surface. *Langmuir*, 1(1):52–66, 1985.

[51] J. Christopher Love, Lara A. Estroff, Jennah K. Kriebel, Ralph G. Nuzzo, and George M. Whitesides. Self-assembled monolayers of thiolates on metals as a form of nanotechnology. *Chemical Reviews*, 105(4):1103–1170, 2005.

[52] O. Shekhah, H. Wang, S. Kowarik, F. Schreiber, M. Paulus, M. Tolan, C. Sternemann, F. Evers, D. Zacher, R. A. Fischer, and C. Wöll. Step-by-step route for the synthesis of metal-organic frameworks. *J. Am. Chem. Soc.*, 129(49):15118–15119, 2007.

[53] O. Shekhah, K. Hirai, H. Wang, H. Uehara, M. Kondo, S. Diring, D. Zacher, R. A. Fischer, O. Sakata, S. Kitagawa, S. Furukawa, and C. Wöll. Mof-on-mof heteroepitaxy: perfectly oriented $[Zn_2(ndc)_2(dabco)]n$ grown on $[Cu_2(ndc)_2(dabco)]_n$ thin films. *Dalton Trans.*, 40:4954–4958, 2011.

[54] E. Castaldelli, K. D. G. Imalka Jayawardena, D. C. Cox, G. J. Clarkson, R. I. Walton, L. Le-Quang, J. Chauvin, S. Ravi P. Silva, and G. J.-F. Demets. Electrical semiconduction modulated by light in a cobalt and naphthalene diimide metal-organic framework. *Nature Communications*, 8(1):2139, 2017.

[55] L. Sun, C. H. Hendon, M. A. Minier, A. Walsh, and M. Dincă. Million-fold electrical conductivity enhancement in $Fe_2(DEBDC)$ versus $Mn_2(DEBDC)$ (E = S, O). *J. Am. Chem. Soc.*, 137(19):6164–6167, 2015.

[56] L. Sun, T. Miyakai, S. Seki, and M. Dincă. Mn_2(2,5-disulfhydrylbenzene-1,4-dicarboxylate): A microporous metal-organic framework with infinite (–Mn–S–)$_\infty$ chains and high intrinsic charge mobility. *J. Am. Chem. Soc.*, 135(22):8185–8188, 2013.

[57] S. S. Park, E. R. Hontz, L. Sun, C. H. Hendon, A. Walsh, T. Van Voorhis, and M. Dincă. Cation-dependent intrinsic electrical conductivity in isostructural tetrathiafulvalene-based microporous metal-organic frameworks. *J. Am. Chem. Soc.*, 137(5):1774–1777, 2015.

[58] L. Sun, M. G. Campbell, and M. Dincă. Electrically conductive porous metal-organic frameworks. *Angew. Chem. Int. Ed.*, 55(11):3566–3576, 2015.

[59] H. Q. Pham, T. Mai, N.-N. Pham-Tran, Y. Kawazoe, H. Mizuseki, and D. Nguyen-Manh. Engineering of band gap in meta-organic frameworks by functionalizing organic linker: A systematic density functional theory investigation. *J. Phys. Chem. C*, 118(9):4567–4577, 2014.

[60] A. A. Talin, A. Centrone, A. C. Ford, M. E. Foster, V. Stavila, P. Haney, R. A. Kinney, V. Szalai, F. El Gabaly, H. P. Yoon, F. Leonard, and M. D. Allendorf. Tunable electrical conductivity in metal-organic framework thin-film devices. *Science*, 343(6166):66–69, 2014.

[61] T. Neumann, J. Liu, T. Wächter, P. Friederich, F. Symalla, A. Welle, V. Mugnaini, V. Meded, M. Zharnikov, C. Wöll, and W. Wenzel. Superexchange charge transport in loaded metal organic frameworks. *ACS Nano*, 10(7):7085 7093, 2016.

[62] C. J. Cramer. *Essentials of computational chemistry*. John Wiley and Sons, 2004.

[63] W. Koch and M. C. Holthausen. *A chemist's guide to density functional theory*. Wiley-VCH, 2001.

[64] K. Burke and friends. *The ABC of DFT*, April 2007.

[65] D. S. Sholl and J. A. Steckel. *Density functional theory - A pratical intoduction*. John Wiley and Sons, 2009.

[66] P. Puschnig. *Fundamentals of Electronic Structure Theory*. Institut für Physik, Fachbereich Theoretische Physik, Karl-Franzens-Universität Graz, December 2018.

[67] W. Kohn. Nobel lecture: Electronic structure of matter-wave functions and density functionals. *Rev. Mod. Phys.*, 71:1253, 1999.

[68] P. Hohenberg and W. Kohn. Inhomogeneous electron gas. *Phys. Rev.*, 136:B864–B871, 1964.

[69] F. Jensen. *Introduction to Computational Chemistry*. John Wiley and Sons, 2007.

[70] M. Levy. Electron densities in search of hamiltonians. *Phys. Rev. A*, 26:1200–1208, 1982.

[71] E. H. Lieb. Density functionals for coulomb systems. *Int. J. Quant. Chem.*, 24:243–277, 1983.

[72] W. Kohn and L. J. Sham. Self-consistent equations including exchange and correlation effects. *Phys. Rev.*, 140:A1133–A1138, 1965.

[73] L. H. Thomas. The calculation of atomic fields. *Camb. Phil. Soc.*, 23(5):542–548, 1927.

[74] E. Fermi. The calculation of atomic fields. *Rend. Acad. Maz. Lancei*, 6:602, 1927.

[75] L. Spruch. Pedagogic notes on thomas-fermi theory (and on some improvements): atoms, stars, and the stability of bulkmatter. *Rev. Mod. Phys.*, 63(1):151–209, 1999.

[76] J. P. Perdew, M. Ernzerhof, and K. Burke. Rationale for mixing exact exchange with density functional approximations. *J. Chem. Phys.*, 105:9982–9985, 1996.

[77] J. Heyd, G. E. Scuseria, and M. Ernzerhof. Erratum: "hybrid functionals based on a screened coulomb potential" [J. Chem. Phys. 118, 8207 (2003)]. *J. Chem. Phys.*, 124:219906(E), 2006.

[78] J. Heyd and G. E. Scuseria. Assessment and validation of a screened coulomb hybrid density functional. *J. Chem. Phys.*, 120:7274, 2004.

[79] J. Heyd and G. E. Scuseria. Efficient hybrid density functional calculations in solids: Assessment of the heyd-scuseria-ernzerhof screened coulomb hybrid functional. *J. Chem. Phys.*, 121:1187, 2003.

[80] J. Heyd, J. E. Peralta, G. E. Scuseria, and R. L. Martin. Energy band gaps and lattice parameters evaluated with the heyd-scuseria-ernzerhof screened hybrid functional. *J. Chem. Phys.*, 123:174101, 2005.

[81] J. E. Peralta, J. Heyd, G. E. Scuseria, and R. L. Martin. Spin-orbit splittings and energy band gaps calculated with the heyd-scuseria-ernzerhof screened hybrid functional. *Phys. Rev. B*, 74:073101, 2006.

[82] A. V. Krukau, A. F. Izmaylov O. A. Vydrov, and G. E. Scuseria. Influence of the exchange screening parameter on the performance of screened hybrid functionals. *J. Chem. Phys.*, 125:224106, 2006.

[83] R. G. Parr and W. Yang. *Density-functional theory of atoms and molecules.* Oxford University Press, 1989.

[84] P. Hobza, J. Sponer, and T. J. Reschel. Density functional theory and molecular clusters. *Comput. Chem.*, 11:1315–1325, 1995.

[85] S. Kristyan and P . Pulay. Can (semi)local density functional theory account for the london dispersion forces? *Chem. Phys. Lett.*, 229(3):175–180, 1994.

[86] W. Kutzelnigg. *Einfürung in die theoretische Chemie: Band 2, die chemische Bindung.* Verlag Chemie, Weinheim, 1978.

[87] U. Zimmerli, M. Parrinello, and P. Koumoutsakos. Dispersion corrections to density functionals for water aromatic interactions. *J. Chem. Phys.*, 120:2693, 2004.

[88] Q. Wu and W. Yang. Empirical correction to density functional theory for van der waals interactions. *J. Chem. Phys.*, 116:515, 2002.

[89] X. Wu, M. C. Vargas, S. Nayak, V. Lotrich, and G. Scoles. Towards extending the applicability of density functional theory to weakly bound systems. *J. Chem. Phys.*, 115:8748, 2001.

[90] E. M. Lifshitz. The theory of molecular attractive forces between solids. *J. Exper. Theoret. Phys. USSR*, 29:94–110, 1995.

[91] E. Zaremba and W. Kohn. Van der waals interaction between an atom and a solid surface. *Phys. Rev. B*, 13:2270–2285, 1976.

[92] R. S. Mulliken. Criteria for the construction of good self-consistent-field molecular orbital wave functions, and the significance of LCAO-MO population analysis. *J. Chem. Phys.*, 36:3428, 1962.

[93] P.-O. Löwdin. On the nonorthogonality problem. *Adv. Quantum Chem.*, 5:185–199, 1970.

[94] S. R. Cox and D. E. Williams. On the nonorthogonality problem. *J. Comput. Chem.*, 2(3):304–323, 1981.

[95] R. F. W. Bader. *Atoms in Molecules.* Clarendon Press, 1990.

[96] R. F. W. Bader. On the nonorthogonality problem. *Chem. rev.*, 91(5):893–928, 1991.

[97] P. L. A. Popelier. *Atoms in Molecules: an introduction.* Pearson Education, 1999.

[98] F. L. Hirshfeld. Bonded-atom fragments for describing molecular charge densities. *Theoret. Chim. Acta*, 44:129, 1977.

[99] G. Kresse and J. Hafner. *Ab initio* molecular dynamics for liquid metals. *Phys. Rev. B: Condens. Matter Mater. Phys.*, 47:558–561, 1993.

[100] G. Kresse and J. Hafner. *Ab initio* molecular-dynamics simulation of the liquid-metal-amorphous-semiconductor transition in germanium. *Phys. Rev. B: Condens. Matter Mater. Phys.*, 49:14251–14269, 1994.

[101] G. Kresse and J. Furthmüller. Efficiency of *ab initio* total energy calculations for metals and semiconductors using a plane wave basis set. *Comput. Mater. Sci.*, 6:15–50, 1996.

[102] G. Kresse and J. Furthmüller. Efficiency iterative schemes for *ab initio* total energy calculations using a plane wave basis set. *Phys. Rev. B: Condens. Matter Mater. Phys.*, 54:11169–11186, 1996.

[103] P. E. Blöchl. Projector augmented-wave method. *Phys. Rev. B*, 50:17953–17979, 1994.

[104] Gaussian 09, Revision D.03, M. J. Frisch, G. W. Trucks, H. B. Schlegel, G. E. Scuseria, M. A. Robb, J. R. Cheeseman, G. Scalmani, V. Barone, G. A. Petersson, H. Nakatsuji, X. Li, M. Caricato, A. Marenich, J. Bloino, B. G. Janesko, R. Gomperts, B. Mennucci, H. P. Hratchian, J. V. Ortiz, A. F. Izmaylov, J. L. Sonnenberg, D. Williams-Young, F. Ding, F. Lipparini, F. Egidi, J. Goings, B. Peng, A. Petrone, T. Henderson, D. Ranasinghe, V. G. Zakrzewski, J. Gao, N. Rega, G. Zheng, W. Liang, M. Hada, M. Ehara, K. Toyota, R. Fukuda, J. Hasegawa, M. Ishida, T. Nakajima, Y. Honda, O. Kitao, H. Nakai, T. Vreven, K. Throssell, J. A. Montgomery, Jr., J. E. Peralta, F. Ogliaro, M. Bearpark, J. J. Heyd, E. Brothers, K. N. Kudin, V. N. Staroverov, T. Keith, R. Kobayashi, J. Normand, K. Raghavachari, A. Rendell, J. C. Burant, S. S. Iyengar, J. Tomasi, M. Cossi, J. M. Millam, M. Klene, C. Adamo, R. Cammi, J. W. Ochterski, R. L. Martin, K. Morokuma, O. Farkas, J. B. Foresman, and D. J. Fox, Gaussian, Inc., Wallingford CT, 2016.

[105] V. Obersteiner, M. Scherbela, L. Hörmann, D. Wegner, and O. T. Hofmann. Structure prediction for surface-induced phases of organic monolayers: Overcoming the combinatorial bottleneck. *Nano Lett.*, 17(7):4453–4460, 2017.

[106] M. Scherbela, L. Hörmann, A. Jeindl, V. Obersteiner, and O. T. Hofmann. Charting the energy landscape of metal/organic interfaces via machine learning. *Phys. Rev. Materials*, 2:043803, 2017.

[107] J. Ossowski, G. Nascimbeni, T. Żaba, E. Verwüster, J. Rysz, A. Terfort, M. Zharnikov, E. Zojer, and P. Cyganik. Relative thermal stability of thiolate- and selenolate-bonded aromatic monolayers on the au(111) substrate. *J. Chem. Phys. C*, 121:28031–28042, 2017.

[108] A. M. Track, F. Rissner, L. Romaner, D. Käfer, A. Bashir, G. M. Rannger, O. T. Hofmann, T. Bučko, G. Witte, and E. Zojer. Simultaneusly understanding the geometric and electronic structure of anthraceneselenolate on au(111): A combined theoretical and experimental study. *J. Phys. Chem. C*, 114:2677–2684, 2010.

[109] H. Hälinen. The gold-sulfur interface at the nanoscale. *Nat. Chem.*, 4:443–455, 2012.

[110] K. Forster-Tonigold and A. Groß. A systematic dft study of substrate reconstruction effects due to thiolate and selenolate adsorption. *Surf. Sci.*, 640:18–24, 2015.

[111] A. Togo, F. Oba, and I. Tanaka. First-principles calculations of the ferroelastic transition between rutile type and $CaCl_2$-type SiO_2 at high pressures. *Phys. Rev. B.*, 78:134106, 2008.

[112] D. Otálvaro, T. Veening, and G. Brocks. Self-assembled monolayer induced Au(111) and Ag(111) reconstructions: Work functions and interface dipole formation. *J. Phys. Chem. C*, 116:7826–7837, 2012.

[113] M. Gärtner, E. Sauter, G. Nascimbeni, A. Petritz, A. Wiesner, M. Kind, T. Abu-Husein, M. Bolte, B. Stadlober, E. Zojer, An. Terfort, and M. Zharnikov. Understanding the properties of tailor-made self-assembled monolayers with embedded dipole moments for interface engineering. *J. Phys. Chem. C*, 122(50):28757–28774, 2018.

[114] T. Abu-Husein, S. Schuster, D. A. Egger, M. Kind, T. Santowski, A. Wiesner, R. Chiechi, E. Zojer, A. Terfort, and M. Zharnikov. The effects of embedded dipoles in aromatic self-assembled monolayers. *Adv. Funct. Mater.*, 25(25):3943–3957, 2015.

[115] C. Freysoldt, P. Eggert, P. Rinke, A. Schindlmayr, and M. Scheffler. Screening in two dimensions: GW calculations for surfaces and thin films using the repeated-slab approach. *Phys. Rev. B: Condens. Matter Mater. Phys.*, 77:214517, 2008.

[116] J. D. Jackson. *Classical electrodynamics*. Wiley: New York, 1999.

[117] J. Neaton, M. Hybertsen, and S. Louie. Renormalization of molecular electronics levels at metal-molecules interfaces. *Phys. Rev. Lett.*, 97:216405, 2006.

[118] A. Levstik, C. Filipič, and I. Levstik. Dielectric properties of biphenyl. *J. Phys.: Condens. Matter*, 2:3031–3033, 1990.

[119] Li Y., D. Lu, and G. Galli. Calculation of quasi-particle energies of aromatic self-assembled monolayers on au(111). *J. Chem. Theory Comput.*, 5:881–886, 2009.

[120] D. A. Egger, Z.-F. Liu, J. B. Neaton, and L. Kronik. Reliable energy level alignement at physisorbed molecule-metal interfaces from density functional theory. *Nano Lett.*, 15:2448–2455, 2015.

[121] C. L. A. Lamont and J. Wilkes. Attenuation length of electrons in self-assembled monolayers of n-alkanethioles on gold. *Langmuir*, 15:2037–2042, 1999.

[122] O. T. Hofmann, D. A. Egger, and E. Zojer. Work-function modification beyond pinning: When do molecular dipoles count? *Nano Lett.*, 10(11):4369–4374, 2010.

[123] L. Romaner, G. Heimel, and E. Zojer. Electronic structure of thiol-bonded self-assembled monolayers: Impact of coverage. *Phys. Rev. B*, 77(4):045113, 2008.

[124] J. Tersoff and D. R. Hamann. Theory of the scanning tunneling microscope. *Phys. Rev. B: Condens. Matter Mater. Phys.*, 31:805–813, 1985.

[125] Y. Ge, T. Weidner, H. Ahn, J. E. Whitten, and Zharnikov M. Energy level pinning in self assembled alkanethiol monolayers. *J. Chem. Phys. C*, 113:4575–4583, 2009.

[126] B. De Boer, A. Hadipour, M. M. Mandoc, T. Van Woudenbergh, and P. W. M. Blom. Tuning of metal work functions with self-assembled monolayers. *Adv. Mater.*, 17:621–625, 2005.

[127] B. H. Hamadani, D. A. Corley, J. M. Ciszek, J. W. andTour, and D. Natelson. Controlling charge injection in organic field-effect transistors using self-assembled monolayers. *Nano Lett.*, 6:1303–1306, 2006.

[128] G. Kresse and D. Joubert. Ultrasoft pseudopotentials to the projector augmented-wave method. *Phys. Rev. B: Condens. Matter Mater. Phys.*, 59:1758–1775, 1999.

[129] H. J. Monkhorst and J. D. Pack. Special points for brillouin-zone integrations. *Phys. Rev. B: Condens. Matter Mater. Phys.*, 13:5188–5192, 1976.

[130] G. Henkelman, A. Arnaldsson, and H. Jónsson. A fast and robust algorithm for bader decomposition of charge density. *Comput. Mater. Sci.*, 36:354–360, 2006.

[131] E. Sanville, S. D. Kenny, R. Smith, and G. Henkelman. Improved grid-based algorithm for bader charge allocation. *J. Comput. Chem.*, 28:899–908, 2007.

[132] W. Tang, E. Sanville, and G. Henkelman. A grid-based bader analysis algorithm without lattice bias. *J. Phys.: Condens. Matter*, 21:084204, 2009.

[133] M. Yu and D.R. Trinkle. Accurate and efficient algorithm for bader charge integration. *J. Chem. Phys.*, 134:064111, 2011.

[134] *http://theory.cm.utexas.edu/henkelman/code/bader/*, Visited on the 25.02.2019.

[135] J. V. Barth, R. Schuster, R. J. Behm, and G. Ertl. The system K/Au(111): adsorption and surface restructuring. *Surf. Sci.*, 348:280, 1996.

[136] L.-Y. Gan, R.-Y. Tian, X. B. Yang, and Y.-J. Zhao. Surface structure and phase transition of K adsorption on Au(111): by *ab initio* atomistic thermodynamics. *J. Chem. Phys.*, 136:044510, 2012.

[137] P. Van der Heide. *X-ray Photoelectron Spectroscopy, An Introduction to Principles and Practices.* John Wiley and Sons, 2012.

[138] G. J. Kraberger, D. A. Egger, and E. Zojer. Tuning the electronic structure of graphene through collective electrostatic effects. *Adv. Mater. Interfaces*, 2:1500323, 2015.

[139] C. Winkler, S. S. Harivyasi, and E. Zojer. Controlling the electronic properties of van der Waals heterostructures by applying electrostatic design. *2D Mater.*, 5:03519, 2018.

[140] V. Obersteiner, A. Jeindl, J. Götz, A. Perveaux, O. T. Hofmann, and E. Zojer. Electrostatic design of 3D covalent organic networks. *Adv. Mater.*, 29(27):1700888, 2017.

[141] K. Momma and F. Izumi. Vesta: a three-dimensional visualization system for electronic and structural analysis. *J. Appl. Crystallogr.*, 41:653–658, 2008.

[142] A. Kokalj. Xcrysden - a new program for displaying crystalline structures and electron densities. *J. Mol. Graph. Model.*, 17:176–179, 1999.

[143] F. Rissner, A. Natan, D. A. Egger, O. T. Hofmann, L. Kronik, and E. Zojer. Dimensionality effects in the electronic structure of organic semiconductors consisting of polar repeat units. *Org. Electron.*, 13(12-2):3165–3176, 2012.

[144] J. Topping. On the mutual potential energy of a plane network of doublets. *Proc. R. Soc. London Ser. A*, 114:68–72, 1927.

[145] D. Prochowicz, K. Sokołwski, and J. Lewinński. Zinc hydroxides and oxides supported by organic ligands: Synthesis and structural diversity. *Coord. Chem. Rev.*, 270-271:112–126, 2014.

[146] S. Mendiratta, C. H. Lee, S.-Y. Lee, B.-C. Chang Y.-C. Kao, Y.-H. Lo, and K.-L. Lu. Structural characteristics and non-linear optical behaviour of a 2-hydroxynicotinate-containing zinc-based metal-organic framework. *Molecules*, 20(5):8941–8951, 2015.

[147] G. Wu, J. Huang, Y. Zang, J. He, and G. Xu. Porous field-effect transistors based on a semiconductive metal-organic framework. *J. Am. Chem. Soc.*, 139(4):1360–1363, 2017.

[148] J. Heyd, G. E. Scuseria, and M. Ernzerhof. Hybrid functionals based on a screened coulomb potential. *J. Chem. Phys.*, 118:8207, 2003.

[149] N. Seiki, Y. Shoji, T. Kajitani, F. Ishiwari, A. Kosaka, T. Hikima, M. Takata, T. Someya, and T. Fukushima. Rational synthesis of organic thin films with exceptional long-range structural integrity. *Science*, 348:1122–1126, 2015.

[150] H. Shioya, Y. Shoji, N. Seiki, M. Nakano, T. Fukushima, and Y. Iwasa. Raising the metal-insulator transition temperature of VO2 thin films by surface adsorption of organic polar molecules. *Appl. Phys. Express*, 8:121101, 2015.

[151] F. K.-C. Leung, F. Ishiwari, T. Kajitani, Y. Shoji, T. Hikima, M. Takata, A. Saeki, S. Seki, Y. M. A. Yamada, and T. Fukushima. Supramolecular scaffold for tailoring the two-dimensional assembly of functional molecular units into organic thin films. *J. Am. Chem. Soc*, 138:11727–11733, 2016.

[152] T. Yokota, T. Kajitani, R. Shidachi, T. Tokuhara, M. Kaltenbrunner, Y. Shoji, F. Ishiwari, T. Sekitani, T. Fukushima, and T. Someya. A few-layer molecular film on polymer substrates to enhance the performance of organic devices. *Nat. Nanotech.*, 13:139–144, 2018.

[153] F. Ishiwari, Y. Shoji, and T. Fukushima. Supramolecular scaffolds enabling the controlled assembly of functional molecular units. *Chem. Sci.*, 9:2028–2041, 2018.

[154] F. Ishiwari, G. Okabe, H. Ogiwara, T. Kajitani, M. Tokita, M. Takata, and T. Fukushima. Terminal functionalization with a triptycene motif that dramatically changes the structural and physical properties of an amorphous polymer. *J. Am. Chem. Soc.*, 140:13497–13502, 2018.